Accelerator and Detector Research

2024 Principal Investigators' Meeting

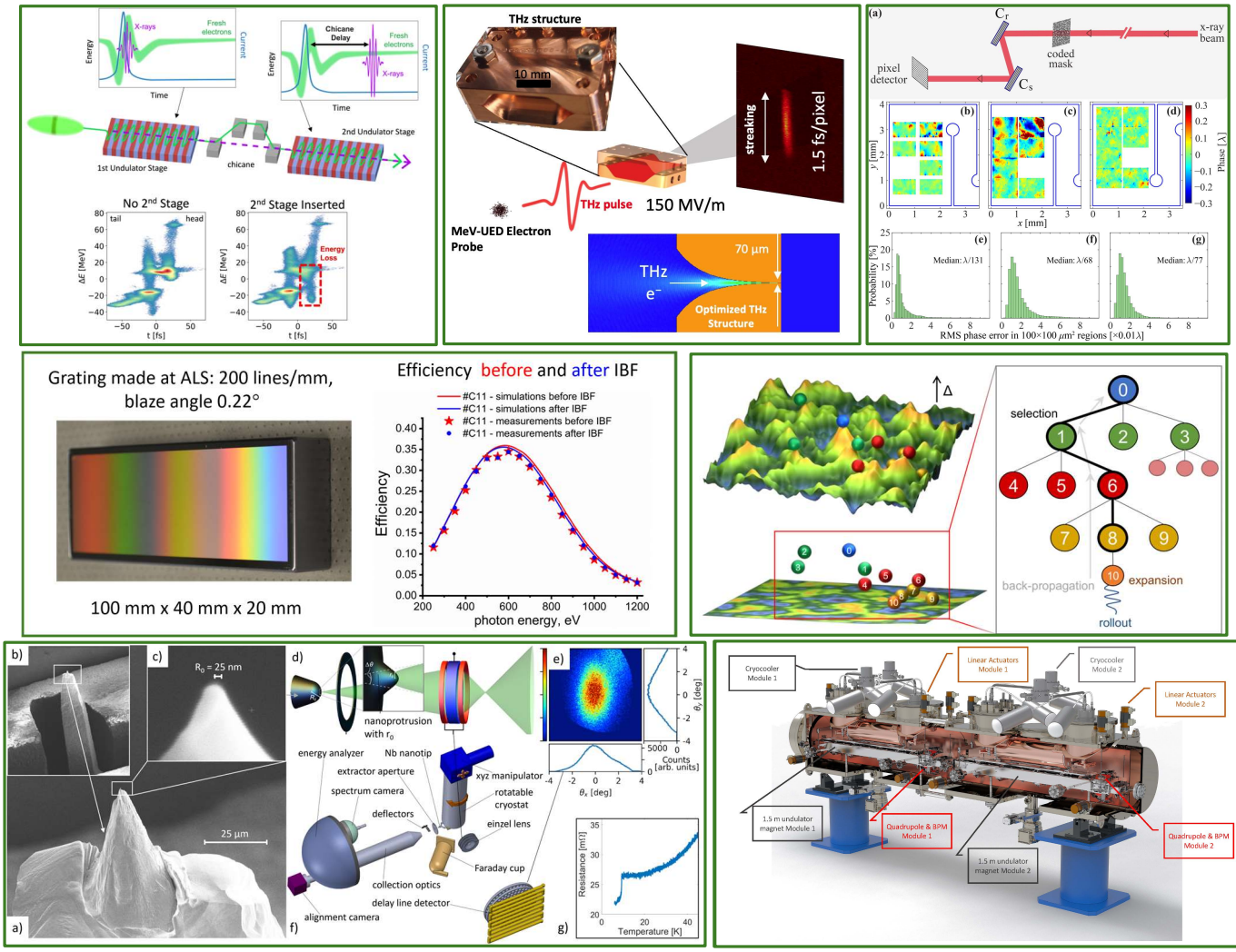

Virtual Meeting April 16-19, 2024

U.S. DEPARTMENT OF ENERGY | Office of Science

Office of Basic Energy Sciences

Scientific User Facilities Division

On the Cover

Top Row Left: In this cascading amplification experiment, an electron bunch (represented in green) is used in an x-ray free-electron laser to generate an attosecond x-ray pulse (represented as a purple line). By overlapping the x-ray pulse with an unused part of the electron bunch, the pulse can be re-amplified in a second undulator, in a process called superradiant amplification. The data shows the measured distribution of electrons as a function of energy and time, showing how the energy of the electrons is transferred to the x-rays. This process gives rise to soliton-like behavior in the x-ray laser, and results in the generation of pulses with terawatt-scale peak power. Courtesy: P. Franz et al. "Terawatt-scale Attosecond X-ray Pulses from a Cascaded Superradiant Free-electron Laser",*Nature Photonics* (2024). https://doi.org/10.1038/s41566-024-01427-w. **Center:** A short electron probe bunch and a terahertz (THz) pulse are incident upon a copper deflecting structure (detailed in upper left inset). The terahertz pulse excites a transverse field of 150 MV/m inside the 70-micron channel of the structure (bottom inset field plot). The electrons sample the time-varying deflection, such that the head and the tail of the bunch are deflected in opposite directions, producing a vertically streaked image on a downstream detector. The streaked image displays the time profile of the electron bunch with 1.5 femtosecond per pixel resolution. Courtesy: Mohammed Othman, SLAC National Accelerator Laboratory, M. A. K. Othman et al., "Efficient THz Time-Stamping of Ultrafast Electron Probes," *2022 47th International Conference on Infrared, Millimeter and Terahertz Waves* (IRMMW-THz) (2022). https://doi.org/10.1109/IRMMW-THz50927.2022.9895642. **Right**: Characterization of the x-ray wavefront upon Bragg diffraction from diamond crystal mirrors selected for the cavity-based x-ray free-electron laser (CBXFEL) project. (a) Schematic of the experimental setup at APS beamline 1-BM, which includes a binary coded mask as a wavefront sensor, reference crystal Cr, and sample diamond crystal Cs. (b)-(d) Measured x-ray wavefront phase error maps for the selected diamond crystals. (e)-(g) Distribution of the rms phase errors in 100x100 μm2 regions of the corresponding crystals. The median, and mean rms wavefront phase errors are within the λ/70-tolerance level required for the CBXFEL project. Courtesy: Peifan Liu, et. al., *Journal of Synchrotron Radiation* (2024). Accepted for publication.

Center Row Left: Nanometer-level planarity post-production correction of a low blaze angle grating (left) using Ion Beam Figuring (IBF) coupled with stitching Interferometry (NSLS-II). The NSLS-II IBF process based on a robust dwell time algorithm provides deterministic surface correction at low frequency while the saw-tooth groove shape and diffraction efficiency are highly preserved (right). Courtesy: https://doi.org/10.1364/OE.501418. **Right:** Schematic of the continuous action Monte Carlo Tree Search (c-MCTS) algorithm developed by us for exploration of high-dimensional potential parameter surfaces. Simplistic representation of an objective landscape for a two-parameter search problem is shown on the left. In-plane axes correspond to (two) independent model parameters. The out-of-plane axis corresponds to objective values, which is defined as the weighted sum of the error in model predicted energies of clusters with respect to target energies. This objective is minimized by our c-MCTS algorithm shown in right. The spheres represent candidates of different model parameters within an MCTS run, where differences in their vertical positions indicate differences in their objective values. Courtesy: Subramanian Sankaranarayanan, Argonne National Laboratory and University of Illinois, Chicago, Manna et. al,*Nature Communication*, (2022), https://doi.org/10.1038/s41467-021-27849-6.

Bottom Row Left: A novel superconducting niobium nanotip emitter and the setup for characterizing its capabilities is shown. Panels (a)-(c) present scanning electron microscopy images of the emitter. Atop the 25nm-radius tip, a 1.3nm-nano protrusion (panel d) has formed, inducing extraordinary field emission with a small angular distribution angle (panel e). Panel (f) shows the characterization setup at The Molecular Foundry, where the tip is cryo-cooled and energy, current and timing are measured. Panel (g) demonstrates the superconductivity of the tip, evidenced by a sudden drop in resistivity at the transition temperature. Courtesy: Alexander Stibor, Lawrence Berkeley National Lab, Johnson et al., *Phys. Rev. Lett.* **129**, 244802 (2022); Johnson et al., *Phys. Rev. Applied* **19**, 034036 (2023). **Right:** Two adjacent cryomodules are shown, each module housing a 1.5 m SC undulator magnet mounted on an alignment girder (grey), together with a focusing quadrupole and beam position monitor (red). The alignment girder is suspended from external linear actuators (brown) and aligned to the beam with micron accuracy after the magnets have been cooled to 4.2K by the cryocoolers mounted on the top turrets. The cryomodules are being designed and fabricated at ANL for installation on the LCLS beamline at SLAC to produce more powerful X-rays than can be achieved with the present permanent magnet undulators. Courtesy: Patrick Krejcik, SLAC National Accelerator Laboratory and Efim Gluskin, ANL.

Foreword

This booklet presents the collection of extended abstracts submitted to the Accelerator and Detector Research Principal Investigators meeting. The virtual meeting was sponsored by the Department of Energy, Office of Basic Energy Sciences (BES), Scientific User Facilities (SUF) Division, and held on April 16-19, 2024.

The purpose of the Principal Investigators meeting is to bring together all the principal investigators and their co-PIs who are supported by the Accelerator and Detector Research program to share the latest exciting scientific knowledge and discoveries, facilitate exchange of ideas and promote collaborations. This meeting brings together leading experts in topical areas of research supported by the program and is designed to stimulate and inspire new ideas. For BES and the participating investigators, the meeting serves the purpose of providing an overview and assessment of the whole program, which helps BES to identify new research areas and chart the program's future directions.

The Accelerator and Detector Research program supports basic research in accelerator physics, x-ray and neutron detectors, and x-ray-optics. The program encourages the development of advanced concepts for new types of x-ray instruments as well as innovative uses of existing instruments, especially in the area of novel techniques for new experimental capabilities, advanced x-ray optics development, and applications of artificial intelligence and machine learning algorithms to data manipulation and analysis.

The 2024 Principal Investigators meeting brought together over one hundred researchers. The meeting confirmed the breadth of instrumentation, accelerator physics, and a rich portfolio in many ground-breaking, exciting, and high-risk high-reward research projects supported by the program. Among the many highlights were the first demonstration of low-loss stable storage of X-rays at Angstrom-wavelength achieved at the SLAC X-ray free electron laser (FEL) cavity; the first demonstration of attosecond x-ray pump/probe capabilities and the generation and measurement of Terawatt-scale superradiant pulses at the X-ray Laser-enhanced Attosecond Pulse Generation (XLEAP) instrument; and the validation of X-ray oscillators producing intense, fully coherent, transform-limited pulses. Also highlighted were the developments of a plasma-based modality of electron beam injectors which can revolutionize light source facilities; APS's ultrafast x-ray optics-on-a-chip based on MEMS, which is capable of modulating hard x-ray pulses at frequencies 103 times higher than any other mechanical modulator; development of a strip detector and of a high-rate neutron reflectometer that meet the performance metrics for current and future neutron facilities; and initial steps towards demonstration of the technical advantages and feasibility of an all-superconducting (SC) electron microscope to study quantum phenomena and the physics of devices for quantum information science. Many innovative results were presented on artificial intelligence (AI/ML) methods applied to experimental data –e.g., the integrated physics modeling and online ML for characterization and tuning of accelerator

systems, and the development of AI- methods to reconstruct 3-dimensional (3D) tensor quantities in crystalline materials from neutron or X-ray hyperspectral tomography systems. Finally, the MLExchange research project, whose effort towards an ecosystem where users can access a variety of analytical and ML-based software solutions, presented an excellent example of the strong collaboration among diverse groups the program advocates.

I appreciate the contributions of all investigators for sharing their exciting ideas and latest findings. I am grateful for the outstanding support of Dr. Yiping Feng, IPA from SLAC, Mr. Paul Hudson of the Oak Ridge Institute for Science and Education, and Ms. Teresa Crockett of MSE.

Eliane Lessner
Program Manager
Accelerator and Detector Research Program
Division of Scientific User Facilities
Office of Basic Energy Sciences
Department of Energy
April 2024

Table of Contents

Agenda..... viii

Abstracts

Optical Cavity Based X-ray Free-Electron Lasers
Z. Huang, G. Lanza, R. Lindberg, and M. White 2

Population inversion X-ray Laser Oscillator
Aliaksei (Alex) Halavanau, Claudio Pellegrini, Uwe Bergmann, and Andrei Benediktovitch 8

Attosecond Science with High Repetition Rate Xray Free-Electron Lasers
Agostino Marinelli 12

Extending the reach of light source facilities with precision laser plasma injectors
Sam Barber..... 18

Enhanced Self Seeding and Coherent Control of X-Ray Free Electron Lasers
Erik Hemsing 23

Beam on Demand for Superconducting Based X-Ray Free-Electron Lasers
Zhen Zhang 27

Research and Development of High-Power, High Repetition-Rate THz Capabilities for LCLS-II
Z. Huang, A. S. Fisher, M. Henstridge, M. C. Hoffmann, A. Naji, and M. Othman 32

Laser-based THz Radiation for Advances in Ion Accelerators
M. Doleans, G. Hine, and C. Moss 37

On the Prospects for Terawatt X-ray Free-Electron Lasers
Henry P. Freund, Patrick G. O'Shea, and Thomas M. Antonsen 41

Electron Beam Magnetic Field Mapping Technology for Undulators and Magnets
Marcos Turqueti..... 46

Double Nb3Sn Superconducting Undulator for the Advanced Photon Source
Efim Gluskin..... 49

Superconducting Undulator R&D for World-Leading X-ray FEL Capabilities
Patrick Krejcik 51

Cryogenically-cooled-silicon mirrors for diffraction-limited storage rings and free-electron lasers
Lahsen Assoufid, Lei Huang, Grant Cutler, and Thomas Rabedeau 54

Diffraction-limited and wavefront preserving reflective optics development at NSLS-II
Mourad Idir, Lei Huang, and Tianyi Wang 60

Development of PFIB-Xray System for Multi-scale Analysis
Si Chen 66

Diffraction-limited Radiation Enhancement with Adaptive Mirrors for x-ray coherent beamlines
Antoine Islegen-Wojdyla 71

Monolithic 2D MLL optics for high-resolution hard X-ray microscopy
E. Nazaretski 76

21st Century Methods for Making Gratings
Dmitriy Voronov, and Howard Padmore 80

Investigate Wavefront Preservation Methods for the Bragg Reflection from Diamond Crystals in X-Ray FEL Oscillators (XFELO)
Yuri Shvyd'ko, and Kwang-Je Kim 85

Integrated Cryocooling and Strain-free Mounting of Ultra-Thin Diamond Crystals for Hard X-Ray Self-Seeding (HXRSS) System
Yanbao Ma, and Juhao Wu 90

New Capabilities for Simulation of Coherent X-ray Scattering Experiments at Light Sources
Oleg Chubar 95

X-ray Beam Position Monitor R&D for Coherent Soft X-ray Beamlines
Boris Podobedov, Claudio Mazzoli, and Dmitri Donetski 101

Advanced MEMS-Based Dynamic Optics-on-A-Chip for New-Generation X-ray Sources
Jin Wang 106

Applications of the Superconducting Helical Undulator at the APS
Jin Wang 111

Evaluation of Hi-Z Detector Materials for X-ray Science
Julia Thom-Levy, Nino Micelli, Abdul K. Rumaiz, and Julie Segal 116

SparkPix-RT: An edge computing engine for ultra-fast photon science detectors
Angelo Dragone, Antonino Miceli, Jana Thayer, ... 120

Germanium drift detector for synchrotron sciences
Abdul K. Rumaiz 125

Timepix Detectors for Soft X-ray Photon Correlation Spectroscopy
Sujoy Roy, Anton Tremsin, Yi-De Chuang, Sophie Morley, and Steve Kevan 128

Very High-Speed Electron Spectroscopy Detector
Peter Denes 133

Towards an Ultra-Stable, Ultra-Cold Transmission Electron Microscope
Peter Denes 136

The Potential of Lithium-Containing Semiconductors at Neutron Scattering Facilities
Eric Lukosi, and Mercouri Kanatzidis 140

Neutron detector development for high-rate neutron reflectometry at the Second Target Station of Oak Ridge National Laboratory
Xianfei Wen, and Jason P. Hayward 145

Quantum Limited Parametric Amplifiers for X-Ray Sensors
Douglas Bennett 148

Development of Sensors and Readout for Multi-GHz Particle Beam Characterization
Bruce A. Schumm, Eric Prebys, Carl Grace, Jonathan Smedley, and Mark Gulley 153

Next-generation Photoinjectors for High-Brightness Beams and XFELs
Sergio Carbajo 158

High Brightness Photocathodes in Photoinjectors
Siddharth Karkare 164

High Brightness Electronically Tunable Negative Electron Affinity Cathodes for Accelerator Applications
Rehan Kapadia 169

Photocathode material for the LCLSII-HE SRF gun
John Smedley, Jared Maxson, Siddharth Karkare, Pietro Musumeci, Theodore Vecchione, and Tianhuan Luo 174

Control of Bright Electron Beams at Small Spatiotemporal Scales for Probing Materials Far from Equilibrium
Jared Maxson 178

Enabling Ultrafast Structural Dynamics at the Nanoscale in MeV-UED Setups
Joel England 183

Enabling ultrafast structural dynamics at the nanoscale in MeV-UED setups
Dan Wang 187

Integrated Physics Modeling and Online Machine Learning for Characterization and Tuning of Particle Accelerator Systems
Auralee Edelen 191

Machine Learning for Autonomous Control of Accelerators
Daniel Ratner, Michael Borland, Guimei Wang Auralee Edelen, and Xiaobiao Huang 196

Machine Learning for Improving Accelerator and Target Performance
Willem Blokland and Malachi Schram 201

Actionable Information from Sensor to Data Center
Jana Thayer, Ryan Coffee, Ryan Herbst, Ian Foster, Peter Kenesei, Michael Prince, Hemant Sharma, Antonino Miceli, Nicholas Schwarz, and Rajkumar Kettimuthu 207

MLExchange: A Collaborative Machine Learning Platform for Scientific Discovery
Alexander Hexemer, Daniel Allan, Apurva Mehta, Nicholas Schwarz, Subramanian Sankaranarayanan, and Rama K. Vasudevan 213

Intelligent Acquisition and Reconstruction for Hyperspectral Tomography Systems: Solving Tensor Tomography
Hassina Bilheux, Singanallur (Venkat) Venkatakrishnan, Jean Bilheux, Shimin Tang, Stuart Campbell, Xiaogang Yang, Nghia Vo, Dmitri Gavrilov, Charles Bouman, Gregery Buzzard, and Mohammad Samin Nur Chowdhury 219

Artificial Intelligence for MultiModal Analysis (AIMM): Integrated Platform for Multimodal Data Capture, Exploration and Discovery Driven by AI Tools
Eli Stavitski, Daniel Allen, Stuart Campbell, Deyu Lu, Xiaohui Qu, Shinjae Yoo, Maria K. Chan, Steve M. Heald, Nicholas Schwarz, Chengjun Sun, Dylan McReynolds, and Wanli Yang 225

A Digital Twin for Spatiotemporally Resolved Experiments
Subramanian Sankaranarayanan, Maria K. Chan, Pierre Darancet, Henry Chan, Tom Peterka, Mathew Cherukara, Bobby Sumpter, and Stephen Whitelam 231

Electron Distillery 2.0: Massive Electron Microscopy Data to Useful Information with AI/ML
Andrew Minor..... 237

Author Index 243

Participant List.....246

Agenda

PI/Speaker	Institute	Title	Category	Presentation (Invited)	Presentation Number	Start Time (all time Eastern)	Moderator
Day - One (4/16/24) - All Time Eastern							
Eliane Lessner	BES	Opening Remarks (20 mins)				**10:00**	
Mike Dunne	SLAC/LCLS	Sources for Next Generation Sciences		Plenary	**P1**	**10:20**	E. Hemsing
Zhirong Huang	SLAC	The promise and potential of Cavity-Based X-ray FEL (CBXFEL)	XFEL (partner)	y	D1-1	11:05	
Alex Halavanau	SLAC	X-ray Oscillator (Renewal)	XFEL	y	D1-2	11:35	
Agostino Marinelli	SLAC	Attosecond Science with High Repetition Rate X-ray Free-Electron Lasers	XFEL	y	D1-3	12:05	
Samuel Barber	LBNL	Extending the reach of light source facilities with precision laser plasma injectors	Accel Physics	y	D1-4	12:35	
Break - 1 (30 mins)						13:05 - 13:35	
Erik Hemsing	SLAC	Enhanced Self Seeding and Coherent Control of X-Ray Free Electron Lasers	XFEL	y	D1-5	13:35	S. Barber
Zhen Zhang	SLAC	Beam on Demand for Superconducting Based X-Ray Free-Electron Lasers	XFEL	y	D1-6	14:05	
Zhirong Huang	SLAC	Research and Development of High-Power, High-Repetition-Rate THz Capabilities for LCLS-II	THz	y	D1-7	14:35	
Marc M. Doleans	ORNL	Laser-Based THz Radiation for Advances in Ion Accelerators	THz	y	D1-8	15:05	
Break - 2 (25 mins)						15:35 - 16:00	
Henry Freund	U. of Maryland	On the Prospects for Terawatt X-ray Free-Electron Lasers	XFEL	y	D1-9	16:00	O. Chubar
Marcos Turqueti	LBNL	Electron Beam Magnetic Field Mapping Technology for Undulators and Magnets	Undulators	y	D1-10	16:30	
Efim Gluskin	ANL	Double NB3Sn Superconducting Undulator for the APS	SCU	y	D1-11	17:00	
Patrick Krejcik	SLAC	Superconducting Undulator R&D for World-Leading X-ray FEL Capabilities	SCU (partner)	Y	D1-12	17:30 - 18:00	

PI/Speaker	Institute	Title	Category	Presentation (Invited)	Presentation Number	Start Time (all time Eastern)	Moderator
Day - Two (4/17/24) - All Time Eastern							
Andreas Scholl	LBNL	Next Generation Optics/Diagnostics/Instrumentation		Plenary	**P2**	**10:00**	
Thomas Rabedeau	SLAC	Cryogenically-cooled-silicon mirrors for diffraction-limited storage rings and free-electron lasers	Optocs (partner)	Y	D2-1	10:45	E. Nazaretski
Mourad Idir	BNL	Diffraction-limited and wavefront preserving reflective optics development at NSLS-II	Optics	y	D2-2	11:15	
Si Chen	ANL	Development of PFIB-Xray System with Machine Learning Method to Realize Comprehensive Analysis from Macro- to Nano-scale	Optics	y	D2-3	11:45	
Antoine Wojdyla	LBNL	Diffraction-limited Radiation Enhancement with Adaptive Mirrors for x-ray coherent beamlines	Optics	y	D2-4	12:15	
Break - 1 (30 mins)						12:45 - 13:15	
Evgeny Nazaretski	BNL	Monolithic 2D MLL Optics for High ResolutionHard X-ray Microscopy	Optics	y	D2-5	13:15	S. Chen
Dmitriy Voronov	LBNL	21st century methods for making x-ray gratings	Optics	y	D2-6	13:45	
Yury Shvydko	ANL	Investigate wavefront preservation methods for the Bragg reflection from diamond in X-Ray FEL Oscillators	Optics	y	D2-7	14:15	
Yanbao Ma	UC Merced	Integrated Cryocooling and Strain-free Mounting of Ultra-Thin Diamond Crystals for Hard X-Ray Self-Seeding (HXRSS) System	Optics Cryo-cooling (partner)	y	D2-8	14:45	
Break - 2 (30 mins)						15:15 - 15:45	
Oleg Chubar	BNL	New Capabilities for Simulation of Coherent X-ray Scattering Experiments at Light Sources	Optics	y	D2-9	15:45	M. Idir
Boris Podobedov	BNL	X-Ray Beam Position Monitor R&D For Coherent Soft X-Ray Beamlines	X-Ray Diagnostics	Y	D2-10	16:15	
Jin Wang	ANL	Advanced MEMS-Based Dynamic Optics-on-A-Chip for New-Generation X-ray Sources	Optics	y	D2-11	16:45	
Jin Wang	ANL	Applications of the Super Conducting Helical Undulator at the APS	X-ray Instrument	y	D2-12	17:15 - 17:45	
All Participants		Overflow Free Discussion				17:45 - 18:00	

PI/Speaker	Institute	Title	Category	Presentation (Invited)	Presentation Number	Start Time (all time Eastern)	Moderator
Day - Three (4/18/24) - All Time Eastern							
Heinz Graafsma	DESY	Next Generation Detectors		Plenary	**P3**	**10:00**	
Julia Thom-Levy	Cornell	Evaluation of Hi-Z Detector Materials for X-ray Science -Collaboration	Detectors (partner)	Y	D3-1	10:45	P. Denes
Antonino Miceli	ANL	SparkPix-RT: An Edge Computing Engine for Ultra-Fast Photon Science Detector- Collaboration w/ ANL	Detectors (partner)	y	D3-2	11:15	
Abdul Rumaiz	BNL	Germanium drift detector for synchortron sciences	Detectors	y	D3-3	11:45	
Sujoy Roy	LBNL	Timepix Detectors for Soft X-ray Photon Correlation Spectroscopy-Renewal	Detectors (Experiment)	y	D3-4	12:10	
Break - 1 (30 mins)						12:35 - 13:05	
Peter Denes	LBNL	Very High-Speed Electron Spectroscopy Detector	Detectors	y	D3-5	13:05	G. Carini
Peter Denes	LBNL	Towards an Ultra-Stable, Ultra-Cold Transmission Electron Microscope	Detectors	y	D3-6	13:30	
Eric D. Lukosi	U. of Tennessee, Knoxville	A State-of-the-Art Neutron Imaging Sensor for DOE User Facilities	Detectors	y	D3-7	13:55	
Jason P. Hayward	U. of Tennessee, Knoxville	Neutron detector development for high-rate neutron reflectometry at the Second Target Station of Oak Ridge National Laboratory	Detectors	Y	D3-8	14:20	
Douglas Bennett	NIST	Quantum-Limited Parametric Amplifiers for X-ray Sensors	Detectors	y	D3-9	14:45	
Bruce Schumm	UC Santa Cruz	Development of Sensors and Readout for Multi-GHz Particle Beam Characterization	Detectors (partner)	Y	D3-10	15:10	
Break - 2 (35 mins)						15:40 - 16:15	
Sergio Carbajo	UCLA	Next-generation Photoinjectors for High Brightness Beams and XFELs	Photoinjector	y	D3-11	16:15	J. Maxson
Siddarth Karkare	ASU	High Brightness Photocathodes in Photoinjectors	Photoinjector	y	D3-12	16:40	
Rehan Kapadia	U. of Southern California	High Brightness Electronically Tunable Negative Electron Affinity Cathodes for Accelerator Applications	Photoinjector	y	D3-13	17:05	
Siddarth Karkare (ASU) for John Smedley	SLAC	Proposal for studies to determine the optimal photocathode material for the LCLSII- HE SRF gun and to specify its operating parameters	Photoinjector (partner)	y	D3-14	17:30 - 18:00	

PI/Speaker	Institute	Title	Category	Presentation (Invited)	Presentation Number	Start Time (all time Eastern)	Moderator
Day - Four (4/19/24) - All Time Eastern							
Bobby Sumpter	ORNL	Data Science		Plenary	**P4**	**10:00**	
Jared Maxson	Cornell	Control of Bright Electron Beams at Small Spatiotemporal Scales for Probing Materials Far from Equilibrium	UED	y	D4-1	10:45	R. Kapadia
Joel England	SLAC	Ultrafast High-Brightness Electron Beam & Detector R&D at SLAC MeV-UED	UED	y	D4-2	11:15	
Dan Wang	LBNL	Enabling ultrafast structural dynamics at the nanoscale in MeV-UED setups	UED (partner)	Y	D4-3	11:45	
Break - 1 (30 mins)						12:15 - 12:45	
Auralee Edelen	SLAC	Integrated Physics Modeling and Online Machine Learning for Characterization and Tuning of Particle Accelerator Systems	ML	y	D4-4	12:45	H. Bilheux
Daniel Ratner	SLAC	Machine Learning for Autonomous Control of Accelerators	DAIML (partner)	y	D4-5	13:15	
Willem Blokland	ORNL	Machine Learning for Improving Accelerator and Target Performance	DAIML (partner)	y	D4-6	13:45	
Jana Thayer	SLAC	Actionable Information from Sensor to Data Center	DAIML (partner)	y	D4-7	14:15	
Alexander Hexemer	LBNL	Collaborative Machine Learning Platform for Scientific Discovery	DAIML (partner)	y	D4-8	14:45	
Break - 2 (25 mins)						15:15 - 15:40	
Hassina Bilheux	ORNL	Intelligent Acquisition and Reconstruction for Hyperspectral Tomography	DAIML (partner)	y	D4-9	15:40	J. Thayer
Eli Stavitski	BNL	Integrated Platform for Multimodal Data Capture, Exploration and Discovery Driven by AI Tools	DAIML (partner) NCE	Y	D4-10	16:10	
Subramanian Sankaranarayanan	ANL	A Digital Twin for In-silico Spaciotemporally-resolved Experiments	DAIML (partner)	y	D4-11	16:40	
Andrew Minor	LBNL	4DCamera Distillery: From Massive Electron Microscopy Scattering Data to Useful Information with AI/ML	DAIML (partner)	y	D4-12	17:10	
Eliane Lessner, Yiping Feng	BES	Closing Remarks (20 mins)				17:40 - 18:00	

Abstracts

Session One

Accelerator Physics

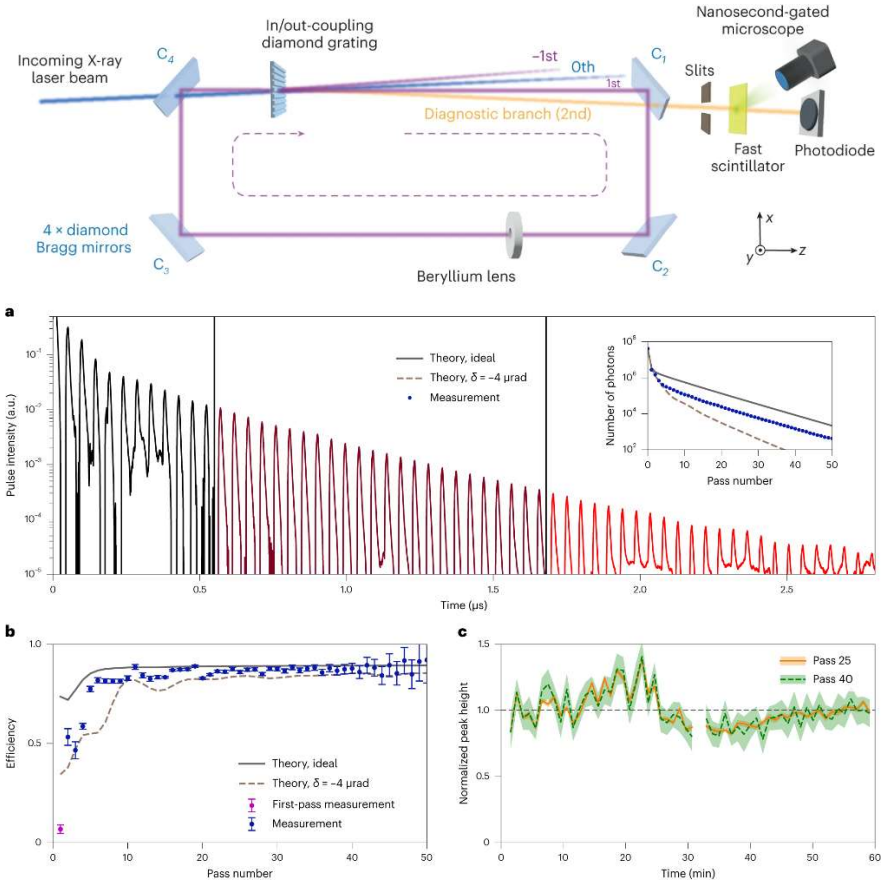

Four diamond Bragg mirrors are used as the main cavity optics. A portion of the incoming X-ray laser beam (blue, zeroth order) is injected into the cavity by a diamond transmission grating using its first-order diffraction (purple). The purple rectangle indicates the circulating beam trajectory inside the cavity once the correct photon energy has been chosen and the Bragg mirrors are aligned. A beryllium lens can be inserted into the beam path to stabilize the beam propagation over many round trips. The orange beam path indicates the first-order diffraction of the circulating beam (at second-order position with respect to the zeroth-order incoming beam) as it passes through the diamond grating each time. This beam was isolated and used for beam dynamics monitoring with a high-speed imager consisting of a fast scintillator and a nanosecond-gated microscope. The transmitted beam through the thin scintillator is measured by a downstream photodiode. Courtesy: Margraf, R., Robles, R., Halavanau, A. et al. Low-loss stable storage of 1.2 Å X-ray pulses in a 14 m Bragg cavity. *Nat. Photon*. **17**, 878–882 (2023). https://doi.org/10.1038/s41566-023-01267-0.

Optical Cavity Based X-ray Free-Electron Lasers

Z. Huang, G. Lanza, R. Lindberg, M. White for the CBXFEL collaboration (ANL/SLAC)

Keywords: FEL, XFELO, XRAFEL, Bragg Cavity, X-ray optics

Research Project Scope

Optical cavities are typically employed to define the stable modes of a laser and to achieve high temporal coherence. While the first infrared and visible free-electron lasers (FELs) similarly employed optical cavities, scaling such a device to X-rays has significant technological barriers. For this reason, all current XFELs have adopted the single-pass, high-gain design, wherein the initial spontaneous radiation is amplified to produce X-ray pulses that are intense and transversely coherent but suffer from relatively poor temporal coherence. Nevertheless, improving X-ray temporal coherence has been one of the main avenues of FEL research, with X-ray cavities being one of the most promising. Significantly, recent advances in the production of defect- and strain-free synthetic diamond crystals, along with improvements in the design and fabrication of ultra-precise mechanical stages, have shown that a cavity-based XFEL is feasible, setting the stage for fully coherent X-ray laser output of unparalleled stability and brightness.

The Cavity-Based X-ray Free Electron Laser (CBXFEL) R&D project is a joint Argonne National Laboratory, SLAC National Accelerator Laboratory, and RIKEN SPring-8 collaboration aimed at studying the physics of cavity-based FEL schemes and enabling their future implementation at high-repetition-rate facilities. To do this, the project has designed and is in the process of building a rectangular X-ray cavity that will enclose the first seven hard X-ray undulators at the LCLS. The project's primary scientific goal is to use a pair of electron bunches from the SLAC copper linac to measure the two-pass FEL gain for both the high-gain X-ray regenerative amplifier (XRAFEL) [1] and the low-gain X-ray free-electron laser oscillator (XFELO) [2] schemes. In addition, cavity ring-down measurements will be made, from which the optical alignment accuracy and stability can be determined. These experiments are designed to demonstrate the feasibility of a full-scale CBXFEL with the requisite X-ray optical cavity tolerances needed for future operation with a high repetition rate electron beam from LCLS-II-HE.

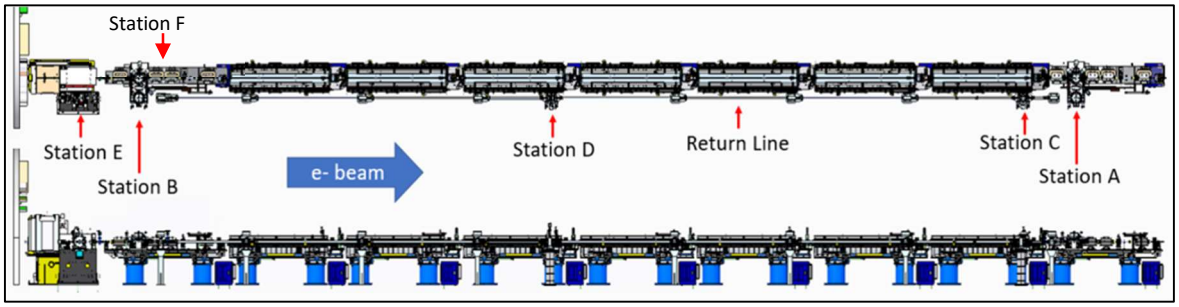

Figure 1 Top (upper) and side (lower) view of the CBXFEL system at the LCLS undulator hall.

The layout of our planned experiment is shown in Fig.1. Here, the four diamond crystal mirrors are mounted on independent nano-positioning stages in a rectangular geometry that can be longitudinally scaled to the full length of the undulator hall. The crystals (in Stations A and B) provide high reflectivity within the spectral and angular bandwidths of 75 meV and 8 microrad, respectively, thereby returning a nearly monochromatic seed for amplification by the second electron bunch using Station C, D and the return line. The refractive lenses focus the X-rays, while

the numerous screens, diodes, and pinholes provide the required diagnostics for alignment (in Stations A, B, C, D, E, F).

Recent Progress

High-resolution rocking curve imaging (RCI) of diamond crystals was performed at both APS and SSRL. Wavefront phase errors upon Bragg reflection from diamond crystals were successfully measured. Best crystals have errors within specs: λ/70 on a footprint of 100 μm in diameter. Six diamond Bragg crystal mirrors, two of which have drumhead membranes for X-ray out-coupling, have been manufactured, laser cut for strain relief, characterized, and are ready for installation in the cavity.

Two CBXFEL electron beam chicanes were installed in the undulator hall. The chicanes are commissioned and shown to provide the required delays when powered. They do not adversely affect the normal LCLS operation when not powered.

Four ultra-fast, transverse electromagnetic stripline kickers were built and installed in the LCLS linac. These kickers will be used to independently adjust the trajectories of the two electron bunches to ensure transverse overlap.

Data analysis for an all-in-vacuum, 14-m round trip, rectangular test x-ray cavity was completed. Low-loss x-ray recirculation over 60 passes was observed. The turn-by-turn loss extracted from the data agrees well with ideal theoretical performance estimates. Diamond grating was demonstrated as effective x-ray in/out coupling mechanism.

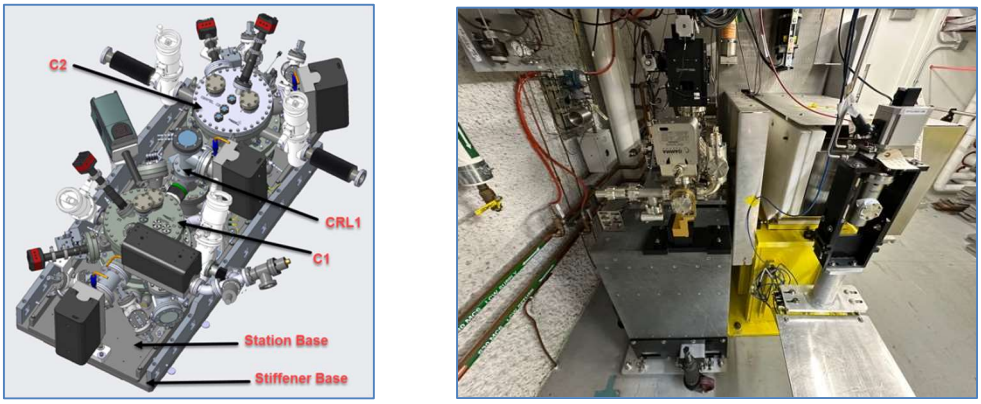

Figure 2: Station A (left) mechanical design and Station E (right) in the undulator hall.

Station A and B vacuum chambers and internals design is complete. Station A (Fig. 2 left) shows the vacuum chamber C1, C2, and CRL1 assembled on station base and stiffener base. C1 chamber and internals manufacturing is complete is undergoing initial vacuum certification in preparation for assembly. C2, C3, C4, CRL1, and CRL2 vacuum chamber manufacturing ranges from 65%-95% complete. Most (85%) of the internal components to be assembled in these five vacuum chambers are in manufacturing.

X-ray diagnostic system and its components were developed for precise alignment of the x-ray optical elements of the CBXFEL cavity with sub-μrad-angular and μm-spatial accuracy as well as for achieving three-dimensional overlapping of the electron and photon beams in the cavity. Different types of x-ray beam profile monitors (XBPMs) and x-ray beam intensity monitors (XBIMs) were designed, prototyped, characterized at the APS and SLAC, and ready for installation into the cavity.

The X-ray return line was fabricated at ANL (Euclid) and delivered to SLAC. Diagnostic stations C and D were shipped to SLAC. Station D is ready for installation and Station C is awaiting an optical component from Argonne that was damaged during the assembly process. Station E or intra-cavity diagnostics is complete and installed in the tunnel (see Fig. 2 right).

Single- and double-electron-bunch experiments have been performed at LCLS in CBXFEL-like conditions to characterize the FEL performance well in advance of x-ray cavity commissioning. High-level applications were developed for CBXFEL commissioning and operations, and subsequently tested using a CBXFEL simulator program. Commissioning plans including the initial checkout and step-by-step alignment procedure of the optical cavity have been developed.

Future Plans

For the remainder of CBXFEL hardware and installation work, we plan to complete fabrication, assembly, integration, and installation of new cable tray, and Stations A, B, C, D, and F. The current plan is to install new cable tray, Stations D and F in the 2024 summer downtime, Station C in the fall, and Stations A and B in the 2024-25 winter downtime.

Controls integration is an important part of the project, so the controls teams in both labs will meet at ANL to check out the integrated C1 motion controls once its fully assembled, which will provide the critical benchmark data for C2, C3 and C4. Station A and B controls integration checkout will be conducted at SLAC in the fall 2024.

Continuing improvement in electron beam (single and double bunch) performance will be pursued with LCLS machine studies. We will also explore self-seeding in CBXFEL-like conditions and use the setup to emulate the cavity crystal 1 angle calibration procedure. Finally, we want to explore the possibilities of controlling the global accelerator RF frequency to vary the two bunch timing for delay scan, in order to complement the limited delay scan provided by motion controls from C1-C4.

We will also further refine the commissioning plan based on the hardware and diagnostics performance tests. The detailed tasks of cavity alignment and gain measurements will also be worked out. Last but not the least, we will continue to investigate future upgrade options of the system to enable full-performance CBXFEL at LCLS-II-HE and elsewhere.

References

1. Z. Huang and R. Ruth, *Fully Coherent X-Ray Pulses from a Regenerative-Amplifier Free-Electron Laser*, Phys. Rev. Lett. 96, 144801 (2006).

2. K.-J. Kim, Y. Shvyd'ko, and Sven Reiche, *A proposal for an X-ray free-electron laser oscillator with an energy-recovery linac,* Phys. Rev. Lett. 100, 244802 (2008).

Publications

1. R. R. Robles, A. Halavanau, G.l Marcus, and Z. Huang, *Fast modeling of regenerative amplifier free-electron lasers*, Phys. Rev. Research **5**, 043254 (2023).

2. X. Shi, X. Z. Qiao, P. Pradhan, P. Liu, L. Assoufid, K.-J. Kim, and Y. Shvyd'ko, *At-Wavelength Characterization of X-ray Wavefronts in Bragg Diffraction from Crystals,* J. Synchrotron Radiation **30**, 1100 (2023).

3. P. Liu, P. Pradhan, X. Shi, D. Shu, K. Kauchha, Z. Qiao, K. Tamasaku, T. Osaka, D. Zhu, T. Sato, J. MacArthur, X.-R. Huang, L. Assoufid, M. White, K.-J. Kim, Y. Shvyd'ko, *Design, Manufacturing, and Characterization of X-ray Optics for the Cavity-Based X-ray Free-Electron Laser Project*, in Proc. of the SPIE Optical Engineering + Applications **12695** (2023).

4. P. Liu, P. Pradhan, A. Miceli, D. A. Walko, D. Shu, J. Sullivan, K. Lang, M. Rivers, D. Zhu, A. Halavanau, and Y. Shvyd'ko, *Design and Characterization of X-ray Diagnostics for the Cavity-Based X-ray Free-Electron Laser Project*, in Proc. of the SPIE Optical Engineering + Applications **12694** (2023).

5. R. Margraf, R. Robles, A. Halavanau, J. Kryzywinski, K. Li, J. MacArthur, T. Osaka, A. Sakdinawat, T. Sato, Y. Sun, K. Tamasaku, Z. Huang, G. Marcus, and D. Zhu, *Low-loss stable storage of 1.2 Å X-ray pulses in a 14 m Bragg cavity*, Nature Photonics **17**, 878 (2023).

6. J. Tang, Z. Zhang, J. Morgan, E. Hemsing, and Z. Huang, *Active Q-Switched X-Ray Regenerative Amplifier Free-Electron Laser*, Phys. Rev. Lett. **131**, 055001 (2023).

7. A. Halavanau, R. Margraf, R. Robles, J. MacArthur, Z. Qu, G. Marcus, J. Wu, T. Sato, D. Zhu, C. J. Takacs, R. Arthur, O. Kraynis, B. Johnson, and T. Rabedeau, *Experimental Setup for High-Resolution Characterization of Crystal Optics for Coherent X-ray Beam Applications*, J. Appl. Cryst.. **56**, 155 (2023).

8. A. Halavanau, A. Romero, A. Krasnykh, A. Lutman, T. Beukers, J. Hugyik, A. Le, K. Luchini, E. Jongewaard, A. Sy, A. Ibrahimov, A. Benwell, A. Marinelli and F.-J. Decker, *Ultra-fast transverse beam orbit control in LCLS copper linac*, Journal of Instrument 17, P11031 (2022).

9. P. Qi and Y. Shvyd'ko, *Signatures of Misalignment in X-ray Cavities of Cavity-Based X-ray Free-Electron Lasers*, Phys. Rev. Accel. Beams **25**, 050701(2022).

10. G. Tiwari and R. Lindberg, *Misalignment effects on the performance and stability of x-ray free electron laser oscillator*, Phys. Rev. Accel. Beams 25, 090702 (2022).

Population inversion X-ray Laser Oscillator

Aliaksei (Alex) Halavanau, Claudio Pellegrini (SLAC), Uwe Bergmann (University of Wisconsin, Madison), Andrei Benediktovitch (CFEL, DESY)

Keywords: X-ray Lasers, Bragg Cavity, Laser Oscillators, XFEL Pump

Research Project Scope

Oscillators are at the heart of optical lasers, providing stable, fully coherent, transform-limited pulses. Until now, laser oscillators have been available only in the infrared to visible and near-ultraviolet (UV) spectral regions. In our research project, we study the feasibility of an oscillator operating in the 5- to 12-keV photon-energy range, XLO. We show that using the $K\alpha_1$ line of transition metal compounds as the gain medium, an X-ray free-electron laser (XFEL) as a periodic pump, and a Bragg crystal optical cavity, it is possible to build X-ray oscillators producing intense, fully coherent, transform-limited pulses. As an example, we consider the case of a solid copper gain medium generating $\sim 3 \times 10^8$ photons per pulse with 37-fs pulse length and 65-meV spectral resolution at 8-keV photon energy. Our theoretical study and simulation of this system show that, because of the very large gain per pass, the oscillator saturates and reaches full coherence in four to six optical-cavity transits. We also show that the oscillator can be pumped by a superconducting linac-based XFEL, like LCLS-II-HE, which is being built at SLAC. XLO can operate at a repetition rate as large as 125 kHz, giving an average x-ray power of about 70 mW. We study the feasibility and design of the x-ray optical cavity and other parts of the oscillator needed for its realization, opening the way to extend x-ray based research beyond current capabilities.

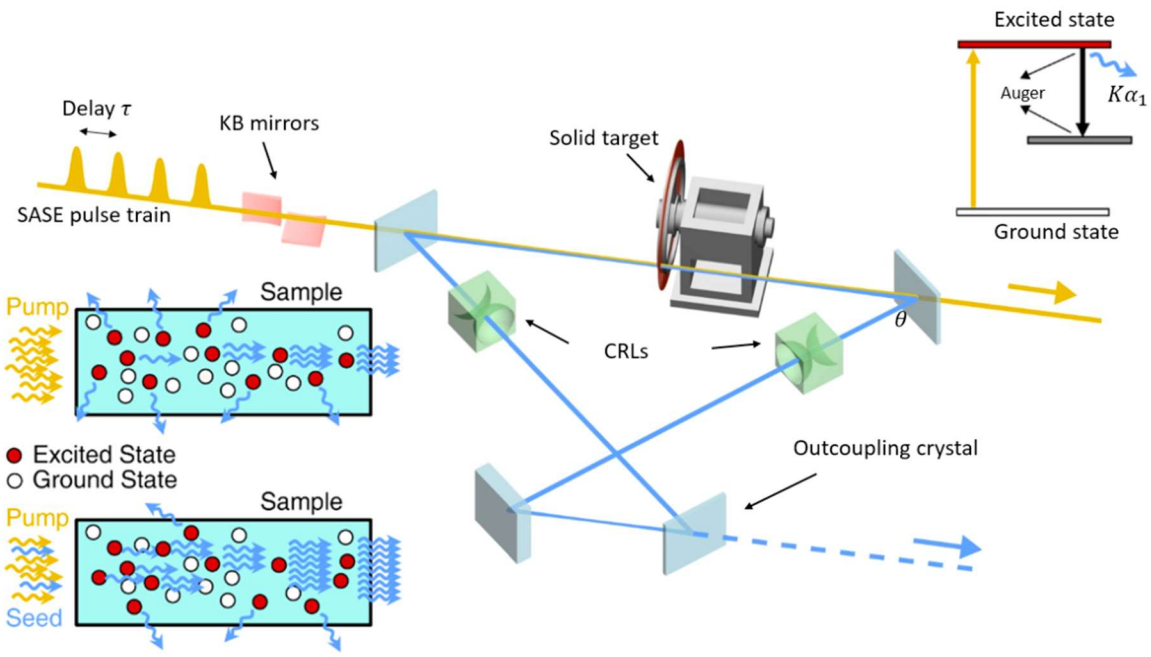

Figure 1: The schematics of the x-ray laser oscillator (not to scale). For this study we consider copper as the gain medium. A 9 keV SASE pump pulse impinges on a fast-moving, solid target; the resulting amplified spontaneous, or seeded, emission at 8.048 keV is recirculated in the Bragg bow-tie cavity and overlapped with the next consecutive pump pulses for further amplification until saturation is reached.

The experimental layout is shown in Figure 1. Four Bragg crystals in bow-tie geometry form a closed optical cavity. Inside the cavity, there is a rotating copper disk that is impinged by a nano-focused beam from LCLS XFEL. As a result of pumping, amplified spontaneous emission (ASE) is produced and recirculated inside the Bragg cavity. Initial work and cavity installation are performed at the CXI user end station. Based on the results of this work, we developed a concept suitable for LCLS-II-HE, where the XLO can operate continuously at a high repetition rate.

Recent Progress

XLO cavity design has been refined from the original proposal and finalized. The proof-of-concept experiment will use two XFEL pulses, about 30 ns apart. The gain medium was changed from jet to solid copper foils, to reduce the pump intensity requirements, and control gain medium damage.

A high-speed rotating target for the XLO experiment has been developed and tested in collaboration with RadiaBeam. The target is capable of rotating at a speed of 250 m/s for about 1 hour while maintaining longitudinal positional accuracy of 50 microns, well within the Rayleigh range of the focused pump beam.

An extensive, state-of-the-art simulation tool was developed. The simulated ASE pulses agree with and corroborate experimental data obtained at LCLS and SACLA. The code was used to design a seeded experiment which confirmed significant angular collimation of the stimulated emission, when a weak XFEL seed pulse of 8 keV is used. At LCLS, it is possible to generate seed pulses using the new variable gap hard x-ray undulator.

A high-resolution crystal characterization setup was developed at SSRL and used for the qualification of the XLO optics crystals. We determined that Si crystals in the XLO cavity are essentially defect-free, perfect Bragg reflectors with minimal lattice strain.

Future Plans

Finish proof-of-concept experiments at LCLS-CXI using the copper linac in the two bunch configuration, four ultra-fast kickers and cathode shaper. In the experiment we will commission the high-speed rotating target, and complete commissioning of the x-ray optics.

Fully develop the concept of XLO-II – a high-repetition rate x-ray laser oscillator. XLO-II is being designed for LCLS-II-HE. For this concept we will work with SACLA and J-Tech, to develop and commission a nano-focusing Wolter-type mirror.

Develop science case for XLO-class beams. Due to its unique characteristics – high brightness, transform-limited, small intensity fluctuations, new types of experiments are made possible by XLO. We will explore, together with interested user, applications in metrology, quantum X-ray optics, imaging and more.

References

A. Halavanau, et. al. - *Population Inversion X-ray Laser Oscillator*, PNAS, 117 (27), (2020)

Publications

A. Halavanau, R. Margraf, R. Robles, J. MacArthur, Z. Qu, G. Marcus, J. Wu, T. Sato, D. Zhu, C. J. Takacs, R. Arthur, O. Kraynis, B. Johnson, and T. Rabedeau, *Experimental Setup for High-Resolution Characterization of Crystal Optics for Coherent X-ray Beam Applications*, J. Appl. Cryst.. **56**, 155 (2023).

A. Halavanau, A. Romero, A. Krasnykh, A. Lutman, T. Beukers, J. Hugyik, A. Le, K. Luchini, E. Jongewaard, A. Sy, A. Ibrahimov, A. Benwell, A. Marinelli and F.-J. Decker, *Ultra-fast transverse beam orbit control in LCLS copper linac. Part I,* Journal of Instrumentation, Volume 17, November (2022).

S. Chuchurka, A. Benediktovitch, S. Krusic, A. Halavanau, N. Rohringer, *Stochastic modeling of x-ray superfluorescence,* Phys. Rev. A, 109, 3, pp. 033725 (2024)

M. Doyle, A. Halavanau, et. al., *Seeded stimulated X-ray emission at 5.9 keV*, Optica 10 (4), 513-519, (2023)

C. Pellegrini, A. Halavanau, A. Benediktovitch, U. Bergmann, *XLO-II, a high-repetition rate X-ray laser oscillator*, https://arxiv.org/abs/2310.04019, submitted FOR PUBLICATION (2024)

N. Welke, N. Majernik, A. Halavanau, et. al., *Development of spinning-disk solid sample delivery system for high-repetition rate x-ray free electron laser experiments*, Review of Scientific Instruments 94 (10), (2023)

F.J. Decker, A. Lutman, A. Halavanau, et. al., *Two- and multi-bucket X-ray Free-Electron laser at LCLS*, Nat. Sci. Rep, 12, 3253 (2022)

Y. Zhang, T. Kroll, A. Benediktovitch, A. Halavanau, U. Bergmann, C. Pellegrini, et. al., *Generation of Intense Phase-Stable Femtosecond Hard X-ray Pulse Pairs*, PNAS, 119 (12), (2022)

R.R. Robles, A. Halavanau, D. Cesar, A. Lutman, G. Stupakov, *Reconstruction of x-ray free-electron laser pulse duration and energy chirp from spectral intensity fluctuations*, PRAB 26 (3), 030701, (2023)

Attosecond Science with High Repetition Rate Xray Free-Electron Lasers

Agostino Marinelli, SLAC National Accelerator Laboratory

Keywords: x-ray, free-electron laser, attosecond

Research Project Scope

X-ray free-electron lasers (XFELs) have emerged as the most powerful sources of isolated attosecond pulses, with a peak brightness that surpasses table-top high-harmonic sources by more than seven orders of magnitude. Recent work at the Linac Coherent Light Source (LCLS) has demonstrated isolated X-ray pulses shorter than 500 as and a peak power on the order of 100 GW [1]. Key to this effort have been the development of beam-shaping methods capable of enabling single-spike FEL operation, as well as the development of diagnostic tools with sub-fs resolution.

The current project aims at developing attosecond science capabilities at the Linac Coherent Light Source-II. The main goals of this work are:

- demonstration of attosecond pump/attosecond probe experiments using two-color FELs

- demonstration of advanced attosecond pulse shaping capabilities for coherent control

- development of high peak power attosecond XFEL modes.

- extension of attosecond XFEL operation to the high-repetition rate LCLS-II linac.

In my presentation I will report progress on two field-work proposals (FWPs): the first one, titled “Attosecond science capabilities at the Linac Coherent Light Source II” is in its final stages, with all the main goals accomplished and major results being published in peer-reviewd journals (most notably: two articles recently accepted in Nature Photonics). The second FWP, named “Attosecond science with high-repetition rate X-ray free-electron lasers” is in its first year and already producing important results, with one article submitted to Phys. Rev. Lett.

Recent Progress

The most important recent results have been the demonstration of attosecond x-ray pump/probe capabilities and the generation and measurement of Terawatt-scale superradiant pulses.

In the first experiment (illustrated in Fig. 1), the LCLS-II soft x-ray undulator was setup in two-color mode and used to generate attosecond pulses with a modulated electron bunch. By operating in a harmonic scheme, where the second color was tuned to the second harmonic of the first, we were able to generate two attosecond pulses and scan the delay down to roughly 300 as. We characterized the two pulses with an angular streaking diagnostic, which allowed us to measure the delay under different FEL conditions. Finally, we employed this experimental setup to measure

ultrafast dynamics in core-ionized para-Aminophenol, showing a shift in the binding energy of core electrons measured with attosecond time resolution. This work was accepted for publication in Nature Photonics [2]. A second experiment co-led by our group has demonstrated the observation of coherent valence electronic dynamics in Aminophenol using this technique and a publication is currently in preparation.

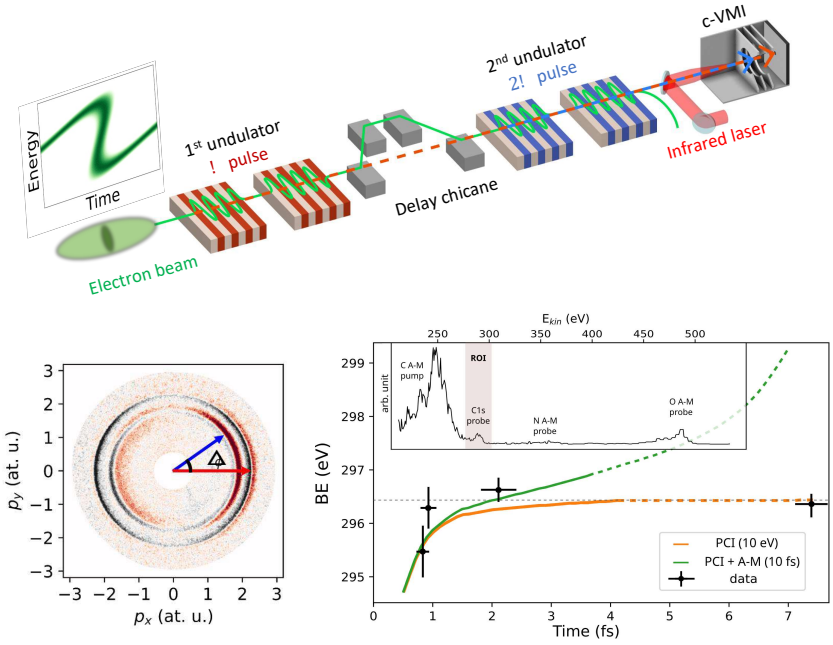

Figure 1: Top: schematic representation of a two-color attosecond pump/probe scheme. Bottom left: angular streaking pattern showing two pulses separated by 300 as. Bottom right: results of an attosecond pump/probe experiment in aminophenol, showing the ultrafast shift in the binding energy at the Carbon site following ionization by the pump pulse.

The second experiment is illustrated in Figure 2. An attosecond X-ray pulse, generated using the enhanced self-amplified spontaneous emission method, was amplified by a fresh slice of the electron bunch, in a cascaded XFEL scheme. The measured peak power is in the Terawatt scale, with a measured pulse duration of hundreds of attosecond. The brightest shot measured had a peak power of 1.1 TW. In addition to providing the highest X-ray peak power reported to date, these pulses show strong evidence of soliton-like superradiant behavior, pointing towards the generation of even shorter pulses by exploiting the strongly non-linear superradiant regime. This work was also recently accepted for publication in Nature Photonics.

Both methods have also been successfully employed in user experiments, resulting in prestigious publications in collaboration with LCSL user groups (see e.g. [3]).

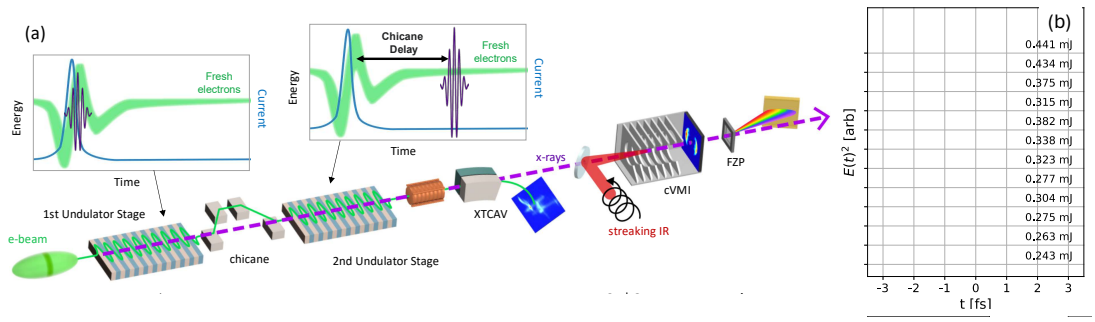

Figure 2. (a) Schematic of a cascaded amplification experiment: an electron bunch with a high-current spike is employed to generate a sub-fs X-ray pulse. By delaying the electron bunch with a magnetic chicane, the x-rays are overlapped with a fresh slice of the electron bunch and further amplified well beyond the saturation limit. (b) Measured temporal profiles of the x-ray pulses, with Terawatt-scale power.

The experimental work on cascaded amplification has inspired a new theoretical development in non-linear FEL physics. Our group has developed a fully analytical description of superradiance in three dimensions. This theory has excellent agreement with numerical simulations performed with the Genesis 1.3 simulation code and explains several interesting features observed in our experiment. This work is an important step forward in FEL theory and provides the theoretical basis for future attosecond XFEL sources. A manuscript about this work is under review with Phys. Rev. Lett.

Building on the work on cascaded amplification, our group has also developed a coherent pulse shaping method that takes advantage of post-saturation interaction in tapered undulators to shape the Wigner function of attosecond X-ray pulses. The dynamic interplay between gain and slippage can be used to shape an attosecond pulse by re-amplifying it in a magnetic undulator with variable taper, mapping the taper profile to the Wigner function of the X-rays. A paper detailing this development is under review with Phys. Rev. Lett.

Additional results include the conceptual development of electron beam-based pump/probe methods [4], the demonstration of laser-heater shaping for multiplexed operation (article in under review), and the application of the XLEAP modulation method to the hard X-ray line of LCLS, which significantly improves the performance over previous results obtained with nonlinear compression and emittance spoiling.

Future Plans

In the immediate future we plan to demonstrate the generation of attosecond X-ray pulses at high repetition rate with the superconducting LCLS-II linear accelerator. We will initially focus on extending our bunch shaping methods to the new linac, and then measure the pulse duration using the well-established angular streaking method.

Following this initial demonstration, we plan to experimentally test our X-ray pulse shaping ideas. We will characterize the shaped pulses with angular streaking and apply them to a coherent control experiment, with the aim of demonstrating coherent shaping of electronic wavepackets in core-excited molecules.

We also plan to finalize our beam-based pump/probe technique with an experimental demonstration in solid-state samples. Preliminary experiments performed with the LCLS copper linac showed significant promise, but we expect that the higher beam stability enabled by the superconducting linac will allow us to acquire high-quality pump/probe data.

Finally, we plan to perform conceptual studies for attosecond pulse generation with the LCLS-II HE upgrade.

References

[1] Joseph Duris, Siqi Li,, Taran Driver, Elio G. Champenois, James P. MacArthur, Alberto A. Lutman, Zhen Zhang, Philipp Rosenberger, Jeff W. Aldrich, Ryan Coffee, Giacomo Coslovich, Franz-Josef Decker, James M. Glownia, Gregor Hartmann, Wolfram Helml, Andrei Kamalov, Jonas Knurr, Jacek Krzywinski, Ming-Fu Lin, Jon P. Marangos, Megan Nantel, Adi Natan, Jordan T. O'Neal, Niranjan Shivaram, Peter Walter, Anna Li Wang, James J. Welch, Thomas J. A. Wolf, Joseph Z. Xu, Matthias F. Kling, Philip H. Bucksbaum, Alexander Zholents, Zhirong Huang, James P. Cryan and Agostino Marinelli "Tunable isolated attosecond X-ray pulses with gigawatt peak power from a free-electron laser." *Nature Photonics* 14.1 (2020): 30-36.

[2] Zhaoheng Guo, Taran Driver, Sandra Beauvarlet, David Cesar, Joseph Duris, Paris L Franz, Oliver Alexander, Dorian Bohler, Christoph Bostedt, Vitali Averbukh, Xinxin Cheng, Louis F DiMauro, Gilles Doumy, Ruaridh Forbes, Oliver Gessner, James M Glownia, Erik Isele, Andrei Kamalov, Kirk A Larsen, Siqi Li, Xiang Li, Ming-Fu Lin, Gregory A McCracken, Razib Obaid, Jordan T ONeal, River R Robles, Daniel Rolles, Marco Ruberti, Artem Rudenko, Daniel S Slaughter, Nicholas S Sudar, Emily Thierstein, Daniel Tuthill, Kiyoshi Ueda, Enliang Wang, Anna L Wang, Jun Wang, Thorsten Weber, Thomas JA Wolf, Linda Young, Zhen Zhang, Philip H Bucksbaum, Jon P Marangos, Matthias F Kling, Zhirong Huang, Peter Walter, Ludger Inhester, Nora Berrah, James P Cryan, Agostino Marinelli arXiv preprint arXiv:2401.15250.

[3] Shuai Li, Lixin Lu, Swarnendu Bhattacharyya, Carolyn Pearce, Kai Li, Emily T Nienhuis, Gilles Doumy, RD Schaller, S Moeller, M-F Lin, G Dakovski, DJ Hoffman, D Garratt, Kirk A Larsen, JD Koralek, CY Hampton, D Cesar, Joseph Duris, Z Zhang, Nicholas Sudar, James P Cryan, A Marinelli, Xiaosong Li, Ludger Inhester, Robin Santra, Linda Young "Attosecond-pump attosecond-probe x-ray spectroscopy of liquid water." *Science* (2024): eadn6059.

[4] D. Cesar, A. Acharya, J. P. Cryan, A. Kartsev, M. F. Kling, A. M. Lindenberg, C. D. Pemmaraju, A. D. Poletayev, V. S. Yakovlev, and A. Marinelli, "Ultrafast quantum dynamics driven by the strong space-charge field of a relativistic electron beam," Optica 10, 1-10 (2023)

Publications

1) Siqi Li, Taran Driver, Philipp Rosenberger, Elio G Champenois, Joseph Duris, Andre Al-Haddad, Vitali Averbukh, Jonathan CT Barnard, Nora Berrah, Christoph Bostedt, Philip H Bucksbaum, Ryan N Coffee, Louis F DiMauro, Li Fang, Douglas Garratt, Averell Gatton, Zhaoheng Guo, Gregor Hartmann, Daniel Haxton, Wolfram Helml, Zhirong Huang, Aaron C LaForge, Andrei Kamalov, Jonas Knurr, Ming-Fu Lin, Alberto A Lutman, James P MacArthur, Jon P Marangos, Megan Nantel, Adi Natan, Razib Obaid, Jordan T O'Neal, Niranjan H Shivaram, Aviad Schori, Peter Walter, Anna Li Wang, Thomas JA Wolf, Zhen Zhang, Matthias F Kling, Agostino Marinelli, James P Cryan "Attosecond coherent electron motion in Auger-Meitner decay" *Science* 375.6578 (2022): 285-290.
2) D. Cesar, A. Acharya, J. P. Cryan, A. Kartsev, M. F. Kling, A. M. Lindenberg, C. D. Pemmaraju, A. D. Poletayev, V. S. Yakovlev, and A. Marinelli, "Ultrafast quantum dynamics driven by the strong space-charge field of a relativistic electron beam," Optica 10, 1-10 (2023)
3) Gilbert Grell, Zhaoheng Guo, Taran Driver, Piero Decleva, Etienne Plésiat, Antonio Picón, Jesús González-Vázquez, Peter Walter, Jonathan P Marangos, James P Cryan, Agostino Marinelli, Alicia Palacios, Fernando Martín "Effect of the shot-to-shot variation on charge migration induced by sub-fs x-ray free-electron laser pulses." *Physical Review Research* 5.2 (2023): 023092.
4) Zhaoheng Guo, Taran Driver, Sandra Beauvarlet, David Cesar, Joseph Duris, Paris L Franz, Oliver Alexander, Dorian Bohler, Christoph Bostedt, Vitali Averbukh, Xinxin Cheng, Louis F DiMauro, Gilles Doumy, Ruaridh Forbes, Oliver Gessner, James M Glownia, Erik Isele, Andrei Kamalov, Kirk A Larsen, Siqi Li, Xiang Li, Ming-Fu Lin, Gregory A McCracken, Razib Obaid, Jordan T ONeal, River R Robles, Daniel Rolles, Marco Ruberti, Artem Rudenko, Daniel S Slaughter, Nicholas S Sudar, Emily Thierstein, Daniel Tuthill, Kiyoshi Ueda, Enliang Wang, Anna L Wang, Jun Wang, Thorsten Weber, Thomas JA Wolf, Linda Young, Zhen Zhang, Philip H Bucksbaum, Jon P Marangos, Matthias F Kling, Zhirong Huang, Peter Walter, Ludger Inhester, Nora Berrah, James P Cryan, Agostino Marinelli arXiv preprint arXiv:2401.15250.
5) Shuai Li, Lixin Lu, Swarnendu Bhattacharyya, Carolyn Pearce, Kai Li, Emily T Nienhuis, Gilles Doumy, RD Schaller, S Moeller, M-F Lin, G Dakovski, DJ Hoffman, D Garratt, Kirk A Larsen, JD Koralek, CY Hampton, D Cesar, Joseph Duris, Z Zhang, Nicholas Sudar, James P Cryan, A Marinelli, Xiaosong Li, Ludger Inhester, Robin Santra, Linda Young "Attosecond-pump attosecond-probe x-ray spectroscopy of liquid water." *Science* (2024): eadn6059.
6) Randy Lemons, Nicole Neveu, Joseph Duris, Agostino Marinelli, Charles Durfee, Sergio Carbajo. "Temporal shaping of narrow-band picosecond pulses via noncolinear sum-frequency mixing of dispersion-controlled pulses." *Physical Review Accelerators and Beams* 25.1 (2022): 013401.

7) River R Robles, Kirk A Larsen, David Cesar, Taran Driver, Joseph Duris, Paris Franz, Douglas Garratt, Nicholas Sudar, Jun Wang, Zhen Zhang, James Cryan, Agostino Marinelli arXiv preprint arXiv:2403.02189 (Under review with Phys. Rev. Lett.)
8) River R Robles, Luca Giannessi, Agostino Marinelli arXiv preprint arXiv:2403.02153 (Under review with Phys. Rev. Lett.)
9) Jingyi Tang, Joseph P Duris, Gabriel Marcus, Agostino Marinelli "Electron beam shaping for actively outcoupling radiation from an x-ray regenerative amplifier free-electron laser." *Physical Review Accelerators and Beams* 25.8 (2022): 080701.
10) Andre Al-Haddad, Solène Oberli, Jesús González-Vázquez, Maximilian Bucher, Gilles Doumy, Phay Ho, Jacek Krzywinski, Thomas J Lane, Alberto Lutman, Agostino Marinelli, Timothy J Maxwell, Stefan Moeller, Stephen T Pratt, Dipanwita Ray, Ron Shepard, Stephen H Southworth, Álvaro Vázquez-Mayagoitia, Peter Walter, Linda Young, Antonio Picón, Christoph Bostedt "Observation of site-selective chemical bond changes via ultrafast chemical shifts." *Nature Communications* 13.1 (2022): 7170.

Extending the reach of light source facilities with precision laser plasma injectors

Sam Barber, Lawrence Berkeley National Lab

Keywords: laser plasma accelerator, injector, free electron laser

Research Project Scope

Light source facilities provide an invaluable tool to a robust community of scientific users. The x-ray free electron laser (XFEL), in particular, allows scientists unparalleled access to spatial and temporal scales at the angstrom and femtosecond scale, respectively. Advances in FEL physics and improvements in the constituent accelerator components, are now needed to make new research paradigms accessible. For example, access to brighter electron beams can enable a variety of new capabilities including higher energy x-rays (>25 keV) needed in scientific areas like transformative manufacturing, quantum materials characterization and imaging of emerging high density microelectronics devices. Access to harder x-rays at XFELs would also create a wealth of opportunity for thick or dense samples, including matter in extreme conditions. In addition, brighter beams also provide a natural path towards shorter FEL pulses needed for improved temporal resolution of dynamic molecular and atomic processes.

With this in mind, a radical new approach to the generation and acceleration of electron beams is gaining wide spread attention for its potential to produce ultra-high brightness electron beams, which in turn promises a major breakthrough in XFEL performance both for current facility upgrades and new facilities. Plasma-based accelerators provide an environment naturally conducive to the production of high-quality electron beams due to the exceptionally high acceleration gradients (>10 GeV/m) typical of a plasma accelerator cavity, combined with space charge shielding effects from the background ion column. With regards to the stringent stability and reliability requirements of light source facilities, however, plasma-based accelerators have thus far remained notably deficient.

In this project, we aim to demonstrate the production of ultra-high brightness electron beams generated by a laser plasma accelerator (LPA) with a level of stability, precision control and reliability comparable to the rigorous requirements of light source facilities. The work performed as part of this project will provide a blueprint for the development of a plasma-based modality of electron beam injectors which can revolutionize light source facilities in a number of ways, including, but not limited to, i) injector upgrades for large scale facilities like LCLS and ii) driving complementary light sources at existing facilities or at future, smaller facilities with unique capabilities. This demonstration can only be made possible with transformative advances in LPA technology. The highest brightness electron beams produced in plasma-based accelerators require sophisticated triggered injection mechanisms. To fully exploit these mechanisms requires order of magnitude improvements in laser stabilization and control which incorporate high bandwidth active feedback and intelligent optimization algorithms. Experiments will be carried out at the world-class BELLA Center, making use of two newly built LPA beamlines, with a focus on the following objectives:

- Demonstrate high brightness, reliable electron beams from triggered injection modalities of LPA (density down ramp and two-color ionization injection) specifically targeting multi kA beams with sub 100 nm normalized transverse emittances.

- Design and implement active feedback controls capable of stabilizing critical parameters of amplified low repetition (<5 Hz) laser with ~100-500 Hz bandwidth, which enable system wide performance tuning and optimization (from oscillator to electron beam).
- Develop electron beam diagnostics specifically tailored to characterize high brightness LPA beams, in particular, focusing on characterization of longitudinal phase space.
- Create a framework for deploying customized machine learning techniques to optimize performance and identify 'hidden' parametric dependences.
- Explore opportunities and advantages of using an LPA based injector as an upgrade for conventional XFEL facilities through start-to-end simulations.

Recent Progress

Assembling a team: A critical a critical component to executing the experimental side of this research project is building and training a capable team. The facilities to be used for this work, the Hundred Terawatt Undulator (HTU) and Hundred Terawatt Thomson (HTT) beamlines consist of complex, state-of-the art laser and accelerator systems. Daily operations, much of the maintenance, upgrades, control system development, data analysis and more are the responsibility of the scientific team at the BELLA Center.

Two postdocs, Chris Doss and Kyle Jensen, have been hired in July 2023 and January 2024, respectively, and are working 50% on this ECRP with the remainder of their time being dedicated to synergistic activities on the HTU system. Additionally, a 2nd year PhD candidate from University of Hamburg, Finn Kohrell, is working 100% time on the HTU system.

Additional support through a CRADA with Tau Systems provides additional funding to operate, upgrade and maintain the HTU system. The aims of the CRADA with Tau are make use of the high brightness e-beam source to study prospects of compact LPA driven FELs.

Laser/system maintenance and improvements: Between August 2023 and February 2024, critical hardware failures prevented meaningful accelerator operations. Nonetheless, this provided an opportunity to reassess and address certain aspects of the laser system not performing to full potential. In particular, as a team, through meticulous alignment, characterization and benchmarking, we made substantial improvements to the main amplifier chain. Qualitatively, the transverse profile of the amplified beam was made far more symmetric. At the same time, we increased the max output energy from ~3.9J to north of 5J and reduced the energy jitter from ~2% to less than 1%.

The final compressor, which includes two very large high value gratings, was rebuilt. After nearly 5 years in operation, the surfaces had become contaminated with some small damage spots on one grating. We identified a safe method for cleaning the gratings, and replaced the damaged one with a previously purchases spare grating. Meticulous alignment of the two gratings led to excellent cancellation of higher spectral phase as well as spatial and angular chirp. Pulse durations of ~35 fs

were measured, matching the shortest duration from the front end. Additionally, this work substantially increased the energy transmission through the compressor from 55% to 68%.

Laser stabilization topics: As noted in the project scope, improving the stability/reliability of LPA produced electron beams is essential. Entering this project, a number of critical laser parameters were identified as requiring dedicated efforts to improve their stability. Additionally, it is the aim of this research to uncover and address additional sources laser instability that affects e-beam performance. On both of these fronts, substantial progress has been made:

i) Fluctuations in longitudinal focal position of the laser are well understood to be a key source of e-beam instability [1]. We have assembled a closed loop longitudinal focal stabilization (LFS) system and completed initial lower power tests showing shot-to-shot stability improvement of already a factor of 2 or more.

ii) The installation of a non-destructive, on-shot measurement of the amplified laser pulse spectral phase and temporal profile using a specially designed chirped mirror-based compressor and Grenouille has revealed a strong correlation between the natural fluctuations of the linear chirp parameter and e-beam charge.

Deploying ML/AI tools: Substantial efforts on the development of accelerator specific toolsets are underway. By engaging with experts in the field on these topics, we are starting to build the capabilities to utilize these resources in meaningful ways. Through direct collaboration with Ryan Roussel and Auralee Edelen at SLAC, we recently made use of their technique [2] to extract greater information and detail from standard quadrupole scans.

My team has also spearheaded the development of a robust python API that integrates with the existing BELLA Center developed, Labview-based GEECS control system. This API has now been used in conjunction ML-based optimization tools XOPT [3] and Badger [4]. First use cases include automating otherwise tedious and time-consuming alignment tasks. Some early attempts have been made to optimize accelerator performance.

Building framework for wide range, high fidelity PIC simulations: Through a collaboration with Sarah Schroeder, who, at the time, was a postdoc at DESY, we developed a platform for producing high fidelity PIC simulations using laser and plasma parameters measured on the HTU system and we explored the impact of variations in these parameters commensurate with the level of jitter observed in experiment. Results of the simulations are in excellent agreement with the observed e-beam parameters.

Future Plans

Some near term plans include implementing and demonstrating e-beam stability improvements resulting from our work on the LFS system and spectral phase control. For the LFS system, a high power demonstration is anticipated to improve e-beam charge stability by 50%. Kyle Jensen is

leading this effort and it is expected the results from these experiments will be written up this year and that the LFS system will be integrating into regular operations.

We will continue exploring the impact of spectral phase variations on e-beam production, which is a relatively fresh topic for us. Some key activities will include: i) taking datasets at high repetition rate, ii) compile comprehensive synchronous spectral phase/e-beam data, and iii) explore avenues for reducing spectral phase jitter and/or introduce correction loops. This topic is a core part of Finn Kohrell's PhD thesis and it is expected results of this work will be written up this coming year.

A critical technical experimental improvement is currently in development. We are making some upgrades to the vacuum system to allow full 5Hz operation of our LPA. The target chamber volume will be isolated from the remainder of the laser system using thin anti-reflection coated pellicles that are non-disruptive to the laser. An increase in the capacity of the roughing pumps is expected to be sufficient to keep the background pressure in the target chamber to a low enough level to prevent degradation of the laser pulse via ionization induced defocusing, a topic that was studied through simulations by Chris Doss. Increasing the rep rate from 1 to 5Hz will have a dramatic impact on efficiency and effectiveness of executing the experimental tasks.

My team is also carrying out the initial experimental design work needed to make first attempts at passively streaking LPA produced beams for the purpose of a longitudinal phase space diagnostic. First experiments on this topic should take place by the end of next year.

For the start-to-end simulation effort for simulating LPA to linac to FEL, we are exploring various opportunities and are in close discussions with developers of WarpX and ImpactX. Several features have already been added to ImpactX at our request that will aid our simulation efforts. Additionally, building on the first round of detailed PIC simulations of our density downramp injector, we are looking for avenues to improve the computational efficiency. Sarah Schroeder has now joined the BELLA Center as a project scientist and she has determined full 3D PIC is only essential for accurately modelling the injection process and more streamlined codes could be used to simulate subsequent plasma acceleration. Stitching together multiple codes in this way could greatly expand our ability to do large parameter scans.

References

1. A. R. Maier, N. M. Delbos, T. Eichner, L. Hübner, S. Jalas, L. Jeppe, S. W. Jolly, M. Kirchen, V. Leroux, P. Messner, M. Schnepp, M. Trunk, P. A. Walker, C. Werle, and P. Winkler, *Decoding Sources of Energy Variability in a Laser-Plasma Accelerator* Phys. Rev. X **10**, 031039 (2020)
2. R. Roussel, A. Edelen, C. Mayes, D. Ratner, J. P. Gonzalez-Aguilera, S. Kim, E. Wisniewski, and J. Power, *Phase Space Reconstruction from Accelerator Beam Measurements Using Neural Networks and Differentiable Simulations,* Phys. Rev. Lett. **130**, 145001 (2023)

3. R. Roussel., et al., *Xopt: A simplified framework for optimization of accelerator problems using advanced algorithms*, in Proc. IPAC'23, Venezia.doi:https://doi.org/10.18429/JACoW-14th International Particle Accelerator Conference-THPL164
4. Zhang, Z., et al. *Badger: The missing optimizer in ACR*, in Proc. IPAC'22, Bangkok. doi:10.18429/JACoW-IPAC2022-TUPOST058

Enhanced Self Seeding and Coherent Control of X-Ray Free Electron Lasers

Erik Hemsing, SLAC National Accelerator Laboratory

Keywords: coherence, stability, spatiotemporal polarization shaping

Research Project Scope

This three-year research project focused on the study of advanced x-ray FEL pulse shaping schemes for LCLS-II that have potential to produce brilliant x-ray pulses with laser-like shot-to-shot stability and coherence, and with customizable temporal, spatial, and polarization properties. The program supported two postdocs (Research Associate, RA), plus some travel. The techniques under investigation included, but were not limited to, Enhanced Self Seeding (ESS), femtosecond polarization switching, and Fully Structured Light/Poincare beams. Opportunities to reach seeded tender x-rays were also explored, as were several other adjacent ideas that formed in the course of study.

Recent Progress

Substantial progress was made on developing the electron beam shaping techniques and establishing optimal parameters for Enhanced Self-Seeding, both nomically and in theory. ESS is a recently conceived concept designed to overcome the statistical limitations of conventional self-seeding [1]. While with conventional self-seeding there is a trade-off between coherence and stability, ESS avoids that constraint by making use of the stabilizing properties of x-ray FEL pulses produced by ultrashort electron beams. The concept is shown in Figure 1. In ESS, the electron beam is tailored to have an ultrashort spike portion of duration 3-7 the FEL cooperation times (about 1 fs in most cases for soft x-rays) and a long lower current portion. The short beam produces a saturated single spike FEL pulse (much like what has been demonstrated at LCLS with XLEAP) with a wide coherent FEL bandwidth that fills the SXRSS monochromator on every shot. The mono then notches out a high power and narrow portion of the spectrum to be amplified by the flat, long section of electron beam in the second stage. Amplification of the narrowband, high-power seed stabilizes the x-ray pulse energy and the spectrum bringing relative rms pulse fluctuations down to the few percent level at saturation. The final coherent FEL pulses have statistical properties similar to a fully coherent optical laser.

As part of this program, we explored a variety of advanced e-beam shaping techniques for the spike formation. Simulations showed that the desired longitudinal phase space for ESS can be produced by cathode shaping and by laser heater shaping on both LCLS and LCLS-II, and feasible parameters were obtained for realizing ESS experimentally.

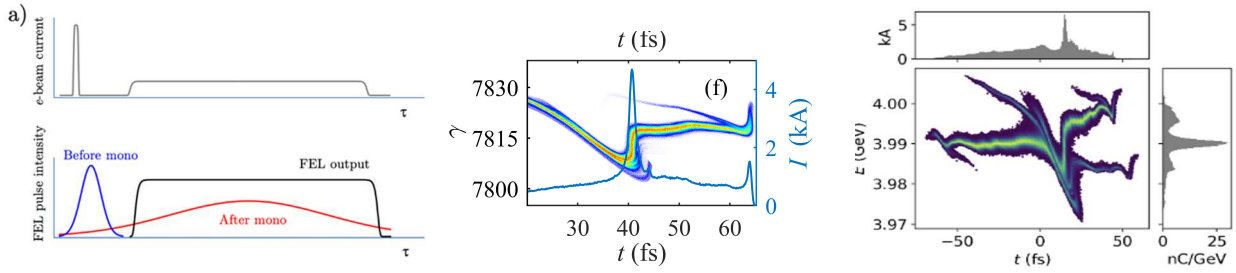

Figure 1. The enhanced self-seeding concept and beams. Left: The electron beam temporal profile is tailored to have an ultrashort current spike and a long, flat portion. The high-current, short beam lases to saturation in the SASE FEL section to produce a single spike pulse (blue). The self-seeding mono stretches the spike (red) to overlap the long, flat section of electron beam that amplifies it to saturation, producing a stable coherent narrowband pulse in the FEL output. Center: Beam distribution obtained from laser heater shaping. Right: Beam distribution obtained from laser cathode shaping

For these studies we built a start-to-end (S2E) optimization framework for general beam-shaping tasks. The workflow is as follows. A python interface chains the initial beam generator (DISTGEN) to the injector simulator (ASTRA) and the accelerator simulator (ELEGANT). A python optimizer XOPT is used to control the start-to-end simulation chain and optimize the parameters in all of the components. The targets of the optimization are extracted from the final longitudinal phase space of the electron beams at the entrance of the soft x-ray undulator line. By maximizing the peak current and minimizing the energy spread of the flat section, we are able to obtain the desired electron beams for ESS: e-beams with a 4-5 kA short current spike and 40 fs long and flat section with average current about 1 kA. These S2E beams were then confirmed with Genesis and Puffin FEL simulations to exhibit the required stable performance of the ESS scheme. The inclusion of strong tapering shows stable narrowband pulses (2e-4 relative BW) of 1 mJ can be produced. Moreover, the strong lasing produces about 3% of stable, narrowband nonlinear third harmonic, which means that the ESS scheme can be used to extend the self-seeding system into the 1.2 – 4.5keV tender x-ray regime.

Unfortunate difficulties and delays with commissioning both LCLS-II and the Soft Xray Self-Seeding system precluded experimental testing of the ESS concept within the window of the 3-year program. However, there are plans to perform experiments later in 2024 using results of our optimization studies.

The ESS scheme relies heavily on FEL operations in the nonlinear and time-dependent regime because the short pulse saturates and is slippage-dominated. However, there is currently no satisfactory analytic model one can use to extract basic scaling and optimization in this regime to clearly establish, for example, the saturation length and optimal bunch length. Thus, a portion of study in this program was put toward developing an analytic framework for nonlinear time-dependent FELs. From recent results we can predict from the theory the saturation power,

saturation point, pulse length, bandwidth and central frequency of the short FEL pulse as a function of the e-beam bunch length. This provides simple and necessary guidance to tune and optimize the system at any x-ray wavelength.

Studies on tailoring the temporal profile of the FEL pulse were also performed. In Ref [2], we proposed a method to produce X-ray FEL pulses in which the polarization switches at femtosecond timescales by interleaving an s-polarized pulse train with a p-polarized pulse train. This enables new coherent control schemes for probing and manipulating core electrons, electron wave-packets, or atomic and molecular excitations in the EUV to x-ray regime. Last year, as part of this program, we experimentally demonstrated this scheme in a collaboration at FERMI@Elettra by producing two counterrotating circularly polarized pulses combined with adjustable delay from two cross-polarized undulators. The polarization profile confirmed by photoemission and by ionization measurements.

Late last year, we also did a first experimental demonstration of Fully Structured Light (FSL) at FERMI based on an idea we proposed in 2020 [3]. FSL beams have polarization topologies that vary spatially, and the Poincare beam (shown in Figure 2) is one such beam in which the polarization states span that full Poincare sphere. We produced this beam by combining the 2nd harmonic emission from one undulator with the 1st harmonic emission of a cross-polarized second undulator at the same wavelength. The polarization was mapped using a polarizer screen as a function of phase between pulses, and results show that such a FSL beam can indeed be produced in FELs, enabling single-shot probing with a controlled distribution of polarization states.

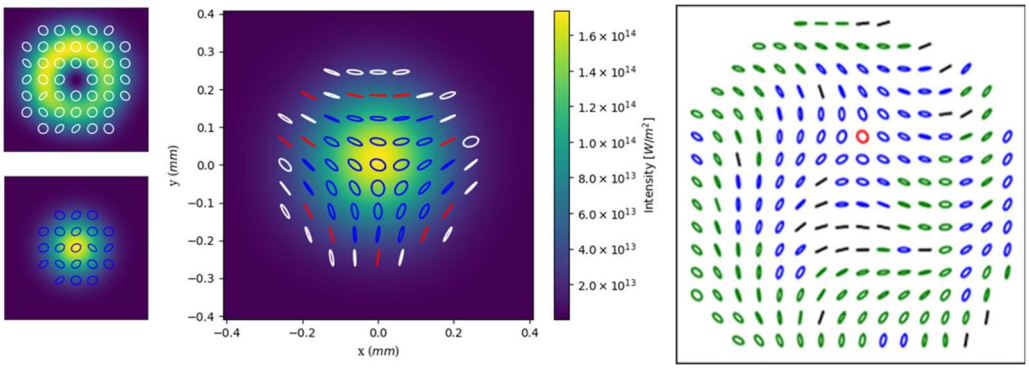

Figure 2. Producing Fully Structured Light. Radiation from two consecutive undulators (left) a polarization distribution that spans the Poincare sphere (middle). Measured polarization at FERMI (right).

Ancillary ideas emerged during the primary studies, and begat fruitful concepts. One is a simple but novel active Q-switching scheme that can significantly enhance hard x-ray outcoupling in a cavity-based FEL. Another is a combination of the fast polarization switching concept with FSL beam generation, allowing fast switching of light's orbital angular momentum.

With the successful demonstrations of fast polarization switching and FSL beams, most of the goals of the project were met and milestones achieved. The final goal to complete the project would be an experimental demonstration of ESS, which is planned for later this year. A successful outcome is a path to ESS as an LCLS-II capability.

Future Plans

Aside from plans to test the ESS concept at LCLS-II and to finalize papers in progress, we are also engaged in a coordinated effort with colleagues from Pulse, FERMI, and DESY to flesh out critical science drivers and perform application experiments for FPS and FSL beams and their combinations. We are also examining emerging ideas, including coherent pulse tailoring from sub-cycle electron beams, and producing phase-locked FEL pulse pairs.

References

1. E.Hemsing, A. Halavanau, and Z. Zhang, *Enhanced Self-Seeding with Ultrashort Electron Beams,* PRL **125**, 044801 (2020)
2. N. Sudar, R. Coffee, and E. Hemsing, *Coherent x rays with tunable time-dependent polarization,* Phys. Rev. Acc. Beams **23**, 120701 (2020), J. Morgan and B. W. J. McNeil, *Attosecond polarization modulation of x-ray radiation in a free-electron laser*, Phys. Rev. Accel. Beams **24**, 010701 (2021).
3. Jenny Morgan, Erik Hemsing, Brian W. J. McNeil, and Alison M. Yao, *Free Electron Laser Generation of X-Ray Poincare Beams*, New Journal of Physics Fast Track Communication 22 072001 (2020)

Publications

1. J. Morgan and B. W. J. McNeil, *X-ray pulse generation with ultra-fast flipping of its orbital angular momentum,* Opt. Express **30**, 31171-31181 (2022)
2. A. F. Habib, et al., *Attosecond-Angstrom free-electron-laser towards the cold beam limit*, Nature Communications **14**:1054, (2023)
3. G. Perosa et. al, *Femtosecond Polarization Shaping of Free-Electron Laser Pulses,* Phys. Rev. Lett. 131, 045001 (2023)
4. J. Tang, Z. Zhang, J. Morgan, E. Hemsing, and Z. Huang. *Active Q-Switched X-Ray Regenerative Amplifier Free-Electron Laser,* Phys. Rev. Lett. **131**, 5 055001 (2023):
5. J. Morgan, et. al., *First Experimental Demonstration of Fully Structured Light in an EUV FEL,* Paper in progress
6. E. Hemsing, *A Model for Nonlinear Time-Dependent FELs with Semi-Short Beams,* Paper in progress

Beam on Demand for Superconducting Based X-Ray Free-Electron Lasers

Zhen Zhang, SLAC National Accelerator Laboratory

Keywords: high-repetition-rate FELs, multiplexing capability, beam on demand, chirper cavity, beam shaping

Research Project Scope

The multiplexing capabilities have been a crucial feature of superconducting-based X-ray free-electron lasers (FELs) such as the LCLS-II. The high-repetition rate of electron beams, up to megahertz, in these facilities make it feasible to feed multiple undulator lines simultaneously, significantly increasing the time available for the user experiments. However, the ability to multiplex using multiple undulator lines and the high flexibility in photon properties has been seen as a paradox. Balancing these demands to accommodate diverse requirements simultaneously poses a significant challenge in beam dynamics and beam manipulation. Therefore, more advanced beam manipulation concepts and techniques beyond traditional ones for normal-conducting FELs are highly desired for superconducting-based FELs.

To maximize the performance of superconducting-based FEL facilities, the concept of “beam on demand” has been proposed and developed at the LCLS-II [1]. This concept involves providing customized beam properties, including beam current, bunch length, beam charge, beam energy and residual energy chirp, for each undulator line at the desired beam repetition rate. This project will combine various strategies to achieve the concept of "beam on demand" at the LCLS-II.

1. A continuous-wave normal conducting cavity, which is called “chirper”, has been proposed and studied to achieve shot-by-shot control of peak current and bunch length [2]. In this project, we propose to build a prototype of the chirper cavity and demonstrate the key technologies and features that are crucial for its future application in the LCLS-II and HE. Subsequently, the R&D results of this project will motivate efforts at SLAC to install a chirper cavity for shot-by-shot compression control for the LCLS-II.
2. Our recent research has demonstrated that it is possible to produce low-emittance electron beams with different beam charges alternately at high repetition rate in the photoinjector through customizing the properties of the drive laser pulses [3]. This project will demonstrate the multiplexed configuration of the LCLS-II injector and linac.
3. The "twin-bunch" method has been employed in the normal-conducting linac of the LCLS to generate high-intensity two-color FEL pulses for pump-probe experiments [4]. This project aims to investigate its potential application in the LCLS-II, where the beam dynamics in the injector differ significantly from those in the LCLS.
4. Laser heater has been demonstrated to be a promising place in the beam line to perform electron beam shaping at interleaving modes in high-repetition-rate FELs [5]. A time-dependent laser heater profile is capable of shaping the bunch current to best suit a variety

of operational modes. This project will explore the application of laser heater shaping in the LCLS-II for various operation requirements.

Recent Progress

This project has received funding since July 2023. A new Research Assistant, Dr. Z. Zhu, joined the project in November 2023. The progress of each strategy in the project is listed below.

1. **Normal-Conducting Chirper Cavity for the LCLS-II**
   - We have completed and officially released the Physical Requirement Document (PRD) under document number SLAC-I-120-260-R0. This document outlines all the necessary physical requirements for the design and operation of the chirper cavity. These requirements are crucial for achieving shot-by-shot control of beam compression over a reasonable range at the LCLS-II and HE. The PRD includes specifications for RF frequency, cavity voltage, filling time, aperture radius, and cavity length.
   - Following group discussions and review, we have chosen to outsource the electrical design of the proposed chirper cavity to Euclid Techlabs. The purchase request is currently undergoing procedures at SLAC and is nearing final approval. Euclid Techlabs is expected to deliver the parametrized HFSS model of the traveling wave structure in approximately 9 weeks.
2. **Multiplexing configuration of the LCLS-II injector**
   - The commissioning of the LCLS-II injector and linac has been underway over the past year. Both the PI and Dr. Z. Zhu have actively participated in this process, including the optimization of injector settings. The optimized emittance for a 50-pC beam charge has been achieved at approximately 0.6 um with a reasonable bunch length of about 1 mm. Additionally, we have conducted measurements and optimizations of the laser spot profiles for different iris sizes. Once the transverse deflecting cavity is ready online (expected in April 2024), we will be able to systematically optimize the injector settings, including the proposed multiplexing configuration.
   - We have conducted optimizations of the multiplexing configuration using the current parameter status of the LCLS-II injector. These optimizations were carried out using the Genetic Algorithm (GA) and Astra. After 150 generations of optimization, we were able to achieve optimal emittance and reasonable bunch length for 20, 50, and 100 pC, respectively. These results are close to the optimal result for each beam charge.
3. **Twin-bunch generation and compression in the LCLS-II**
   - We have conducted simulations to generate twin electron bunches in the LCLS-II injector and linac. However, due to the low energy of the gun and the presence of the buncher cavity, generating twin electron bunches in the LCLS-II injector is not as straightforward as in the LCLS. Through start-to-end optimizations with the Genetic Algorithm, we have identified reasonable solutions for the twin-bunch scheme in the LCLS-II. These solutions allow us to achieve reasonable emittance, beam current, and

energy spread for each of the two bunches. We have also studied methods to vary the time delay and energy separations of the two bunches within a desired range.

Future Plans

The future plans of each strategy in the project are listed below.

1. **Normal-Conducting Chirper Cavity for the LCLS-II**
   - Following the completion of the electrical design of the chirper cavity, the mechanical design will be outsourced to an external company as well.
   - The chirper cavity will be fabricated by the RFSCIENG shop at SLAC. A prototype cavity will undergo testing to verify key parameters, including quality factor, shunt impedance, RF filling time, and maximum cavity voltage.
   - Investigation into the operation of the cavity at various chirping voltage requirements, assuming a 1MHz repetition rate, will also be conducted.
2. **Multiplexing configuration of the LCLS-II injector**
   - Experimental measurements for the multiplexing configuration of the LCLS-II injector will be conducted once the transverse deflecting cavity becomes operational. Laser iris size will be manually adjusted for different beam charges.
   - Investigation into methods for fast control of laser properties will be undertaken. An experimental demonstration for the multiplexed configuration with shot-by-shot control will also be performed.
3. **Twin-bunch generation and compression in the LCLS-II**
   - We will conduct systematic studies on the twin-bunch scheme in the LCLS-II to achieve independent control of the time and energy separation of the two bunches. This work will be summarized in a peer-reviewed journal paper.
   - We plan to perform an experimental demonstration of the twin-bunch scheme in the LCLS-II. The twin bunches will be sent to the undulator to produce two-color FEL pulses.
4. **Laser heater shaping in the LCLS-II**
   - Once the LCLS-II laser heater and the X-band deflecting cavity are ready for use, we will explore the application of laser heater shaping in the LCLS-II to meet various operation requirements, such as attosecond pulse, FEL pulse duration control, current horn suppression, and others.

References

1. Zhen Zhang, Yuantao Ding, and Zhirong Huang. "Beam on Demand for High-Repetition-Rate X-Ray Free-Electron Lasers." In 12th International Particle Accelerator Conference (IPAC'21), Campinas, SP, Brazil, 24-28 May 2021, pp. 3995-3998. JACOW Publishing, Geneva, Switzerland, 2021.

2. Nasr H. Mamdouh, Paul J. Emma, and Sami Tantawi. "A CW Normal Conducting RF Cavity for Fast Chirp Control in the LCLS-II." In 7th Int. Particle Accelerator Conf. (IPAC'16), Busan, Korea, May 8-13, 2016, pp. 1817-1819. JACOW, Geneva, Switzerland, 2016.
3. Zhen Zhang, Yuantao Ding, Zhirong Huang, and Feng Zhou. "Multiplexed Photoinjector Optimization for High-Repetition-Rate Free-Electron Lasers." Front. Phys., Volume 11 – 2023. https://doi.org/10.3389/fphy.2023.1166216
4. A. Marinelli, D. Ratner, A. A. Lutman, J. Turner, J. Welch, F-J. Decker, H. Loos et al. "High-intensity double-pulse X-ray free-electron laser." Nature communications 6, no. 1 (2015): 6369.
5. Siqi Li, Zhen Zhang, Shawn Alverson, David Cesar, Taran Driver, Paris Franz, Erik Isele et al. "" Beama la carte": laser heater shaping for attosecond pulses in a multiplexed x-ray free-electron laser." arXiv preprint arXiv:2404.02299 (2024).

Publications

1. Siqi Li, Zhen Zhang, Shawn Alverson, David Cesar, Taran Driver, Paris Franz, Erik Isele et al. "" Beama la carte": laser heater shaping for attosecond pulses in a multiplexed x-ray free-electron laser." arXiv preprint arXiv:2404.02299 (2024).
2. Li, Shuai, Lixin Lu, Swarnendu Bhattacharyya, Carolyn Pearce, Kai Li, Emily T. Nienhuis, Gilles Doumy et al. "Attosecond-pump attosecond-probe x-ray spectroscopy of liquid water." Science (2024): eadn6059.
3. Jingyi Tang, Zhen Zhang, Jenny Morgan, Erik Hemsing, and Zhirong Huang. "Active Q-switched X-Ray Regenerative Amplifier Free-Electron Laser." Physical Review Letters 131, no. 5 (2023): 055001.
4. Zhen Zhang, Emma Snively, Valery Dolgashev, and Zhirong Huang. "Fast and flexible control of beam longitudinal phase space for high-repetition-rate x-ray free-electron lasers." Review of Scientific Instruments 94, no. 2 (2023).
5. Zhen Zhang, Yuantao Ding, Zhirong Huang, and Feng Zhou. "Multiplexed photoinjector optimization for high-repetition-rate free-electron lasers." Frontiers in Physics 11 (2023): 1166216.
6. Siqi Li, Taran Driver, Philipp Rosenberger, Elio G. Champenois, Joseph Duris, Andre Al-Haddad, Vitali Averbukh et al. "Attosecond coherent electron motion in Auger-Meitner decay." Science 375, no. 6578 (2022): 285-290.
7. Paris L. Franz, Zhaoheng Guo, Dorian Bohler, David Cesar, Xinxin Cheng, Taran Driver, Joseph Duris et al. "Terawatt-Scale Attosecond X-ray Pulses via Cascaded Amplification at a Free Electron Laser." In Laser Science, pp. LM6F-6. Optica Publishing Group, 2023.
8. Zhaoheng Guo, Taran Driver, Sandra Beauvarlet, David Cesar, Joseph Duris, Paris L. Franz, Oliver Alexander et al. "Experimental Demonstration of Attosecond Pump-Probe Spectroscopy with an X-ray Free-Electron Laser." arXiv preprint arXiv:2401.15250 (2024).

9. Karim K. Alaa El-Din, Oliver G. Alexander, Leszek J. Frasinski, Florian Mintert, Zhaoheng Guo, Joseph Duris, Zhen Zhang et al. "Efficient prediction of attosecond two-colour pulses from an X-ray free-electron laser with machine learning." Scientific Reports 14 (2024).
10. River R. Robles, Kirk A. Larsen, David Cesar, Taran Driver, Joseph Duris, Paris Franz, Douglas Garratt et al. "Spectrotemporal shaping of attosecond x-ray pulses with a fresh-slice free-electron laser." arXiv preprint arXiv:2403.02189 (2024).

Research and Development of High-Power, High Repetition-Rate THz Capabilities for LCLS-II

Z. Huang, A. S. Fisher, M. Henstridge, M. C. Hoffmann, A. Naji, M. Othman (SLAC)

Keywords: THz, mirror guide, relay imaging, iris line, waveguide

Research Project Scope

The effective coupling of high-repetition rate THz radiation with the LCLS-II will open many new science opportunities, such as the exploration of strongly driven regimes in condensed matter physics and new possibilities for electron beam and x-ray diagnostics. Current strong-field THz sources rely mostly on difference-frequency mixing of near-infrared laser pulses in crystals at few-kHz repetition rates, but the extension of such sources to higher repetition rates suffers from reduced pulse energies and crystal damage. In Ref. [1], we have proposed an accelerator-based THz source that is driven by the same superconducting linac (that delivers XFEL pulses) and hence provides accurate synchronization between THz and X-rays. The source is tunable between 3-20 THz with an energy of more than 100 μJ per pulse, independent of the accelerator's beam rate, and a relatively narrow bandwidth to explore resonant excitations. However, there are still significant challenges that need to be addressed before implementing such a source in the LCLS-II facility.

While intense THz pulses have been routinely produced from a relativistic electron beam, transporting THz radiation over a wide wavelength range (3-20 THz) and over a long distance constitutes a large challenge. The THz beamline at the FLASH FEL in Hamburg has a net transmission no more than 50% over tens of meters, although the transmission is not optimized due to some small apertures in its transport line. The proposed LCLS-II scheme requires over 120 m of THz transport to the near experimental hall (NEH) and an additional 200-m extension to the far experimental hall (FEH). Thus, as an important next step toward implementing the LCLS-II THz scheme illustrated in Ref. [1], we have identified concepts that should be capable of greater efficiency in transporting THz pulses, without distorting their temporal structure and allowing for an intense focus in the hutch. This THz project involves the design and testing of two promising approaches to THz transport: a quasi-optical mirror guide based on reflective optics and an iris-line waveguide.

Recent Progress

The path length from the prospective wiggler source throughout the underground maze to the NEH of the LCLS is over 120 meters, and it contains two long 30-meter stretches. In our studies, we explore a transport design which would exploit the long Rayleigh lengths associated with transversely large beams to propagate THz radiation over long distances with minimal diffractive effects. Specifically, we aim to simply propagate the large beam over the 30-meter distance in the maze and minimize the number of optics necessary for efficient transport (see below). This design also takes advantage of the 90 degree turns in the maze for the placement of

optical relays consisting of off-axis parabolic mirrors (OAPs) to focus and re-collimate the beam. This approach would allow for the transport of collimated emission from the wiggler over a 120-meter distance to the location of the XPP hutch using 3 pairs of OAPs for optical relays, four planar mirrors, and an OAP to produce the final focus. This gives 11 mirrors in total in this preliminary conceptual design.

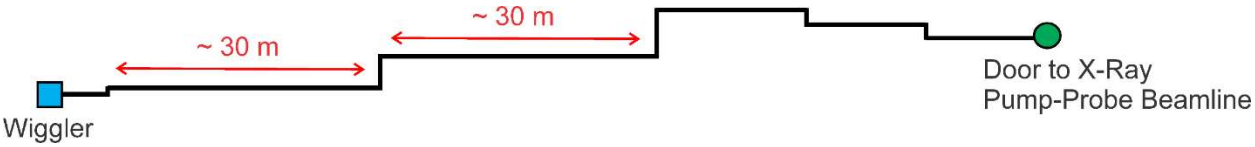

Figure 1: Scaled drawing of the ideal path from the wiggler through the undulator hall, maze, and maze exit to the NEH.

Traditionally, relay imaging involves a "4f" configuration in which an object source is imaged using two lenses or curved mirrors of identical focal length, and the total spacing between the object and the image is four times the focal length of the lenses or mirrors. For the case of a point source, that is, when the size of the source is considerably smaller than the collimated beam, then the nominal 2f spacing between the collimating and focusing optic can be increased. If the distance of the focusing optic from the collimating optic is increased but kept to a point where there is still very little (< 10 %) change in the beam waist, then the beam, as seen by the focusing lens, is still well-collimated and focuses near to the theoretical focal plane of the lens. One aspect of this approach that should be studied is the ability to successfully transport and focus THz sources with bandwidths of at least 10%.

One can test a 120-meter transport concept over shorter, but nevertheless challenging (10 -15 meter) length scales simply by reducing the Rayleigh length of the beam. This can be accomplished by reducing both the wavelength (from 100 μm to 10 μm) and the transverse beam size. Not only does such a test allow us to verify that this transport method is feasible, but this gives us an opportunity to develop alignment practices and hence provide engineering guidelines for the actual long distance transport line.

We carried out an initial test using a 10.6 μm CO_2 laser and standard gold planar mirrors and OAPs from Thorlabs for the testing of a reduced-scale model of the conceptual design shown in Figure 1. Figure 2 shows a qualitative description of the setup and a plot showing the power measured after each mirror in the setup. The linear drop of power after each mirror indicates that the diffraction losses are negligible, and the losses are predominantly ohmic. Simulations of this reduced-scale transport line using VirtualLab Fusion agree with the measurements. Results indicate that the THz emission can be transported over 120 m with an efficiency near 90%. Further testing is underway using the 3.25 THz output (100 μm wavelength) from a quantum-cascade laser.

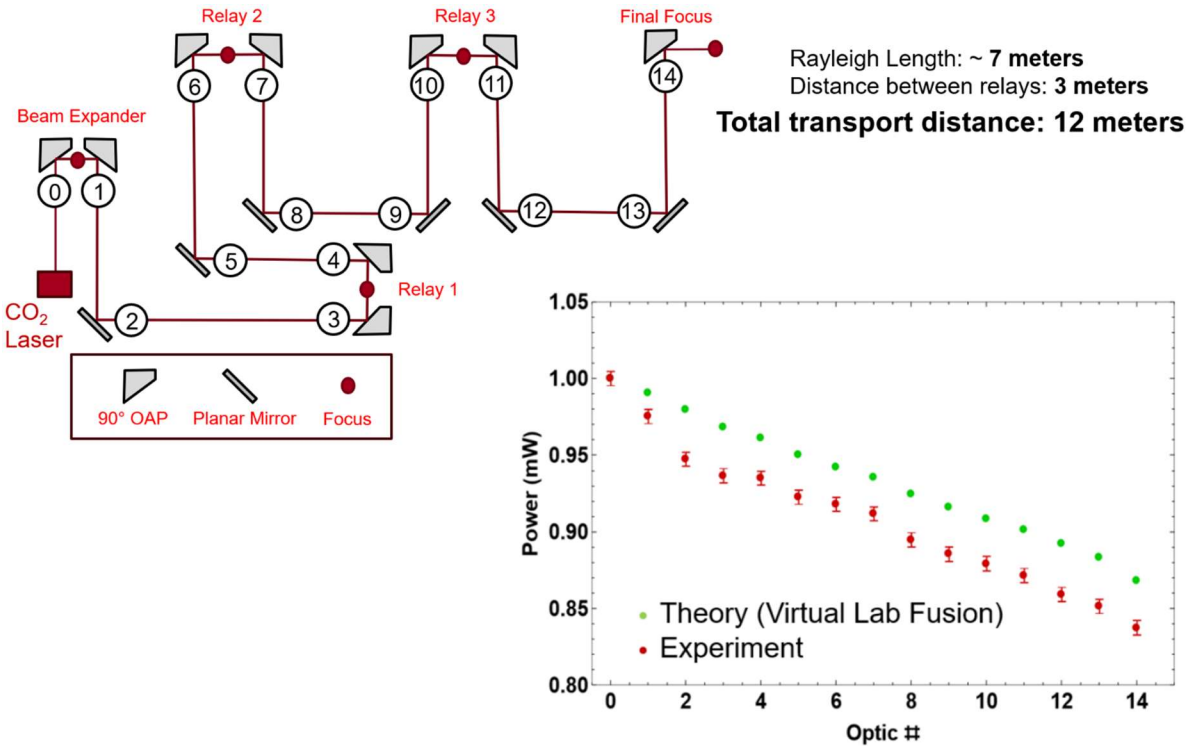

Figure 2: 10.6 um CO2 laser test setup in B40 laser lab and experimental power transmission results

We plan to test an iris-line waveguide [2] that exhibits a low power transmission loss and is attractive to transport THz radiation along the straight 200-m path from the NEH to FEH. Utilizing the iris-line to accomplish transport over a long straight path may offer a more straightforward alignment and installation process compared to the use of reflective optics relays. To address practical questions regarding validation of previous theories, experimental feasibility, manufacturing, as well as cost effectiveness of the iris-line, we plan to test THz transport over a section of reduced size. We will characterize propagation loss due to diffraction and ohmic loss, assess alignment tolerances, manufacturing, and installation process. This study serves as an initial guidance on the optimal design for a long-distance transport line that would span hundreds of meters.

We will use the 3.25 THz QCL system to test a small-scale (~20 meter) transport line. The Gaussian beam input into the iris line waveguide will have a Rayleigh length R=8 meters, hence the ability of the structure to efficiently a guide a beam that would otherwise diverge to more than twice its original size will be tested. To characterize the THz transport along the iris-line we have chosen to set the total length of the line L such that L/R~2.5-3. This iris-line test experiment is designed to investigate the impact of different parameters including iris radius a, iris-line period b, and the iris thickness t. Figure 3 also shows the geometry of the test setup composing of an array of irises mounted in a setup while relaying it back and forth across an optical table. The expected power transmission is over 50% for this setup. The power transmission is calculated using the

Rayleigh-Sommerfeld integration along the iris-line and verified using VirtualLab as well as mode-matching analysis developed inhouse.

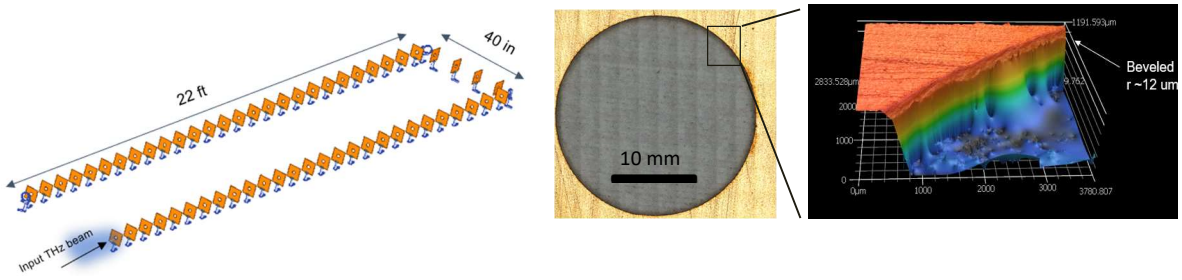

Figure 3 Left: Schematic of the iris line tabletop test experiment. Right: Image of the fabricated iris, and a microscope image of the edge showing the bevel on the iris rim.

Future Plans

In the remainder of this project, we plan to finish the mirror guide test by testing two transport schemes in the 3 THz range using the QCL. The first test is a scaled version of the conceptual NEH setup in which the beam will be transported over a 12-meter distance using standard off-axis parabolic mirrors. The second and more challenging test involves transporting the 3 THz beam over a 20-meter distance with custom-made parabolic mirrors which have unconventionally large diameters and focal lengths, like the optics that would be required for transport to the Near Experimental Hall. The optical table will be enclosed and purged with dry air to eliminate absorption by water vapor in this range. After we complete the mirror-guide measurements, we will test a scaled iris-line scheme using the same laser table and purged enclosure to obtain the experimental results and to compare with theory. These two tests will complete our RD project. We plan to publish our results and further develop our designs for long distance transport of THz radiation from the undulator hall to the LCLS NEH/FEH. We will continue to investigate future upgrades of the system to enable THz/X-ray pump probe at LCLS-II-HE and elsewhere.

References

1. Z. Zhang, A. S. Fisher, M. C. Hoffmann, B. Jacobson, P. S. Kirchmann, W.-S. Lee, A. Lindenberg, A. Marinelli, E. Nanni, R. Schoenlein, M. Qian, S. Sasaki, J. Xu and Z. Huang, "*A High-Power, High-Repetition Rate THz Source for Pump-Probe Experiments at Linac Coherent Light Source II*," J. Synchrotron Radiation **27** 890 (2020).
2. G. Geloni, V. Kocharyan, and E. Saldin, "*Scheme for generating and transporting THz radiation to the X-ray experimental floor at the LCLS baseline*." arXiv, Aug. 04, 2011. doi: 10.48550/arXiv.1108.1085.

Publications

1. A. Naji, G. Stupakov, Z. Huang, and K. Bane, “Field analysis for a highly overmoded iris line with application to THz radiation transport,” Phys. Rev. Accel. Beams 25, 043501 (2022).

2. A. Naji and G. Stupakov, “Paraxial forward-scatter field analysis for a THz pulse traveling down a highly overmoded iris-line waveguide,” Phys. Rev. Accel. Beams 25, 123501 (2022).

Laser-based THz Radiation for Advances in Ion Accelerators

M. Doleans, G. Hine and C. Moss

Keywords: Particle accelerator, terahertz, laser, field emission, broadband pulse

Research Project Scope

This project aims at using laser-driven THz radiation to deliver innovative science and technology for particle accelerators, and particularly for ion accelerators. Intense THz fields will be used for developing novel probing techniques of surfaces such as a field emission scanner, for developing original acceleration schemes for ion beams, and for advancing THz science.

The proposed research will use an existing infrastructure at ORNL [1] where an ultrafast multi-mJ Ti-sapphire drive laser is used to generate intense THz radiation via optical rectification in organic crystals. This tabletop laser system aims at delivering field strength up to GV/m at 1 kHz repetition rate. We propose to develop an innovative field emission (FE) scanner for materials relevant to particle accelerators such as Nb, Cu and newer materials such as Nb3Sn. The FE scanner will provide a new capability to probe the performance of accelerating structure surfaces and synergizes with our research on plasma processing aimed at improving their performance [2]. In the FE scanner, the intense THz radiation will be scanned on a surface and the field emission onset measured before and after a surface process, such as plasma processing, has been applied. Using the FE scanner, the potential improvement of the surface will thus be rapidly assessed without the need to use a complete accelerating structure and without the need to conduct a full test in a cryogenic Dewar or with high RF power.

We are also proposing to use the intense THz radiation to innovate in the acceleration of ion beams. The shorter wavelength of THz radiation compared to microwave radiation and the possibility to generate accelerating gradients above GV/m can lead to breakthroughs for more compact ion acceleration schemes. Our research will focus on exploring designs for non-resonant accelerating structures and for free space acceleration schemes via wave-front shaping for ions at energies from MeVs to GeVs.

Recent Progress

We have redesigned and improved the THz generation stage located after our Ti-sapphire drive laser and OPA. The upgraded THz generation stage is shown in Fig. 1 and uses a new generation crystal (PNPA organic crystal [3]), better optical focusing of THz fields with larger off-

axis parabola mirrors with higher numerical apertures leading to a more concentrated spot. The entire THz stage is enclosed in a nitrogen enclosure to mitigate THz absorption from moisture in air. The new THz emitter was acquired from Johnson-Lab (BYU, THz Innovations). Damage threshold for our 35 fs drive pulse will need to be assessed to determine the maximum field strength from the new THz stage.

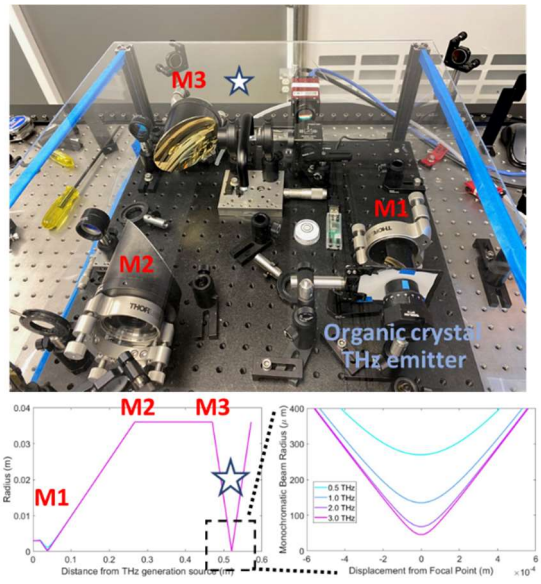

Fig 1: Redesigned and improved THz generation stage to increase THz fields.

A 3D printing platform is now in place for rapid prototyping of elements for terahertz wave manipulation. Prototyping of various elements has been achieved and includes hollow core fibers, Bragg reflectors and off-axis parabolic focusing mirrors. Figure 2 illustrates a few realized elements (gold coated off axis parabola mirror shown for comparison). The rapid prototyping platform is critical to explore and optimize possible concepts for particle acceleration using THz radiation. The current platform uses dual extruding fused filaments with dielectric and metallic compound printing capabilities. Collaboration with ORNL modern manufacturing experts at the Manufacturing Demonstration Facility and/or Center for Nanophase Materials Sciences is planned as necessary moving forward.

Fig 2: Various prototyped elements for THz wave manipulation.

A first electromagnetic design and prototyping of a hollow core fiber at 0.15 THz has been completed. The azimuthal pattern of the dielectric material around the core helps constraining modes radially and confining them in the core region [4]. As the result, minor portion of the radiation power propagates inside the solid fiber material leading to low propagation loss for the core modes. The cross section of the fiber and the field pattern of a core mode are shown in Figure 3. The 3D view of the design and the successfully prototyped fiber are also shown in the same figure. Significant coupling of the narrow band tunable THz source (0.1-0.2 THz) to the fiber has been observed, providing a proof of principle for the EM design and prototyping methods.

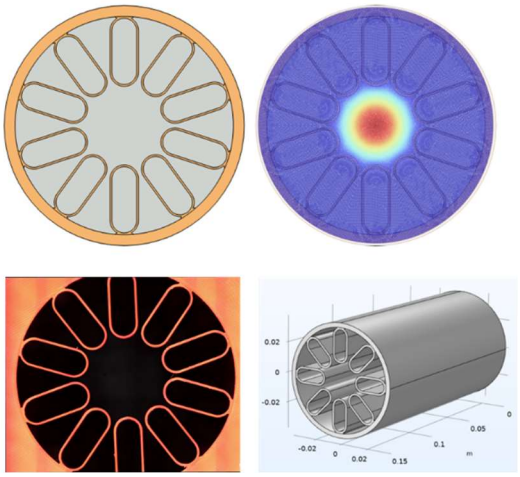

Fig 3: EM design and prototyping of a hollow core fiber at 0.15 THz.

A new temporal form for sub-cycle ultrabroadband pulses using the Faddeeva function has been achieved. Approximating with a superposition of, comparatively, narrow-band spectra is typically used when describing ultrabroadband pulses. But, such approximation has difficulty to capture asymptotic behavior near DC and in high frequency tail. It is also limiting when trying to describe spectra with complicated features arising from resonances in the source material or from dispersive effects for example. The new form using Faddeeva function naturally captures asymptotic behavior at small and large frequencies and benefits from the facts that the derivatives of the Faddeeva function form a complete set of functions and that their power-series representation are convergent. Figure 4 illustrates the decomposition of a THz pulse spectra from a BNA crystal using a small number of ultrabroadband pulses. Each temporal pulse corresponds to a spectral mode and the spectral modes form an orthonormal set. Two free parameters (lowest order mode and spectral width) can be varied to optimize the decomposition.

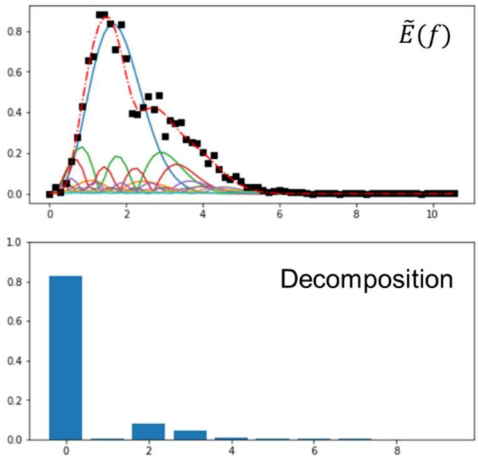

Fig 4: Decomposing of a pulse spectrum (BNA crystal) using Faddeeva functions.

Future Plans

Generation efficiency for PNPA THz emitters is known for 100 fs pump laser [3]. In collaboration with Johnson-Lab (BYU, THz Innovations), we will investigate the generation efficiency and

fluences/damage thresholds of PNPA THz emitters at our shorter 35 fs pump laser. Such study will benefit the THz community and help us maximizing the THz fields with our upgraded THz generation stage. Based on the stronger fields, we then aim at demonstrating field emission on small samples and synergize with our surface preparation R&D such as plasma processing.

We plan to continue the development and prototyping of THz guiding structures such as hollow core fibers. In particular, we will seek to slow down the THz waves and propagate broadband pulses in such structures to enable efficient particle acceleration. To help better understanding the ultrabroadband aspect of sub-cycle THz pulses and their possible harnessing for particle acceleration, we also plan to continue the work on the new temporal formulation using Faddeeva function. We will explore ways to decompose pulsed beams to capture propagation effects and aim at using this framework to propose innovative THz acceleration concepts.

References

[1] G. A. Hine and M. Doleans, Intrinsic spatial chirp of subcycle terahertz pulsed beams, Phys. Rev. A **104**, 032229 (2021)

[2] M. Doleans, Ignition and monitoring technique for plasma processing of multicell superconducting radio-frequency cavities, J. Appl. Phys. **120**, 243301 (2016).

[3] Claire Rader, Zachary B. Zaccardi, Sin-Hang Enoch Ho, Kylie G. Harrell, Paige K. Petersen, Megan F. Nielson, Harrison Stephan, Natalie K. Green, Daisy J. H. Ludlow, Matthew J. Lutz, Stacey J. Smith, David J. Michaelis, and Jeremy A. Johnson, A New Standard in High-Field Terahertz Generation: The Organic Nonlinear Optical Crystal PNPA, ACS Photonics 2022, 9, 11, 3720-3726

[4] Igor A. Bufetov, Alexey F. Kosolapov, Andrey D. Pryamikov, Alexey V. Gladyshev, Anton N. Kolyadin, Alexander A. Krylov, Yury P. Yatsenko and Alexander S. Biriukov, Revolver Hollow Core Optical Fibers, Fibers 2018, 6, 39

On the Prospects for Terawatt X-ray Free-Electron Lasers

Henry P. Freund, Patrick G. O'Shea and Thomas M. Antonsen, Jr.

Institute for Research in Electronics and Applied Physics

University of Maryland College Park, MD 20742

Keywords: Terawatt Generation, X-Ray Free-Electron Lasers, Harmonic Generation

Research Project Scope

Our objective and scope for this program is to study and develop scientific designs for X-ray free-electron laser (XFEL) configurations that can reach TW optical power levels using tapered superconducting undulators. Recent simulation studies [1,2] indicated that terawatt (TW) XFELs are possible and further would require extreme focusing of the electron beam to achieve very high current densities [2]. To put this into context, simulations indicated that current densities of as much as 2.5 GA/cm^2 would be required to reach TW power levels using a tapered undulator line [2] while the LCLS achieved 210 MA/cm^2. The overall scope of this research program is to study the TW XFELs which are relevant to the LCLS-II and LCLS-II HE facilities. This includes both simulations of TW XFEL designs and beam physics studies to determine any limitations which may occur during the compression of the beam prior to injection into the undulator line.

The principal simulation tool to be used is the MINERVA simulation code [3,4] which employs a three-dimensional, time-dependent nonlinear formulation. MINERVA uses the Slowly-Varying Envelope Approximation (SVEA) and the optical field is represented by a superposition of Gauss-Hermite modes. The field equations are averaged over the rapid time scale and, thereby, reduced to equations describing the slowly-varying amplitude and phase. The *x*- and *y*-components of the field are integrated independently; hence, MINERVA is capable of self-consistently simulating an undulator line composed of different polarizations which correspond to **the generation of variably polarized photons**. Particle orbits are integrated using the full Lorentz force equations in the complete optical and magnetostatic fields (undulators, quadrupoles and dipoles). It is important to remark that the use of the full Lorentz orbit analysis allows MINERVA to self-consistently **treat both the entry/exit tapers of undulators, and harmonic generation**.

Recent Progress

To date, activity has centered on nonlinear harmonic generation and polarization control using polarization tunable APPLE-II undulators, and a paper on the harmonic generation work has been accepted for publication in Physica Scripta (see publications below).

The configuration used for the harmonic generation study involved a 13.64 GeV/400 A electron beam with x- and y-emittances of 0.3 μm and an rms energy spread of 0.01%. As such, the beam is similar to that used in the LCLS-I. As in the LCLS-I, the undulators (both planar and helical) were such that the fundamental resonance was at 1.5 Å. The FODO lattice is strongly focusing with a cell length of 2.2 m using quadrupoles with field gradients of 26.4 kG/cm and lengths of 7.4 cm, and this achieved a current density of 2.5 GA/cm^2. Since the undulators are only weakly focusing, the FODO lattice dominated in the propagation of the electron beam which is shown in Fig. 1 where we plot the evolution of the beam envelopes in the x- and y-directions along the undulator line.

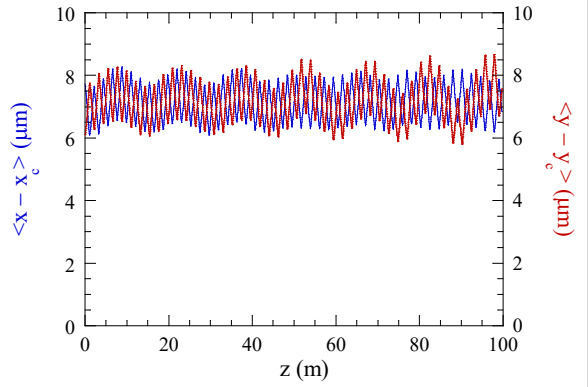

Fig. 1: Evolution of the beam envelope.

Harmonic generation was studied for both planar and helical undulators and for pure SASE and seeded configurations. Note that to reach TW fundamental power levels, the undulator line must be step-tapered and the optimal start-taper point and taper slope was optimized in each case. Substantial harmonic powers were found in all cases, although higher powers are found using planar undulators (as expected), but we focus here on the configuration using SASE with planar undulators. The optimal case is shown in Fig. 2 where we plot the fundamental and first five harmonics versus distance along the undulator line. It is

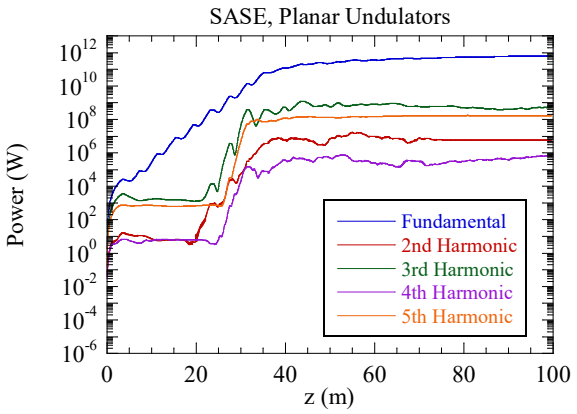

Fig. 2: Evolution of the fundamental and harmonics in the tapered, planar undulator line (SASE).

Harmonic	Wavelength (Å)	Photon Energy (keV)	Power (MW)
2	0.750	16.53	5.78
3	0.500	24.80	498
4	0.375	33.06	0.635
5	0.300	41.33	172

Table 1: Harmonic number, wavelength, photon energy and power in the planar undulator line (SASE).

typically found that the harmonics saturate before the fundamental so that since the taper must start just prior to the fundamental saturation but after the harmonics saturate, the harmonics are unaffected by the taper.

As shown, the fundamental reaches a power level of about 0.63 TW and we expect that the strongest harmonic will reach powers of about 0.1% that of the fundamental. A summary of the wavelength, photon energy and output power for the harmonics from the planar undulator line under SASE is shown in Table 1. Observe that, as expected for harmonics from planar undulators, the odd harmonics are more strongly generated than the even harmonics. The most strongly generated harmonic is the 3rd and is found at a peak power of 498 MW. The 5th harmonic, with a photon energy of 41.33 keV, is much reduced in comparison but is still found at a substantial peak power of 172 MW. A significant result was that a terawatt XFEL using a planar undulator line is capable of potentially generating hundreds of megawatts of 41 keV photons and substantial powers at still higher harmonics which are much higher than what has been previously achieved at similar wavelengths.

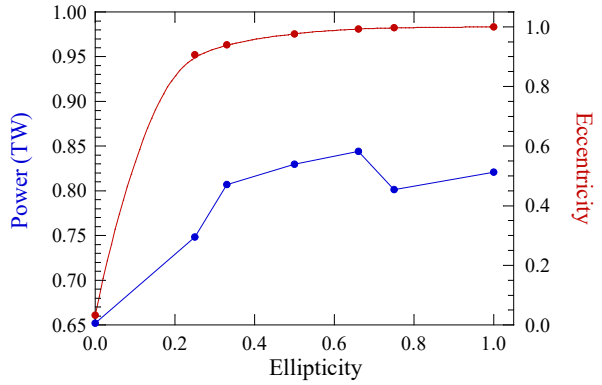

Fig. 3: The variation in the power and eccentricity versus the undulator ellipticity.

Preliminary studies have begun on methods for polarization control including using APPLE-II undulators which can be configured with variable ellipticities and alternating the orientation of a series of planar undulators. Simulations of the first case are complicated by the necessity of optimizing the step-taper profile for each choice of the undulator ellipticity since the undulator field strengths must be adjusted to maintain the same resonant wavelength [4]. The variation in the output power and eccentricity versus the undulator ellipticity is shown in Fig. 3 for the self-seeded configuration.

The eccentricity of the output radiation is found in simulation using a diagnostic procedure that determines the Stoke's parameters where the Stoke's s_3 parameter specifies the polarization and $s_3 = 0$ (1) describes a plane (circular) polarization state. As shown in the figure the s3 parameter declines (slowly) from pure circular polarization corresponding to an ellipticity of 1.0 for the APPLE-II undulators to pure plane polarization for an ellipticity of 0.0. The power tends to decrease with increasing plane polarization because the effective strength of the interaction (governed by the so-called *JJ* parameter) decreases as the polarization of the undulators becomes increasingly planar. The fact that the decrease in the power is not monotonic is due to the fact that the optimal step-taper does not vary smoothly because, while the optimal start-taper point may be found within an undulator segment, we

can only choose the optimal undulator; hence, the optimization procedure necessarily produces a coarse optimization.

Future Plans

Simulation studies will continue including both steady-state and time-dependent simulations of both single-pass SASE and seeded amplifier configurations and cavity-based configurations including X-ray Regenerative Amplifiers (XRAFEL). These studies will treat different undulator configurations to continue the study of different methods of polarization control such as afterburners with different polarizations from the preceding undulators. XRAFEL simulations will employ MINERVA linked to the Optics Propagation Code (OPC) developed at the University of Twente in the Netherlands [5] and which has been used in conjunction with MINERVA to simulate the high average power infrared FEL oscillator experiment at Jefferson Laboratory and an XRAFEL design under an SBIR program through the Department of Energy. In particular, we will:

1. Study the sensitivities of afterburner configurations to the seed power in regard to the control of the polarization of the output radiation.
2. Study the requirements for the generation and propagation of electron beams with the high current densities needed to achieve TW production.
3. Study the sensitivities of TW production to variations in peak current and beam brightness, and to beam mismatch into the undulator line/FODO lattice.
4. Conduct a detailed comparison of the relative benefits of using helical versus planar undulators. This will also extend to studying the production of elliptically polarized x-rays using configurable APPLE-II undulators.
5. Study the sensitivity of TW production to undulator/quadrupole errors.
6. Continue the study of nonlinear harmonic generation under a variety of conditions.
7. Perform XRAFEL simulations for configurations of interest to the LCLS-II and LCLS-II HE experiments at SLAC with the aim of quantizing stability of the spectrum and output power to fluctuations.

This work will be informed by consultations with personnel at SLAC to ensure that it remains relevant to the experimental XFEL and XRAFEL programs underway at SLAC.

References

1. C. Emma, K. Fang, J. Wu, and C. Pellegrini, *High Efficiency, Multiterawatt X-Ray Free Electron Lasers*, Phys. Rev. Accel. Beams, **19**, 020705 (2016).
2. H.P. Freund and P.J.M. van der Slot, *Studies of a Terawatt X-Ray Free-Electron Laser*, New J. Phys. **20**, 073017 (2018).
3. H.P. Freund, P.J.M. van der Slot, D.L.A.G. Grimminck, and P. Falgari, *Three-Dimensional, Time-Dependent Simulation of Free-Electron Lasers with Planar, Helical, and Elliptical Undulators*, New. J. Phys. **19**, 023020 (2017).

4. H.P. Freund and P.J.M. van der Slot, *Variable Polarization States in Free-Electron Lasers*, J. Phys. Commun. **5**, 085011 (2021).
5. J.G. Karssenberg, P.J.M. van der Slot, I.V. Volokhine, J.W.J. Vershuur, and K.-J. Boller, *Modeling paraxial wave propagation in free-electron laser oscillators*, J. Appl. Phys. **100**, 093106 (2006).

Publications

1.H.P. Freund and P.G. O'Shea, *Harmonic Generation in a Terawatt X-Ray Free-Electron Laser*, Physica Scripta, (accepted for publication 2024).

Electron Beam Magnetic Field Mapping Technology for Undulators and Magnets

Marcos Turqueti, Lawrence Berkeley National Laboratory

Keywords: Magnetic Field, Cathode Ray Tube, Undulator, Imaging Sensor, and Electron Beam.

Research Project Scope

The primary aim of this project is to develop a magnetic field probe tailored specifically for the characterization of insertion devices for light sources, with potential applications extending beyond this domain.

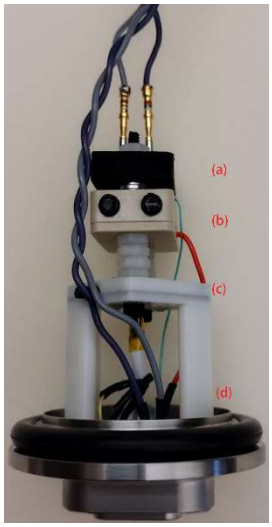

Figure 1. Probe vacuum test article, (a) cathode, (b) scintillator and acceleration ring, (c) imager, and (d) flange interface.

At its core, the probe relies on a measurement medium comprised of a low-energy, low-intensity particle beam. Its key components include an electron gun, which emits a controlled stream of electrons towards an imaging sensor positioned perpendicular to the particle trajectory at the opposite end of the cathode ray tube. Electrostatic deflecting plates can manipulate the electric field to project a distinct pattern onto the imaging sensor delivering enhanced performance. When subjected to a magnetic field, this projected pattern undergoes discernible shifts and alterations, facilitating precise determination of the magnetic field's strength and orientation.

To optimize the magnetometer for its designated purpose, several parameters must be carefully tuned. Among these, the spatial resolution of the probe holds particular significance, as altering the electric field can impact sensitivity inversely. Moreover, adjustments to the accelerating electric field influence the energy spectrum of the electron beam, thereby affecting the performance of the image sensor. The deflecting plates introduce offsets in both horizontal and vertical directions, enabling flexible projection of the electron beam onto different regions of the imaging sensor. This dynamic capability allows for on-the-fly adaptation of the probe, ensuring a broad magnetic dynamic range while preserving sensitivity.

Recent Progress

Substantial progress has been achieved recently through the development of initial hardware prototypes. Throughout this phase, various technical hurdles have been encountered and actively addressed, with invaluable insights gained from prototype feedback informing iterative refinements to theoretical models by the use of test structures such as the one illustrated by figure 1. Consequently, more precise and detailed simulations can now be conducted, facilitating further advancements.

Several pivotal technological decisions have been made, including the selection of lanthanum hexaboride (LaB6) as the preferred cathode material for the electron gun. Extensive testing and simulations have been undertaken to assess the LaB6 cathode optimum configuration.

Another critical aspect lies in the choice of imaging sensor. After meticulous consideration and thorough testing, the decision to employ CMOS technology has been made. However, the deployment of CMOS using either direct or indirect detection methods is currently under evaluation. This assessment is vital to ascertain the most effective and efficient approach moving forward.

Future Plans

In future work, optimizing the magnetic probe's performance remains intricately tied to balancing key parameters such as accuracy, spatial resolution, temperature range, and sensitivity. For our specific application, where a small diameter is crucial for viability, achieving targeted sensitivity while preserving the desired dynamic range presents the primary challenge. To tackle this challenge, proactive strategies are being pursued, including advanced signal processing techniques, exploring alternative scintillator types, and integrating electrostatic deflecting plates. These efforts aim to elevate the prototype's sensitivity to the specified target of 25μT. A hurdle lies in the minimal detectable displacement of the electron beam by the imager, influenced by factors such as suboptimal scintillator material for low-energy electron detection. We are actively investigating alternative scintillating materials capable of effective operation with lower energy electrons. Additionally, long-term plans involve developing a custom-made CMOS imager optimized for direct electron detection.

Utilizing lower energy electrons presents a challenge, further reducing the probe's dynamic range due to excessive beam deflection. Integrating deflecting electrostatic rings aims to counteract magnetic deflection, ensuring efficacy with lower-energy electrons while achieving the desired dynamic range and sensitivity. Another avenue involves enhancing sensitivity by replacing the monolithic scintillator with a pixelated version. With 5 μm by 5 μm pixels, light spreads over multiple pixels, surpassing typical pixel charge capacities. This necessitates light attenuation, ideally achieved through a semi-transparent deposited thin film.

Improvements are anticipated on position resolution, through averaging within each image frame, enhancing the signal-to-noise ratio and aligning with the goal of advancing probe capabilities. The transition to FPGA-based infrastructure promises increased computational efficiency, facilitating more intricate image processing algorithms. The FPGA implementation, currently underway, will enable the probe to function as a standalone system, controlling electrostatic deflection plates to maintain beam spot position. Data from the probe, received via LVDS, is decoded and formatted in real-time for analysis.

References

1. J. Kawai, M.Miyamoto, M.Kawabata, M.Nosé, Y.Haruta and G. Uehara, "Characterization and demonstration results of a SQUID magnetometer system developed for geomagnetic field measurements," *Superconductor Science and Technology, IOP Publishing Ltd,* vol. 30, no. 8, DOI 10.1088/1361-6668/aa733f, 2017.
2. L. a. H. K. Bottura, "Field Measurements," EUROPEAN ORGANIZATION FOR NUCLEAR RESEARCH (CERN), Geneva, 2002.
3. S. Na, L. Xumin and G. Yong, "Research on k-means Clustering Algorithm: An Improved k-means Clustering Algorithm," *Third International Symposium on Intelligent Information Technology and Security Informatics, China,* pp. 63-67, 2010, doi: 10.1109/IITSI.2010.74.
4. A.Temnykh, Y.Levashov and Z.Wolf, "A study of undulator magnets characterization using the vibrating wire technique," *Nuclear Instruments and Methods in Physics Research,* vol. 622, no. 3, p. 650–656, 2010, doi:10.1016/j.nima.2010.06.362.
5. Wei, X. Y.Li, Z.Chen and X. X.Zhang, "Development and magnetic field measurement of a 0.5-m-long superconducting undulator at IHEP," *Journal of Synchrotron Radiation,* vol. 29, no. 4, pp. 997-1003, 2022, doi: 10.1107/S1600577522006166.

Publications

1. Marcos Turqueti, Gustav Wagner, Azriel Goldschmidt, and Rebecca Carley, "Digital Miniature Cathode Ray Magnetometer", MDPI Instruments, accepted for publication, 10.20944/preprints202401.0195.v1, 2024.

2. Marcos Turqueti and Srinidhi Bheesette, "Simulation Studies for an Electron Gun Based Magnetic Probe", IEEE Transactions on Nuclear Science, Volume: 70, Issue: 3, 2023.

Double Nb3Sn Superconducting Undulator for the Advanced Photon Source

Efim Gluskin, Advanced Photon Source at Argonne National Laboratory

Keywords: Superconducting undulator, magnet, Nb_3Sn wire, x-ray spectra

Research Project Scope

The scope of the project includes: a) development, design, and construction of Nb_3Sn superconducting undulators (SCUs); b) assembly, testing, tuning, and magnetic characterization of Nb_3Sn SCUs in vertical and horizontal cryostats; and c) installation of a Nb_3Sn SCU in the Advanced Photon Source (APS) storage ring, characterization of its x-ray spectra, and operation of this device in support of APS users' experiments.

Progress in the Last 5 years (FY2018 through FY2023)

The goal of the project was to develop and build for the first time a Nb_3Sn SCU that demonstrates magnetic performance superior to a NbTi SCU and meets the requirements of an operational x-ray source at a third-generation synchrotron radiation facility. The most challenging part of the project was developing a SCU magnet of high enough magnetic quality that it would meet the strict operational requirements. To that end, an APS SCU team—in collaboration with Nb_3Sn magnet experts from Fermi National Laboratory—designed, built, and tested a total of eight SCU magnet prototypes. In the process of constructing and testing these prototypes, an optimal procedure for high-temperature heat treatment of Nb_3Sn magnets was developed. The development of this heat treatment process was crucial for the successful construction of the 1.1-m-long, 18-mm-period Nb_3Sn SCU magnets. Since a Nb_3Sn SCU, while in operation, stores several times more energy than its NbTi equivalent, a special quench protection system is mandatory for safe operation. Such a system was designed, built, and tested in collaboration with a team from Lawrence Berkely National Laboratory. Another important development—a novel SCU magnet measurement system—was developed by the APS SCU team. This magnet measurement system showed that, as expected, a magnetic peak field was achieved in the Nb_3Sn SCU that was higher than in a NbTi SCU. By the end of 2022 construction and testing of the APS Nb_3Sn SCU was complete. In January of 2023 the Nb_3Sn SCU was installed in the Sector 1 straight section of the APS storage ring, replacing a NbTi SCU of the same length and period. X-ray radiation from the Nb_3Sn SCU was measured, and the required quality of the device's spectral performance was confirmed. From January through April of 2023 the Nb_3Sn SCU operated with 99% reliability, delivering x-rays to more than 20 APS users groups for their experiments.

Future Plans

In 2024-2025 the construction and testing of the second Nb_3Sn SCU will be completed. This device will have the same periodic structure but new end compensation magnets.

Nb_3Sn SCU on the APS storage ring

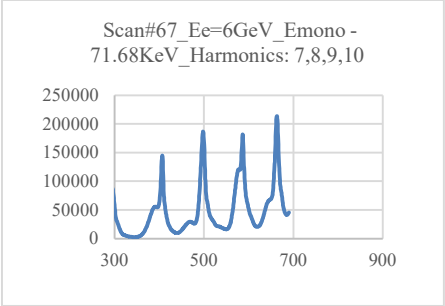

Nb_3Sn SCU magnet current scan

Publications

1. I. Kesgin et al., Fabrication and Testing of 18-mm-Period, 0.5-m-Long Nb_3Sn Superconducting Undulator, IEEE Transactions on Applied Superconductivity, Vol. 31, No. 5, August 2021.
2. E. Barzi et al., Heat Treatment Studies of Nb_3Sn Wires for Superconducting Planar Undulators, IEEE Transactions on Applied Superconductivity, Vol. 30, No. 4, June 2020.
3. I. Kesgin et al., Design, Construction, and Testing of 0.5-m, 18-mm Period Nb_3Sn Superconducting Undulator Magnets, IEEE Transactions on Applied Superconductivity, Vol. 32, No. 6, September 2022.
4. I. Kesgin et al., Quench Behavior of 18-mm Period, 1,1-m Long Nb_3Sn Superconducting Undulator Magnets, IEEE Transactions on Applied Superconductivity, Vol. 34, No. 5, August 2024.

Superconducting Undulator R&D for World-Leading X-ray FEL Capabilities

Patrick Krejcik SLAC National Accelerator Laboratory

Keywords: Superconducting, Undulators, X-ray, FELs

Research Project Scope Our project will demonstrate the superior performance characteristics of Superconducting Undulators (SCUs) in X-ray FELs, taking advantage of the stronger magnetic fields to produce brighter X-rays at shorter wavelengths. Two prototype SCU cryomodules will be installed in the LCLS at SLAC to measure the gain length and other key performance parameters. We leverage the ANL expertise in building SC undulators and combine this with SLAC's experience in operating high-power X-ray FELs. Each SCU cryomodule contains a Nb:Ti planar undulator magnet together with a quadrupole, beam position monitor, and phase shifter. The cryomodules will be integrated into the existing hard X-ray FEL beamline so that we can demonstrate that the necessary beam-based alignment of the components inside the cryomodule can be achieved to micron precision. The design of the SCU magnets and cryomodule is chosen to allow connections of multiple SCUs to form a contiguous line of SCUs for the XFEL.

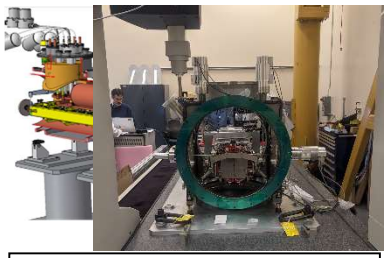

Two adjoining cryomodules each house an SCU, quad, BPM and phase shifter.

Recent Progress

Progress has been made in three key areas of our project. We have built and tested a planar SC undulator magnet to verify that our fabrication technique meets the required tolerances both mechanically and in the final magnetic measurements.

A 1 m long prototype of the undulator magnet has been measured in a vertical cryostat.

The second area of progress is in the design of the cryomodule which houses the SC undulator and other beamline components. The magnets and diagnostic instruments are mounted on an internal strongback girder inside the cryomodule. This girder is suspended from external linear actuators allowing it to be aligned with micron precision during operation with the beam.

The third area of progress is the design and testing of these linear actuators on a Precision Alignment Test Stand (PATS) to verify that the remote actuators can reproducibly position the SCU components even after the internal components are cooled to cryogenic temperatures. Room temperature measurements have been performed on the PATS to verify the functionality and precision of the actuators, resulting in some small design changes to improve the reproducibility of the motion.

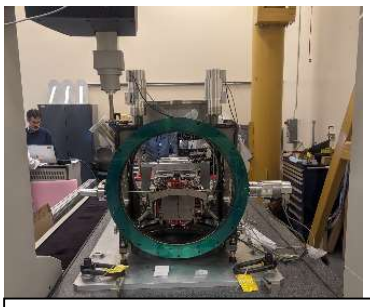

The Precision Alignment Test Stand demonstrates the necessary precision to which the SCU can be aligned.

Future Plans

The next step in our prototype development plan is to test the precision of the alignment system in the PATS at cryogenic temperatures. Our design compensates for the large thermal contraction during cooling and independently measures the position of the components using optical interferometry. As a final step, the position of the magnetic center of the components will be measured warm versus cold to further verify there is no loss of reproducibility in alignment during the thermal cycling of the cryomodule.

With the completion of the PATS testing, we will continue with the completion of the cryomodule fabrication and the assembly of the 1.5 m long SC undulator magnet, incorporating any further lessons learned from the PATS testing.

We then expect to install three cryomodules on the SLAC LCLS beam at the end of the hard X–ray beamline where beam-based alignment of the SCUs will be performed relative to the upstream undulator system. In an X-ray FEL, this must be performed at the micron level to fully realize the maximum FEL gain per module, with the added complication that this must be fully reproducible after multiple cool-down cycles of the cryogenic system.

The final step is to measure the FEL gain of each successive module using the existing LCLS hard X-ray undulator beamline as a pre-buncher.

This demonstration project will allow the ultimate goal of building a fully superconducting undulator FEL beamline at the LCLS using inter-connectable modules, each containing a complete FEL subsystem, to build a high-power, compact X-ray FEL.

References

1. P. Krejcik, G.J. Bouchard, G.L. Gassner, Z. Huang, E.M. Kraft, B. Lam, M.A. Montironi, C.D. Nantista, D.C. Nguyen, H.-D. Nuhn, X. Permanyer, Z.R. Wolf, Z. Zhang, SLAC, Menlo Park, California, USA, J.M. Byrd, J.D. Fuerst, E. Gluskin, Y. Ivanyushenkov, M. Kasa, M.F. Qian, Y. Shiroyanagi, ANL, Lemont, Illinois, USA , "SCU Development at the LCLS for Future FELs", presented at the 67th ICFA Adv. Beam Dyn. Workshop Future Light Sources (FLS'23), Luzern, Switzerland, Aug.-Sep. 2023, paper TH1D3.

2. D.C. Nguyen, G.J. Bouchard, B.M. Dunham, G.L. Gassner, Z. Huang, E.M. Kraft, P. Krejcik, M.A. Montironi, H.-D. Nuhn, T.O. Raubenheimer, Z.R. Wolf, Z. Zhang, SLAC, Menlo Park, California, USA, J.M. Byrd, J.D. Fuerst, E. Gluskin, Y. Ivanyushenkov, M. Kasa, E.R. Moog, M.F. Qian, Y. Shiroyanagi,ANL, Lemont, Illinois, USA "Superconducting Undulators and Cryomodules for X-ray Free-Electron Lasers", in Proc. NAPAC'22, Albuquerque, NM, USA, Aug. 2022, pp. 870-873. doi:10.18429/JACoW-NAPAC2022-THYE3

3. Y. Shiroyanagi, Y. Ivanyushenkov, and M. Kasa, “Magnetic Field Calculation of Superconducting Undulators for FEL Using Maxwell 3D”, in Proc. NAPAC'22, Albuquerque, NM, USA, Aug. 2022, pp. 423-426. doi:10.18429/JACoW-NAPAC2022-TUPA33.

4. M.F. Qian, “SCU Ends Configured as Phase Shifter”, in Proc. NAPAC'22, Albuquerque, NM, USA, Aug. 2022, pp. 420-422. doi:10.18429/JACoW-NAPAC2022-TUPA32.

5. J. Fuerst1, G. Bouchard, G. Gassner, Q. Hasse1, Y. Ivanyushenkov, M. Kasa1, E. Kraft, P. Krejcik, X. Permanyer, “Cryostat Design for an FEL SCU Demonstrator”,in Proc. CEC/ICMC 2023, Jul 9 – 13, 2023, Honolulu, Hawaii.

6. C.D. Nantista, A.A. Haase, and P. Krejcik, “A Cryogenic RF Cavity BPM for the Superconducting Undulator at LCLS”, in Proc. IBIC'22, Kraków, Poland, Sep. 2022, pp. 241-244. doi:10.18429/JACoW-IBIC2022-TUP11

Session Two

Optics, Diagnostics, Instrumentation

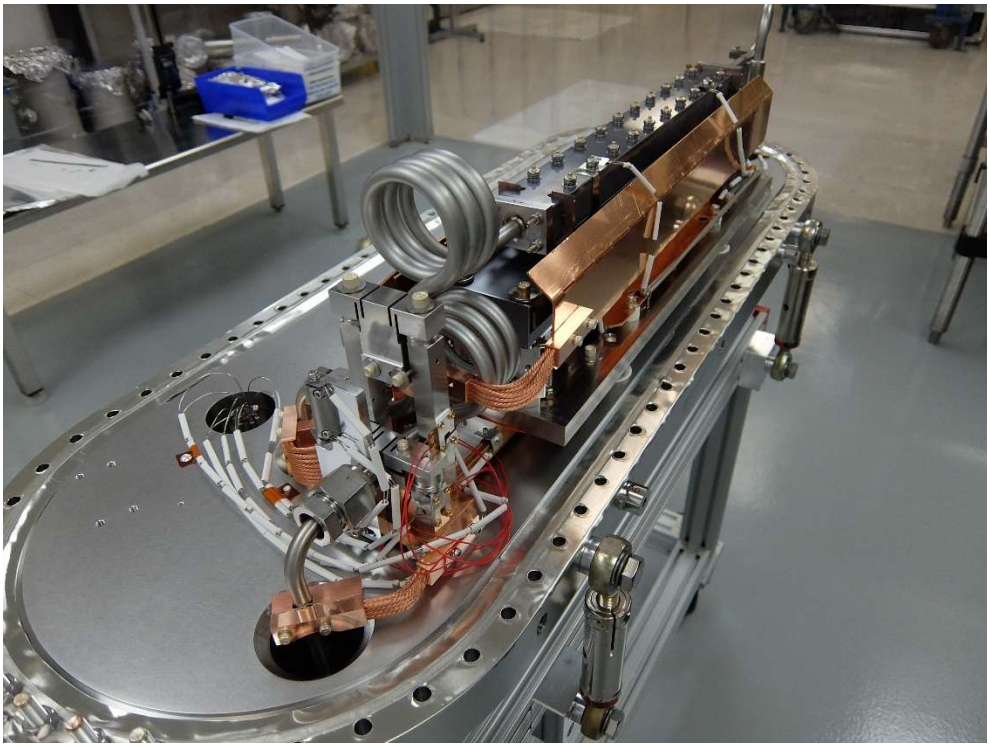

Liquid argon cooled x-ray mirror and heat exchangers as seen during assembly. Compensatory heating of the cryogen is employed to maintain this mirror at the ~125K ideal temperature for minimal thermal deformation independent of absorbed x-ray power load. Courtesy: Jim Tracey, SLAC National Accelerator Laboratory

Cryogenically-cooled-silicon mirrors for diffraction-limited storage rings and free-electron lasers

Lahsen Assoufid (ANL), Lei Huang (BNL), Grant Cutler (LBNL), Thomas Rabedeau (SLAC)

Keywords: cryo-mirror, cryo-metrology, at wavelength metrology

Research Project Scope

Wave-front preservation is essential to realizing the capabilities of new and upgraded diffraction-limited storage ring and free electron laser sources. Cryo-mirrors, by exploiting the vanishing thermal expansion coefficient and high thermal conductivity of silicon at a temperature near 125K, offer the promise of sub-nm mirror shape stability in the presence of high powers, high power densities, and dynamically varying power profiles[1-2]. Realizing the benefits of cryo-mirrors demands collaborative development of new technologies to meet the associated challenges: thermally optimized, low-strain, stable cryo-mirrors, laboratory-based, and at-wavelength metrology to support cryo-mirror development and characterization.

Cryogenic silicon has been used for thermal deformation management of monochromator crystals since the 1990s[3], and a few prototype cryogenically-cooled, silicon mirrors[2, 4-5] exist as well. Typically, these systems employ liquid nitrogen (LN) cooling and often operate outside the optimal ~125K temperature for minimum distortion. The objective of the current research effort is to develop a prototype hard-x-ray-capable cryo-mirror system employing feed-forward compensatory cryogen heating to maintain the mirror at the optimal temperature for minimum thermal deformation over a range of absorbed power and power densities including dynamically varying absorbed power. Employing LN at the optimum temperature involves unrealistically high cryogen pressure, so the prototype mirror employs liquid argon cooling allowing cryogen pressure reduction of 10-15 bar relative to LN.

To realize the thermal performance advantages of a cryo-mirror system requires an effective heat exchanger that minimizes mirror cool-down strain, maintains the mirror at the optimal temperature for minimum strain over a range of absorbed power, and minimizes cryogen flow-induced vibration of the mirror assembly. An essential element of the proposed development effort is the accurate simulation and optimization of cryogen flow to ensure the requisite thermal performance and dynamic stability of the cryo-mirror.

To guide the design of the mirror system and refine its manufacturing process—and to evaluate its performance—it is necessary to measure cryo-mirror surface deformation to sub-nanometer precision. While laboratory-based metrology tools with this precision exist, they only operate at room temperature. Therefore, this scope of work includes development of a reliable, lab-based, optical-metrology system to measure the mirror shape error at cryogenic temperatures. Our system employs a commercial interferometer located outside the mirror vacuum system but utilizes a transmission flat in vacuum and a custom optical window to minimize the deleterious impacts of the vacuum chamber glass viewport incorporated into the interferometer optical path.

Finally, to validate the performance of the prototype mirror system it will be transported to APS where dual in-line undulators of 28-ID operated in concert with optimized wave front characterization tools allow careful study of the thermal deformation as a function of absorbed x-ray power.

Recent Progress

After extensive finite element analysis (FEA) of the mirror system thermal performance, prototyping and testing of supportive technologies such as the 15 bar cryo-seals, interface thermal impedance studies, and flow induced vibration studies, the mirror system design was finalized and manufactured. The first two quarters of FY2023 were primarily focused on preparing for the at-wavelength mirror thermal performance characterization beam time on APS 28-ID scheduled for March and April, 2023. There were several parallel thrusts of activity.

Cryo-mirror room temperature metrology – Grazing-incidence, room temperature metrology of the mirror mounted in its cradle was performed in November 2022. Some mirror twist about the longitudinal axis was measured. The result was deemed to be within acceptable limits.

Lab-based cryo-metrology – In anticipation of lab-based cryogenic testing of the mirror system with an infrared laser heater prior to mirror deployment to APS 28-ID for at wavelength testing, the cryo-metrology team explored various approaches to minimize the deleterious impacts of the vacuum chamber viewport that is by necessity part of the interferometer optical path. After exploring several options for improving the viewport quality, the best results were obtained with

a thick λ/10 optical flat Viton™ sealed to a conflat receiver. Measurements with a short LN-cooled mirror at ALS revealed that radiative cooling of the viewport creates a weak gradient in the viewport index of refraction which degrades the fidelity of the interferometric metrology. To minimize the impact of the viewport, the transmission reference flat is moved inside the mirror vacuum chamber, such that any viewport effects can be normalized out of the interferometry data. Additionally thermal masks are introduced to minimize the radiative thermal exchange between the cold mirror and the viewport. Unfortunately, assembly schedule slippage precluded lab-based cryo-mirror metrology prior to mirror system shipment to APS for at-wavelength studies.

Cryo-cooler – The liquid argon cryo-cooler with the specified 600W heater for feed forward cryogen temperature control was delivered by the vendor in December, 2022. The cryo-cooler pressure safety was reviewed and approved by the SLAC pressure safety officer prior to SLAC acceptance testing. The cryo-cooler performance was validated thereafter.

Air Bearing Pedestal – The primary support of the cryo-mirror system consists of a pair of granite blocks with an integral air bearing that provides adjustment of the mirror horizontal position and angle with respect to the incident beam. The air bearing system was explicitly designed to provide a very stable mirror platform to minimize vibration effects. The air bearing pedestal system was assembled and tested prior to shipment to APS for the spring beam time.

Cryo-mirror Assembly – Despite extensive and successful prototype studies of the cryogen manifolds to silicon heat exchanger C-ring seal as referenced above, the initial assembly of the mirror heat exchangers onto to the manifolds proved not to be leak-tight. Consequently, much of Q1 of FY2023 was spent optimizing the manifold alignment to minimize strain and rebuilding and reassembling the mirror system. Despite this effort, the second round of C-ring seal assemblies also proved somewhat leaky. Ultimately, in order to meet the beam time scheduled at APS, we elected to increase seal force and apply Vacseal resin to seal the manifolds to the silicon cooling bars. This produced leak-tight seals at 16 bar coolant duct force as needed for the thermal performance studies. The mirror assembly was completed in time for shipment to APS for the March 2023 beam time, marking a significant milestone for the project.

APS 28-ID Beam Time Preparation – In the first half of FY2023, the APS team worked to ensure 28-ID beamline was ready for installing and testing the mirror system. Preparation activities included verifying the 28-ID undulator power envelope and power filters the team designed and implemented to avoid damage to the wave front detector system, providing the required infrastructure for installing and testing the cryo-mirror system, and shepherding the proposed mirror test protocol through the beam time safety review and administrative and safety approval process.

The X-ray wave front sensor developed for the power testing was enhanced with a tunable field of view and optimized for the cryo-mirror testing geometry at the 28-ID beamline. Prior to receiving the mirror system, the team conducted multiple tests on the wave front sensor at a low flux level both at the APS 1-BM and 28-ID beamlines, validating the wave front sensor's outstanding performance before the cryo-mirror was delivered and installed in March 2023. The aim of tests was to simulate the mirror set up at a high incidence angle, which would allow for maximum mirror power absorption while transmitting a low flux level for accurate wave front measurements. These tests successfully confirmed that the developed wave front sensor is functioning as expected and is suitable for the planned power tests.

Cryo-mirror Cool Down Failure – The cryo-mirror system was shipped to APS in late February 2023, and the mirror system installation commenced March 2, 2023. The major elements of the cryo-mirror system were installed in the 28-ID hutch and cool down commenced on March 10, 2023. Just after cool down to liquid argon temperature one of the silicon heat exchanger bars cracked as shown in Figure 1. (Actually both of the heat exchanger bars cracked but we believe the second heat exchanger cracked when the displacement of the manifold owing to the first failure introduced a significant moment on the second heat exchanger.) This material failure obliged us to abort the planned at-wavelength testing program and ship the cryo-mirror back to SLAC to conduct failure analysis, redesign, and reassembly.

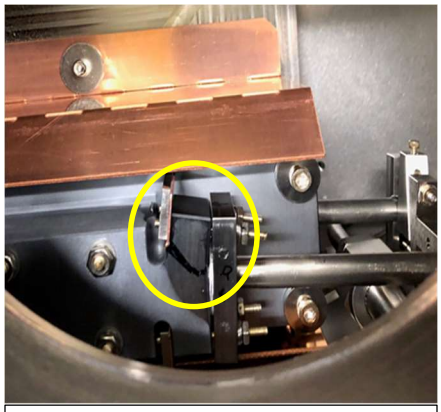

Figure 1 – Highlight shows cracked silicon heat exchanger at the heat exchanger to manifold cryo-seal.

Post-incident failure analysis, including component inspection and FEA, revealed that the increased seal force required to seal the final mirror assembly heat exchanger manifold connection to the silicon heat exchange bars eroded the safety margin of the heat exchanger bar material sufficiently to be a possible source of the failure likely in combination with a minor surface flaw. Our extensive FEA identified no other potential source of the failure.

Future Plans

With the shutdown of the APS for the APS-U installation and the reconfiguration of 28-ID beamline for in situ growth studies (CHEX), access to undulator white beam power for at-wavelength performance testing of the cryo-mirror has been compromised. Instead, we are focusing on using 970-nm IR laser heating and the lab-based cryo-metrology to test the cryo-mirror thermal performance.

Cryo-seal reliability - The first steps to address the cryo-seal failure are to reduce seal stress, enhance the reliability of the cryo-seals, and extensively test the resulting modified cryo-seal. The post-mortem analysis suggested modest modifications to the seal design should reduce the seal stress owing to thermal gradients. More importantly, we are developing and testing a seal augmentation protocol involving silicon resin in combination with a more conservative limit on the C-ring cryo-seal force to ensure greater material safety margin. Tests to date have established that the silicon resin can seal residual vacuum leaks and successfully thermally cycle to LN temperature. We are in the process of assembling a full four-seal prototype heat exchanger for

testing at 15 bar cryogen pressure and repeated thermal cycles. Additionally, we are initiating an effort to explore alternative cryo-seal technologies as a backup plan.

Reassemble and test cryo-mirror – Once the cryo-seal reliability issue is resolved, the cryo-mirror will be reassembled, and the lab-based cryo-metrology protocols discussed above will be used in conjunction with an IR laser heater to explore the cryo-mirror thermal performance. The 300-W IR laser heater can only deposit about 125W in the mirror which should produce < 0.1nm deformation according to FEA modeling. If the lab-based tests produce satisfactory results we will explore options for undulator-based performance studies, which is sufficient to explore the full 400W design maximum absorbed power.

References

1. L. Zhang, M. Sanchez del Rio, G. Monaco, C. Detlefs, T. Roth, A. Chumakov, and P. Glatzel,, "*Thermal Deformation of Cryogenically Cooled Silicon Crystals Under Intense X-ray Beams: Measurement and Finite-Element Predictions of the Surface Shape,"* J. Synchrotron Rad. **20**, 567 (2013).

2. G. Cutler, D. Cocco, B. Bentley, M. Cervantes, P. Chavez, J. Chrzan, S. DiMaggio, R. Hussey, J. Ilmberger, J. Lindsay, E. Lizotte, K. McCombs, S. Morton, G. Paulovits, K. Pearson, C. Redding, N. Smith, K. Tokunaga, D. Zehm, E. DiMasi and H. Padmore, *"Experimental Testing of a Prototype Cantilevered Liquid-Nitrogen-Cooled Silicon Mirror,"* J. Synchrotron Rad. **30**, 76 (2023).

3. L. Zhang, W.K. Lee, M. Wulff, and L. Eybert, *"The Performance of a Cryogenically Cooled Monochromator for an In-vacuum Undulator Beamline,"* J. Synchrotron Rad. **10**, 313 (2003).

4. N.B. Brookes, F. Yakhou-Harris, K. Kummer, A. Fondacaro, J.C. Cezar, D. Betto, E. Velez-Fort, A. Amorese, G. Ghiringhelli, L. Braicovich, R. Barrett, G. Berruyer, F. Cianciosi, L. Eybert, P. Marion, P. van der Linden, and L. Zhang, *"The Beamline ID32 at the ESRF for Soft X-ray High Energy Resolution Resonant Inelastic X-ray Scattering and Polarization Dependent X-ray Absorption Spectroscopy,"* Nucl. Instr. and Meth. **A903** 175 (2018).

5. R. R. Geraldes, G.V. Claudiano, L.M. Volpe, M. S. Souza, A. Sikorski, V. Z. Ferreira, L. Sanfelici, H.C.N. Tolentino, and H. Westfahl Jr., *"The Design of Exactly-Constrained X-ray Mirror System for Sirius,"* Proc. MEDSI 2018, 173 (2018).

Publications

K. Woodbury, G. Cutler, M. Kota, H. Najafi, *"Estimation of Multiple Contact Conductances in a Silicon-Indium-Silicon Stack,"* Journal of Heat and Mass Transfer, 2024 (accepted).

M. Frith, M. Highland, Z. Qiao, L. Rebuffi, L. Assoufid, and X. Shi, Rev. Sci. Instrum. **94**, 123102 (2023).

X. Shi, M. Highland, M. Frith, L. Gades, O. Quaranta, R. Zhang, L. Rebuffi, and L. Assoutfid, Proc. of SPIE **12695**, 126950D (2023).

G. Cutler, C. Austin, L. Huang, L. Lee, D. Cocco, and M. Idir. *"Modeling and characterizing transmission windows for in-situ interferometric measurements of cryogenically cooled mirrors,"* Proc. of SPIE **12695**, 1269508 (2023).

Diffraction-limited and wavefront preserving reflective optics development at NSLS-II

Mourad Idir (PI), Lei Huang and Tianyi Wang (co-PIs) – Brookhaven National Laboratory

Keywords: Diffraction Limited X-ray mirrors, ion beam figuring, dwell time optimization, optical fabrication, optical metrology

Research Project Scope

The emergence of ultra-brilliant synchrotron sources and recent advances in the development of efficient X-ray optics has stimulated significant efforts aimed at producing and utilizing X-ray nanobeams or perfect X-ray wavefront quality beams in many areas of science and technology [1]. X-ray mirrors are essential X-ray optics for transporting and focusing incoming X-ray beams. As dictated by the Maréchal criterion, preserving a diffraction-limited X-ray wavefront requires mirrors with sub-nanometer Root Mean Square (RMS). Despite a decade of advancements since the BES report on X-ray optics [2], current technologies still fall short of meeting the ever-increasing demands for high-quality X-ray mirrors.

To address this challenge, we proposed the development of a complete technological process for manufacturing precise synchrotron X-ray mirrors using ion beam figuring (IBF) combined with advanced optical metrology. Our solution is to (a) upgrade the existing IBF and its partner optical metrology technologies, and (b) demonstrate that such an upgraded new methodologies and systems will be capable of producing diffraction-limited X-ray mirrors up to 600 mm long with figure errors at $\leq$ 0.3 nm RMS level in a fast and cost-effective way.

Recent Progress

As shown in Fig. 1, manufacturing X-ray mirrors is a three steps iterative process. First, a precise optical metrology of the surface under test (SUT) is critical to effectively "drive" the IBF process.

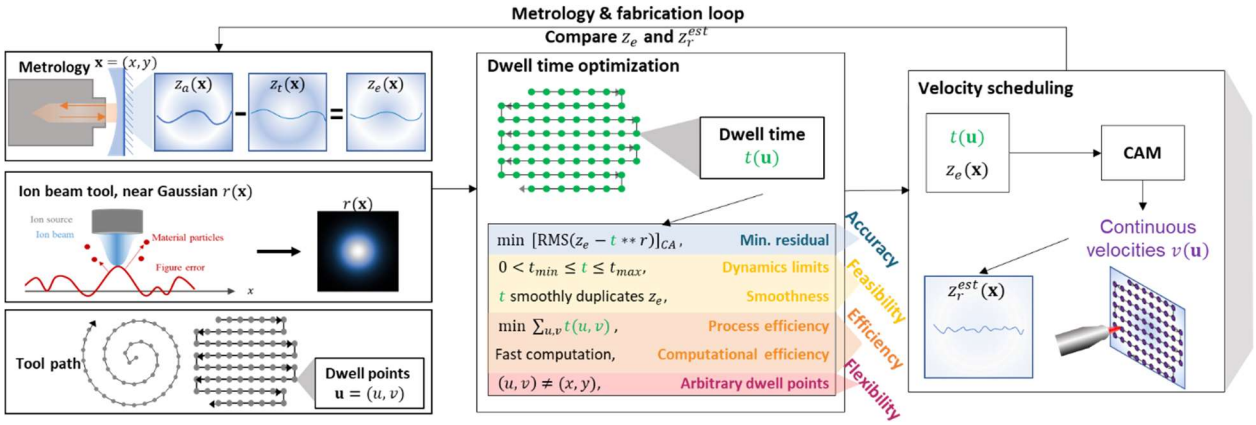

Figure 1. An IBF process is an iterative process of metrology, dwell time optimization, and velocity scheduling.

Then, the IBF process includes two steps: dwell time optimization and velocity scheduling. Dwell time optimization determines the duration required for the ion beam to correct surface errors at each point along the tool path. Velocity scheduling then translates these discrete dwell times to continuously varying velocities, facilitating the precise and seamless implementation of the optimized dwell time. Hence, for a highly deterministic IBF system, minimizing errors arising from each of these steps is important. Recently, we have achieved advancements in optimizing each of these pivotal stages.

Reliable height and slope metrology. We achieved reliable metrology for both surface height and slope errors. For height measurements, depicted in Fig. 2(a), we have an in-house developed Fizeau Stitching Interferometry system (FSI), which serves as the primary method for 2D metrology feedback for our IBF process.

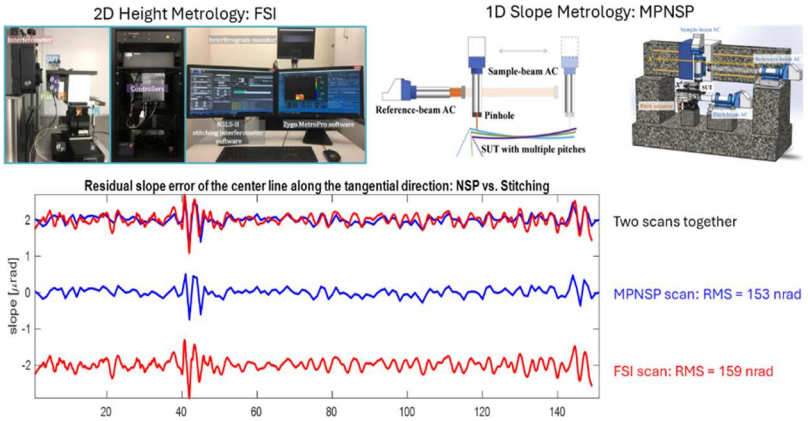

Figure 2. We achieved highly repeatable and comparable metrology results.

In parallel, for slope measurements, shown in Fig. 2(b), we extended the capability of our existing Nano Surface Profiler (NSP) to include a multi-pitch (MPNSP) technique, enhancing its repeatability especially for measuring surfaces with large total slope ranges. As illustrated in Fig. 2(c), despite the differing measuring principles of these systems, they provide comparable metrology results, which proves the reliability of our metrology methodologies.

State-of-the-art dwell time optimization methods. To achieve the targeted 0.3 nm RMS residual shape error, accurate calculation of dwell time is mandatory. In our comprehensive review, we studied various dwell time algorithms and identified four important aspects for accurate dwell time solutions:

1. Minimized residual errors in the clear aperture.
2. Minimized total dwell time.
3. Smooth dwell time profiles.
4. High computational efficiency.

To fulfill these requirements, we proposed three state-of-the-art dwell time optimization methods dedicated to X-ray mirror fabrication, namely Robust Iterative Fourier Transform-based Algorithm (RIFTA), Robust Iterative Surface Extension (RISE), and Universal Dwell time Optimization (UDO). RIFTA automates the inverse filtering threshold selection in Fourier Transform-based deconvolution through integration with a derivative-free optimization algorithm.

Building upon RIFTA, RISE incorporates an iterative surface extrapolation algorithm to effectively mitigate edge effects in deconvolution, thus further minimizing residual errors within the clear aperture. Additionally, UDO combines the strengths of both RIFTA and RISE with a matrix-based discretization approach, enabling flexible distribution of dwell points across the SUT. This facilitates the adoption of advanced and irregular finishing tool paths. Besides, all these methods adopt a dwell time minimization strategy, achieving the expected residual errors with the shortest available total dwell time. Figure 3 illustrates a comparative analysis of our proposed dwell time optimization methods against the ground truth dwell time solution and results optimized by existing methods. Our approaches outperform even the ground truth solution in terms of residual errors within the clear aperture and total dwell time.

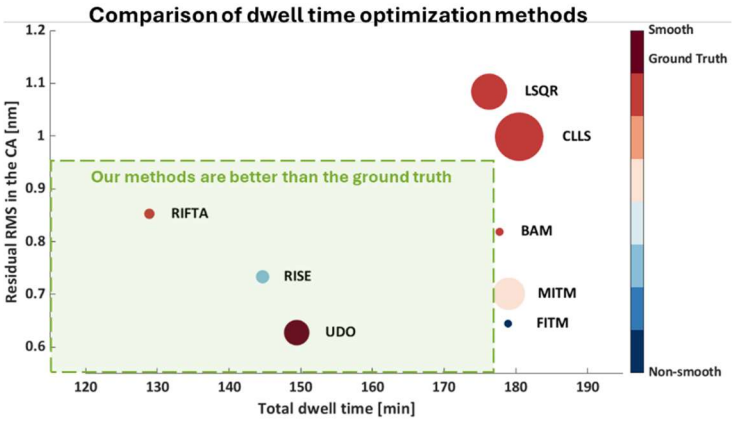

Figure 3. Our dwell time optimization methods outperform the ground truth. LSQR: Least squares with QR factorization; CLLS: Constraint linear least squares; BAM: Bayesian method; MITM: Matrix-form iterative method; and FITM: Function-form iterative method.

Position-Velocity-Time (PVT) based velocity scheduling. Velocity scheduling plays a crucial role in ensuring precise surface generation. Rather than directly implementing dwell time, it is converted into continuously varying velocities, alleviating stress on the translation stages. Conventionally, the constant-acceleration velocity scheduling model, depicted in Fig. 4, was utilized, but it struggled to produce smooth and continuous velocities during IBF machining. With the increasing support for advanced motion control modes like PVT in modern motion controllers, we proposed modeling the velocity scheduling problem in the PVT framework for our IBF system. Here, positions are represented as cubic polynomials, and we introduced smoothness and boundary constraints to ensure smoother scheduled velocities compared to the constant-acceleration model. Recently, we introduced an enhanced PVT (E-PVT) method, incorporating three key

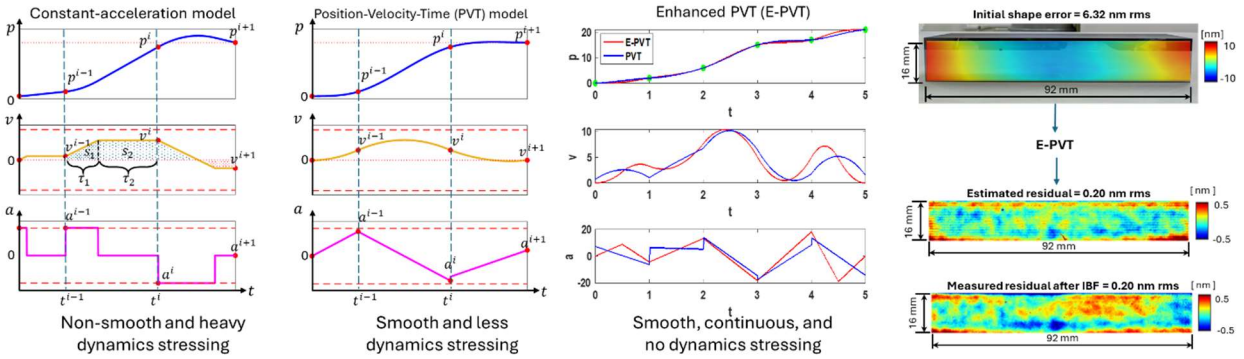

Figure 4. Enhanced Position-Velocity-Time (E-PVT) generates smooth and continuous velocities from dwell time without exerting dynamics stressing to the machine, achieving highly deterministic figuring result.

enhancements. Firstly, we significantly improved computational complexity from $O(n^3)$ to $O(n)$ by restructuring the linear system into a tri-diagonal form. Secondly, we added acceleration and jerk continuity constraints to ensure linear accelerations throughout the entire motion range. Thirdly, we introduced a compensation method to address situations where dynamics constraints might be exceeded, incorporating an additional time constant between dwell points. We employed particle swarm optimization to minimize this extra time to largely guarantee the overall processing efficiency. With these enhancements, depicted in Fig. 4, our IBF system demonstrates exceptional determinism, with the estimated residual error matching the actual measured residual error.

Producing hard X-ray mirrors for synchrotron beamlines in the US. Our innovative advancements shown above have enabled us to implement our X-ray mirror manufacturing solution at NSLS-II, as shown in Fig. 5, resulting in the successful production of numerous hard X-ray optics for synchrotron beamlines across the US, including NSLS-II, ALS, and APS. Presently, we demonstrated our capability to manufacture hard X-ray mirrors accurately and efficiently, such as KB mirrors with a total slope of < 0.6 mrad.

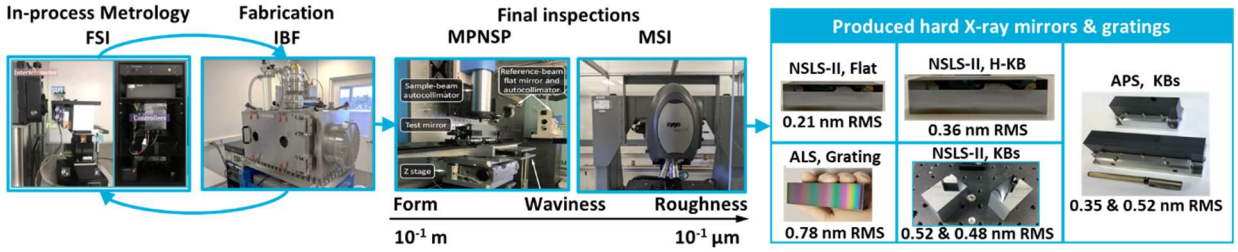

Figure 5. Established synchrotron X-ray mirror manufacturing solution at NSLS-II.

Future Plans

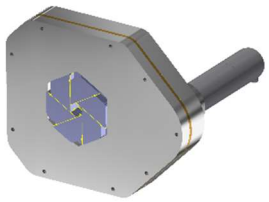

Figure 6. Motorized pinhole system

Our nest steps focus on further enhancing the processing efficiency of our current IBF process and achieving the targeted 600 mm mirror length. To enhance efficiency, we have developed a novel pinhole system enabling in-situ adjustment of the ion beam size, as depicted in Fig. 6. This advancement allows simultaneous machining with various beam sizes, eliminating the need to remove the mirror during processing. Additionally, for processing the 600 mm mirror, we've finalized the design of our new motion stages. Upon receipt of the stages (May 2024), we'll proceed with testing and implementation. We believe that, with these new instruments, we will achieve the claimed manufacturing capacity as mentioned in our research scope, which are producing diffraction-limited X-ray mirrors up to 600 mm long with figure errors at $\leqslant$ 0.3 nm RMS level in a fast and cost-effective way.

References

1. G. E. Ice, D. Budai. John, and WL. Pang. Judy, *The race to x-ray microbeam and nanobeam science*, Science **334** (6060), 1234-1239 (2011).

2.D. Mills, H. Padmore, and E. Lessner, *X-ray optics for BES light source facilities*. Brookhaven National Lab (BNL), Upton, NY (United States) (2013).

Publications

1. T. Wang, X. Ke, L. Huang, Q. Cui, Z. Zhang, C. Wang, H. Kang, W. Pullen, H. Choi, D. Kim, V. Negi, Q. Kemao, Y. Zhu, S. Giorgio, P. Boccabella, N. Bouet, C. Austin, and M. Idir, *A comprehensive review of dwell time optimization methods in computer-controlled optical surfacing,* Light: Advanced Manufacturing, **Accepted** (2024)**.**

2. X. Ke, J. Fan, T. Wang, L. Huang, Y. Zhu, C. Austin, H. Choi, H. Kang, D. Kim, V. Negi, Z. Zhang, C. Wang, S. Chen, N. Bouet, and M. Idir, *E-PVT: Enhanced Position-Velocity-Time scheduler for computer-controlled optical finishing with comprehensive considerations of dynamics constraints, continuity and efficiency*, Optics Express**, Under review** (2024).

3. L. Huang, T. Wang, C. Austin, D. Kim, and M. Idir, *Two-step retrace error calibration removing tilt ambiguity in coherence scanning interferometry*, Optics Letters, **49**(3), 590-593 (2024).

4. L. Huang, T. Wang, C. Austin, L. Lienhard, Y. Hu, C. Zuo, D. Kim, and M. Idir, *Collimated phase measuring deflectometry*, Optics and Lasers in Engineering **172**, 107882 (2024).

5. T. Wang, L. Huang, Y. Zhu, S. Giogio, P. Boccabella, N. Bouet, and M. Idir, *Ion Beam Figuring System for Synchrotron X-Ray Mirrors Achieving Sub-0.2-μrad and Sub-0.5-nm Root Mean Square.* Nanomanufacturing and Metrology **6**(1), 20 (2023).

6. D. L. Voronov, T. Wang, S. Park, L. Huang, E. M. Gullikson, F. Salmassi, C. Austin, H. A. Padmore, and M. Idir, *Nanometer flat blazed x-ray gratings using ion beam figure correction*, Optics Express **31**(21), 34789-34799 (2023).

7. L. Huang, L. Lienhard, T. Wang, F. Polack, J. Nicolas, S. Hulbert, and M. Idir, *Multi-pitch nano-accuracy surface profiler for strongly curved X-ray mirror metrology*, Optics and Lasers in Engineering **162**, 107428 (2023).

8. T. Wang, X. Ke, L. Huang, V. Negi, H. Pullen, D. Kim, Y. Zhu, and M. Idir, *Computer-controlled finishing via dynamically constraint position-velocity-time scheduler*, Journal of Manufacturing Processes **87**, 97-105 (2023).

9. T. Wang, L. Huang, X. Ke, Y. Zhu, H. Choi, W. Pullen, V. Negi, D. Kim, and M. Idir, *Hybrid height and slope figuring method for grazing-incidence reflective optics*, Journal of Synchrotron Radiation **30**, 1 (2023).

10. X. Ke, T. Wang, Z. Zhang, L. Huang, V. S. Negi, W. C. Pullen, H. Choi, D. Kim, and M. Idir, *Multi-tool optimization for computer controlled optical surfacing,* Optics Express **30** (10), 16957-16972 (2022).

Development of PFIB-Xray System for Multi-scale Analysis

Si Chen, X-ray Science Division, Argonne National Laboratory

Keywords: synchrotron hard x-ray microscopy, fluorescence microscopy, plasma focused ion beam, multi-scale analysis, cryogenic capabilities

Research Project Scope

Many scientific questions in materials and biological sciences center around the relationship between hierarchical structures and macroscale functional performance, requiring a unique characterization platform for linking chemical, structural, and functional properties across all relevant length scales. Inspired by the upgrade of the synchrotron light source at the Advanced Photon Source (APS), hard x-ray nanoprobes approaching <10 nm spatial resolution are under development. However, upscaling nanoimaging to examine samples beyond the microscopic scale faces many intrinsic challenges. This project aims to directly address these challenges by developing a PFIB-Xray instrument with associated data analysis methods. The instrument combines an x-ray nanoimaging system and a Xenon plasma focused ion beam (PFIB) probe to allow in-situ sample manipulation to facilitate and optimize x-ray imaging from macro- to nano-scale on one integrated platform, as illustrated in Fig. 1. Novel data analysis including machine learning methods will be developed to correlate data collected at different scales and extract critical scientific information. With this new technique, one will be able to perform analysis across scales from the level of a functional device to single gains or deeply buried interfaces. A new landscape of scientific applications will be enabled including investigation of performance degradation at various structural levels of perovskite solar cells, multiscale characterization of additively manufactured alloys, imaging of microbe dynamics in undisturbed soil aggregates, and mapping of hierarchical structures in biological tissues. The development of the PFIB-Xray will take advantage of the upcoming APS Upgrade, and in turn fully realize its potential for hard x-ray microscopy.

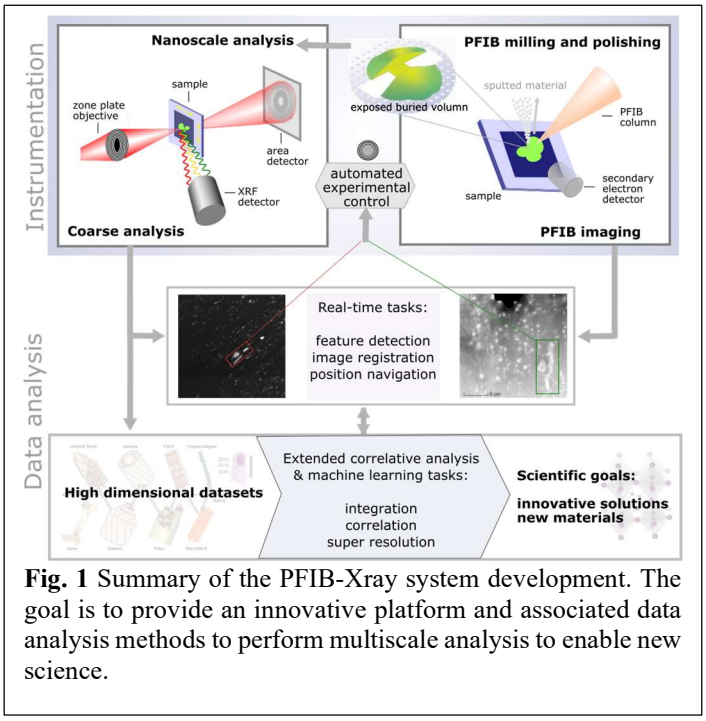

Fig. 1 Summary of the PFIB-Xray system development. The goal is to provide an innovative platform and associated data analysis methods to perform multiscale analysis to enable new science.

The PFIB-Xray system will be built based on the second-generation Bionanoprobe (BNP-II) platform [1]. The efforts funded by this project focus on fully integrating the technique,

facilitating interactive operation between x-ray imaging and ion beam milling, and conducting structural and chemical analysis at the highest instrumentation performance level, spanning from macron to nanometer length scales.

Recent Progress

Concept demonstration: Using a commercial Ga+ focused ion beam system in conjunction with the x-ray fluorescence (XRF) microprobe at the 2IDE beamline and the BNP at the APS, we performed a proof-of-concept multiscale 3D analysis of HeLa cells [2]. The workflow involves iterative and multiscale XRF data collection, with intermediate sample processing using the FIB system between measurements at different length scales. Initial assessment with a microscale spatial resolution, combined with precise sample manipulation via FIB, allows for the direct removal of sample regions obstructing both the incident x-ray beam and outgoing XRF signals. This significantly expands the angular coverage of subsequent nanoscale tomography data collection and, thus, improves the 3D data reconstruction quality (Fig. 2).

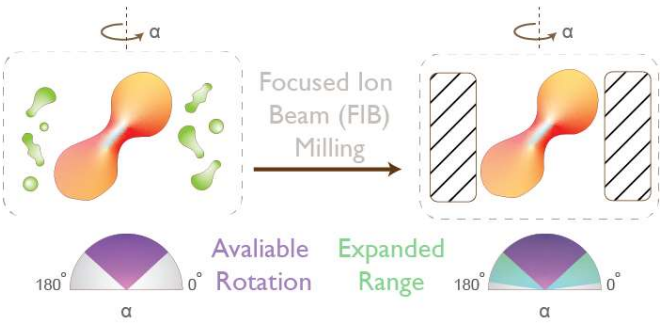

Fig. 2 Sample geometry manipulation by focused ion beam milling expands the angular coverage for the subsequent nano-tomography data collection.

The downside of using the Ga+ FIB system, as expected, is the implantation of Ga+ into the samples, which adversely affects the subsequent elemental analysis using x-ray microscopy. This has confirmed our need for a plasma FIB column with a non-contaminant noble gas ion source. In addition, the high milling speed of a plasma FIB, i.e. 50x faster than the most powerful Ga+ FIB, makes it possible to operate in-line with x-ray microscopy [3].

PFIB procurement and commissioning: The initial plan was to integrate a PFIB column directly to the BNP-II system during the APS 'dark' period, when the x-ray beam and user program were paused for the storage ring upgrade. However, the schedule for the BNP-II design has been delayed due to the APS Upgrade scope change. Instead of waiting for the readiness of the BNP-II, we identified a Zeiss 1540 FIB/SEM system at the Center of Nanoscale Materials (CNM), recently decommissioned from the CNM user program, as the host instrument and testing bench. We then procured a plasma FIB column with a Xenon ion (Xe+)

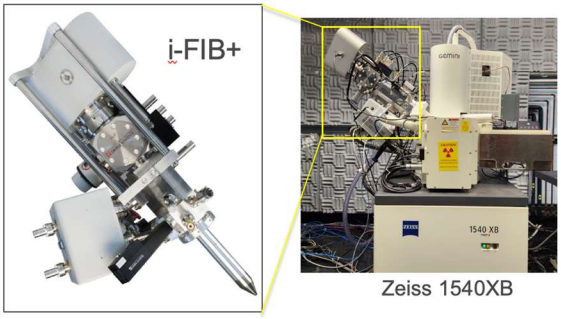

Fig. 3 Installation of an Orsay Physics i-FIB+ Xe+ focused ion beam column to a Zeiss 1540 system.

source (i-FIB+) from Orsay Physics (France), which is compatible with the host instrument. The primary ion source of the i-FIB+ unit is Xe+, but the system has the potential to be equipped with O2+, N2+, or Ar+ sources for future applications. The beam energy ranges from 3-30 keV, with a probe current from 1 pA to 3 µA. In October 2023, we successfully installed the i-FIB+ (Fig. 3) and demonstrated the performance on standard silicon samples. Current efforts are focused on comparing the milling operation with Xe+ source to the most conventionally used Ga+ source and developing protocols for milling various materials. We have also correlated our experimental results with a Monte Carlo-based simulation using the SRIM software (Stopping and Range of Ions in Matter) to gain a better understanding.

BNP-II development: To accommodate the i-FIB+ apparatus at the future BNP-II instrument, a robotic sample exchanger has been designed to transfer samples between the BNP-II and the PFIB system. The robot will be housed in a vacuum chamber connecting the BNP-II main chamber and the PFIB chamber (Fig. 4). The robot has a 50 mm vertical travel range and the capability of a 360º full rotation. It is designed to handle both samples at the room temperature and frozen samples in cryogenic conditions close to the temperature of liquid nitrogen. A set of piezo stages will be mounted at the tip of the robotic arm for moving the gripper with a positioning accuracy of a few microns. For proper reception of the sample from the robot, the sample stage stack in the PFIB chamber (with a pre-tilt mount on the top) will be tilted to a certain angle, as shown in Fig. 4.

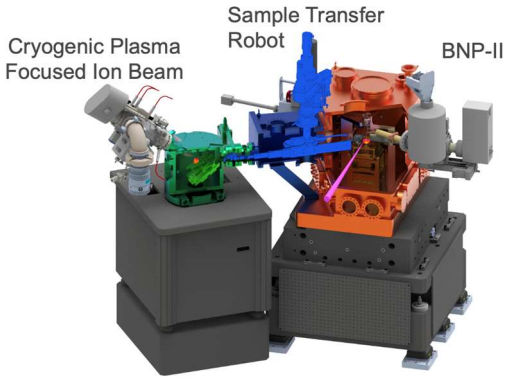

Fig. 4 The BNP-II chamber and the PFIB chamber are connected through a smaller vacuum chamber housing a sample transfer robot.

Future Plans

Instrumentation: We plan to install a cryogenic stage with a cold trap to enable operation in the cryogenic conditions at a temperature close to the liquid nitrogen temperature. Additionaly, we plan to install a gas injection system (GIS) to perform amorphous carbon coating during both room-temperature and cryogenic operations to protect samples and improve surface conductivity. The goal is to complete the installation by the end of calendar year of 2024. We will continue our efforts in developing protocols for working with different materials and gaining a better understanding of the i-FIB+ performance. Meanwhile, we will develop the user program around the future PFIB-Xray system and extend the applications to soft materials.

Data pipeline and analysis: With the PFIB-Xray system, we will produce increasingly vast and complex data across scales and from different modalities. These vast amounts of data will contain unprecedented rich information but can also make it harder to reach desired scientific insights. Innovative solutions for data analysis are critical to unmasking the complexity and fully

realize the potential of the proposed PFIB-Xray system. In addition, interactive x-ray imaging and sample manipulation at the PFIB-Xray heavily relies on real-time feature recognition and registration. We plan to collaborate with the data science team (Computational X-ray Science group and data scientists in the Microscopy group) at the APS and leverage their efforts to tackle these data challenges. The effort will be focused on two interconnected thrusts: (1) providing real-time feedback to guide and automate experimental process, and (2) efficiently integrating complex data across length scales to extract strategic information.

References

1. S. Chen, J. Deng, Y. Yuan, C. Flachenecker, R. Mak, B. Hornberger, Q. Jin, D. Shu, B. Lai, J. Maser, C. Roehrig, T. Paunesku, S. C. Gleber, D. J. Vine, L. Finney, J. VonOsinski, M. Bolbat, I. Spink, Z. Chen, J. Steele, D. Trapp, J. Irwin, M. Feser, E. Snyder, K. Brister, C. Jacobsen, G. Woloschak, and S. Vogt, *The Bionanoprobe: hard x-ray fluorescence nanoprobe with cryogenic capabilities*, J. Synchrotron Radiat. **21**, 66-75 (2014).

2. Y. Luo, T. Paunesku, O. Antipova, Y. Liu, N. Zaluzec, Z. Di, G. Woloschak, and S. Chen, *A reliable workflow for improving nanoscale X-ray fluorescence tomographic analysis on nanoparticle-treated HeLa cells*, Metallomics **14**, mfac025 (2022).

3. K. Höflich, G. Hobler, F. I. Allen, T. Wirtz, G. Rius, L. McElsee-White, A. V. Krasheninnikov, M. Schmidt, I. Utke, N. Klingner, M. Osenberg, R. Córdoba, F. Djurabekova, I. Manke, P. Moll, M. Manoccio, J. M. De Teresa, L. Bischoff, J. Michler, O. De Castro, A. Delobbe, P. Dunne, O. V. Dobrovolskiy, N. Frese, Armin Gölzhäuser, P. Mazarov, D. Koelle, W. Möller, F. Pérez-Murano, P. Philipp, F. Vollnhals, 22, and G. Hlawacek, *Roadmap for focused ion beam technologies*, Appl. Phys. Rev. **10**, 041311 (2023).

Publications Supported by BES

1. B. G. Duersch, Y. Luo, S. Chen, S. A. Soini, D. M. R. Somu, and V. Merk, *Synchrotron-based X-ray fluorescence microscopy mapping the ionome of a toxic freshwater cyanobacterium*, Environ. Pollut. **334** (1) (2023).

2. J. Li, S. Chen, D. Ratner, T. Blu, P. Pianetta, and Y. Liu, *Nanoscale chemical imaging with structured x-ray illumination*, Proc. Natl. Acad. Sci. USA, **120** (49) e2314542120 (2023).

3. Y. Luo, S. Zhang, J. Chen, X. Ma, K. Ma, J. Deng, Y. Jiang, L. Li, B. Lai, S. Chen, S. Wieghold, and L. Dou, *Photo-induced halide redistribution in 2D halide perovskite lateral heterostructures*, Joule **7** (2023).

4. Y. Lin, J. Shi, W. Feng, J. Yue, Y. Luo, S. Chen, B. Yang, Y. Jiang, H. Hu, C. Zhou, F. Shi, A. Prominski, D. V. Talapin, W. Xiong, X. Gao, B. Tian, *Periplasmic biomineralization for semi-artificial photosynthesis*, Sci. Adv. **9** (29) eadg5858 (2023).

5. D. Strenkert, S. Schmollinger, Y. Hu, C. Hofmann, K. Holbrook, H. Liu, S. Purvine, C. Nicora, S. Chen, M. Lipton, T. Northen, S. Clemens, and S. Merchant, *Zn deficiency disrupts Cu and S homeostasis in Chlamydomonas resulting in over accumulation of Cu and Cysteine,* Metallomics **15**(7) (2023).

6. S. Schmollinger, S. Chen, and S. S. Merchant, *Quantitative elemental imaging in eukaryotic algae*, Metallomics **15**, mfad025 (2023).

7. Y. Lin, X. Gao, J. Yue, Y. Fang, J. Shi, L. Meng, C. Clayton, X. Zhang, F. Shi, J. Deng, S. Chen, Y. Jiang, F. Marin, J. Hu, H. Tsai, Q. Tu, E. W. Roth, R. Bleher, X. Chen, P. Griffin, Z. Cai, A. Prominski, T. W. Odom, B. Tian, *A soil-inspired dynamically responsive chemical system for microbial modulation*, Nature Chem. **15**, 119-128 (2023).

8. Y. Chen, S. Chen, K. Ok, F. E. Duncan, T. V. O'Halloran, and T. K. Woodruff, *Zinc dynamics regulate early ovarian follicle development*, Journal of Biological Chemistry **299** (1) 102731 (2023).

9. Y. Luo, T. Paunesku, O. Antipova, Y. Liu, N. Zaluzec, Z. Di, G. Woloschak, and S. Chen, *A reliable workflow for improving nanoscale X-ray fluorescence tomographic analysis on nanoparticle-treated HeLa cells*, Metallomics **14**, mfac025 (2022).

10. Y. Luo, T. Paunesku, O. Antipova, Y. Liu, N. Zaluzec, Z. Di, G. Woloschak, and S. Chen, *A workflow for improving nanoscale X-ray fluorescence tomographic analysis*, Microsc. Microanal. **28** (Suppl. 1) (2022).

Diffraction-limited Radiation Enhancement with Adaptive Mirrors for x-ray coherent beamlines

Antoine Islegen-Wojdyla, Advanced Light Source, Lawrence Berkeley National Laboratory

Keywords: x-ray, adaptive optics, wavefront sensing, automated alignment, machine-learning

Research Project Scope

The "Diffraction-limited Radiation Enhancement with Adaptive Mirrors" (DREAM beam) project aims to enable automated alignment for coherent beamlines. This will facilitate new capabilities such as coherence engineering and wavefront shaping, maximizing the benefits of the brightness and coherence offered by the upcoming 4th Generation Light sources, including ALS-U, APS-U, and LCLS-II.

To ensure the optimal performance of this new class of diffraction-limited beamlines during user operation, the project leverages recent advancements in machine learning. This integration simplifies calibration routines, making them essential for deployment and user adoption. The project encompasses wavefront sensing and adaptive optics controls – offering both diagnostics and additional degrees of freedom to fine-tune beam quality. Furthermore, we are eager to incorporate technologies from x-ray astrophysics to enhance the speed of adaptive optics. We aim to demonstrate, through simulations and experiments, that wavefront shaping can introduce the high sensitivity of interferometry to x-ray experiments, paving the way for novel experimental capabilities.

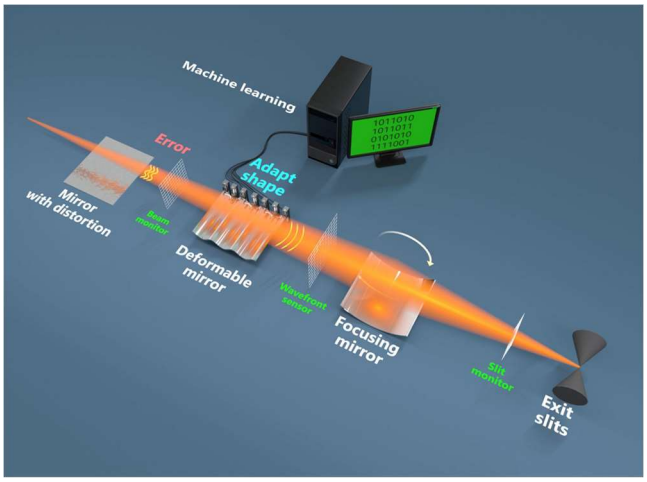

The Dream beam projects aims at enabling automated alignment at diffraction-limited beamline advanced optical device (wavefront sensors and adaptive optics) using machine-learning, based on the EPICS/bluesky framework to make it deployable at scale, and ensure optimal performance for scientific users.

Recent Progress

We have demonstrated that commercially available bimorph mirror that will be used in coherent beamlines can be actuated to reach diffraction-limited performance, using machine learning to alleviate the need for thorough calibration and enable open-loop operation even in the presence of creep and hysteresis [1] that has limited their use in regular operation until now. Those initial results were performed in a metrology lab using a Fizeau interferometer, and the methodology was later demonstrated in operation at APS 28-ID-B with excellent results (<λ/4 residual error at 12keV.) [2]

Wavefront sensors are a key element to assess the performance of a beamline, where measurement in focus are not possible given sub-micron beam size. Since in x-ray it is not possible to split the beam efficiently, all the x-ray wavefront sensors demonstrated so far were fully invasive and did not allow to monitor the beam at regular intervals before it hits the sample, We have developed a new wavefront sensor that works in reflection and that is minimally invasive (retractable is less than a second) for the needs of ALS-U. We have tested it at the ALS at soft x-ray wavelengths, and at the APS at hard x-ray wavelength, with excellent result (λ/100 repeatability) [3], showing that the concept is scalable to any beamline.

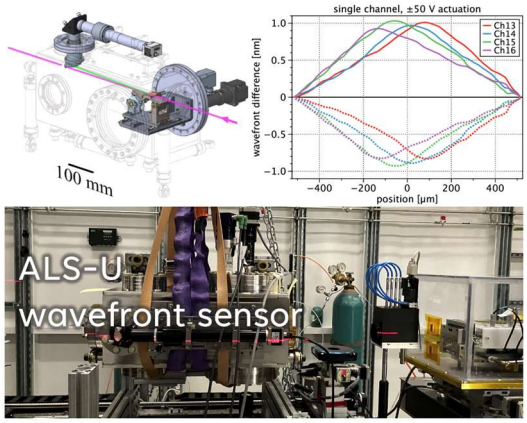

In-line reflective wavefront sensor designed for ALS-U that has been tested at APS (28-ID-B), showing the ease of operation, the precision and the wide range of application of the device.

The instrument control systems for synchrotron instrumentation is highly heterogeneous, but the EPICS/bluesky framework is progressively being adopted as a standard to control beamlines and experimental endstation, as it allows greater flexibility and comprehensive experiment planning. We have completely reworked the instrument controls at ALS beamline 5.3.1 (which were developed in Labview like the rest of the facility), as pilot beamline to make it natively EPICS/bluesky and use it as a testbed for automated experiments. We have demonstrated that the beamline optimization routines developed at NSLS-II (https://nsls-ii.github.io/bloptools/) could be easily deployed at the ALS, and showed that the automated alignment procedures based on

Bayesian optimization could reach the theoretical beam size in less than 5 minutes, while handling 4 degrees of freedom and 2 apertures, which generally constitutes coupled constraints that are hard to optimize manually even for a skilled optical scientist with just two hands. We are currently working on extending this work by integrating wavefront sensing and adaptive optics controls to the optimization software.

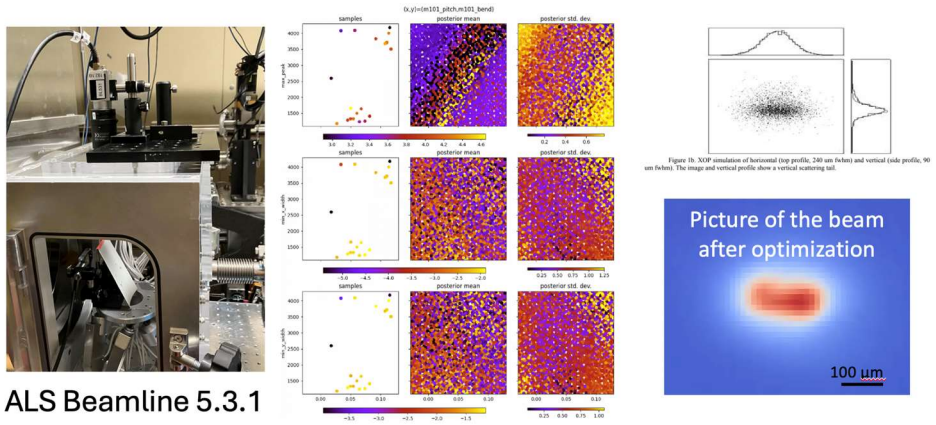

Automated alignment at ALS beamline 5.3.1 based on Bayesian optimization using the EPICS/bluesky framework, optimizing over a large number of dimensions and reaching optimal results in less than 5 minutes.

Future Plans

We are received our first test articles from Penn State University, which has been collaborating with NASA on **thin adaptive optics** [R1]**.** We want to characterize these devices, in order to refine their manufacturing so that they can meet the stringent requirements of synchrotron beamlines. The primary goal of these devices is to interact with the beam at high speed (10kHz) in order to steer the beam and enable coherence control. Eventually, we want to achieve diffraction limited quality, and control the wavefront itself at that rate.

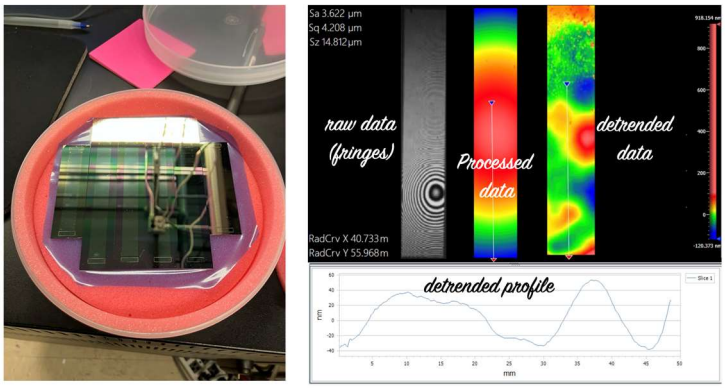

First test article of thin adaptive optics from Penn State University, with initial measurement on a Fizeau interferometer showing expected curvature in absence of stress compensation.

We plan to develop further simulations for wavefront engineering, where we aim to demonstrate that tailoring the light to the sample using adaptive optics can lead to higher sensitivity or a larger density of information that could result in faster measurements, taking advantage of the increased brightness of upgrade light sources [R2]. Those engineered wavefront will be achieved either through diffractive optics (specialized zoneplates) or adaptive optics

We would like to generalize the concept of beamline surrogate (digital twins) so that they can be interrogated at will. We are in discussion with ESNet and NERSC on the best way to implement and deploy these models in order to follow the DOE guidelines on public data access, so that users could plan their experiments before coming to the facility.

Lastly, we want to create community around beamline optimization, and bring together projects with similar goals across facilities (e.g. Dream beam, XSCOPE and ILLUMINE.)

References

1. Mohit Tendulkar, Tianning Liu, Nicole Kirchner-Hall, Nathan Bishop, Quyen Tran, Casey T DeRoo, Vincenzo Cotroneo, Vladimir Kradinov, Vanessa Marquez, Paul B Reid, Susan Trolier-McKinstry, Thomas N Jackson, *Process development for adjustable X-ray mirrors*, Optics for EUV, X-Ray, and Gamma-Ray Astronomy X, (2021)
2. Abraham Levitan, Kahraman Keskinbora, Umut T. Sanli, Markus Weigand, and Riccardo Comin, *Single-frame far-field diffractive imaging with randomized illumination*, Optics Express Vol. 28, Issue 25, pp. 37103-37117 (2020)

Publications

1. G. Gunjala, A. Wojdyla, K. A. Goldberg, Z. Qiao, X. Shi, L. Assoufid and L. Waller,*Data-driven modeling and control of an X-ray bimorph adaptive mirror*, J. Synchrotron Rad.. **30**, 57-64 (2023) https://doi.org/10.1107/S1600577522011080
2. L. Rebuffi, X. Shi, Z. Qiao, M. J. Highland, M.G. Frith, A. Wojdyla, K. A. Goldberg, and L. Assoufid, *Real-time machine-learning-driven control system of a deformable mirror for achieving aberration-free X-ray wavefronts,* Optics Express **31**, 13 (2023) https://doi.org/10.1364/OE.488189
3. K. A Goldberg, A. Wojdyla, D. Bryant, X. Shi, L. Rebuffi, M. Frith, M. Highland, L. Assoufid, Y. Ichii, T. Inoue, K. Yamauchi, *X-ray wavefront sensor development at the Advanced Light Source*, Proceedings of SPIE 12695, Advances in Metrology for X-Ray and EUV Optics X; **126950B** (2023) https://doi.org/10.1117/12.2679136
4. T. W. Morris, Y. Du, M. Fedurin, A. C. Giles, P. Moeller, B. Nash, M. Rakitin, B. Romasky, A. L. Walter, N. Wilson, A. Wojdyla, *Latent Bayesian optimization for the autonomous alignment of synchrotron beamlines*, Proceedings of SPIE 12697, Advances in Computational Methods for X-Ray Optics VI; **126970B** (2023) https://doi.org/10.1117/12.2677895

5. P. Luna, A. Wojdyla, *Exploring the use of x-ray adaptive optics in soft x-ray grating monochromators with wavefront propagation simulations*, Proceedings of SPIE 12697, Advances in Computational Methods for X-Ray Optics VI; **1269705** (2023) https://doi.org/10.1117/12.2677719

Monolithic 2D MLL optics for high-resolution hard X-ray microscopy

E. Nazaretski, NSLS-II, Brookhaven National Laboratory

Keywords: X-ray optics, Multilayer Laue lenses, X-ray microscopy, X-ray microscopy instrumentation

Research Project Scope

X-ray microscopy is an invaluable and powerful characterization tool applied in many scientific fields, such as materials science, biology, environmental science, and energy research[1,2,3]. Multilayer Laue lenses (MLLs) have been proposed and successfully implemented for x-ray focusing in the hard x-ray regime yielding ~10 nm imaging resolution in 2D[4]. An MLL is a linear diffractive optic, and therefore two of them need to be aligned orthogonally with respect to each other to achieve a point focus; this involves eight independent motions with nanoscale resolution each, which in turn makes MLL microscopy systems extremely complex[5]. Furthermore, when approaching a 5 nm point focus, conventional alignment methods do not work due to the spatial constraints imposed by the geometry of MLLs themselves. The scope of this research project targets the development of monolithic 2D MLL optics and aims to overcome the technological difficulties associated with the implementation of 1D MLLs for high-resolution imaging experiments. The fabricated 2D MLL optics utilize microfabrication technologies used to manufacture MEMS devices and are compatible with more conventional and widely used X-ray microscopes equipped with Fresnel zone plates. The developed 2D focusing optics provide a route to enable high-resolution hard X-ray imaging experiments at various beamlines of NSLS-II and other synchrotron facilities within the DOE complex.

Recent Progress

Design and Fabrication of MEMS-based Templates for 2D MLL Optics. We have designed and fabricated MEMS-based Si templates tailored for 2D MLL optics targeting a sub-10 nm point focusing resolution (Figure 1a). The templates can accommodate two individual MLLs with various dimensions and physical parameters and provide a sub-10 millidegree accuracy of angular orthogonality between the two lenses (this parameter is critical for nm-scale focusing). Also, the placement of individual lenses along the X-ray beam is controlled on a micrometer scale. A high degree of angular alignment is achieved through the utilization of microfabricated alignment ‘teeth’. The cantilever-type silicon springs effectively secure the position of two linear MLLs mounted onto the template. To validate the approach and mechanical robustness of these newly developed templates, we modeled, fabricated, and tested a series of various templates with different cantilever springs. Figures 1b,c illustrate an example of the microfabricated MEMS template for 2D MLLs.

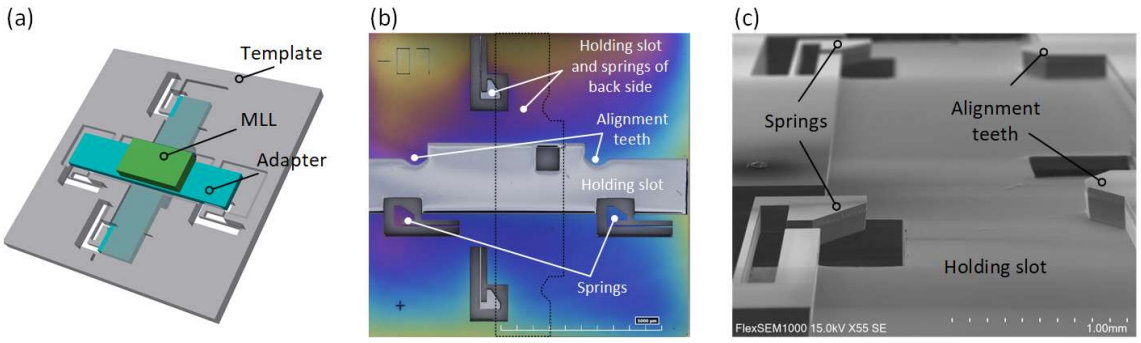

Figure 1: (a) A MEMS template for 2D MLL X-ray nano-focusing optics suitable for sub-10 nm focusing measurements. (b-c) An example of the microfabricated MEMS templates (b: optical image, c: SEM image).

Post-processing and Characterization of MLL Optics. The integral part of the project involves the fabrication, post-processing, and characterization of MLLs (in collaboration with the optics fabrication group at NSLS-II). The MLL optics were fabricated through magnetron sputtering deposition, reactive ion etching, and FIB milling. The surface morphology was characterized using SEM and white light interferometers, and the focusing performance was tested at the HXN beamline at NSLS-II. Various sets of MLLs were fabricated for installation onto the Si templates. Some examples include a set of two flat MLLs (direct imaging resolution of 13 x 14 nm^2 at 13.6 keV), a set that combines a flat MLL and a wedged MLL (as shown in Figure 2; direct imaging resolution of 15 x 20 nm^2 at 16 keV), and a set of two wedged MLLs (direct resolution of 8.9 x 9.8 nm^2 at 15 keV photon energy).

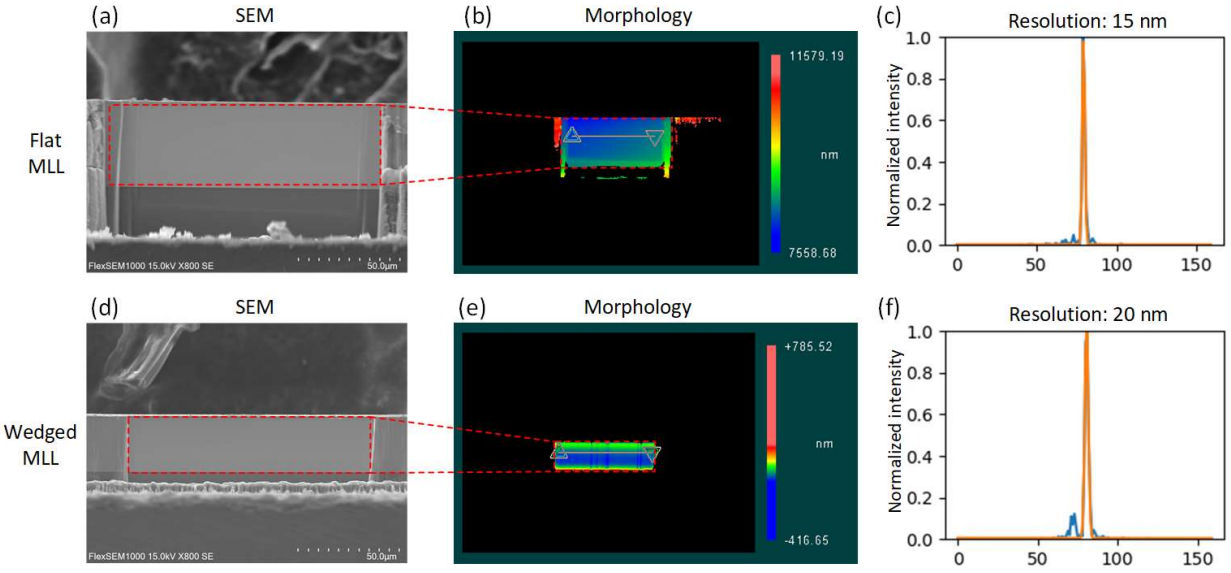

Figure 2: SEM images, surface morphology measurement, and focusing performance of a set of MLL optics including a flat MLL (a-c) and a wedged MLL (d-f). The focusing performance was measured at the HXN beamline at NSLS-II.

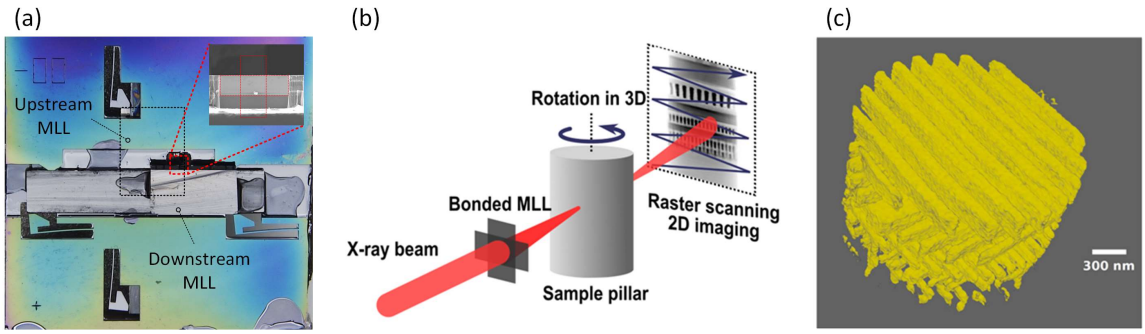

Figure 3: (a) Assembled 2D MLL optics. The inset shows the overlapped zone areas. (b) 2D bonded MLL is used for rapid nanoscale ptychographic tomography at the HXN beamline. (b) 3D image of a cylindrical microelectronics sample extracted from an Intel processor.

Assembly, Characterization, and Application of 2D MEMS-based MLL Optics. We have assembled a number of 2D MLL optics with orthogonality error, measured by a white light interferometer, of sub-10 millidegrees and accuracy of placement along the beam direction in the range of a few μm (as shown in Figure 3a for an example of two flat MLLs). A new method for orthogonality measurements has been developed by integrating machine learning algorithms with interferometer measurements, it facilitates precise and automated assessment of a small orthogonality error between individual MLLs. The developed method streamlines the alignment of 2D MLL and allows for precise and rapid corrections of possible misalignments within a Si template. After assembly and characterization, the set shown in Figure 3a demonstrated a direct imaging resolution of 19 x 20 nm^2 at 15 keV (mainly limited by the lenses themselves). Figure 3b-3c shows an example of imaging experiments performed for rapid scanning ptychographic tomography at the HXN beamline at NSLS-II. The 2D optics demonstrated outstanding stability throughout the 3D measurement (data acquisition rate over 600 Hz limited by the detector speed and the signal quality, total data acquisition time ~ 53 minutes), and Fig. 3c shows a 3D image of a 2x3 μm^2 microelectronics sample extracted from an Intel processor. The reconstruction voxel size equals ~ 6 nm, and the smallest features in the sample are ~30 nm wide copper connectors.

Future Plans

Improvement of MEMS-based template for 2D MLL optics. Building upon the insights gained from the current MEMS template, we aim to refine and optimize its design to enhance its effectiveness for 2D MLL optics.

Design of next generation 2D MLL optics. Leveraging our knowledge and experience gained from the initial generation of 2D MLL optics, we will develop the next generation of 2D MLL optics, which will feature the capability to fine-tune the orthogonality and overlapping of 1D lenses.

2D MLL optics and APS-U Ptychoprobe beamline. Expanding on our advancements in 2D MLL optics, we are collaborating with the APS-U Ptychoprobe beamline team. Within this

collaboration, we will provide a set of 1D and 2D MLL lenses to the beamline team, which will be used as focusing optics in their endstation instrument.

References

1. A. Michelson, B. Minevich, H. Emamy, X. Huang, Y.S. Chu, H. Yan, and O. Gang, "*Three-dimensional visualization of nanoparticle lattices and multimaterial frameworks,*" Science **376**, 203 (2022)
2. T.A.S. Doherty, S. Nagane, D.J. Kubicki, Y.-K. Jung, D.N. Johnstone, A.N. Iqbal, D. Guo, K. Frohna, M. Danaie, E.M. Tennyson, S. Macpherson, A. Abfalterer, M. Anaya, Y.-H. Chiang, P. Crout, F.S. Ruggeri, S. Collins, C.P. Grey, A. Walsh, P.A. Midgley, and S.D. Stranks, "*Stabilized tilted-octahedra halide perovskites inhibit local formation of performance-limiting phases,*" Science **374**, 1598 (2021)
3. P.M. Csernica, S.S. Kalirai, W.E. Gent, K. Lim, Y.-S. Yu, Y. Liu, S.-J. Ahn, E. Kaeli, X. Xu, K.H. Stone, A.F. Marshall, R. Sinclair, D.A. Shapiro, M.F. Toney, and W.C. Chueh, "*Persistent and partially mobile oxygen vacancies in Li-rich layered oxides,*" Nature Energy **6**, 642 (2021)
4. H. Yan, N. Bouet, J. Zhou, X. Huang, E. Nazaretski, W. Xu, A. P Cocco, W. K S Chiu, K. S. Brinkman and Y. S. Chu, *"Multimodal hard x-ray imaging with resolution approaching 10 nm for studies in material science,"* Nano Futures **2**, 011001 (2018)
5. E. Nazaretski, K. Lauer, H. Yan, N. Bouet, J. Zhou, R. Conley, X. Huang, W. Xu, M. Lu, K. Gofron, S. Kalbfleisch, U. Wagner, C. Rau, and Y. S. Chu, *"Pushing the limits: an instrument for hard x-ray imaging below 20 nm,"* Journal of Synchrotron Radiation, **22**, 336 (2015)

Publications

1. W. Xu, W. Xu, N. Bouet, J. Zhou, H. Yan, X. Huang, L. Huang, M. Lu, M. Zalalutdinov, Y. S. Chu, and E. Nazaretski, "*Machine learning assisted automatic recognition and precise positioning of marker layer in multilayer Laue lenses*," in preparation.
2. W. Xu, W. Xu, N. Bouet, J. Zhou, H. Yan, X. Huang, L. Huang, M. Lu, M. Zalalutdinov, Y. S. Chu, and E. Nazaretski, *"A machine-learning-based approach for angular alignment of 2D multilayer Laue lenses for high-resolution hard X-ray microscopy,"* Proceedings of SPIE, **12698**, 1269803 (2023)
3. W. Xu, W. Xu, N. Bouet, J. Zhou, H. Yan, X. Huang, M. Lu, M. Zalalutdinov, Y. S. Chu, and E. Nazaretski, *"Machine-learning-based automatic small-angle measurement between planar surfaces in interferometer images: A 2D multilayer Laue lenses case,"* Optics and Lasers in Engineering **161**, 107331 (2023).
4. W. Xu, W. Xu, N. Bouet, J. Zhou, H. Yan, X. Huang, M. Lu, M. Zalalutdinov, Y. S. Chu, and E. Nazaretski, *"Achieving High-Resolution Hard X-ray Microscopy using Monolithic 2D Multilayer Laue Lenses,"* Microscopy Today **30**, 28 (2022).

21st Century Methods for Making Gratings

Dmitriy Voronov, Howard Padmore, Lawrence Berkeley National Laboratory

Keywords: diffraction grating, e-beam lithography, nanofabrication, direct write lithography, linear zone plate

Research Project Scope

Gratings are at the heart of all experiments that are conducted using synchrotron radiation in the UV, VUV, Soft and Tender x-ray regions. Today they are made either by diamond scribing, or using holography each of which have serious problems for the most challenging applications. This project is developing two new technologies for production of near perfect gratings based on replication of nm accurate electron beam lithography (EBL) fabricated patterns and direct optical writing.

We use EBL to define a nanometer accurate binary grating pattern on a quartz plate, which is then transferred into a thick silicon grating substrate through several processes of nanofabrication. (Fig. 1a). The aim of this work is perfect pattern transfer followed by production of perfect saw-tooth grooves with a blaze angle up to 3°. A blaze angle reduction process based on a planarization and plasma etch has been developed to achieve an ultra-low blaze angles down to 0.03° required for tender x-rays as well as free electron laser applications (Fig. 1b).

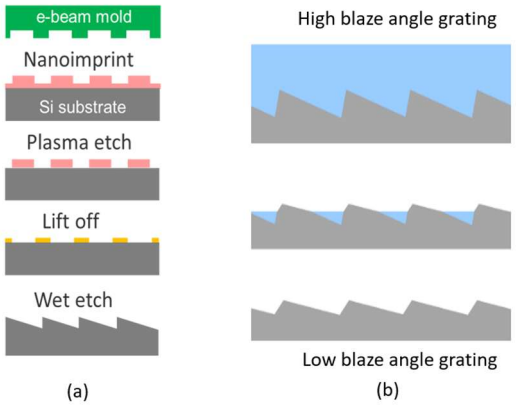

Fig. 1 Nanofabrication approach for making ultra-precise x-ray gratings: transfer of an e-beam written pattern into a grating substrate and shaping of grating grooves (a); blaze angle reduction process for low blaze angle gratings (b).

Since EBL written gratings are limited in size, development of a new system is required to make gratings longer than 150 mm. This is based on a direct write optical lithography approach but uses UV light and a linear zone plate to print a straight-line for each groove of the grating. A photoresist covered grating substrate is then translated under this focused line, and the light intensity is modulated according to the position measured by an interferometer. The writing time should be as short as 1000 seconds, i. e. orders of magnitude less than a ruled grating. The short write time means that the system should be insensitive to environmental changes. Variation of the light intensity also should allow grey scale lithography, enabling writing of blazed grooves directly into silicon.

Recent Progress

A reliable nanofabrication process was developed to transfer an e-beam written grating pattern into a grating substrate. A quartz plate with an e-beam patterned layer of Cr is etched with a plasma to make binary grooves, to be used as a stamp for the following nanoimprinting step. The nanoimprint step is carefully optimized to achieve a uniform layer of resist over the substrate surface, with a residual layer of minimal thickness. The replica is etched with an oxygen plasma which provides residue-free etching through the residual layer. Then a thin Cr layer is deposited and following a lift off-process removes the resist and leaves Cr stripes on the Si surface, which are used as a hard mask for the following anisotropic wet etching to form slanted facets of the saw-tooth grooves. The process was successfully implemented [1] for making gratings with a groove density as high as 6000 lines/mm and a blaze angle of 2.9° (Fig. 2)

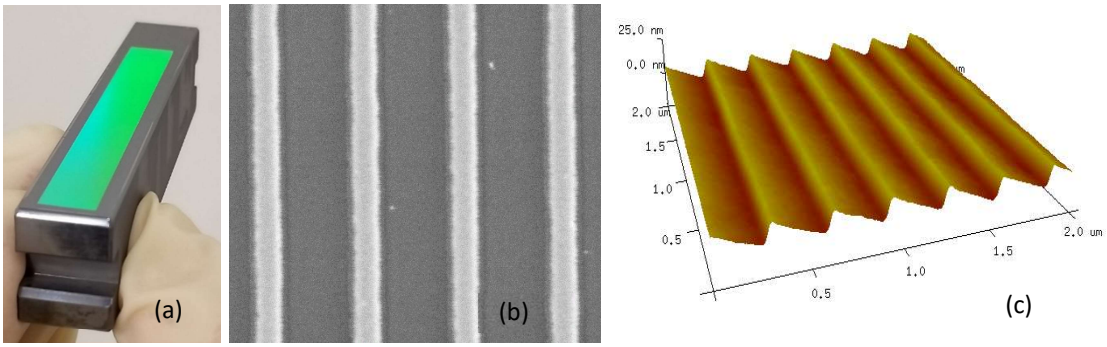

Fig. 2. High groove density x-ray grating fabrication: (a) replicated resist pattern of the Si substrate, (b) Cr hard mask on Si surface, (c) final 3000 lines/mm blazed grating.

A blaze angle reduction process based on planarization and plasma etch, depicted in Fig. 1b, has been demonstrated [2]. A 100 lines/mm blazed grating with a blaze angle of 3.7° (Fig. 3a) was planarized by a polymer material down to an almost perfectly level surface (Fig. 3b). An optimized plasma etch process provided etching of both the polymer material and Si with very close etch rates and resulted in a blaze angle of 0.42° for the final grating. We found that a reduction factor as high as 10 can be achieved using this approach. We demonstrated fabrication of a multilayer coated grating with an ultra-low blaze angle of 0.04° obtained by 3 cycles of planarization and etching [3].

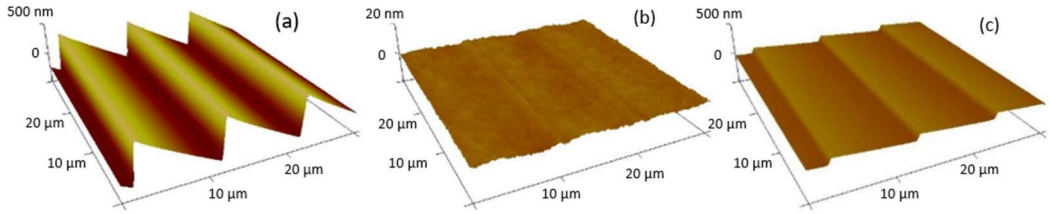

Fig. 3. AFM images of a blazed grating after wet anisotropic etching (a), planarization (b), and plasma etch (c).

An alternative blaze angle reduction process by double replication and etching, which allows virtually unlimited reduction factor in a single reduction cycle was developed [4]. A master Si blazed grating (Fig. 4a) is replicated by a nanoimprint resist on a quartz plate (Fig. 4b) which serves as a stamp for the 2nd replication to transfer the original saw-tooth surface of the master grating on the final grating substrate (Fig. 4c). The 2nd resist replica is processed with a plasma etch which provides a very high etch rate ratio for the resist and Si, which defines the final groove

depth and the blaze angle (Fig. 4d, e). The process was adapted for massive x-ray grating substrates and fabrication of a low blaze angle grating with dimensions of 100 mm × 40mm × 18 mm, groove density of 200 lines/mm, and a blaze angle of 0.2°. Near-perfect groove profile and very low roughness of the blaze facets resulted in a very high diffraction efficiency of the grating, very close to the theoretical predictions (Fig. 4f).

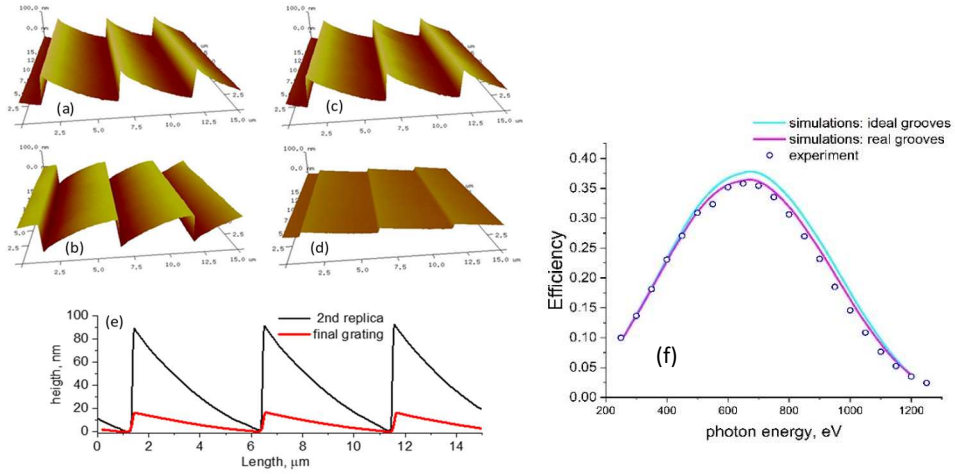

Fig. 4. AFM images of the master grating (a), 1st replica (b), 2nd replica (c), and the final low blaze angle grating (d), and profiles of the 2nd replica and the final grating (e).

Significant progress in development of the grating writer has been achieved. A laboratory has been completed for the grating writer, as shown in Fig. 5. This includes a geophone-based piezo-controlled ultra-low vibration table, the grating writer chamber, and two separate areas used for testing linear zone plates, and motion and interferometry systems.

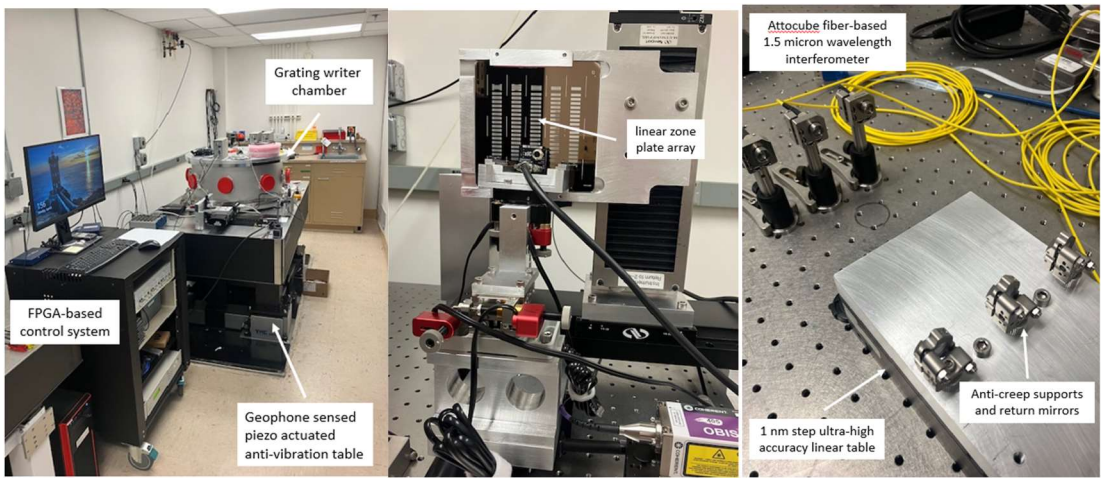

Fig. 5. Left: Shows the new grating development lab, Center: shows a system for testing linear zone plates and Right: shows a fiber interferometer system under test.

The lab is finished and most work so far has been directed towards determining the optimum way to translate a grating blank under the fixed linear focus and make sure that the whole system is spatially coordinated. When you translate, even the highest quality stages pitch and yaw by 1 – 2 orders of magnitude more than is required. Therefore, we have to measure the motion of the

grating substrate, and use this information to correct the position of the linear lens. The philosophy has been to do this measurement using laser interferometry, and to feedback this information to correct the relative position of the lens, which is mounted on a 4-axis linear and angular piezo driven flexure. The present version of the system uses this method, but testing has shown several complications that mean in future versions we will use capacitive sensing against flat reference surfaces as well as grid-based linear encoding.

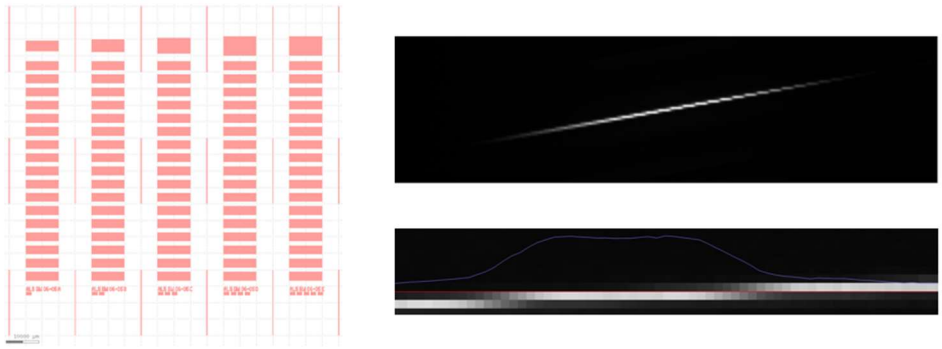

Fig. 6. Left: shows a photomask layout, 5 columns x 18 rows. Right shows a view of a line image inclined to the detector, and lower shows a closeup of the transition regions.

We are currently completing testing of our first generation linear zone plates. This takes a spherical wave (405 nm) from a pinhole, and forms a line focus, i.e. it converts a spherical to a cylindrical wave. For lithography, we need to have constant light intensity along the focused lines, and so as a particular pinhole gives a certain width Airy pattern, the grating mark to space ratio is changed along each grating line to enhance or diminish the diffraction efficacy, so as to keep a constant illumination intensity. As the wave has to pass through the glass of the grating mask, some spherical aberration is introduced, and has to be compensated. For this reason, our prototype consists of an array of 5 columns (for intensity correction) and 18 rows (for spherical aberration correction). We have used inclined edge and other tests (right panel of Fig. 6) to demonstrate diffraction limited resolution (0.78 microns for our present NA). The grating writer is contained in a large stainless steel chamber. This will be enclosed in a thermal isolation box and temperature regulated. We believe that the use of constant temperature at atmospheric pressure may be sufficient to achieve the long term stability we need for laser interferometry, without resorting to vacuum. These tests are underway.

Future Plans

We've developed the fabrication process for x-ray gratings up to around 170 mm in length and we have shown that we can produce near atomically perfect gratings that have the nm flatness required for coherent applications. Based on this work, new work will focus on achieving higher efficiency and higher resolution using multilayer coated gratings. In parallel with this, the most important new goal is to demonstrate production of much longer gratings required for ultra-high resolution RIXS and FEL measurements. This requires completion of R&D on the grating writer, completion of a new system based on reference surfaces and grid encoders, and testing and validation. We have made enormous progress in the present grant period. There is a world-wide race in this area due to the enormous potential for revolutionary new science enabled by a new

generation of grating optics. We have a significant lead, but we need to hammer home our advantage by making our technology routine, and by taking our technology to the absolute limit.

References

1. D. L. Voronov, S. Park, E. M. Gullikson, F. Salmassi and H. A. Padmore, *6000 lines/mm blazed grating for a high-resolution x-ray spectrometer*, Opt. Express **30** (16), 28783-28794 (2022).
2. D. L. Voronov, E. M. Gullikson, H. A. Padmore, *Ultra-low blaze angle gratings for synchrotron and Free Electron Laser applications*, Opt. Express **26** (17), 22011-22018 (2018).
3. D. L. Voronov, S. Park, E. M. Gullikson, F. Salmassi, H. A. Padmore, *Highly efficient ultra-low blaze angle multilayer grating*, Optics Express **20** (11), 16676-16685 (2021).
4. D. L. Voronov, S. Park, E. M. Gullikson, F. Salmassi and H. A. Padmore, *Advanced low blaze angle x-ray gratings via nanoimprint replication and plasma etch*, Opt. Express **31**(16), 26724-26734 (2023).

Publications

1. D. L. Voronov, T. Wang, S. Park, L. Huang, E. M. Gullikson, F. Salmassi, C. Austin, H. A. Padmore, and M. Idir, *Nanometer flat blazed x-ray gratings using ion beam figure correction*, Opt. Express **31** (21), 34789-34799 (2023).
2. D. L. Voronov, S. Park, E. M. Gullikson, F. Salmassi and H. A. Padmore, *Advanced low blaze angle x-ray gratings via nanoimprint replication and plasma etch*, Opt. Express **31**(16), 26724-26734 (2023).
3. S. Park, D. L. Voronov, A. Wojdyla, E. M. Gullikson, F. Salmassi, H. A. Padmore, *Fabrication of low blaze angle gratings by replication and plasma etch*, SPIE proc. **12240**, 1224008 (2022).
4. D. L. Voronov, S. Park, E. M. Gullikson, F. Salmassi and H. A. Padmore, *6000 lines/mm blazed grating for a high-resolution x-ray spectrometer*, Opt. Express **30** (16) 28783-28794 (2022).

Investigate Wavefront Preservation Methods for the Bragg Reflection from Diamond Crystals in X-Ray FEL Oscillators (XFELO)

Yuri Shvyd'ko, Kwang-Je Kim Argonne National Laboratory

Keywords: x-rays crystals diffraction wavefront XFELO

Research Project Scope

A well-functioning diamond crystal optics is essential for realization of the x-ray free-electron laser oscillator (XFELO). Prior to this project, our group at the APS made significant progress in developing diamond crystal optics for the XFELO, demonstrating that the required high Bragg reflectivity is close to the theoretical prediction, that the diamond crystal maintains its structural integrity under the intense x-ray exposure anticipated in the XFELO cavity, and that commercially available paraboloidal Beryllium x-ray lenses can serve as focusing optical elements, as well as several other important cavity-related aspects. One of the next critical tasks was to determine how much the wavefront of the Bragg-reflected light could suffer from distortions in the best available diamond crystals and if these distortions could be mitigated to minimize impact on XFELO performance. Even in practically flawless diamond crystals, internal strain of various origins can result in Bragg planes slope errors and significant wavefront distortions. Studies were therefore required to experimentally measure Bragg plane slope errors and wavefront distortion in commercially available diamond crystals and to develop methods of its reduction below the admissible levels.

The project goals are to perform focused R&D on:

- Characterization of Bragg planes distortions in diamond crystal caused by internal or external strain using X-ray rocking-curve imaging (RCI).
- Wavefront characterization using x-ray wavefront sensors of x-rays Bragg reflected from pre-selected with RCI best diamond crystals.
- Develop approaches of internal strain reduction such as various types of thermal treatment: high-temperature (1500^{o}C in vacuum), medium-temperature (650^{o}C in air), etc.
- Develop and test schemes for strain-free diamond crystal mounting including mounting under low-temperature (90 K) conditions required for XFELO operations.
- Apply the acquired knowledge to realization of XFELO & XRAFEL within the CBXFEL project.

Recent Progress

The main goals of the project are already achieved, as detailed below. But there is still an ongoing effort to perform RCI characterization of the diamond crystals at low temperature ~90K.

Bragg plane slope errors in diamond crystals. Perfect crystals with flat Bragg planes is a prerequisite for wavefront preservation in Bragg diffraction. However, nothing is perfect. How flat can Bragg crystal planes be in the best available diamond crystals? What are the smallest-achievable Bragg-plane slope errors and how do they compare to those of perfect silicon crystals? These questions were addressed in experimental studies performed within multiple experiments at the APS beamline 1BM in 2019-2021 using x-ray rocking curve imaging (RCI). We found that the smallest specific slope errors in the best diamond crystals are about 0.15−0.2 μrad/mm^2, which were only a factor of two larger than the 0.1 μrad/mm^2 specific slope errors we were measuring in perfect silicon crystals. The RCI studies were performed both on free-standing diamond crystals and on diamond crystals firmly mounted (clamped) in crystal holders, as it is required in XFELO operations. In the second case, dedicated crystal samples were designed and manufactured with strain relief features machined with lasers to ensue mechanically stable strain-free mounting and efficient thermal transport. The obtained results are very promising in view of the realization of the XFELO.

Following the initial plan, in the next step we have studied an effect of high-temperature (1450°C) annealing of diamond crystals on Bragg-planes slope errors. For this purpose, we used a high-temperature, high-vacuum furnace specially purchased for this project. The results are very promising, showing that the specific slope errors in the highest-quality diamond crystals can be further reduced to 0.1 μrad/mm^{2,} to values very close to those in silicon crystals. The results of these studies were presented in a paper published in Journal of Synchrotron Radiation [1].

Further these studies were extended to diamond drumhead crystals with ultra-thin (15 μm) membranes, which are required for output coupling of x-rays from the XFELO cavity. The drumhead crystals were manufactured by a domestic vendor using femtosecond laser pulse ablation. The RCI characterization revealed high quality of the drumhead membranes appropriate for output coupling x-rays from the XFELO x-ray cavities. Results were presented in paper "Fabrication of ultra-thin single crystal diamond membrane by using laser ablation" in SPIE 2022 proceedings [3].
The knowledge acquired in these studies was applied for manufacturing and characterization of diamond crystals for the funded by DOE cavity based XFEL (CBXFEL) project [5]

X-ray wavefront measurements upon Bragg diffraction. RCI measurement of the Bragg-plane slope errors provide indirect information on how well crystals may preserve x-ray wavefront upon Bragg diffraction. To obtain direct information, x-ray wavefront sensing experiments were performed at the APS beamline 1BM. Different techniques and geometries were used for characterizing the wavefront quality of Bragg-diffracted beam from diamond crystals. Our primary initial technique used the grating interferometry and one crystal Bragg diffraction, which seamed to be the most straightforward setup and offered robust data analysis process. The

initial experiments revealed a series of problems that were analyzed, solved, and resulted in a novel experimental setup and measurement procedures.
The following modifications were introduced. We used a double-diamond-crystal setup at the APS 1-BM beamline. By using two diamond crystals, the diffracted beam remains parallel to the direct beam with only a small vertical offset. This geometry makes the measurements of the direct and diffracted beams much easier, without the need of multiple corrections leading to uncertainties in wavefront measurements. To further improve the angular sensitivity and spatial resolution of the measurement, we also applied the speckle-tracking methods with specially designed coded mask.

The successful measurements performed on best diamond crystals selected with RCI showed very small wavefront distortions with rms phase error of about $\lambda/60$ (Strehl ratio of 99.0%) over a 200×200 μm^2 area for the double crystal reflection, or about $\lambda/90$ for a single Bragg reflection, which is very close to the admissible phase error ascertained by numerical simulations. The results are published in Journal of Synchrotron radiation [4].

Low-temperature sample chamber design, manufacturing, and tests. A low-temperature sample chamber is required for RCI and wavefront studies of diamond crystals at 90 K, a temperature appropriate for XFELO operations. The RCI studies demand angular stability of the crystals mounted in such chamber at a level of about 100 nrad, which in turn demand the chamber with a very low level of vibrations. Such low-temperature low-vibration chambers are not available commercially. A preliminary design of the low-temperature chamber was finalized, manufactured, and was under study since April 2020. The first tests revealed deficiencies in the mechanical design. Several studies pointed to insufficient thermal isolation as a problem, which required changes in the design. Execution of the laboratory test experiments and delivery of additional equipment was hampered by COVID-19. The design of the modified low-temperature chamber was finalized in the fall of 2021. The chamber was manufactured beginning of 2022. The low-temperature laboratory tests and several several modifications finally allowed us to achieve a temperature of 115 K and maintain it for more than 30 minutes sufficient for one RCI measurement.
The first RCI studies of diamond crystals at low temperature were performed at APS beamline 1BM in 2022. The chamber allowed us to perform low-temperature almost vibration free measurements with a high 0.1-μrad angular resolution. RCI maps show that lowering the temperature to 120 K does not produces significant crystal deformations, which is a promising result. However, we have still to improve the chamber performance, first of all in achieving a lower temperature of 90 K, and perform RCI measurements at 90 K.

Future Plans

The low-temperature crystal chamber is being redesigned to improve performance and to achieve 90 K on the diamond sample in the chamber. Detailed studies will be performed of Bragg plane slope errors in mounted diamond crystals at 90 K. This will serve as a prototype of low-temperature XFELO operations and diamond crystal mounting.

References

Kwang-Je Kim, Yuri Shvyd'ko, and Sven Reiche. *A proposal for an x-ray free-electron laser oscillator with an energy-recovery linac.* Phys. Rev. Lett., **100**, 244802 (2008).

Yu. V. Shvyd'ko, S. Stoupin, A. Cunsolo, A.H. Said, and X. Huang. *High-reflectivity high-resolution x-ray crystal optics with diamonds.* Nature Physics, **6,** 196–199 (2010).

Yu. V. Shvyd'ko, S. Stoupin, V. Blank, and S. Terentyev. *Near 100% Bragg reflectivity of x-rays.* Nature Photonics, **5**, 539–542 (2011).

Tomasz Kolodziej, Yuri Shvyd'ko, Deming Shu, Steven Kearney, Stanislav Stoupin, Wenjun Liu, Thomas Gog, Donald A. Walko, Jin Wang, Ayman Said, Tim Roberts, Kurt Goetze, Maria Baldini, Wenge Yang, Timothy Fister, Vladimir Blank, Sergey Terentyev, and Kwang-Je Kim. *High Bragg reflectivity of diamond crystals exposed to multi-kW/mm^2 X-ray beams*. Journal of Synchrotron Radiation, **25**,1022–1029 (2018).

Tomasz Kolodziej, Preeti Vodnala, Sergey Terentyev, Vladimir Blank, and Yuri Shvyd'ko. *Diamond drumhead crystals for X-ray optics applications.* Journal of Applied Crystallography, **49**, 1240–1244 (2016).

Publications

1. Paresh Pradhan, Michael Wojcik, Xianrong Huang, Elina Kasman, Lahsen Assoufid, Jayson Anton, Deming Shu, Sergey Terentyev, Vladimir Blank, Kwang-Je Kim, and Yuri Shvyd'ko. *Small Bragg-plane slope errors revealed in synthetic diamond crystals. Journal of Synchrotron Radiation*, **27**, 1553–1563 (2020).

2. J.W.J. Anton, P. Pradhan, D. Shu, and Yu. Shvyd'ko. *Design of Vacuum Chamber With Cryogenic Cooling of Samples for Bragg-Plane Slope Error Measurements.* In Proc. MEDSI'20, number 11 in Mechanical Engineering Design of Synchrotron Radiation Equipment and Instrumentation, pages 327–329. JACoW Publishing, Geneva, Switzerland, 10 2021. https://doi.org/10.18429/JACoW-MEDSI2020-WEPC10.

3. Paresh Pradhan, Sergay Antipov, and Yuri Shvyd'ko. *Fabrication of ultra-thin single crystal diamond membrane by using laser ablation.* Advances in X-Ray/EUV Optics and Components XVII, **12240**, page 122400A. International Society for Optics and Photonics, SPIE, 2022.

4. Xianbo Shi, Zhi Qiao, Paresh Pradhan, Peifan Liu, Lahsen Assoufid, Kwang-Je Kim, and Yuri Shvyd'ko. *At-wavelength characterization of X-ray wavefronts in Bragg diffraction from crystals.* Journal of Synchrotron Radiation, **30**, 1100–1107 (2023).

5. Peifan Liu, Paresh Pradhan, Xianbo Shi, Deming Shu, Keshab Kauchha, Zhi Qiao, Kenji Tamasaku, Taito Osaka, Diling Zhu, Takahiro Sato, James MacArthur, XianRong Huang, Lahsen Assoufid, Marion White, Kwang-Je Kim, and Yuri Shvyd'ko. Design, fabrication, and characterization of x-ray optics for the cavity-based x-ray free-electron laser project. Advances in Metrology for X-Ray and EUV Optics X, **12695**, page 126950C. International Society for Optics and Photonics, SPIE, 2023.

Integrated Cryocooling and Strain-free Mounting of Ultra-Thin Diamond Crystals for Hard X-Ray Self-Seeding (HXRSS) System

PI: Yanbao Ma, Department of Mechanical Engineering, University of California Merced, 5200 North Lake Road, Merced, CA 95343

Co-PI: Juhao Wu, SLAC National Accelerator Laboratory, 2575 Sand Hill Rd, Menlo Park, CA 94025

Keywords: Hard X-ray Self-Seeding, Cyrogenic Cooling, mounting of X-ray optics, thermos-mechanical-optical analysis, coefficient of thermal expansion mismatch

Research Project Scope

A transmissive Hard X-Ray Self-Seeding (HXRSS) system with a diamond monochromator has been adopted in LCLS system. After upgrading the XFEL system from LCLS to LCLS-II-HE, the average spectral brightness will increase three orders of magnitude from 10^{22} to 10^{25} photons/s/mm^2/mrad^2/0.1%BW. Due to instantaneous photo absorption of X-ray in the diamond monochromator in the HXRSS system, the average heating power onto the crystal monochromator also increases about three orders of magnitude from a few milliwatts in LCLS to a few watts in LCLS-II-HE. Consequently, there are remarkable temperature increases, which lead to thermal expansion and stress wave propagation (see Fig. 1). In turn, the thermal-induced deformation and displacement will cause adverse effects on optical performance, including shifting and distorting Bragg energy and bandwidth, attenuating X-ray radiation brightness, inhibiting the XFEL process, and even damaging crystal optics. Therefore, an active cryocooling system is required to stabilize the optical performance of the diamond monochromator in the HXRSS system.

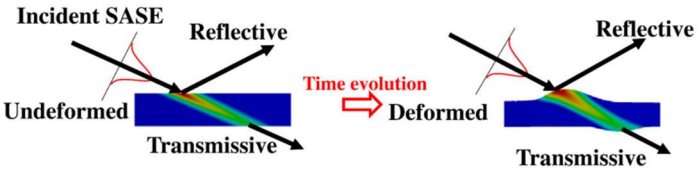

Figure 1. Illustration of the incident SASE pulse which will induce thermal deformation and negatively affected the coherent seed generated from the diamond monochromator.

The project goal is to build up knowledge and experience. The outcomes facilitate the design and optimization of cryocooling and strain-free mounting of ultra-thin diamond crystals for stable operation of the HXRSS system in LCLS-II-HE. The R&D is carried out through systematical study of the strain and thermal impedance for different mounting schemes in both current and an alternative two-stage HXRSS systems. The R&D goal will be achieved through the following five measurable objectives:

1. Develop thermal and stress characterization tools to evaluate the cryocooling performance with average heating power about 5 Watts and mounting-induced deformation;
2. Apply the thermal and stress characterization tools to evaluate two different mounting strategies and find the one with better performance between clamping mounts and stress-free welding mounts for ultra-thin diamond crystals;
3. Identify optimal operating temperature range for ultra-thin diamond crystals with minimum thermal expansion under 5-Watt local heating;
4. Demonstrate an integrated cryocooling and strain-free mounting of ultra-thin diamond crystals to keep the optimal operating temperature under 5-Watt local heating; and

5. Develop a new HXRSS system with reflective configuration to facilitate cryocooling or water cooling, and evaluate the tunability and multi-color options.

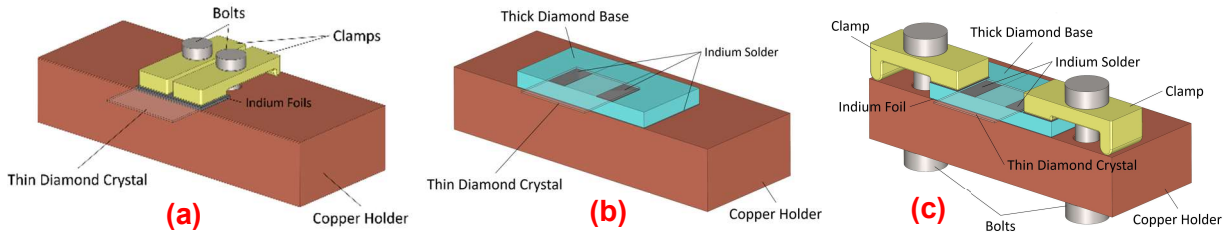

Figure 2. Three different mounting designs for thin diamond crystals. (a) Clamping; (b) soldering; (c) hybrid clamping-soldering.

Recent Progress

In this reporting period, we conducted thermomechanical analysis for three different mounting designs and compared their performance in stain and slope changes for the diamond monochromator in the HXRSS System. As shown in Fig. 2, the three mounting designs include clamping, soldering, and a hybrid clamping-soldering approach. Table 1 summarizes the advantages and disadvantages of three different designs.

Table 1. Comparison of three different mounting designs.

	Pros	Cons
Clamping	▪ Simple design ▪ Simple assembly ▪ Adjustable contact ▪ Enabling reuse of the crystal ▪ Enabling sliding	▪ High mounting distortion ▪ Low contact area ▪ High thermal interface impedance
Soldering	▪ Strong bonding ▪ Low thermal interface impedance	▪ Complexities of soldering processes ▪ Mismatch of thermal expansion coefficients
Hybrid	▪ Strong bonding ▪ Low thermal interface impedance ▪ Enable sliding ▪ Enabling reuse of the crystal	▪ Complexities of soldering processes

Clamping Design

Clamping is a straightforward mounting method that does not require complex phase changes or chemical processes. It has been shown to provide excellent thermal contact conductance (TCC) of about 0.5 W/(mm^2·K) for X-ray optics when using indium foil as an interstitial material (see Fig. 2a). Clamping also allows the crystal to be recycled for other projects when needed. However, there have been limited successful implementations of this method due to high strain and high thermal interface impedance associated with clamping thin crystals.

Soldering Design

Soldering provides excellent mechanical and thermal bonding, with TCC values that can easily reach 1-100 W/(mm^2·K). With vacuum soldering, it is possible to minimize voids or air pockets, approaching the theoretical limit of thermal contact. In this study, a conservative value of 1.5 W/(mm2·K) is used for all soldered contacts. Despite its potential advantages, soldering thin crystals for XFEL applications has been relatively uncommon due to the complexity of the soldering process and the external strain generated during the process. In addition, the large CTE mismatch is also a concern. To mitigate the large CTE mismatch between the oxygen-free high thermal conductivity (OFHC) copper and diamond, a diamond base with lower quality is introduced as a buffer to minimize the strain resulting from the CTE mismatch. The thin diamond is soldered to the diamond base with a thickness of 1 mm, and the diamond base can alsobe soldered to the holder (Fig. 2b).

Hybrid Design

The hybrid design involves both clamping and soldering approaches. The thin diamond device is initially soldered to a thick diamond base (same dimension as in soldering design), and the base is then clamped to a copper holder (Fig. 2c).

Strain-relief cut

To mitigate optical distortion induced either by mounting or thermal expansion, strain relief cuts are introduced to the crystal near the two edges. These two cuts are 2.16 mm away from the front edge of the crystal. They are symmetric on each side of the crystal with a cut length of 1.5 mm and cut width of 0.08 mm (see Fig. 3).

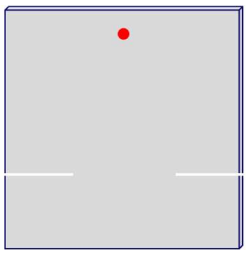

Figure 3. New strain-relief cut design to minimize reduction in thermal conductance.

Identifying the best mounting design

Table 2 shows a summary of surface slope and strain induced by (a) mounting (at 300 K) without thermal load and (b) a fixed thermal load of 15 W with cryocooling (at 90 K). The acceptable surface slope change is less than 7.56 μrad for Darwin width at 9.83 kev for C(0 0 4). For ideal diamond crystal, the surface is flat before mounting. However, there exists surface waviness and tilt (WT) in real diamond crystal devices. Compared with clamping and hybrid cases with WT crystals, there is the minimum surface slope change induced by mounting for WT soldered case. However, thermal induced slope change at cryocooled condition for all WT uncut crystals surpasses 7.56 μrad. After stain-relief cut, the surface slope change in WT hybrid mounting design can satisfy the design requirement (surface slope change < 7.56 μrad), while clamping design and soldering design cannot satisfy such requirement. Therefore, hybrid mounting design with strain-relief cut has been identified as the best solution.

Reflective HXRSS System

High thermal load is a big challenge for approaching the lower side of the tender X-rays. Recently, a two-stage cascaded HXRSS system has been demonstrated at megahertz repetition rate at the European XFEL[1]. The novel approach and promising results from the thermal management study

Table 2. Summary of surface slope and strain for call cases.

	Surface slope (μrad)			Strain		
	min	max	RMS	min	max	RMS
Flat clamped uncut 300 K	−3.62	3.58	1.78	-1.26×10^{-7}	1.58×10^{-8}	6.98×10^{-8}
Flat soldered uncut 300 K	−19.33	19.38	9.71	-7.19×10^{-7}	2.24×10^{-6}	9.76×10^{-7}
Flat hybrid uncut 300 K	−1.60	1.60	0.80	4.90×10^{-8}	3.23×10^{-7}	1.93×10^{-7}
WT clamped uncut 300 K	−270.08	271.32	135.98	-4.07×10^{-6}	4.08×10^{-6}	2.29×10^{-6}
WT soldered uncut 300 K	−2.34	4.29	1.39	-6.69×10^{-7}	2.13×10^{-6}	9.73×10^{-7}
WT hybrid uncut 300 K	−11.46	11.74	5.78	-9.69×10^{-8}	2.63×10^{-7}	1.30×10^{-7}
WT clamped uncut cooled	−312.09	308.68	156.02	-4.79×10^{-6}	4.66×10^{-6}	2.69×10^{-6}
WT soldered uncut cooled	−13.20	12.49	5.15	-2.32×10^{-6}	7.00×10^{-6}	3.20×10^{-6}
WT hybrid uncut cooled	−9.07	15.45	6.46	2.57×10^{-8}	6.55×10^{-7}	3.66×10^{-7}
WT clamped cut cooled	−153.67	154.04	77.80	-2.22×10^{-6}	2.23×10^{-6}	1.21×10^{-6}
WT soldered cut cooled	−39.33	37.73	19.13	-2.42×10^{-6}	3.63×10^{-6}	1.47×10^{-6}
WT hybrid cut cooled	−3.72	4.19	1.78	-9.09×10^{-8}	8.93×10^{-8}	4.11×10^{-8}

*WT: waviness and tilt

enable us to design Hard X-Ray Self-Seeding (HXRSS) FEL below 4 keV at the lower side. This opens a tremendous opportunity to reach high energy photon, e.g. 11.2 keV via the harmonic lasing scheme with baseline electron bunch parameters. The previous scheme will fully rely on the low-emittance electron bunch from the low-emittance injector. Here, we explored the possibility to expand the cryocooling to four-bounce silicon monochromator for harmonic lasing[2].

Future Plans (We will request one-year non cost extension)

1. Conduct experiments to identify optimal operating temperature range for ultra-thin diamond crystals with minimum thermal expansion under 5-Watt local heating;
2. Demonstrate an integrated cryocooling and strain-free mounting of ultra-thin diamond crystals to keep the optimal operating temperature under 5-Watt local heating; and
3. Develop a new HXRSS system with reflective configuration to facilitate cryocooling or water cooling and evaluate the tunability and multi-color options.

References

1. S. Liu, C. Grech, M. Guetg, S. Karabekyan, V. Kocharyan, N. Kujala, C. Lechner, T. Long, N. Mirian, W. Qin, S. Serkez, S. Tomin, J. Yan, S. Abeghyan, J. Anton, V. Blank, U. Boesenberg, F. Brinker, Y. Chen, W. Decking, X. Dong, S. Kearney, D. La Civita, A. Madsen, T. Maltezopoulos, A. Rodriguez- Fernandez, E. Saldin, L. Samoylova, M. Scholz, H. Sinn, V. Sleziona, D. Shu, T. Tanikawa, S. Terentiev, A. Trebushinin, T. Tschentscher, M. Vannoni, T.Wohlenberg, M. Yakopov, and G. Geloni, *Cascaded hard X-ray self-seeded free-electron laser at megahertz repetition rate, Nature Photonics*, Vol. 17, 984-991, (2023).
2. C. Emma, Y. Feng, D. C. Nguyen, A. Ratti, and C. Pellegrini, *Compact double-bunch x-ray free electron lasers for fresh bunch self-seeding and harmonic lasing*, Physical Review Accelerators and Beams, **20**, 030701 (2017).

Publications

Z. Qu, Y. Ma, and J. Wu, *Exploring Mounting Solutions for Cryogenically Cooled Thin Crystal Optics in High Power Density X-ray Free Electron Lasers*, Accepted by Review of Scientific Instruments

New Capabilities for Simulation of Coherent X-ray Scattering Experiments at Light Sources

O. Chubar (Tchoubar), NSLS-II, Brookhaven National Laboratory

Keywords: Synchrotron Radiation, Light Sources, Physical Optics, Coherent X-ray Scattering

Research Project Scope

Recent progress in accelerator physics has driven a very substantial reduction of electron beam emittances in storage ring based light sources. This emittance reduction results in a dramatic, 1-2 orders of magnitude, increase of the spectral brightness, as well as very substantial increase of the coherent flux portion of generated X-rays. Great successes were also reached over the last years in the construction and operation of X-ray free electron lasers (XFELs). To ensure maximal benefits from these source improvements for user experiments, beamlines at the new light source facilities need to be optimized to preserve the high brightness, high degree of coherence and wavefront quality all the way to the samples. Furthermore, the experimental end-stations, including sample environments, analyzers, and detection schemes, also need to be optimized to carry out experiments with the coherent X-rays most effectively. Such optimizations can only be done with software written based on electrodynamics / physical optics principles, allowing for high-accuracy calculation of the emission and propagation of partially coherent synchrotron radiation (SR) and, where possible, simulation of the SR interaction with experimental samples and subsequent propagation of the scattered radiation to a detector. The simulation software must be easily accessible and user-friendly, to make ensure that not only developers of new light sources, but also scientists from different domains, who consider using these facilities for their research, are able to run the simulations – e.g. to verify feasibility of their proposed experiments and possibly test experimental data processing methods. The major goal of this project is to create such a software system for the simulation of coherent X-ray scattering experiments, capitalizing on previously developed physical optics methods for SR propagation through beamlines. The system has to enable fast calculations on client computers and on powerful HPC clusters, such as DOE's NERSC facility, via Python and web-browser based user interfaces.

Recent Progress

A brief description of the main accomplishments for different sub-goals is given below.

1) *Adapting existing and implementing new methods in the SRW code for the simulation of coherent scattering experiments; benchmarking accuracy of the simulations by measurements.*

To simulate samples in many coherent X-ray scattering experiments, a 2D "thin optical element" propagator, consisting in multiplication of frequency-domain electric field describing fully coherent incident radiation by a complex transmission function, can be used. The electric field modified by this function is then propagated to a detector, using an appropriate version of the Fresnel free-space propagator. Several methods were implemented in SRW for defining samples

in 2D from different inputs: based on images (e.g. produced by scanning electron microscopy) or distributions of nanoparticles with given refractive properties [1], produced by other, e.g. molecular dynamics (MD), calculations. To simulate propagation through a 3D sample beyond the "thin" approximation, the "split operator" approach is applied. In this approach, wavefront propagation is done in multiple "steps", with each "step" representing propagation through a small "slice" of the 3D sample. This approach enables taking into account multiple scattering within one sample [2]. The definition of sample models in 2D and 3D was illustrated in several Python example scripts that were added to the SRW repository (at https://github.com/ochubar/SRW).

Multiple tests were performed to make sure that the implementation of the "thin optical element" and "drift space" propagators in SRW offers sufficient accuracy for the simulation of coherent scattering experiments. For these purposes, detailed comparisons of simulations with measurements were done for the experiments at the Coherent Hard X-ray (CHX) beamline of NSLS-II, with artificial nano-fabricated samples produced at BNL's Center for Functional Nanomaterials [1]; a remarkably good agreement was obtained in all cases. SRW simulations were also benchmarked vs. measurements of soft X-ray diffraction / scattering by a special zone plate with perturbed topology of zones (considered for ptychography experiments), see fig. 1.

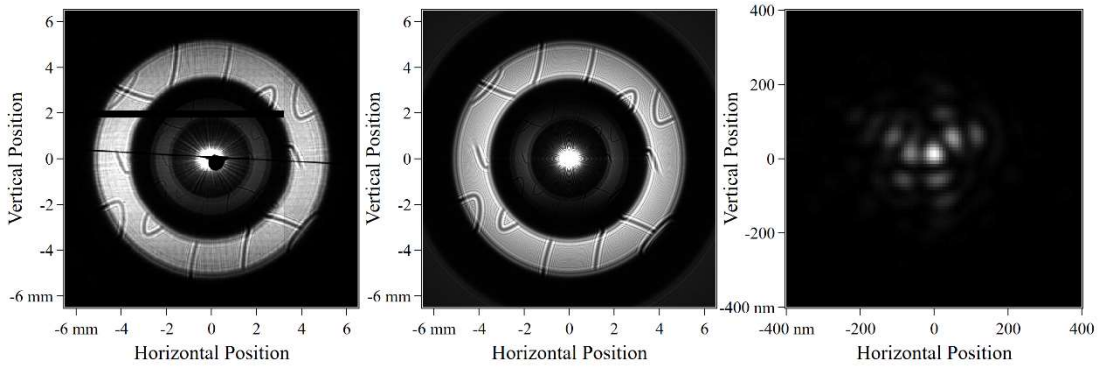

Figure 1: Measured (at Coherent Soft X-ray beamline of NSLS-II, left) and simulated (center) intensity distributions of 938 eV undulator radiation, formed by a special zone plate with dislocations of zones, observed after focus, and the corresponding simulated intensity distribution at the focus (right). The image after the focus is created by two different zone plate diffraction "orders". Dislocations of zones result in dark lines with diffraction fringes on sides. The nano-scale intensity distribution at the focus (right) can be obtained only from the simulation.

In another test, simulation of silica nanoparticles' dynamics was performed with LAMMPS MD code (https://www.lammps.org), followed by coherent X-ray scattering simulations with SRW and the XPCS processing. Results of these simulations were compared to experimental data obtained for such a specimen at the CHX beamline, and a very good agreement was obtained [3].

2) *Improving accuracy and level of detail in simulations of X-ray optics imperfections.*

New experimental and simulation results were published in Proc. of SPIE (vol. 11493, 114930M) for compound refractive lenses (CRLs) made out of Beryllium and diamond (test exemplars developed by Euclid Labs). The quality of X-ray focusing by the new test diamond CRLs appeared

to be inferior to that of Be CRLs, however, the amount of parasitic X-ray scattering produced by them appeared to be considerably smaller, making this type of CRL very promising for multiple future applications at beamlines (provided that their surface quality will improve). The experimental results obtained at the CHX beamline were supported by SRW simulations. Miscellaneous misalignment cases of Be CRLs and the corresponding aberrations were studied with SRW simulations and reported in the same SPIE proceedings (vol. 11493, 114930J).

3) *Implementing optimization and machine learning algorithms to address inverse problems related to development of sources, X-ray optics and experiments.*

Optimization methods were added both to the SRW code (in the "virtual beamline" module of its Python part) and to the Sirepo web browser interface. These methods are now extensively used for the development of new beamlines for NSLS-II and other light sources. The forward-simulation functions of the SRW code were also used in high-accuracy electron beam emittance and energy spread measurements at the CHX beamline of NSLS-II, where an accurate value of the electron beam emittance ($\varepsilon_x \approx 0.76$ nm) was obtained with due regard for damping effects not only from damping wigglers, but also from undulators.

4) *Extending the existing Sirepo framework to support simulation of experiments on servers via web interface and making this service available for users and developers of light sources.*

The definition of models of experimental samples for the simulation of coherent X-ray scattering experiments can be done now from the Sirepo web browser interface [4]. The capabilities of the Sirepo framework were extended to enable execution of physical optics calculations with SRW directly at NERSC. This greatly improved the capacity of the SRW and Sirepo framework for numerically intensive partially coherent simulations for X-ray beamlines and experiments.

5) *Improving reliability, generality, accuracy and efficiency of physical optics simulations for sources, X-ray optics and experiments.*

Two new efficient methods for the coherent mode decomposition of the 4D cross-spectral density of SR were developed and implemented in the SRW code [5], allowing for a considerable, 1-3 orders of magnitude, acceleration of partially coherent calculations for multiple applications. This development is of very high practical importance for modern storage ring light sources, dramatically increasing feasibility and applicability of partially coherent calculations for solving a large variety of problems related to the development and optimization of new beamlines, start-to-end simulation of experiments, and processing of experimental data.

Extensive testing of parallel performances of the SRW code was carried out at NERSC. This included the message passing interface (MPI) parallelization implemented for partially coherent emission and wavefront propagation calculations for storage ring sources, and OpenMP based shared-memory parallelization of XFEL pulse propagation calculations. The MPI based calculations were found to scale very well with the number of processes used, routinely offering

2-3 order of magnitude speedup compared to a sequential calculation, whereas the OpenMP based calculations (executed on one server node) demonstrated the speedup by factor of ~20.

A new version of the SRW code with many time-critical functions (used in wavefront propagation calculations) ported from their sequential versions for CPU to parallel versions for GPU was developed using NVIDIA CUDA. The corresponding speedup reached a factor of ~100 (compared to the sequential execution on CPU). The new GPU-enabled version of the code was successfully used for the simulation of time-dependent coherent X-ray scattering experiments [3].

Future Plans

Simulation of experiments is now naturally included in the entire development process for new beamlines / instruments at light sources – to make sure that these instruments will fully and optimally address the corresponding needs and expectations of science and industry. The demand for such simulations only continued to grow over the last years. In view of this high demand, we plan to extend the simulations to cover different types of experiments that are performed at light sources. Work is currently in progress in collaboration with teams from different labs on full-scale simulation of ptychography experiments that are or can be performed at storage rings and XFELs for such important industrial applications as diagnostics of integrated circuits. Further extensions of the simulation capabilities are planned for the Bragg CDI and powder diffraction experiments that will be performed at new beamlines of the NEXT-II and -III projects at NSLS-II, and beamlines at a planned ultra-low-emittance NSLS-II Upgrade. Efforts will also be dedicated to improvement of sample reconstruction and experimental data processing methods benefiting from the approaches developed for the forward-simulation of experiments.

References

1. O. Chubar, R.A. Coles, L. Wiegart, A. Fluerasu, M. Rakitin, J. Condie, P. Moeller, R. Nagler, "Simulations of coherent scattering experiments at storage ring synchrotron radiation sources in the hard X-ray range," Proc. SPIE 11493, 1149310 (2020); doi: 10.1117/12.2568833.

2. O. Chubar, L. Berman, A. Fluerasu, Y. Gao, H. Goel, A. He, M. Rakitin, L. Wiegart & G. Williams, "Applications of "Synchrotron Radiation Workshop" Code," Synchrotron Radiation News 36 (5), pp. 15-22 (2023); doi: 10.1080/08940886.2023.2274739.

3. H. Goel, O. Chubar, R. Li, L. Wiegart, M. Rakitin and A. Fluerasu, "Efficient end-to-end simulation of time-dependent coherent X-ray scattering experiments," Journal of Synchrotron Radiation 31 (3), May 2024; doi: 10.1107/S1600577524001267.

4. M.S. Rakitin, P. Moeller, R. Nagler, B. Nash, D.L. Bruhwiler, D. Smalyuk, M. Zhernenkov, and O. Chubar, "Sirepo: an open-source cloud-based software interface for X-ray source and optics simulations," Journal of Synchrotron Radiation 25, 1877-1892 (2018); doi: 10.1107/S1600577518010986.

5. R. Li and O. Chubar, “Memory and CPU efficient coherent mode decomposition of partially coherent synchrotron radiation with subtraction of common quadratic phase terms,” Optics Express 30 (4), 5896-5915 (2022); doi: 10.1364/OE.452247.

Publications

1. R. Li and O. Chubar, “Memory and CPU efficient coherent mode decomposition of partially coherent synchrotron radiation with subtraction of common quadratic phase terms,” Optics Express 30 (4), 5896-5915 (2022); doi: 10.1364/OE.452247.

2. L. Huang, T. Wang, O. Chubar, G. Dovillaire, A. He, M. Rakitin, and M. Idir, “Simulation of X-ray Hartmann wavefront sensing with the Synchrotron Radiation Workshop,” Optics Express 30 (23), 41061-41074 (2022); doi: 10.1364/OE.470197.

3. S. Kongtawong, O. Chubar and T. Shaftan, “Simulation of synchrotron radiation from electron beams affected by vibrations and drifts,” Phys. Rev. Accel. Beams 25, 024601 (2022); doi: 10.1103/PhysRevAccelBeams.25.024601.

4. H. Goel, O. Chubar, L. Wiegart, A. Fluerasu, R. Li, A. He, M. Rakitin, P. Moeller and R. Nagler, “Developments in SRW code and Sirepo framework supporting simulation of time-dependent coherent X-ray scattering experiments,” Journal of Physics Conference Series 2380 (1), 012126 (2022); doi: 10.1088/1742-6596/2380/1/012126.

5. O. Chubar, G. Williams, Y. Gao, R. Li, and L. Berman, “Physical optics simulations for synchrotron radiation sources,” Journal of the Optical Society of America A 39 (12), C240-C252 (2022); doi: 10.1364/JOSAA.473367.

6. O. Chubar, L. Berman, A. Fluerasu, Y. Gao, H. Goel, A. He, M. Rakitin, L. Wiegart & G. Williams, “Applications of “Synchrotron Radiation Workshop” Code,” Synchrotron Radiation News 36 (5), 15-22 (2023); doi: 10.1080/08940886.2023.2274739.

7. M. Labat, O. Chubar, J. Breunlin, N. Hubert, and Å. Andersson, “Bending Magnet Synchrotron Radiation Imaging with Large Orbital Collection Angles,” Physical Review Letters 131, 185001 (2023); doi: 10.1103/PhysRevLett.131.185001.

8. O. Chubar, T. Tanaka, R. Li, "Comparing coherent mode decomposition methods for undulator radiation in modern synchrotron light sources," Proc. SPIE 12697, 1269704 (2023); doi: 10.1117/12.2677842.

9. A. He, O. Chubar, J. Dvorak, W. Hu, "New wavefront split propagator in SRW code and its application in simulation of high-resolution Fresnel zone plate," Proc. SPIE 12697, 1269703 (2023); doi: 10.1117/12.2677572.

10. H. Goel, O. Chubar, R. Li, L. Wiegart, M. Rakitin and A. Fluerasu, “Efficient end-to-end simulation of time-dependent coherent X-ray scattering experiments,” Journal of Synchrotron Radiation 31(3), May 2024; doi: 10.1107/S1600577524001267.

X-ray Beam Position Monitor R&D for Coherent Soft X-ray Beamlines

Boris Podobedov (BNL), Claudio Mazzoli (BNL), Dmitri Donetski (Stony Brook University)

Keywords: Pixelated detectors, GaAs, white X-ray beam diagnostics, storage-ring light sources

Research Project Scope

Despite a growing need, non-invasive soft X-ray beam position monitors (BPMs) are not yet available. This project aims to demonstrate micron-scale resolution for a novel soft X-ray BPM (sXBPM) design that uses gallium arsenide (GaAs) detector arrays positioned to probe the outer portions of white X-ray beams. The principle of the device is illustrated in the figure.

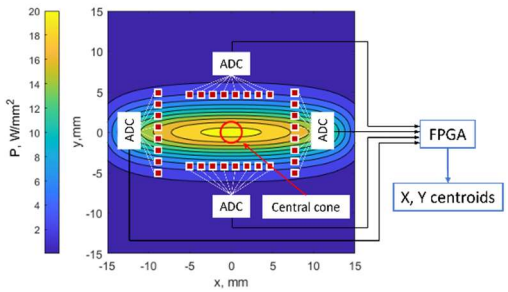

sXBPM concept (detector pixels shown overlaid on the X-ray power density distribution 26 m away from CSX EPU)

Our primary goal was to achieve micron-scale positional resolution ~30 m away from the undulator source, without interfering with user experiments, especially the most sensitive ones exploiting coherent properties of the beam.

Our secondary goal was to demonstrate enhanced diagnostics capabilities that come from multi-pixel detector arrays. In addition to more efficient beam position measurement, these capabilities include an instantaneous sampling of the beam cross-sections at the array locations, the ability to measure the entire x-y plane cross-section of X-ray beam power, providing efficient diagnostics for fine-tuning the canted undulator angle and beam overlap, and others.

The project is essentially completed, and both goals have been achieved.

The sXBPM was installed and tested in the 23-ID First Optical Enclosure (FOE) of NSLS-II. This FOE houses the upstream portions of both the Coherent Soft X-ray Scattering (CSX) and the In situ and Operando Soft X-Ray Spectroscopy (IOS) beamlines. The sXBPM is located just outside the ring tunnel and upstream of any optical components. It can probe white X-ray beams from one or two undulators (EPU49, L=2 m) which can be set up in either canted or straight configuration.

The project is largely experimental. Major milestones included 1) development, fabrication, and tests of GaAs detector arrays suitable for this application; 2) mechanical design, fabrication, and installation of components that allow for positioning of the detectors with micron-scale accuracy, and provisions for possible intercepts of kW-level beam power in abnormal conditions; 3) tests of sXBPM under high-power X-ray beam including during regular user operations of NSLS-II.

Positioning of an R&D device in the upstream section of two operating beamlines with heavy user load presented major installation and schedule constraints and lower risk tolerance. Conversely, the chosen sXBPM location arguably provides the most practically relevant testing environment.

Recent Progress

Detector development, fabrication, and testing

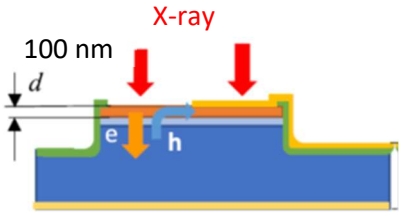

Photodiode cross-section sketch

Several generations of detector array prototypes were manufactured from GaAs wafers grown by Molecular Beam Epitaxy. They were extensively characterized with a high-power Ar-ion laser and subsequently tested in monochromatic beams in both soft- and hard X-ray beamlines at NSLS-II.

For good positional resolution and low photo-current density in high-power undulator beams, sXBPM detectors require high soft X-ray responsivity and low hard X-ray responsivity. This response was accomplished by using a shallow p–n junction obtained by epitaxial growth of a p-layer on an n-substrate.

Significant effort was spent on UHV-compatible detector packaging, heat transfer issues, and alignment techniques. Photodiode responsivity vs. temperature was thoroughly characterized and was shown to vary ~0.1% per degree C, meeting one of the sXBPM design goals.

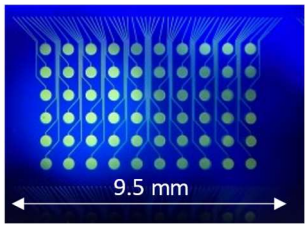

50-pixel GaAs detector array with contact pads (pre-cleaving, pixels on top)

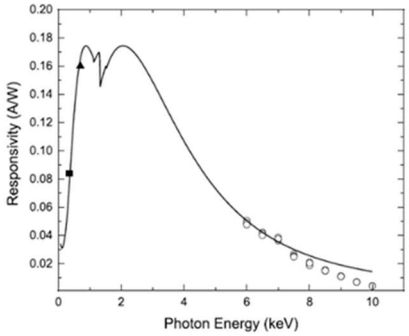

Measured responsivity

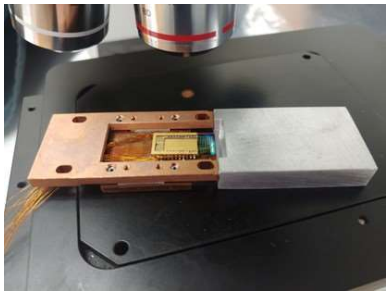

Detector assembly pre-alignment

Mechanical design, fabrication, and installation

Mechanical design, fabrication, and installation were the most time-, labor-, and resource-consuming parts of the project at BNL. The sXBPM contains up to four water-cooled blade assemblies (a.k.a. heat-sinks), each of which can have a GaAs detector assembly mounted within it. Each blade assembly can be inserted into the X-ray beam with sub-micron accuracy and resolution using a custom linear shift mechanism (a.k.a. a manipulator). The primary challenges in the design of the sXBPM included: 1) mechanical stability and alignment, 2) management of

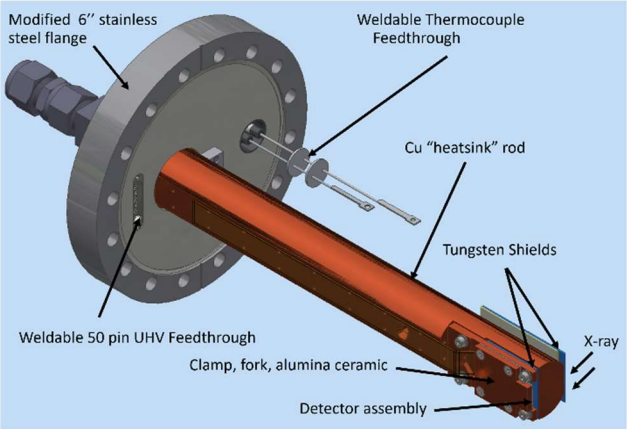

Heat-sink assembly with detector array

sXBPM installed in 23-ID FOE

the heat load from the X-ray beam to protect GaAs detectors, 3) compactness to fit within 23-ID FOE, and 4) accessibility for modifications.

In addition to the detector-carrying heat-sink assemblies, the sXBPM system includes a high-stability Invar stand, a customized 6-way vacuum cross, vacuum isolation valves, gauges, etc.

To make space for the sXBPM some beamline components had to be relocated. Major installations could only be performed during long machine shutdowns three times a year. The presently installed configuration includes top and bottom (vertically moving) heat-sink assemblies, with the provision to have the horizontal pair installed in the future. An unoccupied flange for one of the assemblies is presently used as a viewport seen in the right Figure.

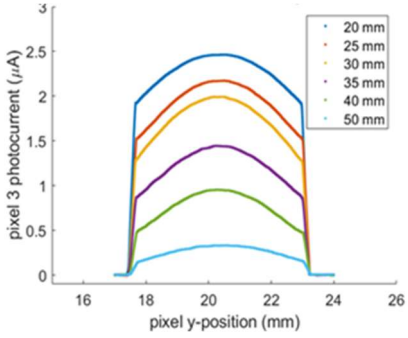

Vertical beam cross-sections at different EPU gaps

White X-ray beam tests

The project milestone of the sXBPM detecting first X-ray signals was reached in July 2023. For that installation, only the top blade was installed with 4 array pixels connected to the data acquisition electronics outside. During low-current machine studies, we scanned the detector vertically across the entire X-ray beam while varying the EPU gaps. Figure to the right shows the photocurrent from one of the pixels recorded during these scans, when the gap of the downstream EPU was varied. The signals traced the expected X-ray beam shapes, decreasing in intensity and narrowing with larger ID gaps.

Importantly, no noise or parasitic signals were observed when the detector was positioned outside of the upstream aperture.

As the vacuum conditions improved, we were able to expose the detector to higher beam intensities. During user operations at 500 mA, the pixel signals were reading up to ~120 uA (depending on the EPU gap settings) with fairly low noise. They were changing, as expected, in response to the topoff injections, small orbit motions, EPU gap and polarization changes, etc.

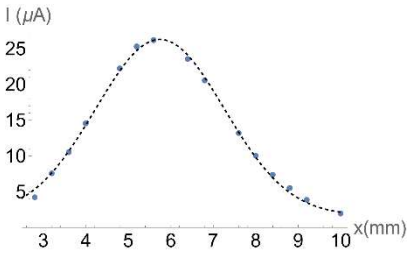

Pixel photocurrents and fit

In the Fall of 2023 we installed the top and bottom sXBPM blades with 25 detector pixels wired for each. This symmetric configuration allowed us to calculate beam position from the measured pixel photocurrents, just as was envisioned in the original proposal. Due to finely spaced pixels, we are also able to determine the horizontal beam position by shape-fitting (top Figure). Because no calibration is required, this method is superior to the difference-over-sum method, used in RF BPMs or conventional X-ray BPMs. We have also demonstrated that the sXBPM easily reaches sub-micron resolution (see talk).

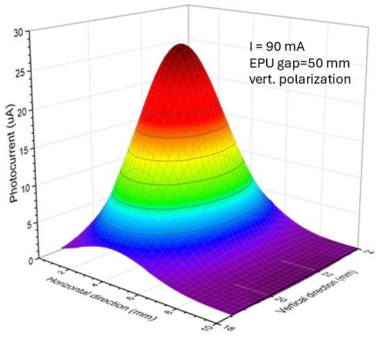

2D EPU beam cross-section

Finally, by scanning the detector arrays through the X-ray beam we are now able to measure the x-y plane distributions of undulator radiation intensity (right Fig.). To the best of our knowledge, our measurements represent the first successful attempt to use multi-pixel semiconductor detectors as diagnostics for high-power white-beam undulator radiation.

Future Plans

The project is complete pending the submission of the final report. Now that we have successfully demonstrated the concept, we plan on applying for future funding to capitalize on our successes to date. Specific topics may include the following.

- Further exploration of sXBPM benefits
  1) Exploration of the ultimate performance limits of a feedback system that uses sXBPM-provided signals and storage ring correctors to maintain undulator source stability
  2) Demonstration of discrimination of SR from parasitic sources e.g. dipole magnets, correctors, the other canted undulator, etc. (long-standing problem for all XBPMs)
  3) Demonstration of further-improved resolution by operating the detectors at the edge of the shadow from upstream slits
- Further optimization of GaAs detector design, fabrication, and packaging
  4) Investigation of GaAs/AlGaAs heterostructures with n-doped AlGaAs barriers with graded Al compositions to provide further flexibility in spectral responsivity shaping

5) Investigation of aging properties of the detectors (if any), and exploring mitigation techniques, e.g. optimizing mesa diode passivation and top metallization

- Reduction of the cost and complexity of the device; expanding the scope
  6) Exploration of a simpler sXBPM design with fixed-position detectors or with detectors mounted on (adjustable) front-end slits
  7) Exploration of locating in-vacuum ADCs immediately adjacent to the detector followed by a serial communication to the electronics outside.
  8) Development of a GaAs array-based XBPM for tender- or hard X-ray beamlines

Publications

1. B. Podobedov, D.M. Bacescu, C. Eng, S. Hulbert, C. Mazzoli, C.S. Nelson, D. Donetski, K. Kucharczyk, J. Liu, R. Lutchman, *Novel White X-ray Beam Position Monitor for Coherent Soft X-ray Beamlines*, to be presented at IPAC'2024, Aug 27-Sep. 1, 2023
2. B. Podobedov, D.M. Bacescu, C. Eng, S. Hulbert, C. Mazzoli, C.S. Nelson, D. Donetski, K. Kucharczyk, J. Liu, R. Lutchman, *Novel X-ray Beam Position Monitor for Coherent Soft X-ray Beamlines*, presented at FLS 2023, 67th ICFA Advanced Beam Dynamics Workshop on Future Light Sources, Aug 27-Sep. 1, 2023, TH3B2
3. J. Zhao, K. Kucharczyk, D. Donetski, B. Podobedov, *GaAs/AlGaAs Photodetector Arrays for Soft X-ray Beam Position Monitoring*, ACCGE-23, Tucson, AZ, Aug 13-Aug 18, 2023
4. K. Kucharczyk, J. Liu, R. Lutchman, D. Donetski, D. Bacescu, C. Eng, S. Hulbert, C. Mazzoli, C. Nelson and Boris Podobedov, *Development of GaAs Photodetector Arrays for Soft X-ray Beam Position Monitoring*, presented at the 65th Electronic Materials Conference (EMC'23), June 28-30, 2023
5. B. Podobedov, D.M. Bacescu, C. Eng, S. Hulbert, C. Mazzoli, C.S. Nelson, D. Donetski, K. Kucharczyk, J. Liu, R. Lutchman, *Recent Developments of the Soft X-ray Beam Position Monitor Project*, presented at North American Particle Accelerator Conference (NAPAC'22) August 7-12, 2022, THZE5
6. D. Donetski, K. Kucharczyk, J. Liu, R. Lutchman, S. L. Hulbert, C. Mazzoli, C. Nelson, B. Podobedov, *High power density soft X-ray GaAs photodiodes with tailored spectral response*, Semiconductor Science and Technology **37**, 085024 (2022)
7. C. Eng, D. Donetski, S. Hulbert, J. Liu, C. Mazzoli, B. Podobedov, *Mechanical Design of a Soft X-ray Beam Position Monitor for the Coherent Soft X-ray Scattering Beamline*, presented at 11th International Conference on Mechanical Engineering Design of Synchrotron Radiation Equipment and Instrumentation (MEDSI'2020), July 26-29, 2021, MOPC01
8. J. Liu, C. Eng, S. Hulbert, C. Mazzoli, B. Podobedov, K. Kucharczyk, R. Lutchman, D. Donetski, *Progress towards Soft X-ray Beam Position Monitor Development*, proceedings of International Particle Accelerator Conference (IPAC'21), May 24-28, 2021, MOPAB121
9. J. Liu, K. Kucharczyk, R. Lutchman, D. Donetski, C. Mazzoli, B. Podobedov, *GaAs detector array for soft X-ray beam position monitoring in storage ring light sources*, presented at Conference on Laser and Electro Optics (CLEO), May 9-14, 2021

Advanced MEMS-Based Dynamic Optics-on-A-Chip for New-Generation X-ray Sources

Jin Wang, X-ray Science Division, Argonne National Laboratory

Keywords: X-ray optics, microelectromechanical systems, X-ray pulse manipulator, time-resolved synchrotron experiments, synchrotron x-ray source

Research Project Scope

Time-resolved synchrotron X-ray techniques have become a powerful tool for understanding structures and dynamics in fast-evolving systems in physics, chemistry, materials science, biology, medicine, and environmental science. The challenge of time-resolved X-ray science at the current and future low-emittance synchrotron X-ray sources has brought the impetus for developing future-generation ultrafast and dynamic X-ray optics that can generate the photon pulses suited for the timing experiments. The research project scope on developing microphonics/MEMS-based optics-on-a-chip devices suitable for the APS and other DOE synchrotron facility beamline operation. We use the widely available silicon-on-insulator technology to implement the on-chip nanosecond to picosecond synchrotron pulse shaper that shapes the hard X-ray pulses at individual beamlines with high flexibility and efficiency, even beyond the synchrotron pulse length limit. The unique ultrafast and dynamic devices offer straightforward but versatile timing tools for investigating structural dynamics from condensed matter to biological systems with temporal resolution better than the limit of current and future synchrotron sources. Beyond manipulating synchrotron X-rays, the devices can also find applications at high-rep-rate and high-energy XFELs.

Recent Progress

Ultrafast MEMS X-ray optics capable of modulating hard X-ray pulses exceeding 350 MHz

Optical MEMS are developed for dynamic spatiotemporal control in light wave manipulation and communication as modulators, switches, multiplexers, spectrometers, etc. However, they have not been shown to function similarly in sub-nm wavelength regimes, namely, with hard X-rays. We demonstrate ultrafast x-ray optics-on-a-chip based on MEMS capable of modulating hard x-ray pulses exceeding 350 MHz, 103× higher than any other mechanical modulator, with a pulse purity $>10^6$ without compromising the spectral brilliance (Figure 1). Moreover, the timing characteristics of the devices can be tuned on the fly to deliver optimal pulse properties to create a host of dynamic x-ray instruments and applications, impossible with traditional optics of 109× bulkier and more massive. The advent of the ultrafast optics-on-a-chip heralds a new paradigm of X-ray photonics, time-domain science, and accelerator diagnostics, especially at the future-generation light sources, such as the upgraded Advanced Photon Source that offer coherent and high-frequency pulses. We should note that at the APSU, the standard operational timing mode is 324 to achieve the lowest-emittance X-ray beams.

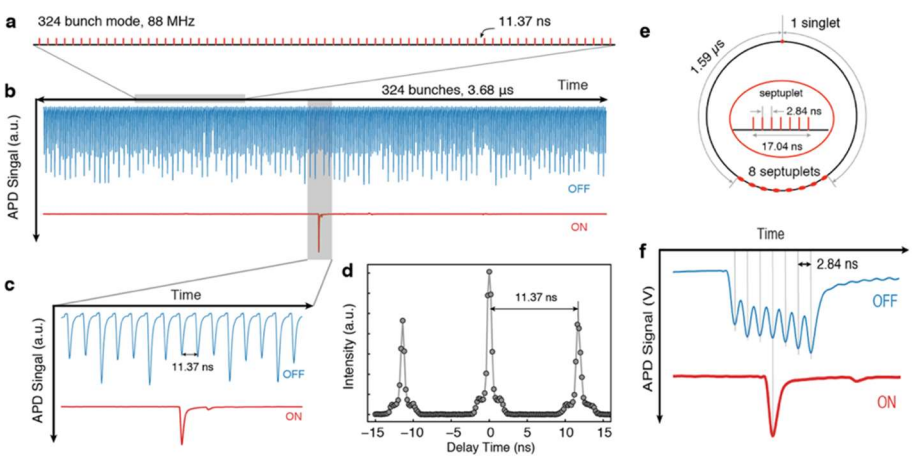

Figure 1. *Modulating X-ray pulses in the APS 324-bunch and singlet-hybrid modes using MEMS devices. a) Schematic of x-ray fill pattern in the 324-bunch mode (88 MHz frequency and 11.37-ns pulse intervals), b) 324 pulses from a complete synchrotron cycle when the device is off, and one single pulse selected when the device is on, (c) magnified view of the x-ray pulses in the vicinity of the selected pulse when the device is off and on, d) illustration of the chopper function by a delay scan of delaying the chopper timing window with respect to the synchrotron phase. The scan covers three adjacent x-ray pulses over 30 ns with a delay step of 0.2 ns, e) schematic diagram of the electron fill pattern of the hybrid-singlet mode at the APS, f) real-time X-ray response of a set of the septuplet pulses measured by a transiently digitized signal from an ultrafast APD when the MEMS-based X-ray chopper is off and on, demonstrating its ability to pick a single X-ray pulse from the 352-MHz pulse train with 2.84-ns pulse interval.*

2. *Designed and fabricated (using MEMSCAP) novel MEMS chips*

To achieve functional MEMS optics applicable to the APS/APSU, there were two design objectives to consider. The APS and APS-U have a storage-ring frequency of P0 = 271.55 kHz. Most of the previous MEMS were designed to have a resonance frequency of P0/4 and operated at P/2 or slower. There are advantages to having MEMS at higher frequencies, from P0 to 4P0, or higher – better temporal resolution and higher pulse selection duty cycles (higher output pulse frequency or flux). Therefore, the first objective is to design MEMS with such high resonance frequencies (resonance at 2P0 at 543.1 kHz and driving at 1.086 MHz) to operate above 1 MHz for the first time. The design focuses on improving mechanical driving characteristics by strengthening comb finger support, optimizing the force arm for higher torque, and

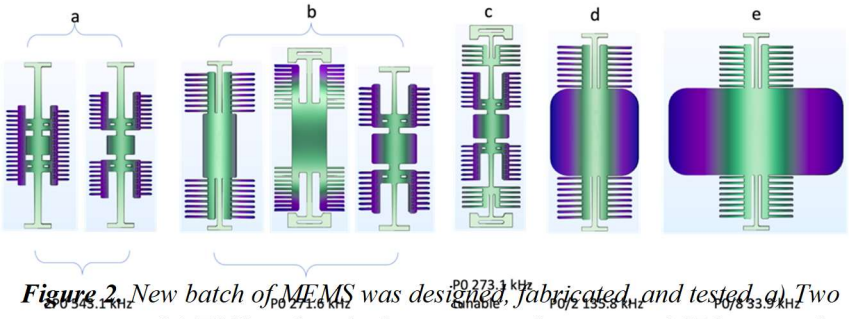

Figure 2. *New batch of MEMS was designed, fabricated, and tested. a) Two variations of MEMS with a high resonance frequency of 2P0 are to be operated at 1.086 MHz, the first time when the MEMS-based X-ray optics ran above 1 MHz, b) variation of MEMS with a high resonance frequency of P0 and to be operated at 543.1 kHz. c) a new class of P0-MEMS that can be operated in a linear regime to respond to driving signals with a broader range of frequencies, d) a medium-range MEMS with a resonance frequency of P0/2 and running at P0 271.6 kHz, optimized for diffraction beam size and pulse frequency, can be deployed to the APS-U beamlines readily after the upgrade is complete, e) 'slow' MEMS with a larger diffraction element of 250 x 500 µm^2 for large X-ray beams and synchronization to high-power lasers running at P0/4 67.8 kHz.*

increasing comb finger numbers. The second objective is to implement real-time diagnostics for feedback/feedforward control systems by implementing extra on-board circuitry for capacitive diagnostics. Last but not least is producing a set of MEMS for laser-pump X-ray probe experiments that require a large MEMS diffracting surface (millimeter scales) but a lower pulse rate limited by the laser operation. Samples of all types of the MEMS chip have been wire-bounded, tested, and proven to work. Most of the data collected in this project were from the new batches of MEMS.

X-ray Correlation Spectroscopy Using Whitebeam from the SCHU

Diffracting optics based on MEMS are suitable for tailoring X-ray timing structures in Synchrotron Radiation facilities for probing ultra-fast dynamics in materials and chemistry. However, it is impractical to synchronize the micro-scale machine with the macro-scale SR facilities through coherent feedback due to their significant disparity. Instead, we measured phase errors of a stable oscillating resonator in a precise fashion by high repetition X-ray diffraction, providing a feedback source for a closed loop realization of the two systems. Synchrotron X-ray pulses are utilized to oversample phase errors at ultra-high resolution. This is impractical without the sharp rising/falling edge of the rocking curve and high repetition of the NSLS II operation pattern. We observe an overall 0.0075-degree phase error of the system with a resolution of 0.0004 degrees. The full spectrum of the phase noise is achievable by either increasing measuring sampling rate or measuring time. This paved the way for understanding the phase noise and employing the MEMS device as a routinely operated optic-on-chip device on time-resolved X-ray beamlines at fourth-generation synchrotron light source, realized by incoherent feedback closed loop operation.

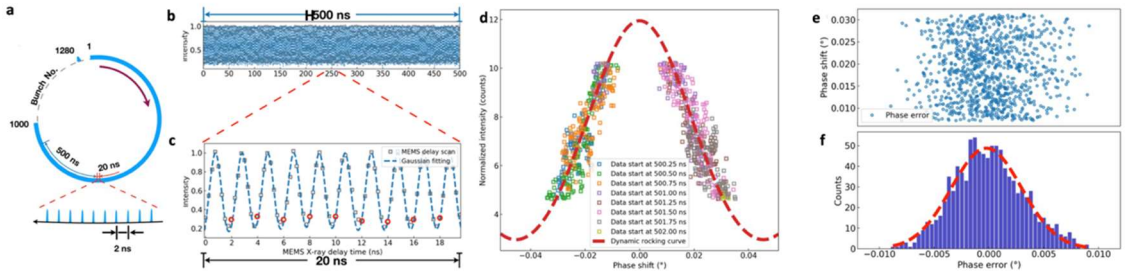

Figure 3. *Ultra-sensitive frequency and phase stability measurement by mapping diffraction time window (DTW) of MEMS using X-ray a high-frequency pulses from a synchrotron source. a) Schematic showing X-ray pulse timing structure of NSLS-II with 1000 pulses at 499.68 MHz and 2.0013-ns pulse intervals, b) DTWs of 500 ns measured from bucket # 681 to # 930 schematically indicated in the previous panel, c) magnified view of the center section of the DTW scan, d) 500-ns data is renormalized into a phase-wrapped frequency-time domain where statistics of the noise are analyzed, e) phase noise is derived from the difference between the data points and the calculated DTW. Only the points at rising/falling edges are used in the plot due to the high sensitivity at both edges, f) histogram of the phase noise shows a Gaussian distribution, where the FWHM at Δf is retrieved from the fitting, and the phase/time noise converted to time domain as 166.1 ps.*

Picosecond synchrotron pulse manipulation and slicing

X-ray pulses produced by the synchrotrons are predetermined in specific patterns and widths, limiting their operational flexibility and temporal resolution. We demonstrated an on-chip picosecond synchrotron pulse shaper that enables the delivery of sub-nm-wavelength hard X-ray pulses flexibly and efficiently at individual beamlines with the potential to go beyond the intrinsic pulse characteristics of those synchrotrons, allowing flexible X-ray manipulations including pulse picking, streaking, and slicing in the majority of synchrotrons across the globe. The pulse shaper is developed using the widely available silicon-on-insulator technology, oscillates in torsional motion at the same frequency or at harmonics of the storage ring, and manipulates X-ray pulses through the narrow Bragg peak of the crystalline silicon. Stable pulse manipulation is achieved by synchronizing the shaper and X-ray timing using electrostatic closed-loop control. Tunable shaping windows down to 40 ps are demonstrated, allowing X-ray pulse picking, streaking, and slicing in most synchrotrons. The compact, on-chip shaper offers a simple but versatile approach to boost synchrotron operating flexibility and investigate structural dynamics from condensed matter to biological systems beyond the current synchrotron-source limit, even at the new-generation low-emittance synchrotron sources.

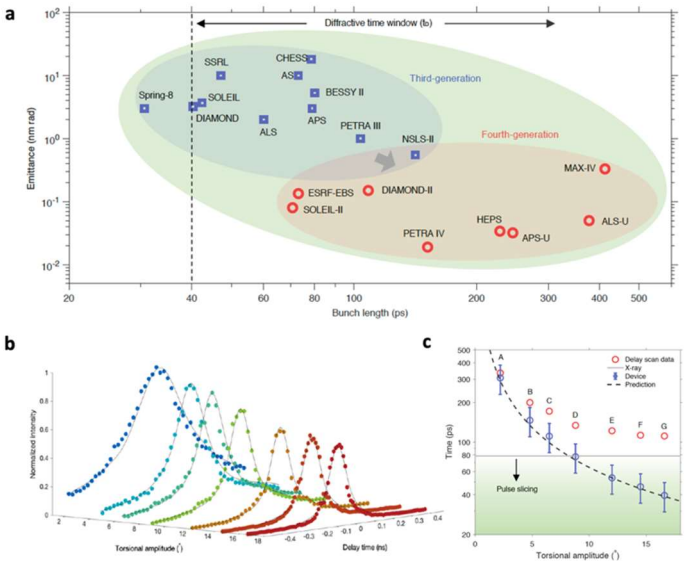

Figure 4. Performance of the on-chip picosecond synchrotron pulse shaper. a) Bunch length (FWHM) of worldwide synchrotron light sources in standard operation mode. b)The shaper allows tunable bunch picking, streaking, and shaping for the majority of light sources. Shaper dynamic rocking curves measured from the delay time scan in the APS 24-bunch mode, c) diffractive time window of the device measured from the delay time scan. The dash line shows the predictions.

Future Plans

As we achieve sub-pulse DTW width at the APS, future success depends on understanding the source of the phase noise and how to reduce it. It is also critical to take advantage of the ultrahigh-resolution determination of the phase noise and design feedback/forward theme to ensure a long-time (hours) phase-lock between the MEMS and the storage-ring RF. More specifically, we will 1) acquire the latest-generation ultra-high bandwidth lock-in amplifier for developing reliable feedback/forward MEMS operation in ultra-low phase error regime (< 0.5 millidegrees or 10s ps), 2) prepare the restart of the synchrotron-based MEMS testing experiments with the new low-emittance X-ray pulses that are essential for all advanced functions of MEMS as ultrafast and dynamic X-ray optics.

Granted Patent:

J. Wang, D.A Walko, P. Chen, I. W. Jung, D. Lopez, ULTRAFAST PHOTONIC MICRO-SYSTEMS, US Patent 11,866,322 B2, (2024).

Publications:

• P. Chen, I.W. Jung, D.A. Walko, Z. Li, Y. Gao, T. Mooney, G.K. Shenoy, D. Lopez, and J. Wang, Optics-on-a-chip for ultrafast manipulation of350-MHz hard X-ray pulses, Optics Express, **29**, 13624-13640 (2021). https://doi.org/10.1364/OE.411023

• The above publication was featured in a weekly News Release by the publisher: Tiny Chip-Based Device Performs Ultrafast Modulation of X-Rays.

• D. Walko, J. Jiang, J. Zhou, B. Guzelturk, X. Zhang, D. Czaplewski, and J. Wang, *Measuring the x-ray flux from MEMS devices for timing applications*. Paper presented at the 2022 SPIE Optics + Photonics, San Diego, CA, US, August 21, 2022 - August 25, 2022.

• J. Zhou, J. Jiang, D.A. Walko, D. Jin, D. Lopez, D.A. Czaplewski, J. Wang, *Picosecond Synchrotron Pulse Shaper on-Chip*, arXiv:2211.03567, http//arxiv.org/abs/2211.03567. (to be submitted to Nature Photonics).

• J. Jiang, P. Chen, D. Walko, and J. Wang, *Probe phase errors of a highly stable torsional resonator with pulsed X-rays*, to be submitted to Nature Microsystems & Nanoengineering.

• P. Chen, D.A. Walko, A. Fluerasu, I. W. Jung, G.K. Shenoy, D. Lopez, J. Wang, *Picking Single Hard X-ray Pulses from 500-MHz Pulse Trains*, to be submitted to Optics Express.

Applications of the Superconducting Helical Undulator at the APS

Jin Wang, X-ray Science Division, Argonne National Laboratory)

Keywords: Superconducting, helical undulator, X-ray imaging, coherent imaging, X-ray photon correlation spectroscopy

Research Project Scope

Taking advantage of the unique beam properties from the new superconducting helical undulator (SCHU) at the Advanced Photon Source (APS), we developed experimental techniques using unfiltered white X-rays for quantitative single-pulse (100-ps) imaging, coherent diffraction imaging, and optics-free x-ray photon correlation spectroscopy with unprecedented coherent flux from the APS storage-ring source. To realize the experiments at 7-ID of the APS where the SCHU was installed and none of the experiments had ever been done before, we built beamline instruments with essential hardware and necessary data processing and reconstruction tools. In this abstract, we highlight the development of novel SCHU white-beam coherent measurements in the hard X-ray regime, in the absence of X-ray optics between the source and the samples, except beam-defining slits. The results show the usefulness of the white beam from SCHU for coherence-based experiments. They should benefit the development of novel X-ray techniques for user experiments using coherence properties of the APS-U, the development of future SCHU for the APS-U storage ring, and potentially the design of SCHU-based free-electron laser sources, for example, LCLS-II-HE.

Recent Progress

Micro Cavitating Flows Probed by Ultrafast Imaging

Cavitation, a widely occurring phenomenon in multiphase fluid flows, can be detrimental in macroscopic hydraulic apparatuses due to its damaging nature. Not much is known about its impact on meso- and microscopic multiphase flows, which are widely used in industrial and technological applications but remain elusive because of the dearth of methods for interrogating their complex dynamics. We developed ultrafast x-ray near-field speckle (XNFS) imaging with 1-μm spatial and 100-ps temporal resolutions, ideally for visualizing the microscale cavitating flows emanating from high-pressure injectors that play the most crucial role in energy conversion processes for improving combustion-engine efficiency and emission (Figure 1). The ultrafast dynamics are sensitive to cavitation through the fluid pressure and, more so, its interplay with the fuel temperature. Flow dynamics characterized by the velocity coefficient can be scaled by a universal dimensionless parameter, the cavitation number, in the extended pressure and temperature range. Promoting the near-nozzle liquid jet to reach 90% of the Bernoulli velocity at high cavitation numbers, cavitation can be harnessed to elevate the conversion efficiency from pneumatic-hydraulic to kinetic energy in the mesoscopic multiphase flows. This direct and quantitative

dynamics visualization should provoke comprehensive experimental and computational work on mesoscale turbulent and cavitating flows.

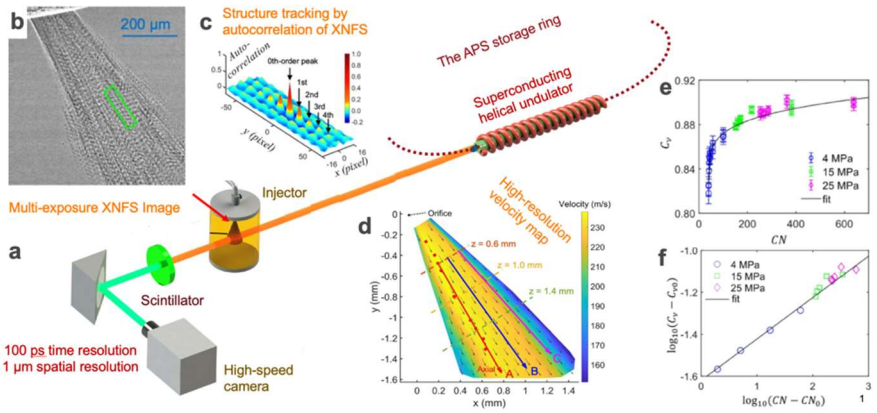

Figure 1. *Harnessing cavitation to elevate the conversion efficiency in the micro cavitation fuel jets. a) experimental setup using the whitebeams from the APS SCHU, b) a single frame multi-exposure XNFS image collected using the high-speed imaging system, c) autocorrelation calculation for evaluating the flow dynamics, d) high-resolution fuel jet velocity map with a high spatiotemporal resolution for evaluating the mean flow velocity in high turbulent jets, d) and e) velocity coefficient C_v (conversion efficiency) is perfectly scaled with cavitation number CN shown in the linear and log plots, respectively.*

Coherent diffraction imaging in small- and ultrasmall-angle scattering regime

Conventional coherent diffraction imaging (CDI) is a lensless imaging method that avoids the limitation of imperfect X-ray optics by illuminating a sample with a coherent monochromatic beam and collecting the scattered light on a detector without optics in between. Even so, beamline optics, such as mirrors, monochromators, and focusing devices, are far from perfect, the reconstruction of the sample structure can be complicated because of the imperfect incident X-ray beam. With a conventional undulator source at a storage-ring facility, it is impossible to use the white X-ray beam directly from the undulator source without any optics in between. In this work, we

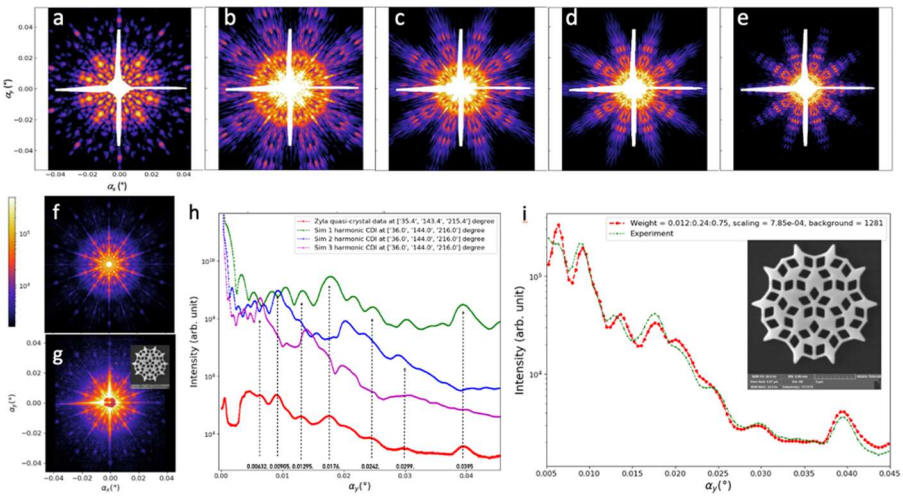

Figure 2. *Coherent scattering imaging of a meso-scaled pattern using the optics-free white beam from the SCHU. a) - e) Unscaled simulated scattering intensity patterns contributed by the first 5 harmonics, respectively, in the white-beam spectrum. f) Simulated scattering pattern using the scaled (or weighted) first 5 harmonics. g) Experimental data of the sample showing the inset. The match between the simulation and experimental patterns is remarkable. h) Linecuts from the first 3 harmonics contribute the most prominent features in the experimental data. i) Best fit of the linecuts from the simulated to the experimental data, demonstrating the quantitative agreement between the simulation and the experimental patterns.*

demonstrated the effectiveness of using the whitebeam from SCHU with no optics for CDI measurement. High-order harmonics from SCHU contribute unique features to the experimental data and provide valuable constraints for future reconstruction algorithms. We also observed that the wide bandwidth of spectra in each harmonic ($\Delta E/E > 1\%$) smears the speckle patterns, but the spatially fluctuating intensity distribution is still distinctive. The simulation and experimental patterns are more clearly illustrated in Figure 2. With the white beam from the APS SCHU at Sector 7 of the APS, we demonstrated that an unfiltered beam from the novel insertion device can be used for CDI of non-periodical mesoscale structures from 10 nm to 10 μm in small-angle and ultrasmall-angle regimes. The new technique benefits the development of novel experimental methods and instruments using APS-U's coherence properties, the development of future SCHU for current APS and APS-U, and the design of SCHU-based lasing devices for LCLS-II and LCLS-II-HE.

X-ray Correlation Spectroscopy Using Whitebeam from the SCHU

Thus far, the partially coherent X-ray beam is the foundation for X-ray Photon Correlation Spectroscopy (XPCS) to probe dynamics in equilibrium and close-to-equilibrium conditions, which are extremely dependent on a temporally stable beam. However, almost all current XPCS beamlines use X-ray optics, such as mirrors and monochromators, to condition the X-ray beam before it is delivered to the sample, inevitably introducing instability to the beam and, in turn, tempering the data quality. Using the optics-free setup with the SCHU source, we demonstrated that it is not only possible to reduce the optics-induced beam instability but also to achieve *high-quality* XPCS measurements in the small-angle scattering regime. We collected ms relaxation time constants and were confident that sub-ms resolution could be achieved using the same setup but with a faster pixel array detector. The correlation function can be perfectly fitted with a simple exponential function, as shown in Figure 3. The XPCS measurements using the SCHU whitebeam are of high quality in probing fast particle dynamics down to ms. Again, the successful XPCS setup can be used as the APSU beamline test ground for

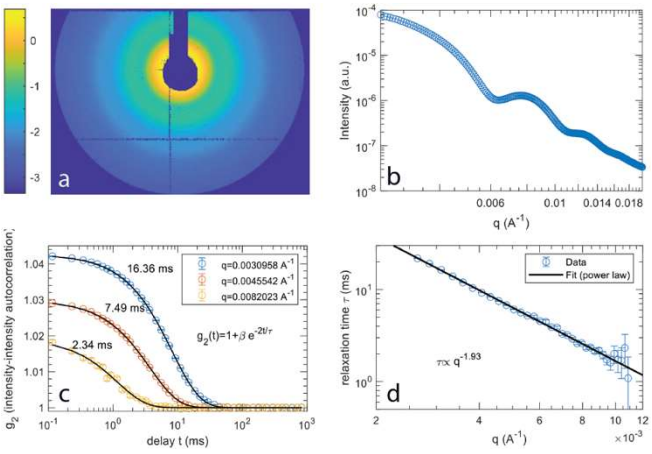

Figure 3. X-ray photon correlation spectroscopy using unfiltered whitebeam from the APS SCHU at Sector 7 beamline. a) Two-dimensional time-averaged x-ray small-angle scattering pattern, b) radially averaged SAXS curve showing the form factor of the monodispersed 150-nm gold particles in the uncorrelated suspension of t. c) intensity-intensity autocorrelation function g2 and the corresponding fitting curves as a function of delay time collected from 100 μs to 1s, over 5 orders of magnitude, at 3.1, 4.6, and 8.2 x 10^{-3} $Å^{-1}$. d) Decay of the particle dynamics relaxation time as a function of the momentum transfer, perfectly agreeing to an exponential function that closely describe Browning motion of the nanoparticle in the dilute suspension.

studying dynamics over a wide spatial and temporal range. Also, the experiment results demonstrated the need for full-size SCHU (2.5 m long) to improve the flux and energy bandwidth so that dynamics at a shorter length scale can be probed with high-contrast scattering speckles.

Grazing-incidence reflective X-ray holography

Similar to Young's double-slit experiments, Lloyd's mirror was another way to show the light's wave properties by shining a narrow but divergent beam onto a mirror so the reflection could overlap and interfere with the unperturbed light, creating a mirror-based Young's experiment. In this work, we observed the peculiar hard X-ray interference speckles from substrate-supported planar patterns in grazing incidence reflection geometry, which resembles Lloyd's mirror condition without a conventional mirror. With this optics-on-a-chip concept, we discovered that an interference image from a single view, constituting a dark-field and high-contrast hologram, is suitable for probing structures at surfaces and buried interfaces, ideally for ultrafine nanocircuit metrology. The X-ray imaging technique also paves the way for visualizing irreversible morphology-transforming physical and chemical processes in a time-resolved, in situ, and operando fashion. The activities benefit the future operation of the APSU new beamline CSSI, where coherent surface scattering in grazing-incidence geometry is one of the major capabilities that can be supported.

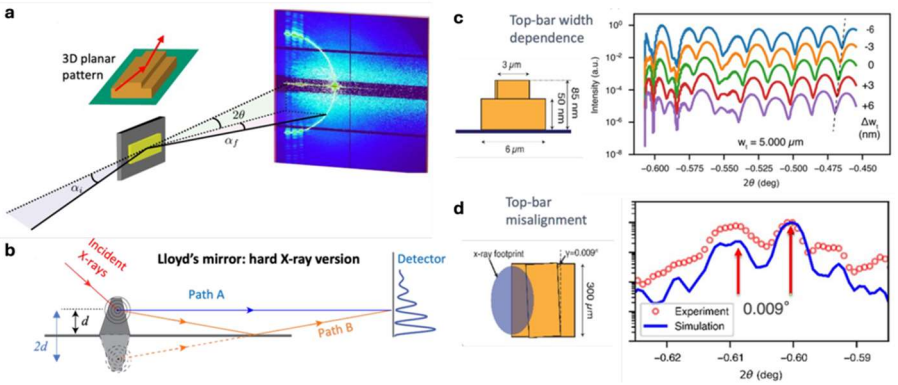

Figure 4. Hard X-ray holographic imaging of a mesoscale, substrate-supported planar surface pattern. a) GI-reflection coherent scattering from with an illustration of the substrate-supported planar but 3D patterns, b) hard X-ray scattering version of Lloyd's mirror, c) holographic analyses revealed variation of speckle patterns as a function of the top-bar width, d) orientational misalignment of 0.009° between the top and bottom bars quantitatively determined by the holographic patterns.

Future Plans

With great progress made in the project, the adverse impact of COVID-19 is significant when the minimum and limited APS operation modes did not allow exploratory experiments that required a large amount of setup effort and constant human intervention during the experiments. After the APSU, the SCHU will not be available for further experiments. Our plans are to 1) finish the computation/simulation/reconstruction of whitebeam CDI data, 2) continue the development of simulation/reconstruction of surface coherent scattering imaging data, which is also badly needed to move the project forward to achieve the reconstruction to prepare future activities using SCHU whitebeams when opportunities arise, and 3) reconstruct quasi-3D liquid morphology from quantitative phase contrast imaging using whitebeam from SCHU. We have revised the project goals accordingly.

Publications

1. Q. Zhang, Y. Gao, M. Chu, P. Chen, Q. Zhang, J. Wang, *Enhanced energy conversion efficiency promoted by cavitation in gasoline direct injection*, Energy **265** 126117 (2023).

2. M. Chu, Z. Jiang, M. Wojcik, T. Sun, M. Sprung, J. Wang, *Probing three-dimensional mesoscopic interfacial structures in a single view using multibeam X-ray coherent surface scattering and holography imaging*, Nat. Commun. **14**, 5795 (2023).

3. J. Jiang, et al., Coherent scattering imaging with optics-free whitebeam from a superconducting helical undulator, in preparation.

4. Z. Jiang, et al., Demonstrating optics-free white beam x-ray photon correlation spectroscopy, in preparation

Session Three

Detectors

Evaluation of Hi-Z Detector Materials for X-ray Science

Julia Thom-Levy, Cornell (PI), Nino Micelli, ANL (co-PI), Abdul K. Rumaiz, BNL (co-PI), Julie Segal, SLAC (co-PI)

Keywords: Hard X-ray sensors, High-Z sensors

Research Project Scope

The goal of this research project is to evaluate and develop high quantum efficiency pixelated sensors (Hi-Z sensors) for very hard X-rays (energies >20 keV) at XFELs and storage rings, using mature and representative detector readout ASICs and testing platforms. The deliverable is a Project Summary Report that includes recommendations to guide future DOE and partner laboratory investments in Hi-Z detector materials.

The Hi-Z collaboration, consisting of detector groups at Cornell, ANL, BNL, SLAC and Northwestern University have embarked on a program of development and evaluation of promising candidate sensor materials. The work builds on advances during the previous grant period.

The following elements of scope are to be completed in collaboration between the partner labs and Universities:
(1) evaluating advanced processing techniques for Germanium,
(2) Cadmium Zinc Telluride (CZT), sensor evaluation.
(3) crystal growing, processing, thin films, and testing of the Perovskite $CsPbBr_3$. (CLB) sensors.

In addition, and as it is possible, we will continue the evaluation of other new and emerging Hi-Z sensors materials. The elements of the work include fabrication and procurement of Hi-Z sensor layers for use in hybrid pixel array detector prototypes, using SLAC's ePix10k and Cornell University's MM-PAD, to more fully evaluate sensors. Tests are done under standard procedures and mutually agreed metrics, with in-lab evaluations to establish operability. In-lab evaluations will be followed by collaborative tests involving members at LCLS-II, APS, NSLS-II, and CHESS to compare performance characteristics in representative DOE science XFEL and diffraction-limited storage ring environments.

Recent Progress

The Hi-Z collaboration has advanced processing methods of the target sensor materials and bonding to ASICs. Cornell has coordinated the effort, provided the MM-PAD ASICs and test platforms, and done much of the evaluation of the sensors:

- BNL and MIT-LL collaborators have developed Ge sensor process and bonding techniques for fine pitch pixels and bonded two sensors to an MM-PAD ASIC. However, bonding failures still occur upon thermal cycling; further R&D on bonding is on-going.

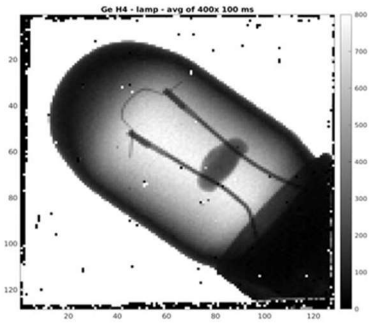

(left) MM-PADs with thin Ge Pixel size: 150µm, 128x128
(right) Radiograph of a light bulb taken with an Ag X-ray tube

- SLAC has developed a microwave anneal technique and is in the process of fabricating sensors, in partnership with BNL.
- High-flux CZT pixelated to BNL specification and tested for quality by Redlen has been procured by BNL, and low temperature CZT bump-bonding processes have been developed at BNL and SLAC.

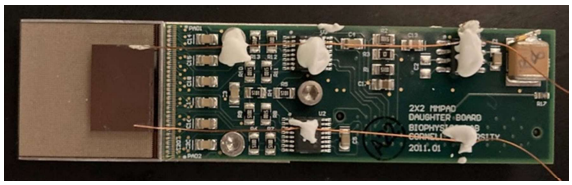

Redlen CZT bonded to an MM-PAD at BNL

- The Kanatzidis group at Northwestern University, in partnership with ANL, has grown CLB crystals in the lab. Single pixel sensors are linear and stable under synchrotron X-rays flux, and a first pixelated sensor has been bonded to an MM-PAD. Testing is scheduled.
- SLAC is investigating thin film deposition of Perovskite on ePix10k.
- The Hi-Z collaboration has also investigated processing of a-Se, and other materials.

Testing of assemblies is ongoing:

- First tests of Redlen “hi-flux” CZT bonded to MM-PADs using an in-lab x-ray sources at Cornell have shown that the polarization behavior is improved compared to standard CZT and CdTe. However, we also have observed a lag in signal response which would limit usefulness for fast framing applications. An investigation into IR illumination of CZT is underway, as IR illumination increases the speed of response to X-ray exposure by creating a steady state defect occupation.
- First lab tests of CLB. Bonded to an MM-PAD revealed promising results, however metal contacts seem to degrade the material and more work is needed before drawing further conclusions.

Future Plans

Future plans include the following elements:

- High-flux testing of CZT bonded to MM-PAD, either at CHESS or ANL, to investigate flux dependence of charge collection efficiency, polarization, and signal lag time.
- Further development of metal contacts and passivation layers on CLB, to allow for stable operation. This is to be followed by lab and high-flux testing, including to CLB bonded to MM-PAD ASICs.
- Tests of Ge and CZT bonded to ePix10k at LCLS
- Continued evaluation of Ge bonding to MM-PAD ASICs.

Publications (partial list)

1. Z. Han, A. Mukherjee, A. Albert, A.K. Rumaiz, I. Harding, M.W. Tate, S.M. Gruner, J.Thom-Levy, A.J. Kuczewski, D.P. Siddons, G.A. Carini, J. Stavro, S. Léveillé, D. Vasileska, W. Zhao, and A. Goldan, *High spatial resolution direct conversion amorphous selenium X-ray detectors with monolithically integrated CMOS readout* J. Inst **18** P04021 (2023)

2. Stephanie H. Bennett, Joydip Ghosh, Eric Gros-Daillon, Ferdinand Lédée, Javier Mayén Guillén, Jean-Marie Verilhac, Julien Zaccaro, Duck Young Chung, Vladislav Klepov, Mercouri G. Kanatzidis and Paul J. Sellin "*Charge Transport Comparison of FA, MA and Cs Lead Halide Perovskite Single Crystals for Radiation Detection*" *Front. Detect. Sci. Technol. - Materials for Detectors* ***1*****,** 01-12. (2023)

3. Michael C. De Siena, Vladislav V. Klepov, Sergei P. Stepanoff, Khasim Saheb Bayikadi, Lei Pan, Indra R. Pandey, Sujita Karki, Duck Young Chung, Douglas E. Wolfe, and Mercouri G. Kanatzidis "*Extreme γ-Ray Radiation Tolerance of Spectrometer-Grade $CsPbBr_3$ Perovskite Detectors*" *Adv. Func. Mater.* 2303244. (2023)

4. Lei Pan, Indra Pandey, Zhifu Liu, John A. Peters, Duck Young Chung, Bruce W. Wessels, Antonino Miceli, and Mercouri G. Kanatzidis "*Study of Perovskite $CsPbBr_3$ Detector Polarization with Ultra-high X-ray Flux*" *J. Appl. Phys.* ***133*****,** 194502 (2023)

5. Vladislav V. Klepov, Michael C. De Siena, Indra R. Pandey, Lei Pan, Serkan Butun, Duck Young Chung, and Mercouri G. Kanatzidis *"Laser Scribing for Electrode Patterning of Perovskite Spectrometer-Grade $CsPbBr_3$ Gamma-ray Detectors" ACS Appl. Mater. Inter.* ***15*****,** 16895-16901 (2023)

6. Lei Pan, Indra Pandey, Antonino Miceli, Vladislav Klepov, Duck Young Chung, Mercouri G. Kanatzidis "*Perovskite $CsPbBr_3$ Single-Crystal Detector Operating at 10^{10} Photons s^{-1} mm^{-2} Ultra-High Flux X-ray Detection*" Adv. Opt. Mater. **11**, 2202946. (2023)

7. Lei Pan, Zhifu Liu, Claire Welton, Vladislav Klepov, John A. Peters, Michael De Siena, Alessandro Benadia, Indra Pandey, Antonino Miceli, Duck Young Chung, G. N. Manjunatha Reddy, Bruce W. Wessels, and Mercouri G. Kanatzidis "*Ultra-High Flux X-ray Detection by Solution-Grown Perovskite $CsPbBr_3$ Single Semiconductor detector*" *Adv. Mater.* 2211840 (2023).

SparkPix-RT: An edge computing engine for ultra-fast photon science detectors

Angelo Dragone [1] (PI), Antonino Miceli [2] (Co-PI), Jana Thayer [1] (Co-PI) [1]SLAC National Accelerator Laboratory, [2]Argonne National Accelerator Laboratory

Keywords: Pixel array detectors, ASIC, compression, edge computing

Research Project Scope This project aims to pursue new approaches to reduce the data size by performing data compression directly on a detector ASIC in a streaming manner before sending it off-chip. In this manner, we will make the most efficient use of the off-chip bandwidth and thus maximize detector frame rates. This proposal aims to demonstrate an edge-computing engine for SparkPix at the rate of at least 100 kHz that could enable on-chip data compression as a pathway to overcome the I/O bottleneck and extend SparkPix's applicability to high occupancy experiments. The multidisciplinary project team is composed of participants from ANL and SLAC. Originally, we had planned for 2 ASIC 48x48 MPW tapeouts, but given the success of the first MPW tapeout (RT1), we have decided that the second tapeout would be an engineering run which would produce a science-grade ASIC consisting of 192x168 pixels (RT2).

Recent Progress

RT1 ASIC

The analog pixel matrix of the prototype 130nm CMOS SparkPix-RT ASIC has been adapted from ePixUHR. The pixel comprises a charge-integrating front-end with a synchronous readout that was developed for FEL applications. A cluster is comprised of 72 pixels (in an array of 6 columns by 12 rows) and a per-cluster Analog-to-Digital Converter (ADC) with a 12-bit resolution and an 8 MSPS operating frequency which converts the analog values to digital. Using the existing approach, the pixel array can achieve frame rates of up to 100 kHz. The size of the pixel matrix of the RT1 ASIC is 48 x 48 on a 100-micron pixel pitch. Pixel data from each column of four 72-pixel clusters passes through a compressor block which reduces the number of bits which need to be transmitted. Since the data transmission rate for the entire detector is limited by the compressor block achieving the lowest compression ratio, it is critical that the output data from the compressors are distributed evenly across all the parallel transmitters. Thus, we have designed a readout to efficiently handle the variable data from the stream of parallel compressors. Each compressor generates fixed-size words at a rate that depends on the compressibility of the data. These streams of data words from each compressor are combined before passing them to the transmitters in order to evenly distribute the data across them. To optimize the use of the repeating structure of the compressor core, a hierarchical design methodology was employed for the digital readout implementation. Alongside the compressor logic, a significant portion of the compressor core's area was allocated to the FIFO SRAM and Dark SRAM. After evaluating the size and orientation of the SRAM, the Dual Compressor partition block was designed to optimize the silicon area. This block incorporates two compressor cores, which interface with two 72-pixel clusters.

At the heart of the digital readout is a compressor core [1]. It is a lightweight and customizable digital compressor core that significantly reduces the amount of data that must be transmitted. The compressor employs a form of zero-suppression that dynamically adjusts the bit-width of pixels, utilizing the minimum number of bits required to represent them. The compressor identifies leading zero bits in neighboring groups of pixels and adjusts the number of bits required to represent those pixels while simultaneously incorporating metadata that allows accurate reconstruction of the original pixel values at the receiver. This compression method is lossless, as the original data can be fully reconstructed. In addition, this lossless compression technique can be combined with user-configured lossy techniques, which can further enhance the compression results. The design can handle the variable data from the parallel compressor stream and transmit it via constant-rate high-speed serial links off-chip. For RT1, we assumed that the detector will operate in a single gain range so that no gain bits need to be transmitted. RT2 adds support for gain switching.

Detector noise can impede efficient data compression. To maximize the number of zeros in the digital pixel values presented to the compressor, a dark image is computed and stored in a Dark SRAM prior to capturing pixel data. As pixel data streams from the pixel matrix, corresponding dark values are read from the Dark SRAM and subtracted from the sampled pixel values. This allows a threshold value to be removed from the image and maximizes the compression. Designed into the readout logic is a user-enabled algorithm which will automatically compute and populate Dark SRAM values for the user based on multiple dark frames. The algorithm is designed so that the resulting dark image is certain to eliminate any background noise by computing the mean of each pixel and adding a multiple of the standard deviation of the background value. If this is too aggressive for some applications, a user generated dark image can be uploaded to the detector instead.

In the readout, each of the eight compressor modules writes data to a Cadence ChipWare FIFO IP Block (Asymmetric I/O Synchronous Dual-Clock FIFO Controller). For storage, each FIFO utilizes a 256-word x 49-bit SRAM that Synopsys Embed-It Integrator generates. Embed-It creates a TSMC 130nm physical layout of the SRAM as well as a Verilog behavioral simulation model for the SRAM automatically. Each FIFO SRAM occupies approximately 660um x 320um. The device's FIFOs can store about 3.5 frames of uncompressed pixel data in total. Additionally, each compressor connects to a 288-word x 12-bit dual-port SRAM that holds dark images. The Dark SRAM is slightly less than half the size of the compressor FIFO SRAM and can be read and written via the on-chip system AXI bus. Together, all the FIFO SRAMs and Dark SRAMs cover roughly half of the digital readout chip area.

Each of the two transmit lanes consists of a small FIFO to compensate for clock skew, a standard 12b14b encoder, and a 1.114 Gbps serializer. Two transmit lanes per prototype ASIC provide enough bandwidth to send uncompressed pixel data at slightly less than a 70 kHz frame rate. 100 kHz frame rates can be achieved with a very modest 1.5 average compression ratio. We anticipate

typical compression ratios to be in the range of 2x-30x [1]. The actual compression achievable is dependent on many factors including the pixel data captured and the quality of the dark image which has been programmed to subtract noise.

RT1 was submitted in May 2023 and received in August 2023. Bare ASICs were on wire bonded to carrier boards in September 2023 and shortly after communication to slow control was established. The bare ASIC testing is largely complete. We are currently waiting for silicon sensor bonding to ASICs. Screen video capture of various tests can be found here: https://anl.box.com/s/g7lewp6u7fyoaj5rqxcy6gq4qkrilxft Below we list the major bare ASICs tests and accomplishments:

- Running at full 35 kHz (uncompressed)
- Running at 100 kHz (compressed) with various patterned sources from SRAM.
- Load binary pattern (SLAC/ANL) into analog pixel matrix (charge injection or ADC calib mode), dark SRAM=0 and turn on/off lossless compression
- Load dark SRAM with logos with grayscale and turn on/off lossless compression.
    - Try with other patterns (diagonal, donut, etc, csv files)
    - Turn on lossy compressions (Poisson & div2) one column at a time.

RT2 ASIC

RT2 increases the size of the pixel matrix from 8-pixel cluster columns of 4 clusters each to 32 pixel cluster columns of 14 clusters each. This increases the total pixel array from 48x48 pixels to 192x168, the same as ePixUHR. This requires 32 compressors and an increase in the number of high-speed serial transmitters from 2 to 16. The main design challenge is that the FIFO and Dark SRAMs must be scaled up in size, occupying more area. This has been accommodated by increasing the balcony area slightly in the vertical direction.

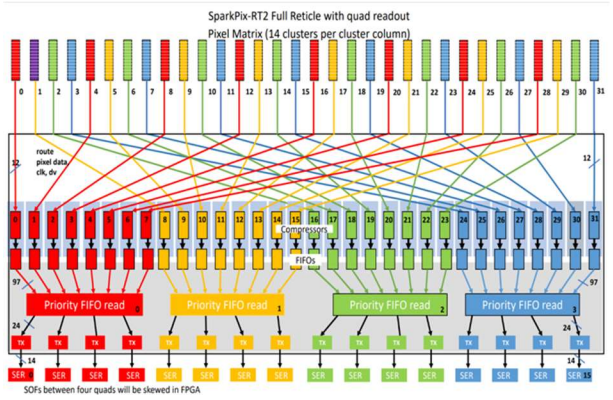

Figure 1: Block diagram of entire RT2 digital readout.

The implementation of the RT2 compressors and priority FIFO read circuits closely follow the RT1 prototype design. As shown in the Figure 1, to process 4 times as many pixel cluster columns as RT1, RT2 implements the equivalent of 4 RT1 compressor groups (shown as red, yellow, green, and blue).

To better distribute the pixel values originating in adjacent columns across different compressors and high-speed transmitters, the paths from the pixel columns to the compressors are interleaved as shown by the colored paths. This allows any localized image which spans adjacent columns to be evenly spread across high-speed transmitter groups instead of all going through the same compressor and transmitters. The interleaving operation is easily dis-interleaved in the

decompressor module inside the receiving FPGA. This interleaving operation is implemented at almost negligible digital logic expense since it is mainly a wire routing operation.

Building on the success and learning of the RT1 prototype, additional compressor enhancements were identified and designed into RT2. The RT2 design was frozen April 1, 2024 and verification (simulations, emulations and mixed-signal) will continue until tapeout in July 2024. Detailed blocked diagrams of the compression related blocks are show in figure 2. A partial list of enhancements designed into RT2 include:

- support for per-pixel gain switching including auto-dark threshold generation
- digital multiplication and division operations to support photonization on either global or pix-pixel basis (PRE_PROCESSING_PER_PIXEL)
- temporal summing (SUM_FRAMES)
- sending difference images (delta's) (OM_TEMPORAL)
- even/odd frame dark correction (PING_PONG_EVEN/ODD/AUTO)
- user-selectable sigma for auto-dark/threshold (conf_dark_sigmas)
- Test pattern generation using two separate programmable images stored in SRAM
- Improvement of slow control to compressors
- Improved performance of dropped frames during FIFO overflow events.
- Optional sending of end-of-frame (EOF) control words

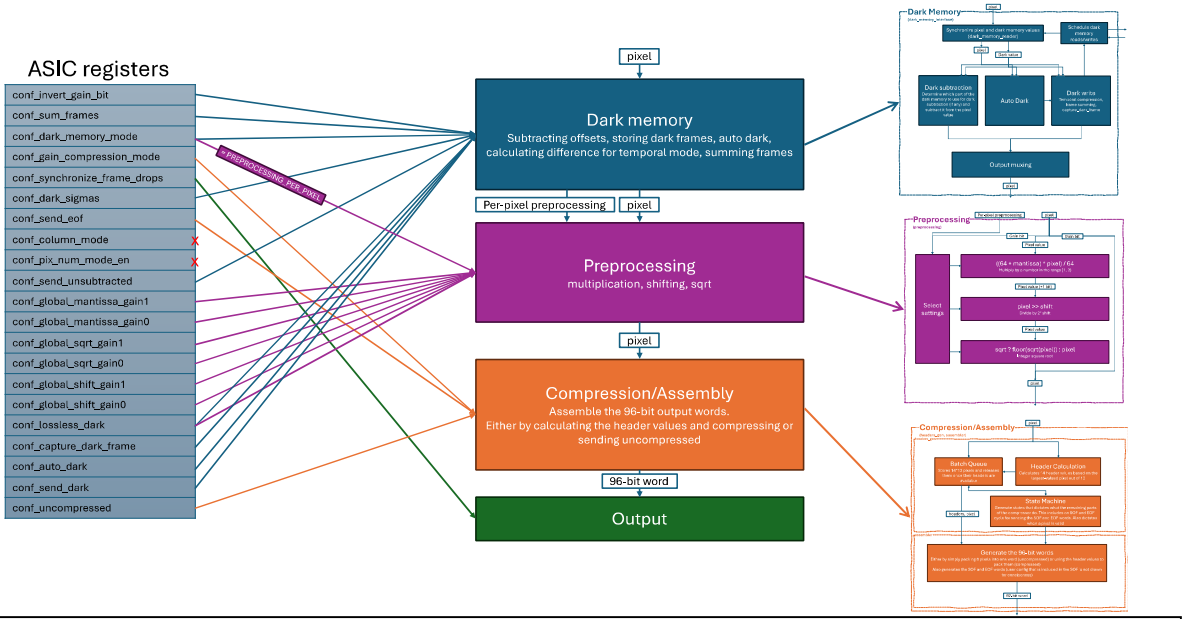

Figure 2: Detailed block diagram of main compressor blocks and corresponding AXI control registers.

Future Plans

The RT2 tapeout is funded 50% from this project and 50% from facility funds. We expect to finish the RT2 detector integration using facility operating funds.

Publications

1. S. Strempfer, T. Zhou, K. Yoshii, M. Hammer, A. Babu, D. Bycul, J. Weizeorick, M J. Cherukara, A. Miceli, A lightweight, user-configurable detector ASIC digital architecture with on-chip data compression for MHz X-ray coherent diffraction imaging, Journals of Instrumentation, 17 **P10042** (2022)
2. M. P. Hammer, A. Gupta, H. Shi, S. Strempfer, L. Rota, P. King, J. Weizeorick, K. Yoshii, T. Zhou, A. Pena-Perez, B. Markovic, D. Doering, J. Thayer, A. Dragone, A. Miceli, *Design of the digital readout of the prototype SparkPix-RT ASIC with variable data velocity*, IEEE Nuclear Science Symposium, (NSS MIC RTSD), (2023)
3. A. Gupta, M. P. Hammer , H. Shi, S. Strempfer, L. Rota, P. King, J. Weizeorick, K. Yoshii, T. Zhou, A. Pena-Perez, B. Markovic, D. Doering, J. Thayer, A. Dragone, A. Miceli, *SparkPix-RT: An ASIC for X-ray imaging using on-chip data compression techniques*, IEEE Nuclear Science Symposium, (NSS MIC RTSD), (2023)

Germanium drift detector for synchrotron sciences

Abdul K. Rumaiz, Physicist, Brookhaven National Laboratory

Keywords: Drift detector, germanium, spectroscopy, synchrotron detectors

Research Project Scope

In X-ray fluorescence spectroscopy, achieving high energy resolution is paramount for distinguishing closely spaced fluorescence lines within complex spectra. While broadening of lines occurs due to statistical factors like Fano noise stemming from electron-hole pairs production, minimizing Equivalent Noise Charge (ENC), which is proportional to the total capacitance at the preamplifier input, is crucial. Efforts to reduce pixel capacitance led to the development of the Silicon Drift Detector (SDD) by Pavel Rehak and Emilio Gatti at BNL [1]. SDDs have found successful applications in spectroscopy beamlines at synchrotrons, electron microscopes, handheld devices, and more. However, silicon becomes X-ray transparent at high energies, posing a challenge for high-energy fluorescence experiments. To overcome this obstacle, we propose the fabrication of a germanium (Ge) drift detector (GDD), a concept that has been attempted but has not yet been realized. The GDD design would incorporate trenches to separate the drift rings and the anode. This single-channel system would utilize commercial low-noise preamplifiers for readout. Recognizing the Department of Energy's (DOE) identification of high-Z sensors as a critical necessity, we note that current efforts have primarily focused on imaging applications, with limited attention to spectroscopy requirements at high energies. We expect that the development of a GDD could fill this crucial gap. In theory, germanium offers the potential for a higher signal-to-noise ratio compared to silicon and could be applied in soft and tender X-ray ranges as well.

Recent Progress

We have successfully fabricated the first planar Ge drift detector (GDD), using amorphous Ge n+ contact (figure 1a). GDD was readout with commercial low-noise charge sensitive pre-amplifier as shown in figure 1b and c [2]. The entire detector was assembled using a small footprint Stirling cryostat as shown in figure 2a. Initial Fe^{55} response shows promising results (figure 2b).

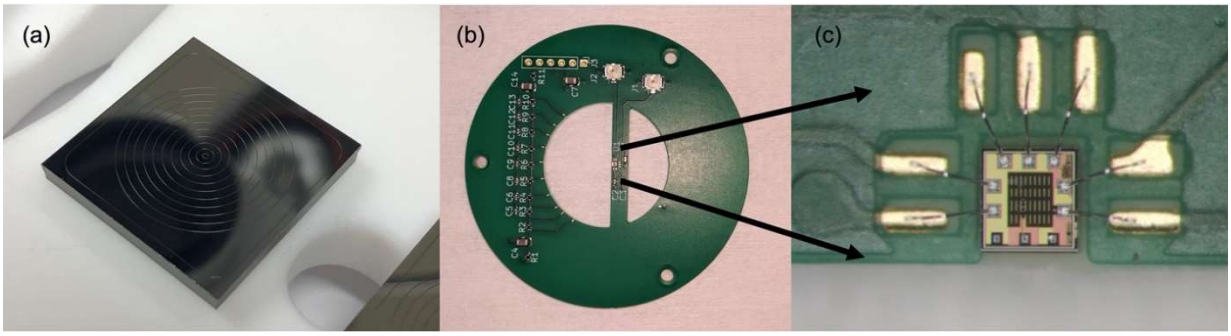

Figure 1: a. Planar GDD b. Read-out board c. zoom of the Cube low noise charge sensitive pre-amplifier

Additionally, we built a 7-channel Ge diode array readout with low-noise charge sensitive pre-amplifier. This detector was developed concurrently with our GDD sensor fabrication effort and served as an integral component of our readout electronics development initiative. Results from the detectors were recently presented at the IEEE NSS MIC conference.

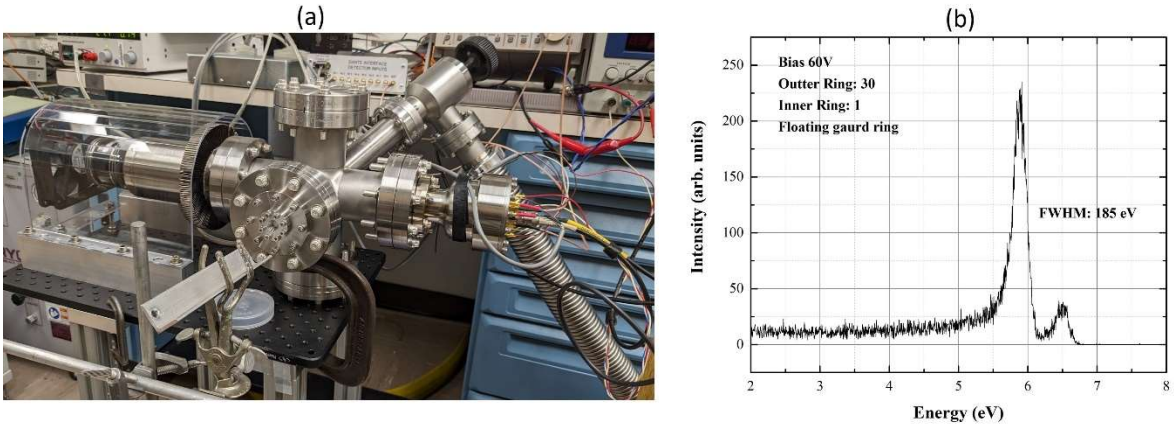

Figure 2: a. Full system GDD b. Fe^{55}response

Future Plans

We are performing voltage optimization of the bias rings to improve the energy resolution. A new readout board with individual control of the bias ring voltage is currently being designed. Based on the cryogenic testing of the sensor and TCAD simulations, we have concluded for optimal drift field we need deeper bias ring isolation trenches. We have started working on a new sensor with deeper trenches. Furthermore, we have an upcoming Extended X-ray Absorption Fine Structure (EXAFS) beamtime to test the 7-channel Ge detector.

References

1. E. Gatti and P. Rehak, *Semiconductor ion chamber-An application of a novel charge transport scheme*, NIM, **225**, 608, (1984).
2. L. Bombelli, C. Fiorini, T. Frizzi, R. Alberti, and A. Longoni, *"CUBE", A low-noise CMOS preamplifier as alternative to JFET front-end for high-count rate spectroscopy*, in Proc. IEEE Nuclear Science Symp. Conf. Rec., 2011, pp. N40–5.

Publications

1. A.K. Rumaiz, C. Weiland, I. Harding, N.S. Nooman, T. Krings, E.L. Hull, G. Giacomini, W. Chen, E. Cokayne, D.P Siddons, and J.C Woicik, *Interface formation and Schottky barrier height for Y, Nb, Au, and Pt on Ge as determined by hard x-ray photoelectron spectroscopy*, AIP Advances, **13**, 015305 (2023)

2. A.K.Rumaiz, A. Kuczewski, S. LaMarra, G. Giacomini, T. Kring and D.P. Siddons, *Development of 7-channel germanium detector for X-ray absorption fine structure*, IEEE Nuclear Science Symposium, Medical Imaging Conference and International Symposium on Room-Temperature Semiconductor Detectors (NSS MIC RTSD) 2023

Timepix Detectors for Soft X-ray Photon Correlation Spectroscopy

Sujoy Roy [1], Anton Tremsin [2], Yi-De Chuang [1], Sophie Morley [1], Steve Kevan [1]
1. Advanced Light Source, Lawrence Berkeley National Lab
2. Space Sciences Laboratory, University of California, Berkeley

Collaborators:

LBNL: Ahmad Us Saleheen (postdoc), Alexander Hexemer, Andreas Scholl, Peter Fischer
University of Kentucky: Margaret McCarter (Postdoc), Todd Hastings, Lance de Long
Argonne National Lab: Justin Woods
SLAC: Josh Turner, Georgi Dakovski
Univ of California San Diego: Eric Fullerton, Sergio Montoya
Univ. California Berkeley: Frances Hellman, T.L. Curtis, D. Tercero, J.V. Vallerga, J.B. McPhate
Techne Instruments: R. Raffanti

Keywords: Photon counting detectors, High dynamic range, Coherent soft X-ray scattering, X-ray Photon Correlation Spectroscopy

Research Project Scope

Studies of spontaneous nanoscale motion using X-ray Photon Correlation Spectroscopy (XPCS) will benefit markedly from diffraction limited storage ring and X-ray Free Electron Laser (FEL). An essential component for a successful nanosecond time scale XPCS is availability of a soft X-ray (250 eV-1 keV) pixelated, event-counting detector with high quantum efficiency that determines the spatial position (X and Y) and time stamps the arrival time (t) of each scattered photon with a temporal resolution in the nanosecond time scale. XPCS is fundamentally a "probe-probe" technique, in which coherent X-ray photons are scattered from a dynamical system and the time delay between the arrival times at the detector of pairs of photons in a single speckle is measured, binned, and normalized. Previously we have fabricated a flange-mounted Microchannel Plate detector with a quad Timepix3 readout. In this renewal proposal we proposed to fabricate an in-vaccum Timepix3 based detector that achieves the above-noted requirements and will be suitable for deployment on existing soft x-ray instruments at ALS, ALSU, and LCLS-2. This proposed detector will be based on the 2x2 array of Timepix3 Readout Specific Integrated Circuit (ROIC) developed by the Medipix consortium hosted by CERN. The Timepix3 chip provides 1.56 ns time resolution in 55 microns pixels and can be synced to the ALS 500 MHz RF system. The Timepix3 2x2 array readout chips will be combined with a Microchannel Plate electron amplifier and a KBr photocathode to achieve single photon sensitivity for soft X-rays. The detector will be packaged and mounted on a UHV compatible soft X-ray diffractometer. We will also establish pipelines to handle the large datasets that Timepix3 generate and develop software to analyze single photon correlation curves. With the successful completion of this detector project, we will have groundbreaking capabilities for XPCS using SR and high rep rate FEL sources. We envision

that the current effort will also lead to detectors based on future generations of Timepix chips (in particular Timepix4 ROIC with sub-ns timing resolution capability).

Recent Progress

Technical Achievements

- Timepix 3 Flange mount detector is completed and installed at the Cosmic Scattering endstation. We have taken the first coherent X-ray magnetic scattering data and also obtained timestamped data.
- Based on our earlier development [1,2], current project involves development of in-vacuum movable detector. In-vacuum detector housing and mounting have been designed and are in the manufacturing stage (see Fig. 1).
- The challenge of transferring high speed signals (640 MHz over 32 data lines) out of high vacuum is addressed by developing multiple approaches for custom cable/feedthrough configurations. We are working with multiple suppliers/vendors various technologies have been considered/evaluated/tested. The selection of the best technology has been accomplished.
- Synchronization/time-tagging relative to the external trigger signal (synchrotron ring trigger) is enabled to a 1 ns accuracy.
- Detector operation is being optimized to XPCS experiments, both in data acquisition software and in the detector hardware to provide required uninterrupted data flow of photon events for XPCS analysis.
- Active tuning of high-speed signal receivers is implemented on the FPGA. All 8 high speed channels per Timepix3 ROIC (32 per detector) can be configured for the best transmission of the measured photon hits on the detector.
- Optimization of power generated by the detector (Timepix3 readout) is ongoing by finding the compromise between detector resolution and power consumed by the ROIC. Heat extraction (not cooling, room temperature operation is fine) is optimized for in-vacuum mounting on the rotation arm.

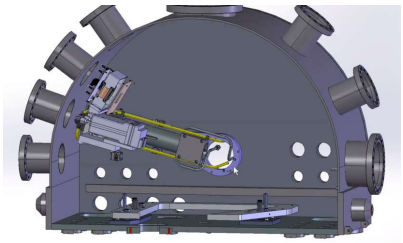

Fig. 1: MCP/Timepix3 detector mounting configuration on a rotatable arm. The detector signals will transferred out of vacuum through a custom set of cables and a ceramic feedthrough welded to a conflat flange.

Scientific Achievements

- We have recently conducted our first experiment with the TimePix3 detector, installed at the Cosmic scattering endstation . The scientific objective of the experiment was to capture the dynamic behavior of domains in an amorphous $Fe_{0.53}Ge_{0.47}$ thin-film sample near phase transition [3]. At low temperatures, this sample is populated with labyrinthine or maze-like domains, which create a resonant X-ray scattering signal as shown in Fig. 2(a), when the incident X-ray energy was

tuned to Fe L_3 edge (707 eV). Due to the coherent nature of incoming X-ray beam at the Cosmic beamline, the diffracted beam has a grainy diffraction pattern, which is known as the speckle pattern (Fig. 2(a)). A change in the speckle pattern over time can be tracked by XPCS [4]. Conventionally, XPCS measurements are conducted by capturing a series of images, and calculating the intensity-intensity autocorrelation function. As an alternative approach that can capture a faster time dynamic, we calculate the autocorrelation function from the photon arrival times of individual photons. This is similar to the technique used in Florescence Correlation Spectroscopy (FCS) [5]. However, it is essential to have a detector such as TimePix3 that can record the individual photon arrival time as well as its pixel coordinates. The photon arrival times up to a few seconds for the ROI shown in Fig. 2(a) is shown in Fig. 2(b).

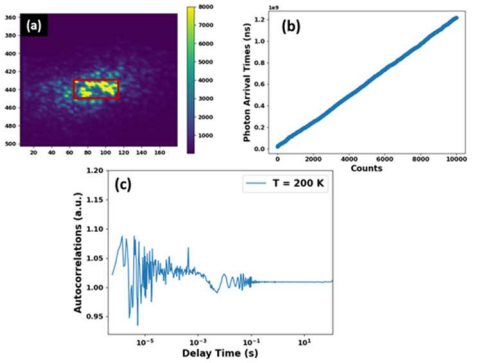

Fig. 2: (a) Magnetic scattering signal from an amorphous FeGe thin film sample captured with TimePix3. The red rectangle represents a region of interest (ROI) for which autocorrelation function was calculated. (b) Photon arrival times in ns. (c) Autocorrelations as a function of delay time calculated for the ROI shown in (a).

- In order to calculate the autocorrelation function, we developed a code written in Python programming language, where the correlation function is calculated using 'PyCorrelate' package[6]. Essentially, the algorithm used for the calculation performs a counting operation where we estimate the probability of detecting a photon at some time t+τ, if there was a photon detected at time t. Here τ is the delay time. In other words, the algorithm calculates how many photon pairs there are at each delay time. Fig. 2(c) shows such a normalized autocorrelation curve plotted as a function of delay time. The curve in Fig. 2(c) remains very close to 1, indicating a lack of correlation or dynamic behavior. This is to be expected since the domains at this low temperature are not supposed to fluctuate due to a lack of thermal energy. The oscillatory behavior in the millisecond regime is most probably due to a vibration present in the beamline. We are in the process of measuring and analyzing data at higher temperatures near the phase transition, which we expect to show more pronounced signature of sample dynamic.
- In parallel we have been also developing multimodal capabilities that will explicitly take advantage of the timing capabilities of TpX3. We have developed a multimodal transport and scattering measurement setup that will enable us to measure simultaneously scattering and transport data. We have done the first measurement suing this setup using commercially available CCDs. Fig. 3 shows a picture of the transport probe that we have already used to measure transport properties, such as magnetoresistance, Hall effect, etc. down to liquid Nitrogen temperatures. When used in conjunction with the TimePix3 detector, it can open up new opportunities to investigate various current induced dynamic behavior, such as the current induced domain wall motion, Skyrmion motion, and so on.

Fig. 3. A probe capable of measuring various transport properties with provisions for cryogenic cooling.

Future Plans

In the coming year our R&D will focus on two different topics.

1. Design and fabrication of the in-vacuum MCP/Tpx3 detector and high-speed signal vacuum interface. Although the team has gained valuable experience and understanding of the Tpx3 detector during Phase 1 research, significant challenges show up in case of in-vacuum Tpx3 detector mounting on a rotatable arm. Two of the major hurdles are to get high speed signals out from inside vacuum to outside data processing electronics, and the managing the heat extraction. These challenges require novel engineering solutions. Therefore, we are focusing on these two major hardware issues and verifying the high-speed detector operation for long signal lines with a custom ceramic vacuum feedthrough. In addition, optimization of data acquisition firmware and software are still ongoing in order to provide the maximum data throughput and best resolution.

2. Scientific commissioning of Tpx3: The scientific commission of the flange mount Tpx3 will be our scientific focus. We plan to perform at least two experiments on photon correlation spectroscopy studies of magnetic and correlated system. One such experiment involves the investigation of dynamic behavior near phase transition temperature in an amorphous FeGe thin film. Another possible experiment would be to investigate field induced fluctuation or instability in the Skyrmion lattice phase of a 2D magnetic system. We will also seek out new timing experiments that the detector will enable, such as, sending current pulse and measuring correlation spectroscopy.

References

1. A.S. Tremsin, J.V. Vallerga, Radiation Measurements, **130**, 106228 (2020).
2. A.S. Tremsin, J.V. Vallerga, O.H.W. Siegmund, J. Woods, L.E. De Long, J.T. Hastings, R.J. Koch, S.A. Morley, Yi-De Chuang, S. Roy, J. Synchrotron Rad. **28**, 1069 (2021)
3. Arnab Singh, Emily Hollingworth, Sophie A. Morley, Xiaoqia106228n M. Chen, Ahmad Us Saleheen, Ryan Tumbleson, Margaret R. McCarter, Peter Fischer, Frances Hellman, Steve D. Kevan, Sujoy Roy, Adv. Funct. Mater. **33**, 2300224 (2023).
4. Felix Lehmkühler, Wojciech Roseker, and Gerhard Grübel, Applied Sciences **11**, 6179 (2021).
5. Ted A. Laurence, Samantha Fore, and Thomas Huser, Optics Letters **31,** 829 (2006).
6. Antonino Ingargiola, Github Repository, 2017, url: https://github.com/tritemio/pycorrelate/blob/master/pycorrelate/pycorrelate.py

Publications

Collaborative Publications

1. A.S. Tremsin, J.V. Vallerga, O.H.W. Siegmund, J. Woods, L.E. De Long, J.T. Hastings, R.J. Koch, S.A. Morley, Yi-De Chuang, S. Roy, *Photon-counting MCP/Timepix detectors for soft X-ray imaging and spectroscopic applications*, J. Synchrotron Rad. **28** (2021) 1069–1080.

2. J. Woods, X. Chen, R. V. Chopdekar, B. Farmer, C. Mazzoli, R. Koch, A. Tremsin, W. Hu, A. choll, S. Kevan, S. Wilkins, W.-K. Kwok, L. D. Long, S. Roy, J.T. Hastings, *Switchable X-ray Orbital Angular Momentum from an Artificial Spin Ice*, Phys. Rev. Let. **126** (2021) 117201.
3. Arnab Singh, Emily Hollingworth, Sophie A. Morley, Xiaoqian M. Chen, Ahmad Us Saleheen, Ryan Tumbleson, Margaret R. McCarter, Peter Fischer, Frances Hellman, Steve D. Kevan, Sujoy Roy, *Characterizing Temporal Heterogeneity by Quantifying Nanoscale Fluctuations in Amorphous Fe-Ge Magnetic Films,* Adv. Funct. Mater. **33**, 2300224 (2023).
4. Margaret R. McCarter, Ahmad I. U. Saleheen, Arnab Singh, Ryan Tumbleson, Justin S. Woods, Anton S. Tremsin, Andreas Scholl, Lance E. De Long, J. Todd Hastings, Sophie A. Morley, Sujoy Roy, *" Antiferromagnetic real-space configuration probed by dichroism in scattered x-ray beams with orbital angular momentum", Phys. Rev. B 107, L060407 (2023). (Editor's suggestion).*

Conference Publications

1. A.S. Tremsin, J.V. Vallerga, T. Curtis, D. Tercero, J.B. McPhate, O. Siegmund, R. Raffanti, S. Roy, Y.-D. Chuang, S. Morley, M. McCarter, A. Saleheen, J. Turner, G. Dakovski, R. Schoenlein, C. Hansson, *Soft X-ray MCP/Timepix Photon Counting Detectors for Synchrotron and FEL Applications*, IEEE Nucelar Science Symposium (IEEE NSS 2023), Vancouver, November 2023.
2. A.S. Tremsin, T.L. Curtis, D. Tercero, J.V. Vallerga, N. Thielemann-Kühn, T. Amrhein, M. Weinelt, C. Schüßler-Langeheine, N. Pontius, S. Roy, S. Morley, R.R. Raffanti, *Photon counting soft X-ray detector capable of gated operation at extremely high input fluxes*, 24th International Workshop on Radiation Imaging Detectors (iWoRiD2023).
3. A.S. Tremsin, J.V. Vallerga, T. Curtis, J.B. McPhate, O.H.W. Siegmund, R.R. Raffanti, S. Roy, Yi-De Chuangc, S. Morley, A. Us Slaeheen, *Optimization of High Count Rate MCP/Timepix Photon Counting Detectors for Synchrotron Applications*, NDIP 20 – New Developments in Photon Detection, Troyes, France, July 2022.

Very High-Speed Electron Spectroscopy Detector

PI: Peter Denes, Lawrence Berkeley National Laboratory

Keywords: Electron Microscopy, EELS, Spectroscopy, Electron Detection

Research Project Scope

The energy spectroscopy of inelastically scattered electrons provides chemical information, and in the case of electron microscopy makes this information possible at atomic resolution. In addition, the ability to detect very small energy losses makes it possible to use energetic probes to study very low energy phenomena such as energy *gain* of the primary electrons, vibrational properties, and optical phenomena. In Electron Energy Loss Spectroscopy (EELS), as shown in Figure 2, scattered electrons are dispersed by a magnetic spectrometer onto a detector. Energy resolution thus translates to position resolution. EELS has long been limited by detector performance due to the simultaneous need for high spatial resolution (δE) with a large number of resolution elements. Detectors have also been challenged by the large number of unscattered electrons (E_0) and desire for speed. This project aims to overcome all of these limitations by developing an EELS detector that can acquire spectra at high speeds, tolerate large beam currents, and operate over the full range of energies typically used (30 to 300 keV).

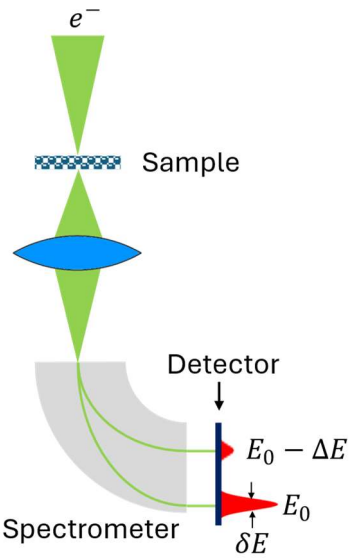

Figure 2 Electron Energy Loss Spectroscopy

Recent Progress

The introduction of electron detectors based on CMOS Image Sensors (CIS) has had a dramatic effect on electron microscopy (EM) as exemplified by the 2017 Nobel Prize in Chemistry. While CIS-based detectors have overtaken traditional fiber-coupled phosphor cameras for EM imaging, they are less used for EELS because of the insufficient well depth to cope with the mostly unscattered incident beam (Zero Loss Peak, ZLP). Techniques to blank the beam at the entrance to the spectrometer make it now possible to use such detectors for EELS, but this (a) only works for beam insensitive materials, since the sample sees the full dose, but only a fraction is used for EELS, and (b) still means that it takes much longer (minutes) to acquire spectrum images with comparable signal/noise as typical STEM images (seconds).

From our earliest developments (1) to the recent 87,000 frame/s 4D Camera (2) we have emphasized the importance of readout speed in combination with the other advantages of CIS-based detectors, as a means to overcome the limited well depth of CIS detectors. The sensor we

have designed and fabricated is shown in Figure 3, and consists of 3264 x 960 pixels, with a pixel size of 6.4 μm.

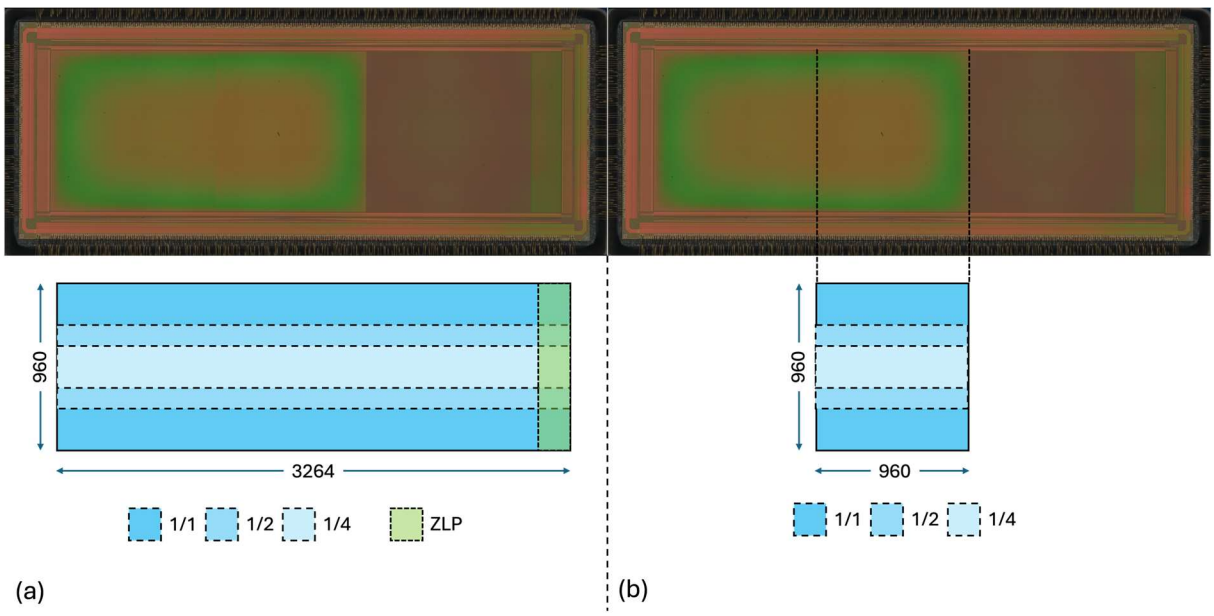

Figure 3 (a) Sensor in "EELS mode" with the ZLP region on the right (b) Sensor in "diffraction mode"

The sensor can be configured to read 240, 480 or 960 rows per image (Figure 3a). At the highest frame rate, this corresponds to 27 μs per frame. Pixels in the ZLP region read out at a four times higher rate than the other pixels and also have programmable gains: at the highest frame rate, each ZLP pixel can record up to ~5 pA (300 keV).

To benefit from the location of the sensor behind the spectrometer, it can be reconfigured to become a version of the 4D Camera: in "diffraction mode", as shown in Figure 3b, the sensor reads out the central region only. As above, the number of rows can be configured, so that 960 x 960 pixel images can be acquired at ~37,000 frames/s and 240 x 960 pixel images can be acquired at ~147,000 frames/s.

CIS-based EM cameras have been "front illuminated" to date, which means that incident electrons pass through inert material prior to entering active silicon. This degrades performance at low electron energy. We have developed methods to remove extraneous silicon at the individual device level, allowing "back illumination" (the 4D Camera sensors are back-illuminated). In addition, commercial foundries have also perfected techniques at the wafer level. The EELS detector will be back illuminated in order to operate at high efficiency at all EM energies.

Device wafers were received in 12/2023 and 01/2024. Following device processing and packaging, along with readout preparation, we have started functional verification of the sensor.

Future Plans

After completion of functional verification of the sensor, in the near term, we will characterize sensor performance at a variety of energies. In preparation for initial deployment in H2 CY2024 at the National Center for Electron Microscopy in the Molecular Foundry, data acquisition and refining methods to collect spectra will be the focus. As the sensor produces copious data, techniques to reduce the data and extract high quality spectra will be critical. While outside the scope of this project, that activity is part of the "Electron Distillery 2.0: Massive Electron Microscopy Data to Useful Information with AI/ML" activity.

References

1. Battaglia M, Contarato D, Denes P, Doering D, Duden T, Krieger B, et al. Characterisation of a CMOS active pixel sensor for use in the TEAM microscope. Nuclear Instruments and Methods in Physics Research Section A: Accelerators, Spectrometers, Detectors and Associated Equipment. 2010;622(3):669-77.
2. Ercius P, Johnson I, Brown H, Pelz P, Hsu S-L, Draney B, et al. The 4D Camera – a 87 kHz Frame-rate Detector for Counted 4D-STEM Experiments. Microscopy and Microanalysis. 2020:1-3.

Towards an Ultra-Stable, Ultra-Cold Transmission Electron Microscope

PI: Peter Denes, Lawrence Berkeley National Laboratory

Keywords: Electron Microscopy, Superconducting magnets and sources, cryogenic microscopy

Research Project Scope

Quantum phenomena such as superconductivity, charge density waves, magnetic phases such as skyrmion lattices, and the physics of devices for quantum information science [QIS] applications are most commonly studied at cryogenic temperatures. To realize the full potential of electron microscopy at temperatures down to ~1K, microscope stability must be improved. Our goal is thus to demonstrate the technical advantages and feasibility of an all-superconducting (SC) electron microscope. We build on previous work that showed the stable, quench-free operation of a prototype SC objective lens along with an ultra-narrow energy width SC electron source.

To establish the performance and practicality of a SC microscope, we will

(1) Demonstrate the effectiveness of SC shielding with the features needed for use in electron microscopy

(2) Demonstrate the effectiveness of cryogenic pressure and temperature stabilization on field stability of our SC lens

(3) Demonstrate the focal stability of the combined electron source and objective lens with an electron beam projected through a sample onto a detector in the far-field

We will accomplish (1) by adding SC shielding to our existing cryostat and measuring the attenuation of electromagnetic noise, (2) by developing a liquid helium level and pressure stabilization system, and (3) by building 5 keV demonstrator. The demonstrator will have a SC emitter, a SC objective lens with persistent current operation and SC shielding. (Persistent current operation allows the magnet to be disconnected from the power supply – thus eliminating power supply noise and drift.) A long drift tube combined with a sensitive electron detector will allow us to measure the focal stability to better than 1 nm.

Recent Progress

We previously designed, built and operated a prototype liquid Helium-cooled SC objective lens at 1.8T (the same field as a commercial 300 keV TEM) in persistent current mode. We implemented and characterized two current stabilization methods (to compensate the slow field droop from the ~pΩ resistance of the SC coil), which were able to maintain a constant field to within a measurement error of $\pm 2.25 \times 10^{-6}$ (dominated here by the accuracy of the Hall probe measurement)(1). We have also demonstrated a novel superconducting niobium (Nb) tip electron

field emitter with an ultra-narrow, tunable energy distribution capable of ΔE < 20 meV FWHM (2) (compared to 750 meV for Schottky field emitters and 300 meV for "cold" field emitters).

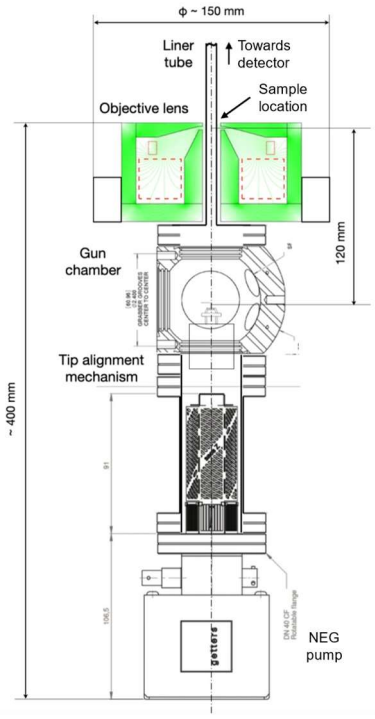

Figure 4 Electron optical

The electron optical system shown in Figure 4 has been designed. The target parameters are: a virtual source size of less 1-5 nm, a brightness of ~ 5×10^8 A/(m^2srV), a beam energy of 5 keV, and an energy spread in the range of 20-75meV at cryogenic temperatures. The aim is to achieve a 1 - 3nm spot at the focus plane with a beam current of 100pA - 1nA.

The design of the SC shielding test has been completed (Figure 5). We have procured the mu metal shielding and are procuring the Nb shielding now.

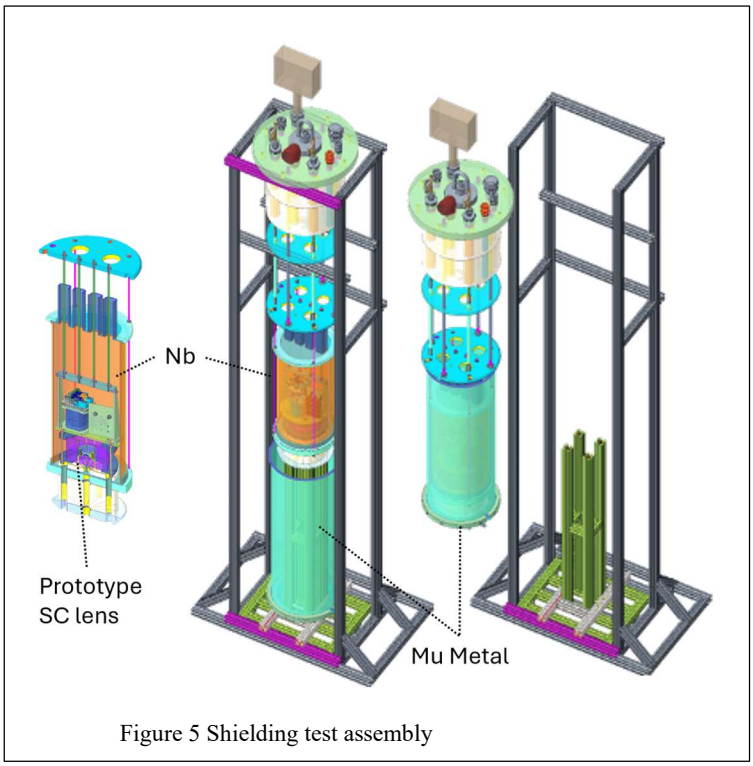

Figure 5 Shielding test assembly

The design of the final 5 keV demonstrator (*Figure 6*) is well advanced. It will be housed in an existing 15" cryostat, and procurement and fabrication of several key components is under way.

Future Plans

In order to validate the performance of SC shielding we will incorporate shielding into our existing 9" dewar and measure the attenuation of magnetic noise in Summer 2024. Our shielding design consists of an inner SC shield which performs the bulk of the shielding at low-temperature together with an outer mu-metal shield, which is optimized to minimize the field on the SC shield when it passes through the transition temperature (~10 K) during cooldown. This minimizes trapped field in the SC shield which impacts shielding performance. Based on requirements for the highest performance TEMs, we intend to demonstrate that the shielding reduces stray fields to $10^{-8}T$ using SQUID devices to overcome limitations of prior measurements using Hall probes.

The electron gun chamber and vacuum system are being assembled, The 9” dewar will be used to test the vacuum performance of the chamber and high voltage feedthroughs at cryogenic temperatures.

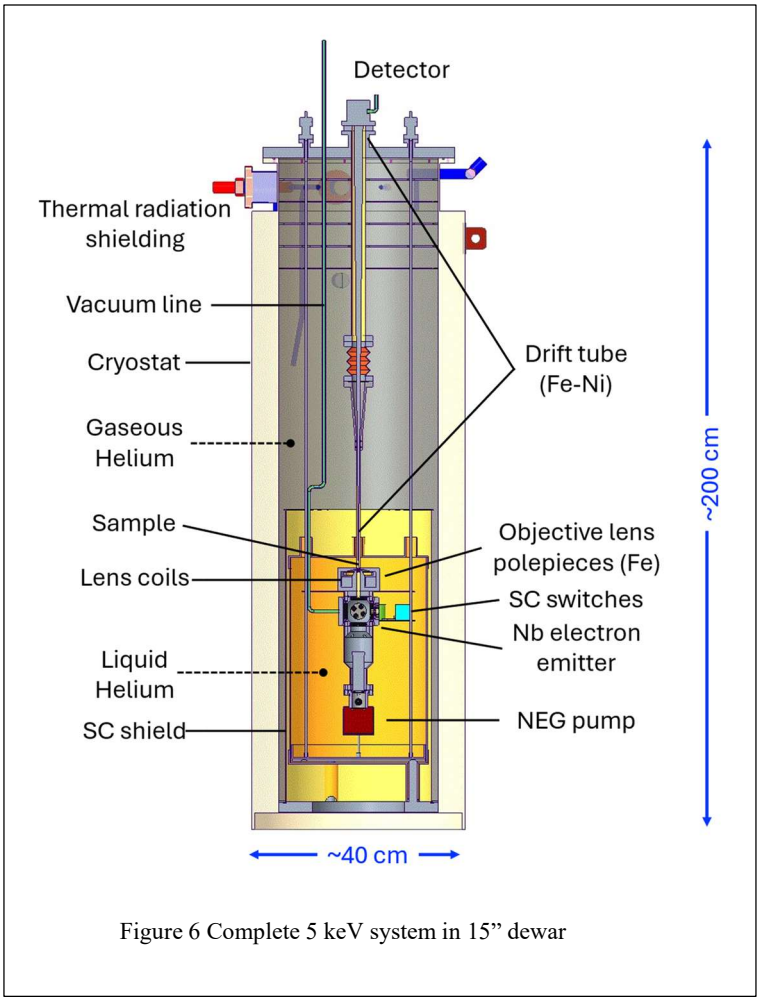

Figure 6 Complete 5 keV system in 15” dewar

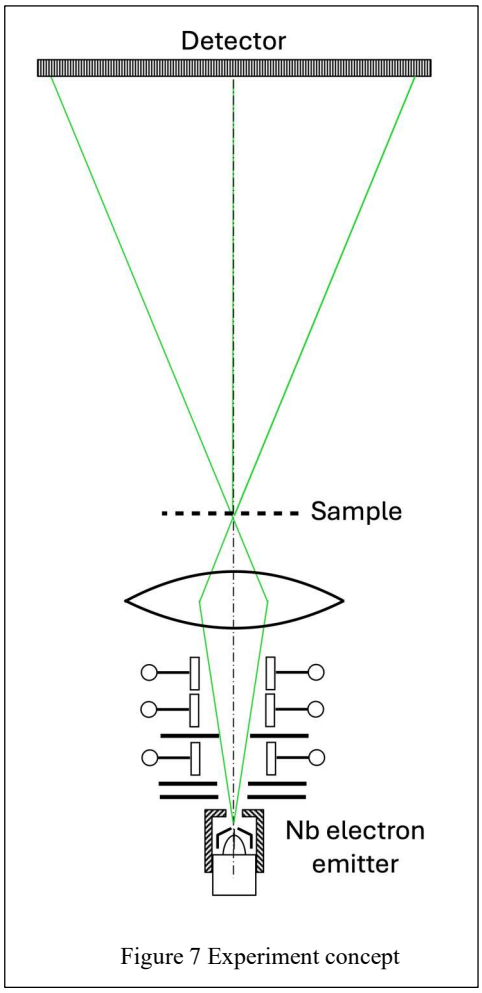

Figure 7 Experiment concept

We will use the 15” cryostat to develop the cryogenic stabilization system. We follow established concepts (3), that show that with appropriate pressure and level control, as well as the right cryostat geometry, pressure variations at the level of $\leq 10^{-3}$ Torr can be achieved. A level control system that continuously refills LHe will be built, consisting of level sensors and monitoring instruments, a LHe refill control valve and control circuits. To obtain precise pressure control and regulation, pressure transducers and a pressure controller with throttle control valves will be installed between the magnet LHe container and the GHe vent line.

After completion of detailed design and component fabrication, the complete 5 keV system will be tested at room temperature, and then integrated into the dewar shown in *Figure 6*.

The optical system forms a focused ~nm spot above the specimen plane, and the image is acquired by the detector ~1m away (*Figure 7*). By monitoring changes in the projected image, we aim to demonstrate the short- and long-term focal stabilities listed in the table below.

Objective	Target ΔB/B	corresponding STEM/ TEM focal stability
long-term drift	10^{-10} / day	~ 1 nm / day
short-term jitter	$2x10^{-12}$ / sec	~ 0.02 nm / sec

Demonstration of an ultra-stable electron beam from an ultra-bright SC source with SC lenses in a shielded, cryogenic environment would pave the way towards construction of a full-energy microscope and a new paradigm for EM. Stable, atomic resolution imaging at low temperature will enable better understanding of quantum phenomena. Adding the low energy width of the Nb source, improved spectroscopies, over a wide range of temperatures will be possible. The extreme stability can even enable ultra-fast time-resolved techniques, all of which require very low beam currents to obtain high spatial resolution.

References

1. Brouwer L, Shen T, Norris R, Hafalia A, Schlueter R, Wang L, et al. Stabilization and control of persistent current magnets using variable inductance. Superconductor Science and Technology. 2022;35(4).
2. Johnson CW, Schmid AK, Mankos M, Ropke R, Kerker N, Wong EK, et al. Near-Monochromatic Tuneable Cryogenic Niobium Electron Field Emitter. Phys Rev Lett. 2022;129(24):244802.
3. Jr. RSVD, Farnham DL, Zafonte SL, Schwinberg PB. Ultrastable superconducting magnet system for a penning trap mass spectrometer. Review of Scientific Instruments. 1999;70(3):1665-71.

The Potential of Lithium-Containing Semiconductors at Neutron Scattering Facilities

PI: Eric Lukosi, University of Tennessee-Knoxville

Co-PI: Mercouri Kanatzidis, Northwestern University

Keywords: Neutron Imaging, Semiconductor Detectors, Detector Modeling, Radiation Tolerance

Research Project Scope

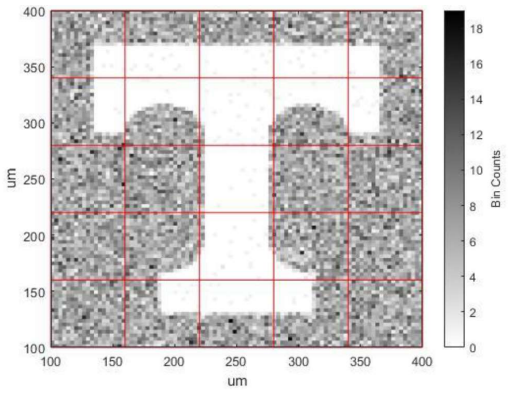

Figure 1: Image of the neutron absorption locations in a LIPSe neutron converter showing a gadolinium Power-T. The square 60 µm grids represent what we call a sub-space, where we move the neutron interaction data into our detector simulation model, reconstruct the neutron image location using advanced algorithms that exploit the charge sharing across the cross-strip electrode design, and then translated back into real space.

To support the capabilities of neutron imaging facilities, we propose to continue development of a double-sided strip detector (DSSD) using a new conversion material, the semiconductor $LiInP_2Se_6$, or LIPSe. The objective of the project is to develop and demonstrate the LIPSe double-sided strip detector as a viable candidate for current and future neutron imaging facilities that meet the desired performance metrics defined by the scientific community. The performance metrics we aim to achieve in the development of the LIPSe DSSD are a spatial resolution in the 1-5 µm range, a high neutron utilization factor approaching 75%, timing performance suitable for energy-resolved imaging, and excellent gamma-ray rejection capability. Simultaneously achieving these metrics will result in the most capable neutron imaging sensor available.

In collaboration with instrument scientists at the DOE neutron imaging facilities, we will provide access of the LIPSe double-sided strip detector for evaluation by scientists that visit the facilities for a wide variety of neutron imaging experiments. Upon successful completion of the project, the developed LIPSe DSSD will provide the necessary evidence that the LIPSe DSSD is a viable candidate for adoption by the neutron imaging scientific community, and will enhance the capabilities of current and future imaging facilities, both domestic and foreign. Therefore, this project has the potential for very high impact, both in the sciences and the general public by supporting research that effects the everyday lives of citizens.

Recent Progress

The development of the LIPSe DSSD has made significant progress. The device has been fully simulated, leading to the development of a novel classification scheme that enables excellent spatial resolution. Historically, the spatial resolution of lithium-containing semiconductors has been limited to the range of the secondary alpha and triton secondary charged particles, or ~34 µm

[1]. However, by utilizing charge sharing across a cross-strip electrode design, we have computationally demonstrated that a spatial resolution of ~10 µm is possible, even with incomplete charge collection and significant electronic noise. We provide an example in Figures 1 and 2. In Figure 1, the results of the MCNP6 neutron transport through a gadolinium Power-T and onto a LIPSe imaging plane is provided. Using this as an input to our full charge transport model, including the random emission of the secondary alpha and triton, the results of our reconstruction algorithm in Figure 2 indicate the potential excellent spatial resolution.

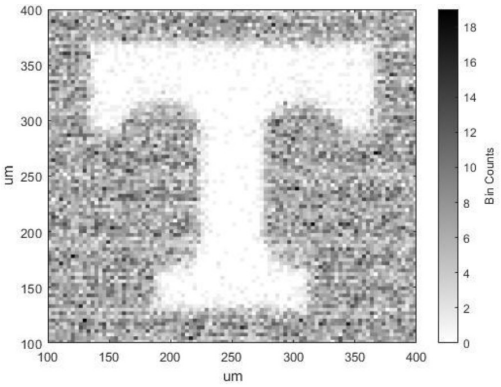

Figure 2: Representative neutron image expected from the LIPSe cross-strip detector from Figure 1.

While the imaging performance may be excellent, the expected lifetime must be known to evaluate the viability of the imaging system for applications in high neutron flux environments. While thermal neutrons don't typically cause significant damage resulting in a reduction in the semiconductor's charge transport properties, each neutron is accompanied by two heavy charged particles (alpha and triton). It is currently unknown what the radiation tolerance is of LIPSe. Therefore, we utilized the Ohio State University TRIGA reactor to conduct radiation tolerance measurements on LIPSe. For this test, we took a LIPSe sample and laser cut it into two halves. One half was not irradiated and the other half was, thereby providing us a measure of systematic control during characterization. Two samples were evaluated at each fluence, which ranged from 10^{12} n/cm^2 to 10^{16} n/cm^2. Characterization included UV-Vis, Raman, XRD, and radiation response measurements using alpha particles.

In Figure 3, representative results are provided for UV-Vis and charge collection efficiency measurements. Here, it was found that the optical and crystallinity of the samples did not show appreciable change after neutron irradiation and that the samples responded to alpha particles after irradiation. However, the samples could not be pre-characterized effectively for radiation response, and it is unfortunate that many of the coupled irradiated and non-irradiated samples showed limited response to alpha particles. Still, this indicates that, at a flux of 10^7 n/cm^2/s, LIPSe may be able to

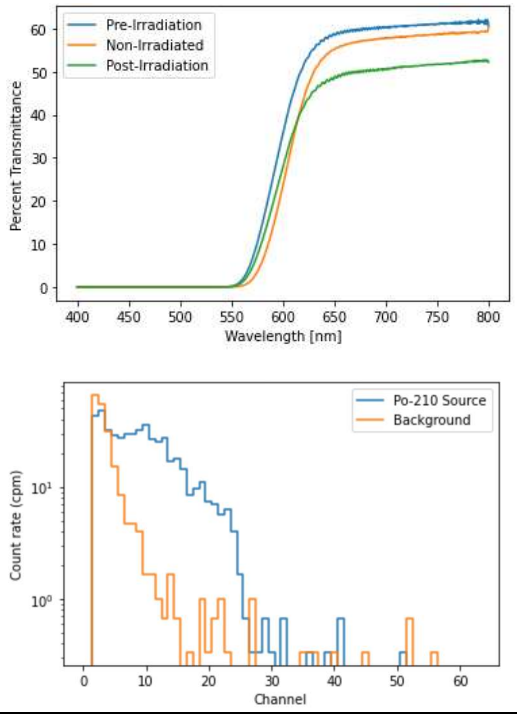

Figure 3: Top: UV-Vis results of the LIPSe samples before and after irradiation at 10^{14} n/cm^2. Bottom: Alpha particle response of a LIPSe sensor irradiated to 10^{15} n/cm^2.

survive for more than 1,000 days of continuing operation while still providing its excellent advantages in neutron imaging, more than sufficient for most imaging applications. Furthermore, many applications do not require more than counting to meet a lower spatial resolution (e.g., >55 μm), which reduces the need for both a cross-strip design and advanced algorithms as well as a lower required radiation tolerance.

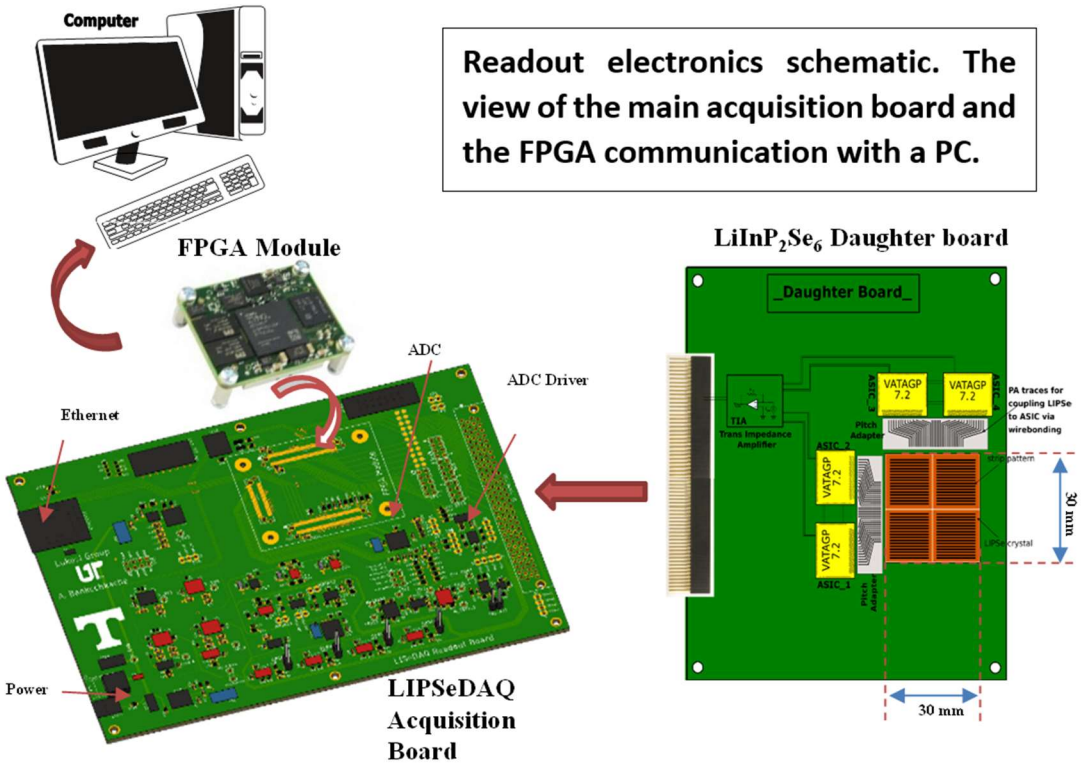

Figure 4: Top: Graphics of the designed daughter and DAQ boards.

Finally, we have constructed the first design of our readout system (see Figure 4). The system's DAQ board is versatile, allowing us to evaluate different daughter boards that utilize the same IDEAS VATA7.2 ASIC. This board controls data collection and pre-processing, communication, ASIC addressing, and all power requirements. For the development of the readout electronics of the $LiInP_2Se_6$ SCD detector prototype, work efforts were focused to continue building the frontend electronics of the detector. Specifically, circuit design enhancements were addressed to the last version of the custom daughterboard designed using the EAGLE Autodesk tool as a multilayer (6-layer) PCB accommodating the $LiInP_2Se_6$ sensors, the pitch adapters, and the ASICs. The following enhancements were considered before the final PCB fabrication and assembly: power planes and ground planes as well as optimizing their dimensions and layer stack-up providing stable power distribution and reducing noise. Also, trace length matching was performed for the various differential signals whether from the different IOs of the ASICs or other circuitries on

board. This is considered a crucial part to minimize timing skew and signal integrity issues. Finally, refining the footprint on board for the DSSD $LiInP_2Se_6$ sensor coupling via ACF bonding was necessary to improve the bonding alignments and minimize shorting adjacent strips during the bonding process given the smaller pitch considered.

Future Plans

We have contracted out to help develop the Firmware and do an independent evaluation of the boards. During firmware testing, we found a few errors that will not allow the ADC to function properly. We are currently fixing these issues and plan to fabricate the second board in the coming couple of months. Once we verify that the boards, we will couple the LIPSe sensor to the daughter board and conduct experiments. Initial evaluation will utilize alpha particles and thermalized PuBe neutrons with a knife edge, but our close relationship with ORNL will allow us to test the sensor on CG-1A during the normal HFIR cycle. After full evaluation, we will utilize the sensor with a currently approved experiment on either CG-1D and/or on SNAP (for energy-resolved imaging tests to evaluate the time-to-digital conversion algorithm).

References

1. E. Herrera, D. Hamm, A. Stowe, J. Preston, B. Wiggins, A. Burger and E. Lukosi, *Neutron Imaging with Timepix Coupled Lithium Indium Diselenide,* Journal of Imaging **4** (1), 10 (2018).

Publications

1. Robert Golduber, Jake Gallagher, Amine Benkechkache, Erick Hoegberg, Huicong Hong, Alireza Kargar, Luis Stand Stracuzzi, **Eric Lukosi**, Radiation Tolerance of Lithium Indium Diselenide Semiconductors, Physica Status Solidi A 2300012.

2. Alireza Kargar, Huicong Hong, Joshua Tower, Paul Guggenheim, Eric Qian, Conner Brown, Mathew Breen, James F. Christian, Kanai Shah, **Eric Lukosi**, Robert Golduber, Jake Gallagher, Amine Benkechkache, Mercouri Kanatzidis, Michael R. Squillante, Thermal neutron detection with lithium-based semiconductors, Proceedings Volume 12241, Hard X-Ray, Gamma-Ray, and Neutron Detector Physics XXIV; 1224108 (2022).

3. M.A. Benkechkache, L. Drouet, J. Gallagher, R. Golduber, **E.D. Lukosi**, Readout Electronics and Development of a Double-Sided Strip Design $LiInSe_2$ Neutron Imaging Detector, 2021 IEEE Nuclear Science Symposium and Medical Imaging Conference.

4. Erick Hoegberg, Eric Qian, Amine Benkechkache, Eric Lukosi, Mercouri Kanatzidis, Luis Stand, *Radiation Tolerance of LIPSe*, In Preparation.

5. Eric Lukosi, Jake Gallagher, Erick Hoegberg, Amine Benkechkache, Enhanced Spatial Resolution of Double-Sided Strip Detectors Using Lithium Indium Diselenide Semiconductor Materials, In Preparation.

Neutron detector development for high-rate neutron reflectometry at the Second Target Station of Oak Ridge National Laboratory

Xianfei Wen, Jason P. Hayward

Department of Nuclear Engineering, University of Tennessee, Knoxville, TN 37996, USA

Keywords: neutron reflectometer detectors; high rate; scintillators; neutron detection; Second Target Station

Research Project Scope

The Second Target Station (STS) at the Oak Ridge National Laboratory Spallation Neutron Source (SNS) is anticipated to produce a neutron source that exhibits a significantly higher peak brightness compared to the First Target Station (FTS), where the reflectometry instruments already fall short of being able to handle the highest available neutron flux by a factor of ~100 [1-3]. The neutron reflectometers at the SNS FTS are not suitable for the reflectometers planned for the SNS STS because of the unprecedentedly high peak brightness and the already limited capabilities of these instruments at high count rates [4]. Furthermore, the high-rate instrument that was investigated is expected to underperform with regard to gamma sensitivity, meaning that signal-to-noise will be reduced, and they will be unable to measure weaker reflectance phenomena in the presence of the significant prompt gamma flash at SNS [5]. To address these challenges, a scalable, 2-D positive-sensitive, pixelated scintillator-based neutron detector module is being developed by using a fast, pulse shape discrimination capable ^{6}Li-loaded plastic scintillator, highly efficient SiPMs, and advanced ASIC readout electronics. The detector module will have the following features that meet or exceed the reflectometer specifications for the SNS STS: a count rate capability of 10 MHz/cm^2, a neutron detection efficiency of 60% at 4 Å, a spatial resolution of 1 - 2 mm, a gamma sensitivity below 1×10^{-6}, and a time resolution of less than 1 μs. The proposed work will have a high impact on future neutron reflectometry instruments and neutron science performed at the SNS STS. In particular, the improved background rejection capability of the developed detector module will extend the available experimental dynamic Q range, allowing our instrument to measure even extremely weak reflectance phenomena. Additionally, the instruments, techniques, and capabilities that are developed from this work will have broader impact for improved high-rate performance in other areas of neutron science, including but not limited to small angle neutron scattering, spectroscopy, diffraction, and imaging.

Recent Progress

The following shows a list of the recent progress we made in this work.

- A C&A 10 × 10 × 1.1 mm LiCAF:Ce single crystal and a 10 × 10 × 17 mm EJ-270 plastic scintillator from Eljen Technology were characterized in a laboratory environment with regard

to light yield, pulse shape discrimination performance, capability to detect thermal neutrons in high gamma environments, and gamma sensitivity. This was performed mostly for determining the promising candidate such that the neutron detector module developed can meet the reflectometer specifications for the SNS STS. The characterization results have been submitted to a peer-reviewed journal.

- A neutron detector module is nearly ready for evaluation. It mainly consists of a pixelated EJ-270 plastic scintillator array with a pixel size of 2 × 2 × 7.6 mm, a Hamamatsu S13361-2050AE-08 MPPC array, and the PETsys TOFPET2 ASIC readout board. The feasibility of pulse shape discrimination of this detector module in real-time is being studied at various count rates. In addition, proposals were submitted to obtain beam time for testing the detector module at the High Flux Isotope Reactor (HFIR) and the SNS FTS.

Future Plans

The neutron detector module will be tested at the CG-1A detector test beamline of the HFIR as well as the BL-4B neutron reflectometer beamline at the SNS FTS. The experiment plans for the testing are briefly described below.

- CG-1A testing (Beam time proposal was approved.)

Count rate capability: The count rate capability of the detector module will be compared to that of a fission chamber-based monitoring detector that can respond linearly over a rather large range of neutron flux. The detectors should be positioned at the same location, and neutron attenuators will be used to produce a range in neutron flux at the detector location.

Neutron detection efficiency: This will be measured by comparing the count rates of the detector module and a well calibrated ^{3}He proportional counter.

Detector cross-talk and response uniformity: Due to the potential optical cross-talk between adjacent pixels and its impact on the count rate capability of the detector module, it is beneficial to understand the response of neighboring pixels when neutrons are detected by a central pixel. A well-collimated neutron beam with a diameter as small as possible/reasonable will be created to investigate the cross-talk and the uniformity of the detector response. The beam will be used to irradiate different locations of the detector module by moving this module through a motorized XY positioning stage.

- BL-4B testing (Waiting for the selection result)

Count rate measurement: The count rate capability of the detector module will also be measured at this neutron reflectometer beamline. Various levels of neutron flux up to the highest possible value will be used for this purpose.

Neutron reflectivity measurement: Typical neutron reflectivity measurements will be performed by using this detector module and the ^{3}He detector deployed at this reflectometer beamline at different neutron flux values for standard iridium and quartz samples. The measurement results obtained from the detector module will be compared to those measured with the ^{3}He detector. The performance of this detector module in measuring neutron reflectivity will be carefully assessed, considering the detector requirements for the neutron reflectometry instruments planned at the SNS STS.

References

1. Second Target Station conceptual design report volume 1: overview, technical and experiment systems, *S01010000-TR0001, R00*, 2020.
2. Technical design report: Second Target Station, *ORNL/TM-2015/24*, January 2015.
3. Second Target Station workshop report, Oak Ridge, Tennessee, October 2015, https://neutrons.ornl.gov/sites/default/files/STS%20Workshop%20Report.pdf.
4. A. Khaplanov, "Detector needs for STS instruments," *ORNL/TM-2022/1843*, January 2022.
5. S. Chong, R. Riedel, L. Funk, T. Visscher, C. Donahue, B. Hannan, C. Montcalm, J. Beal, M. Doucet, J. Hayward, "The development of a Li-based pixelated neutron detector for neutron reflectometry at the Spallation Neutron Source," *Nucl. Instr. and Meth. A*, vol. 1039, pp. 167052, 2022.

Publications

1. Xianfei Wen, Jason P. Hayward, "Characterization of EJ-270 and Ce-doped LiCAF scintillators for the development of high-rate neutron reflectometer detectors," *Nucl. Instr. and Meth. A*, 2024 (under review).
2. S. Chong, R. Riedel, L. Funk, T. Visscher, C. Donahue, B. Hannan, C. Montcalm, J. Beal, J. Hayward, "The development of a Li-based pixelated neutron detector for neutron reflectometry at the Spallation Neutron Source," *Nucl. Instr. and Meth. A*, vol. 1039, pp. 167052, 2022.

Quantum Limited Parametric Amplifiers for X-Ray Sensors

Dr. Douglas Bennett, National Institute of Standards and Technology

Keywords: parametric amplifier, x-ray transition-edge sensor, microwave SQUID multiplexer

Research Project Scope

The DOE's x-ray light sources are among the crown jewels of the U.S. scientific infrastructure. These facilities serve a large community of users from many areas of science with diverse interests and needs. The productivity of the light sources depends on many factors but especially the capabilities of the x-ray detectors used to record properties such as x-ray intensities, energies, arrival times, and arrival positions. Cryogenic detectors based on superconducting elements such as Transition Edge Sensors (TESs) and Microwave Kinetic Inductance Detectors (MKIDs) are promising sensors for x-ray light sources because they combine high spectral resolving power with high photon collection efficiency. Microwave readout techniques are required to build large arrays of these cryogenic sensors. Presently, classical semiconductor amplifiers are used for microwave readout but in this project we are developing parametric amplifiers for use with cryogenic detectors at x-ray light sources.

In a parametric amplifier, the signal of interest is combined or mixed with a stronger pump signal in the presence of an engineered nonlinearity. Energy is transferred from the pump to the signal and the signal is amplified. Because the working medium is a lossless reactance, the noise performance of parametric amplifiers is excellent and, in the last decade, has approached the limits set by quantum mechanics. While parametric amplifiers are now widely used to read out superconducting qubits, the potential of parametric amplifiers for the readout of cryogenic sensors had remained unrealized. Compared to the classical microwave amplifiers such as HEMTs presently in common use with cryogenic sensor arrays, parametric amplifiers offer better noise performance. The major goal of this project was the demonstration of parametric amplifiers as a low noise first stage amplifier for microwave SQUID multiplexer readout and to understand the parameters that need further improvement for the technology to significantly improve the bandwidth utilization and enable scaling to larger arrays for future x-ray TES instruments.

Recent Progress

The recent progress within this project are listed below with the corresponding major goal for this past year.

Goal 1. To demonstrate a significant improvement in magnetic energy sensitivity of a microwave SQUID by using a KIT as the first stage amplifier.

We performed a demonstration of rf-SQUID readout using wmux+KIT, achieving a dramatic improvement in flux noise from 0.45 $\mu Phi_0/(Hz)^{1/2}$ to 0.2 $\mu Phi_0/(Hz)^{1/2}$ at the most sensitive point of the SQUID response curve and from 1.6 $\mu Phi_0/(Hz)^{1/2}$ to 0.77 $\mu Phi_0/(Hz)^{1/2}$ with flux-ramp

modulation, which would be used in a large-scale multiplexed readout. These values correspond to roughly 5× the SQL on amplifier noise and constitute the best magnetic energy sensitivity ever demonstrated with a uMUX readout. Further information about these results can be found in [3].

Even with these dramatic noise improvements, we also believe there are opportunities for further noise reduction. First, we can optimize the microwave circuit between the wmux and the KIT, to reduce the loss and potential impedance mismatch, bringing us within a factor of 2 of the SQL. Second, we can implement a tone-tracking readout scheme. This should improve the flux-ramp-modulated noise by an additional factor of 2 by keeping the microwave probe tone always in a sensitive region of the resonance response. With these improvements, we should be able to reach an ultimate flux noise on the order of 0.25 $\mu Phi_0/(Hz)^{1/2}$, a level competitive with the most sensitive non-multiplexed dc-SQUIDs.

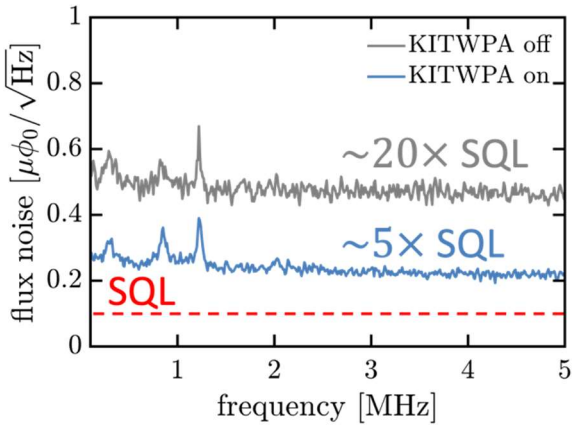

Figure 1. Readout of a single resonator within the microwave SQUID multiplexer with the TES disconnected. The flux noise for the two situations: KITWPA off (gray line) and KITWPA on (blue line) is plotted as a function of frequency.

Goal 2. To demonstrate the readout of a TES microcalorimeter array through a uMUX readout with KIT amplification.

Existing SQUID multiplexers for TES readout do not significantly degrade the sensitivity of the detectors because the mutual inductance of the input coil of the SQUID is tuned so that the intrinsic detector noise dominates the readout noise. The tradeoff is that the size of this mutual inductance also determines the maximum slew rate of magnetic flux in the SQUID, which can require more readout bandwidth to track than the actual bandwidth of the detector signals. Improvement in readout noise therefore can be parlayed into narrower resonator bandwidth, more efficiently utilizing the available microwave bandwidth.

To accomplish this goal, we assembled an experimental package containing a small array of hard x-ray TES microcalorimeters, bias circuitry for the TESs, and a wmux+KIT device. With the wmux device coupled to the microcalorimeters we were able to read out pulses, demonstrating that the wmux+KIT reduces readout noise without affecting the system in other ways. We published these results in [3] and completed an end-to-end system demonstration.

As expected, the improvement in readout noise did not significantly improve ultimate energy resolution, because the intrinsic noise of these TES detectors was dominant. However, the reduced readout noise in the amplifier chain allows a re-optimization of the umux/wmux devices, reducing the input mutual inductance and therefore the slew-rate constrained resonator bandwidth by a factor of 2-3, ultimately increasing the multiplexing factor by the same factor of 2--3. Increasing the bandwidth utilization provided by higher multiplexing factors will increase array size and reduce the cost-per-pixel of the instrument.

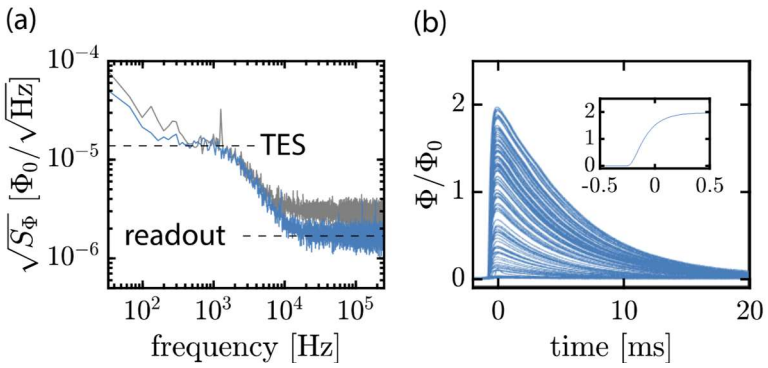

Figure 2 Response of a resonator within the microwave SQUID multiplexer, connected to a biased TES. Below 10kHz the TES noise dominates the noise spectrum. At higher frequencies, we recover the improvement in flux noise when turning the KITWPA on (blue curve) compared to when the KITWPA is off (gray curve). (b) Pulse events due to background radiation have been detected by the TES over 3.5 h. Reproduced from [3].

Goal 3. To continue to improve the KIT design to match the needs of microwave multiplexing readout, particularly by reducing gain ripple and improving IP3.

Our initial work in this area focused on developing a new inverted microstrip KIT architecture (iKIT), and demonstrating that the added noise of the NbTiN based KIT amplifier architecture could be at the quantum limit [4]. This new architecture also provides an avenue for improving other aspects of the amplifier. The iKIT is much less susceptible to defects, enabling amplifier designs that are much longer than were previously fabricated due to yield concerns. These longer amplifiers could be made of thicker NbTiN with a higher characteristic nonlinearity, and hence a greater saturation power. The capacitor thickness would be tuned to maintain the 50 Ohm transmission line. Since the amplifier is longer, less nonlinear phase shift per wavelength is needed to achieve the same total gain. This implies that the amplifier could be biased as a lower fraction of the maximum nonlinearity, avoiding the hot spot failures seen in previous generations.

Additionally, the ground plane of the iKIT is improved compared to the disconnected CPW ground and fewer ground plane modes are allowed. The combination of the longer amplifier and the improved ground plane compared to the previous CPW based amplifiers should result in a high gain, lower ripple amplifier even with the higher RF pump needed to effectively drive the TESs in a uMUX readout.

Summary and Overall Progress

The overall goal of this project was to try to develop a new cryogenic amplifier based on kinetic inductance traveling wave amplifier (KIT) to replace the HEMT amplifiers currently used in

uMUX readout of TES spectrometers. TES spectrometers are one of the more promising new x-ray detection techniques due to their combination of broadband spectral coverage, large collecting area, and high resolving power. A reduction in amplifier noise would allow an increase in the multiplexing factor of the readout of these superconducting detectors, enabling better utilization of the available system bandwidth. This improvement would lead to larger detector arrays and a reduction over in the cost per channel of TES spectrometers.

To this end, we were able to develop a KIT amplifier with suitable noise, gain, bandwidth, and power handling for the requirements for TESs readout through microwave SQUID multiplexer. These KIT devices reduced the readout noise by a factor of 2 over traditional the HEMT technology, with a noise as low as 4.5× the standard quantum limit. This device was successfully integrated with a TES microcalorimeter and used as the cryogenic amplifier of the uMUX readout, and successfully measured a photon and showed no degraded performance in the pixel. Further, we were able to estimate that the improved noise performance would allow a redesign of the wmux+KIT in a way that would allow for a factor of 2 to 3 increase in multiplexing factor and bandwidth utilization for future TES spectrometers.

Future Plans

During this work, we have found that there are possible avenues for future improvements in the readout chain to continue to approach the SQL noise level. The microwave SQID multiplexer can be further optimized, to take advantage of the lower noise level of the KIT. We hope to perform a future demonstration of a further optimized multiplexer design with KIT using the inverted microstrip structure. Within the inverted microstrip structure, we believe we can increase the power handing capability of the KIT by moving to larger cross-sectional area. This optimization was difficult in the generation of KIT used for this work but should be possible in the new inverted microstrip designs [4].

Since the end of the period of performance of this project, we were able perform an initial demonstration of the KITs ability to do quantum squeezing of the microwave photons. A compelling future demonstration would be to use two KITs, one to perform the squeezing and the other to do phase sensitive amplification, in order to measure flux noise in the microwave SQUID multiplexer below the standard quantum limit. With the level of squeezing possible in the current inverted KIT designs, we estimate that another order of magnitude lower noise could be achieved using the squeezed microwave photons.

References

1. M. Malnou, M.R. Vissers, J.D. Wheeler, J. Aumentado, J. Hubmayr, J.N. Ullom, and J. Gao, Three-Wave Mixing Kinetic Inductance Traveling-Wave Amplifier with Near-Quantum-Limited Noise Performance, PRX Quantum, **2**, 010302 (2021).

2. M. Malnou, J. Aumentado, M. R. Vissers, J. D. Wheeler, J. Hubmayr, J. N. Ullom, and J. Gao, Performance of a Kinetic-Inductance Traveling-Wave Parametric Amplifier at 4 Kelvin: Toward an Alternative to Semiconductor Amplifiers, Physical Review Applied, **17**, 044009 (2022)

Publications

3. M. Malnou, J.A.B. Mates, M.R. Vissers, L.R. Vale, D.R. Schmidt, D. Bennett, J. Gao, and J.N. Ullom, Improved microwave SQUID multiplexer readout using a kinetic-inductance traveling-wave parametric amplifier, Applied Physics Letters, **122**, 21 (2023)

4. A. Giachero, M. Vissers, J. Wheeler, L. Howe, M. Malnou, J. Jao, J. Austermann, J. Hubmayr, A. Nucciotti, J. Ullom, Kinetic traveling wave amplifier designs for practical readout applications, In review, Journal of Low Temperature Physics, (2023)

Development of Sensors and Readout for Multi-GHz Particle Beam Characterization

Bruce A. Schumm, Univ. of California, Santa Cruz, and Santa Cruz Inst. for Particle Physics , Eric Prebys, Univ. of California, Davis, and the Crocker Nuclear Laboratory , Carl Grace, Lawrence Berkeley National Laboratory, Jonathan Smedley, SLAC National Accelerator Laboratory, Mark Gulley, Los Alamos National Laboratory

Keywords: High repetition rate, position sensing, pass-through diagnostic, CVD diamond sensor

Research Project Scope

Needs arising at both current and future accelerator facilities call for the development of radiation-hardened position-sensing accelerator beam diagnostics that can operate with multi-GHz repetition rates. Building on the recent work of our Advanced Accelerator Diagnostics (AAD) Collaboration, we are at the beginning of a three-year program of instrumentation development that will produce a deployable position-sensing ionizing-particle diagnostic that can operate with a repetition rate above 5 GHz. As envisioned, this diagnostic will have percent-level pulse intensity resolution, micron-level centroid position resolution, and be able to operate to hadronic beam fluences of at least 5×10^{16} cm^{-3}. Due to its fast signal collection speed and superior capability to withstand the damaging effects of hadronic radiation, the diagnostic will make use of high-grade quadrant CVD diamond sensors, developed and fabricated within the proposed effort. The effort will also include the development of a multi-channel readout ASIC capable of amplifying, buffering and digitizing trains of signals pulses with bandwidth as high as 10 GHz. Initial applications are foreseen at upgraded and next-generation XFEL light sources.

Recent Progress

We have broken down the challenge of providing multi-GHz particle detection into four separate pieces, each of which must be separately capable of operating at or above the target bandwidth:

- Signal charge generation and collection
- Signal path response
- Signal transport from signal path to readout
- Readout (amplification/buffering and digitization)

In addition, once addressed, the strategies used to achieve these requirements must be incorporated into an integrated detection system – for this, advanced 3D RF simulation tools are critical for providing design guidance. Here, we report on progress made over the first six months of funded activity towards the development of the first integrated multi-GHz ionizing particle detection system, and the work getting underway to advance this towards a four-channel, position sensing device capable of accurately determining the centroid location of an ionizing particle beam pulse-by-pulse at a rate between 5 and 10 GHz.

Simulation Tools: In our proposal, we discussed the importance of employing simulation tools as an essential requirement for pushing our designs to the highest possible bandwidth. Over our first six months of effort, we have identified the ANSYS corporation's High Frequency Simulation Software (HFSS) package as the proper tool for out work, and have developed a basic working capability in its use.

Charge Generation and Collection: Diamond, with its saturated drift speed of about 200 μm/ns can collect charge at a rate commensurate with multi-GHz operation for sensor thicknesses of 50 μm or less. In the past we have worked with industrial suppliers to provided 4x4 mm^2 diamond substrates thinned to 25-45 μm; supported by this grant, we have now worked with these partners to produce substrates with lateral dimensions as small as 1.5x1.5 mm^2, and have fabricated two thin single-pad sensors of dimension 2x2 mm^2. Our 3D RF simulations confirm that compactness is key towards achieving high bandwidth performance.

Signal Path Mechanics: Achievement of high-bandwidth performance is expected to be predicated on the development of a compact signal path that encloses minimal area as it returns

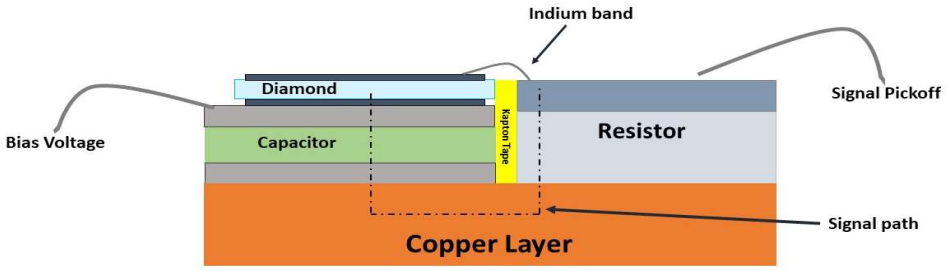

Figure 1: Compact signal path concept. To provide a scale, the diamond sensor is 2x2 mm^2.

the signal charge to the sensor (see Figure 1). Supported by this grant, we have performed a mechanical prototyping study, exploring the best approach to locating the capacitor array beneath the diamond, and also carefully exploring PC-board tolerances at the 1-2 mil level, to optimize our assembly procedures and inform the associated system design. Figure 2 shows an example of on of the questions explored in this study, demonstrating that an open electrode geometry is preferable to one providing separate footprints for the capacitors in the array.

Electronics and Integrated Detection System: Prior to receipt of this award, a four-channel switched-capacitor array, high-bandwidth "FPS" ASIC [1] was designed by the AAD collaboration specifically for the readout of the fast signal-path assembly described above. This initial prototype acquires 40 samples over a configurable digitization window of 1-2 nsec. The work of this proposal to date, in this area, has been to design an integrated multi-GHz detection system – the first of its kind – around this ASIC. The system (Figure 3) consists of a specialty

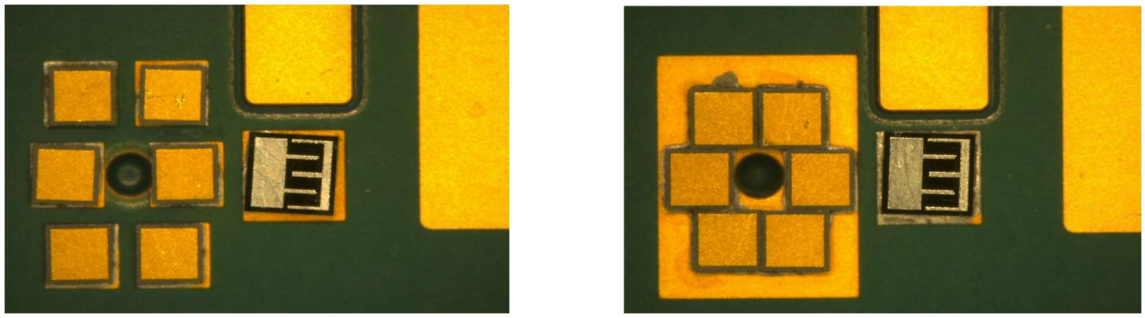

Figure 2: Example of result from mechanical prototyping study showing capacitor array and return-path resistor.

high-bandwidth “carrier board” (Figure 4) that services the ASIC and provides fast trigger and calibration systems, and a control board (Figure 5) that will act as an interlocutor between the FPS ASIC and a Raspberry Pi module that reads out the FPS switched-capacitor array.

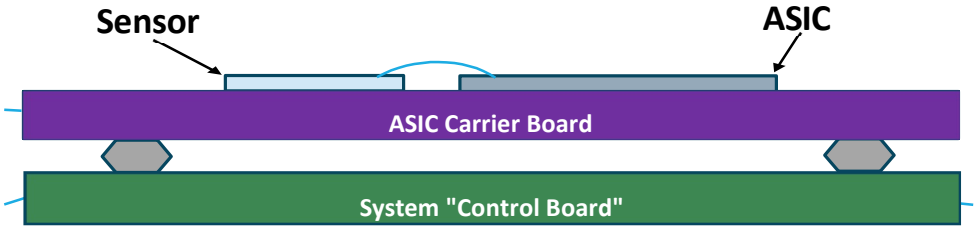

Figure 3: Schematic of the first integrated multi-GHz ionizing particle detection system, using the FPS ASIC and compact signal-path stack-up. Beam enters the sensor near its middle and exits through a hole in the Control Board.

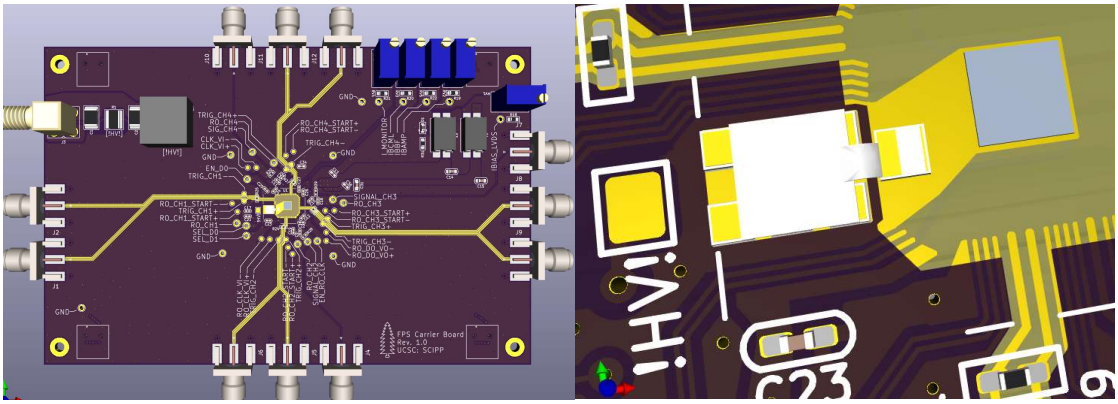

Figure 4: Specialty high-bandwidth FPS Carrier Board (left) and detail of the signal-path and ASIC region (right), currently under assembly in the SCIPP laboratory. The diamond sensor (white) is connected by an indium band to the sense resistor, which will be bonded to the FPS ASIC (gray).

As this report is being drafted, the Carrier Board is in fabrication and due into the SCIPP laboratory for assembly the week of March 25. The control board is nearing completion and should be fabricated and available for assembly the following week.

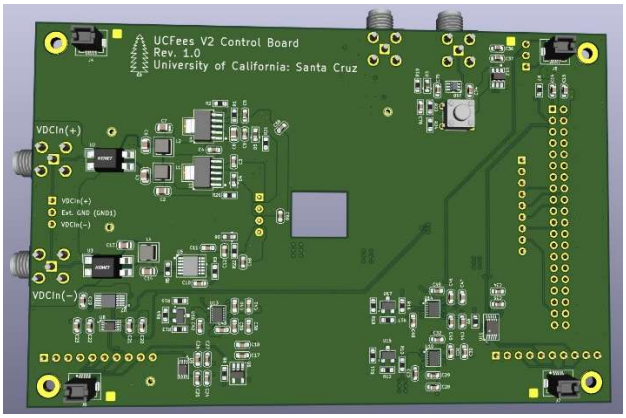

Figure 5: Rendering of FPS Control Board design.

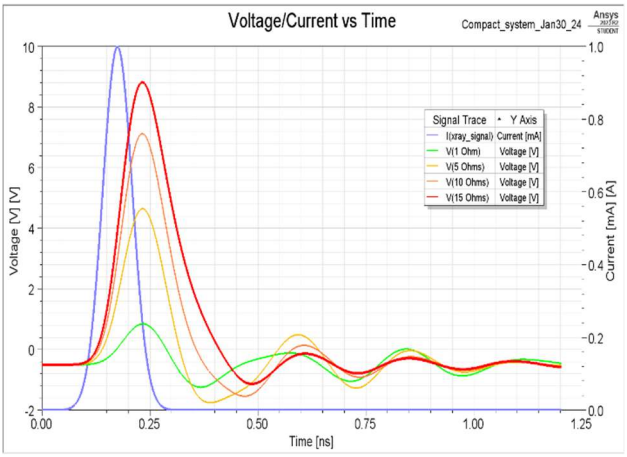

Figure 6: HFSS simulation of signal-path response.

Initial Results from HFSS: The basic signal-path assembly has been modeled in HFSS, and its response to a 5 GHz (~75 ps risetime) signal impulse has been simulated (Figure 6), as a function of the value of the signal-path resistor. For the nominal 10 Ω resistance, signal completion occurs in approximately 200 ps, consistent with a 5 Gs/s readout frame rate. HFSS simulations also suggest that the signal integrity will be retained when picked off by a single short wire-bond connection to the ASIC input.

Future Plans: Approximately 2 ½ years remain on the project. Work over the next 12 months will follow several thrusts. The single-channel integrated detection system will be tested in the lab, and in a test beam at the LCLS or other facility, and results used to inform and calibrate upcoming continued design activity. The design of the four-channel quadrant sensor needed to instrument the position-sensing detection system has been completed, and two 3x3 mm^2 quadrant sensors will soon be fabricated by the LANL group. Discussions are beginning about the design of the next version of the ASIC, which will instrument the quadrant sensor, and a student that will carry out the design under the guidance of the LBNL group has been identified at UC Davis. HFSS studies will continue, guiding the optimization of the signal path, and the detector/readout integration strategy. Our goal is, over the next 12 months, to conduct a testbeam-based study of the single-channel detection system, and then complete the ASIC and signal path designs for the quadrant position-sensing version.

Finally, the group is exploring the application of the high-bandwidth technology to the field of plasma ignition diagnostics. A meeting was held at LBNL on February 8, 2024, to discuss prospects for the use of the technology for fusion research. In addition to AAD collaboration members funded by this award, representatives from Lawrence Livermore National Laboratory and the Second Order Effects corporation participated in the discussion. We intend to continue to look into possible applications in this area over the next year.

References

1. T. Prakash, C. Rowling, *FastPulse Precision Sampler (FPS) Datasheet*, http://scipp.ucsc.edu/~schumm/GHz_readout/UCFEES_V2_(FPS)_DATASHEET_v1.0.pdf

2. Publications

1. R. Padilla, F. Martinez-McKinney, B. A. Schumm, and M. Wilder, *A 50 MHz Position-Sensitive Pass-Through X-ray Diagnostic* (in preparation)

2. M. Nizam, P. Freeman, M. Gulley, M. Kennedy, D. Kim, F. Martinez-McKinney, R. Padilla, E. Prebys, B. A. Schumm, M. Tarka, and M. Wilder, *Real Time Study of Radiation Damage in Diamond Sensors* (in preparation)

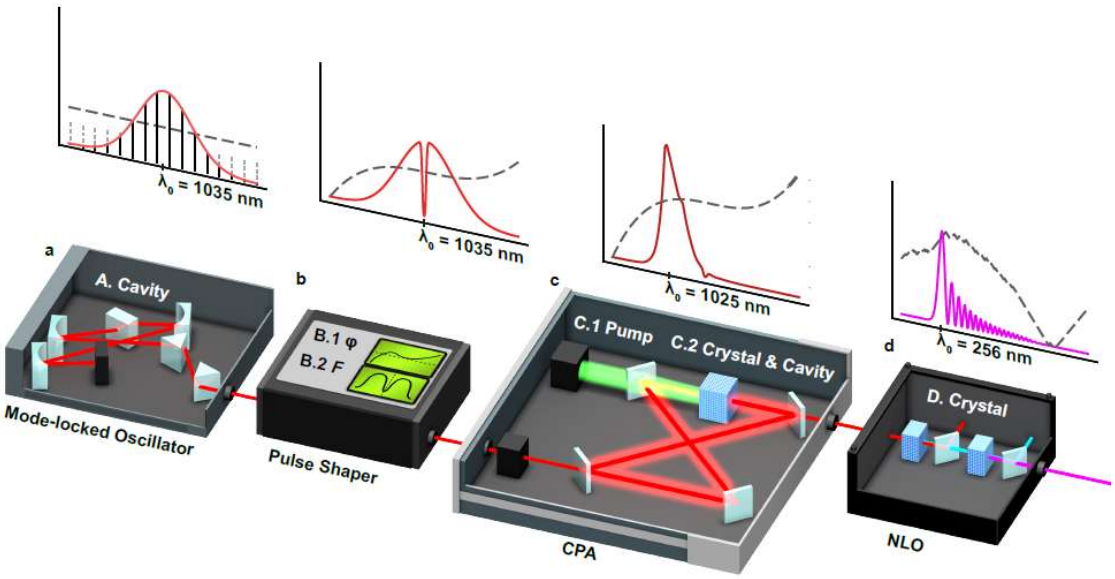

Start-to-end software modeling is integral for fully exploring the capabilities of complex cascaded high-power laser systems. The present system, mimicking the photoinjector laser at SLAC National Accelerator Laboratory's LCLS-II, consists of a mode-locked 1035 nm infrared laser that undergoes spectral intensity and phase shaping, amplification by a chirped pulsed amplifier (CPA), and finally nonlinear optical (NLO) upconversion to ultraviolet. At each step, the spectral and temporal profiles can change drastically depending on the devices and parameters under test. Courtesy: Sergio Carbajo, Jack Hirschman, and Greg Stewart, Stanford University and University of California Los Angeles (Hirschman, et al., Optics Express 32.9, doi:10.1364/OE.520542, 2024) (Lemons, et al., Phys. Rev. Accel. Beams 25, doi.org/10.1103/PhysRevAccelBeams.25.013401, 2022)

Next-generation Photoinjectors for High-Brightness Beams and XFELs

Sergio Carbajo [1-4]

[1]*Department of Electrical and Computer Engineering, University of California Los Angeles, Los Angeles, CA 90095, USA*
[2]*Department of Physics and Astronomy, University of California Los Angeles, Los Angeles, CA 90095, USA*
[3]*SLAC National Accelerator Laboratory, Stanford University, 2575 Sand Hill Road, Menlo Park, CA, USA*
[4]*California NanoSystems Institute, 570 Westwood Plaza, Los Angeles, CA 90095, USA*

Keywords: light shaping, X-ray Free Electron Lasers, nonlinear optics, light-matter interactions, photoemission dynamics.

Research Project Scope

The development of high-quality electron sources plays a critical role in enabling a range of high-impact applications for both DOE and other national funding agencies as well as university- and industry-level research and development. These include the development of short-wavelength high-gain free electron lasers, ultrafast electron diffraction and microscopy, Inverse Compton Scattering, injection into very high gradient advanced accelerators, and high-power THz generation. Even more enticing opportunities could be accessed by pushing the brightness limits of charged-particle sources ushering in new beam physics, enabling a significant reduction in size and cost of future accelerators to tackle urgent societal challenges – spanning discovery science, industrial applications, medicine, and national security.

The first factor limiting electron beam brightness in accelerators and accelerator-based light sources is electron generation physics. As such, the role of photoinjector laser shaping – in time, frequency, and space – is paramount to all photoinjectors, thereby making high-fidelity control of the photoinjector drive laser central to producing electron beams. More specifically, laser spectro-temporally shaping offers a refined knob to tailor the phase space of electrons. Photoinjector lasers lie conventionally in the ultraviolet (UV) range and are very complex and costly to control fully, and thus photoinjectors worldwide lack adequate shaping capabilities. These shortcomings are exacerbated by the emerging requirement to operate at high average power and high repetition rate, imposing unprecedented laser-damage issues that challenge their practical implementation and delivery for a 24/7 science- or industry-level facility.

In pursuit of high-brightness electron beam sources capable of tackling the challenges above, this project aims to develop and test a novel simultaneous up-conversion amplification and spectro-temporal shaping technique that addresses high average power, efficient, high quality, stable, and tunable-wavelength photoinjector laser pulse generation. This method offers human- or artificial intelligence (AI)-based dynamic programmability of the laser and electron beam temporal shapes to reduce emittance and control the 6D-phase space for fast and real-time optimization and photoemission mode multiplexing, among others. As a front-end technology, the new family of photoinjectors enabled by the research and developments in this proposal will have the potential for seminal impact across multi-mission facilities in basic energy sciences and high energy physics, and a strong linkage with strategic DOE and laboratory initiatives in machine learning, ultrafast X-ray sciences, and high data rate computation.

Recent Progress

As an emerging technique, we have designed and deployed a degenerate four-wave mixing (dFWM)-based laser architecture that experimentally demonstrates for the first time temporal shaping and tunable UV-visible photoinjector laser pulse production that tackles the challenges above, primarily represented by (1) programmable spectro-temporal shaping, (2) wavelength tunability, (3) high conversion efficiency, and (4) kW-average and GW-peak power handling and scaling simultaneously.

Simulation and Desing Principles. FWM is a nonlinear optical phenomenon wherein new sum-frequency and difference-frequency signals are produced. In a nominal demonstration approach, we have designed a multi-W average power-driven dFWM system in which the two pump photons with angular frequency ω_p originate from the same pump pulse at around 515 nm wavelength so that a simple second-harmonic stage is used from our 1 MHz Yb-based driver at 1030 nm. The

signal photon (ω_s) comes directly from the Yb front-end at and is finally mixed in dFWM to an idler photon at $\omega_i = 2\omega_p - \omega_s$. The linear wave vector mismatch, $\Delta\beta$, is the propagation constant calculated by considering the full dispersion profile of the fundamental EH_{11} mode of a gas-filled HCF such that by changing the core size, gas species, gas pressure, pump, and seed frequencies, the linear phase-matching condition can be easily fulfilled over multiple octaves. The nonlinear Schrodinger equations (NLSEs) govern the complex amplitudes of the pump, signal, and idler under the slowly varying envelope approximation. Our calculations adopt the Runge-Kutta Fourth Order (RK4) method to solve the coupled NSLEs[1]. We expect moderate to high conversion efficiencies through the interplay between gas pressure and phase-matching conditions. We will also explore higher-intensity approaches – namely, variable seeded and unseeded schemes – whereby, under the appropriate design parameters, other strong (i.e. self-phase modulation) and weak (i.e. solitons) nonlinear effects can cooperate to render

Fig 1: (a) depiction of the idler, signal, and pump in dFWM; (b) peak power and upconversion evolution as a function of HCF position (z) for all pump, signal, and idler waves.

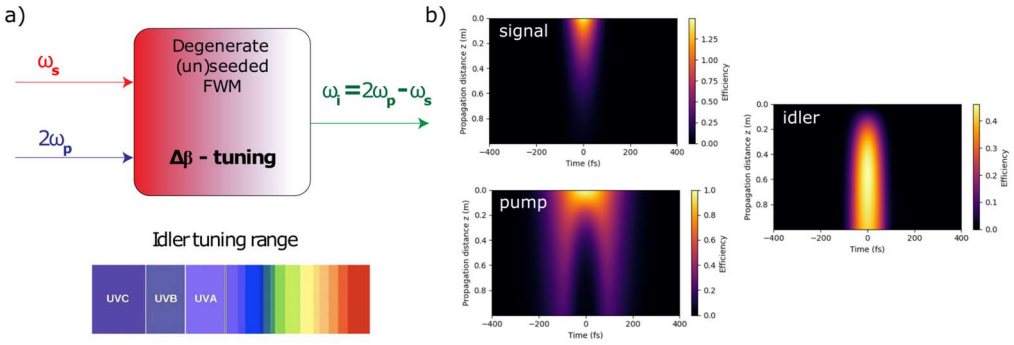

wavelength-tunable sources relying on frequency-broadened and dispersion-managed sum-frequency mixing[2,3]. Fig. 1 depicts the typical energy conversion efficiency from the input signal and pump to UV-Vis (idler) in a gas-filled HCF when pumping at the second harmonic of the Yb:KGW laser and seeding at its fundamental to generate a dFWM signal centered in the UV. By changing the gas-filling, it is indeed possible to directly tune emission wavelength. This technique has been shown to work at different pumping peak powers, from a few MW to several GW, and with different pulse durations from a tends of few femtoseconds to several tens of picoseconds[4], as required by most linac and XFELs. Our NLSE model suggests that 48% conversion efficiency is possible in the UV range under this so-called low-dispersive dFWM regime. In essence, this emerging regime we're exploring sacrifices some of the conversion efficiency in exchange for a direct and quasi-linear mapping of signal to the idler with the pump as a proxy photon state (see "*Spectro-Temporal Shaping Capabilities*").

Experimental Apparatus. The laser system is a 20W, 1 MHz, Yb:KGW chirped-pulse amplifier (PHAROS-SP, LightConversion) with ~150 fs transform-limited duration (schematic in Fig. 2). A delay line ensures that the path of the signal overlaps the signal and pump pulse inside the HCF. To efficiently couple light to the HCF, zoom telescopes are designed to increase the beam size of the pump and signal. The pump and signal beams are combined with a dichroic mirror and focused down to ~65 um in diameter intensity at the HCF input tip. In this configuration, we produce 20 µJ UV pulse energy at up to 1 MHz repetition rate (20 W of average UV power) under the following conditions: 100 µJ pump and signal energy pulses of ~220 fs pulse duration each into a ~1 m long,

100 μm inner-diameter HCF with 0.63 bar pressure of Ar gas. This expected performance exceeds the minimum laser energy required in all planned RF gun testbeds, all in the sub-μJ to few-μJ level, including the LCLS-II photoinjector RF gun and the RadiaBeam ICS beamline.

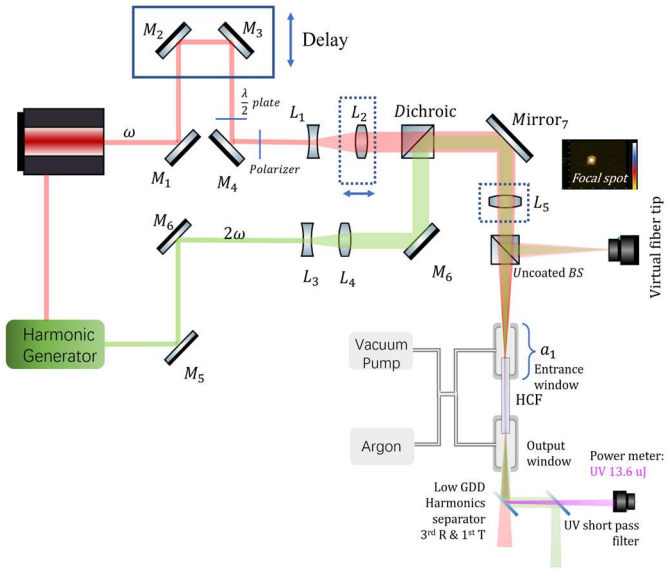

Fig. 2: Experimental schematic of dFWM in a HCF. The 1030 nm (515 nm) laser line is shown with the red (green) line.

Spectro-Temporal Shaping Capabilities. The pulse duration can be easily controlled by a pulse stretcher by adding parabolic Group Delay Dispersion (GDD). We have studied the case where the signal light is stretched while the pump light is still transform limited. Fig. 3 captures these studies showing the spectra for the UV pulse versus different signal-pump delays. Fig. 3.b. and .c represent the IR signal pulse with positive ($GDD \approx 8 \times 10^4\ fs$) and negative ($GDD \approx -8 \times 10^4\ fs$) linear chirp, respectively, with pulses scratched to ~1000 fs in both cases. We also measure the 2000 fs pulse with a negative chirp ($GDD \approx -1.6 \times 10^5\ fs$) as shown in Fig. 3.e. When the signal light precedes the pump, for a positive linear chirped signal beam, the shorter wavelength part will be mixed with the pump, resulting in the UV idler that is shifted to longer wavelengths. As the delay is reduced, the situation is reversed. Based on these spectral trace maps, we can also deduce that the positive chirped signal should induce a negative chirped idler pulse. It should be noted that the trace map in Fig. 3.a is still tilted under the pump and signal energy of $10uJ$ and $5uJ$, which signifies the appearance of self-phase modulation (SPM) in the HCF for the IR beam. SPM could result in a normal dispersion related to its temporal shape. Thus, the generated UV idler would be slightly negative chirped as shown in Fig. 3.a. This tilt could be eliminated by decreasing the total pump & signal power down to $2uJ$ and $1uJ$ per pulse, as shown in Fig. 3.d. The chirp rates were controlled by the pulse stretcher, while the pump light at $515\ nm$ was still transform-limited. The GDD of the signal IR pulse in a, b, c, and e are about 0, $8 \times 10^4\ fs, -8 \times 10^4\ fs, 1.6 \times 10^5\ fs$, under the pump and signal energy at $10uJ$ and $5uJ$. Figure 3d shows near transform-limited IR pulse at $1\ uJ$. f. Description of gas pressure affecting FWM efficiency. The curve embedded in .f is the condition for phase matching of different hybrid modes. The red (yellow) star represented that the peak was the EH_{11} (EH_{12}) mode shown from the red (yellow) curve embedded under the pressure at $0.6\ bar$ ($2.9\ bar$). We did not reach the EH_{13} mode because the phase matching pressure (> 7 bar) is too high for our system.

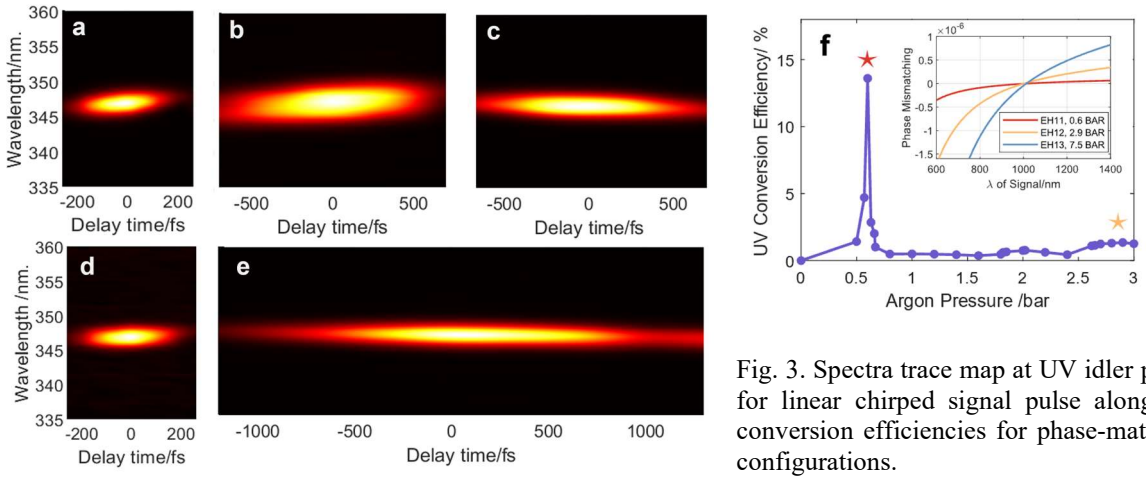

Fig. 3. Spectra trace map at UV idler pulse for linear chirped signal pulse alongside conversion efficiencies for phase-matched configurations.

Future Plans

This versatility alone places FWM-based methodologies at the forefront of next-generation photoinjector laser technology, which Carbajo will leverage using start-to-end simulations and applied ML-optimization routines underway[5–7].

References

1. Hirschman J, Lemons R, Wang M, Saripalli R, Krötz P, Belli F, et al. Linking a start-to-end software model and neural networks for optimization of CPA laser systems. AI and Optical Data Sciences IV. SPIE; 2023
2. Carbajo S, Granados E, Schimpf D, Sell A, Hong K-H, Moses J, et al. Efficient generation of ultra-intense few-cycle radially polarized laser pulses. Opt Lett. 2014;39: 2487–2490.
3. Travers JC, Grigorova TF, Brahms C, Belli F. High-energy pulse self-compression and ultraviolet generation through soliton dynamics in hollow capillary fibres. Nat Photonics. 2019;13: 547–554.
4. Belli F, Abdolvand A, Travers JC, Russell PSJ. Highly efficient deep UV generation by four-wave mixing in gas-filled hollow-core photonic crystal fiber. Opt Lett. 2019;44: 5509–5512.
5. Hirschman J, Lemons R, Coffee R, Belli F, Carbajo S. Towards Real-time Adaptable Machine Learning-based Photoinjector Shaping. Conference on Lasers and Electro-Optics. Optica Publishing Group; 2021. p. STh1B.7.
6. Zhang H, Hirschman J, Lemons R, Sun L, Lu B, Carbajo S. A new integrated machine learning framework for advanced photoemission. Laser Beam Shaping XXIII. SPIE; 2023. pp. 95–98.
7. Hirschman J, Wang M, Carbajo S. LSTM nonlinear dynamics predictor for accelerating data generation in ultrafast optics and laser system design. Optica Open. 2023. doi:10.1364/opticaopen.23605839.v2

Publications

Zhang, Hao, et al. "The LCLS-II Photoinjector Laser Infrastructure." *in press HPLSE*

Hirschman, Jack, Minyang Wang, and Sergio Carbajo. "LSTM Nonlinear Dynamics Predictor for Accelerating Data Generation in Ultrafast Optics and Laser System Design." *in press Optics Express*

Lu, Brittany, et al. "High-efficiency, single-stage tunable optical parametric amplifier for visible photocathode applications." *Optics Letters* 49.3 (2024): 450-453.

Wong, Lee Wei Wesley, et al. "Free-electron crystals for enhanced X-ray radiation." *Light: Science & Applications* 13.1 (2024): 29.

Hirschman, Jack, et al. “Linking a start-to-end software model and neural networks for optimization of CPA laser systems.” *AI and Optical Data Sciences*, 2023.

Lemons, Randy, et al. "Temporal shaping of narrow-band picosecond pulses via noncolinear sum-frequency mixing of dispersion-controlled pulses." *Physical Review Accelerators and Beams* 25.1 (2022): 013401.

Cesar, David, et al. "Electron beam shaping via laser heater temporal shaping." *Physical Review Accelerators and Beams* 24.11 (2021): 110703.

High Brightness Photocathodes in Photoinjectors

PI – Prof. Siddharth Karkare

Keywords: Photocathodes, Photoemisison, Photoinjectors, High Brightness Electron Beams

Research Project Scope

The performance of existing and future ultrafast science instruments like X-ray Free Electron Lasers (XFELs) and Ultrafast Electron Diffraction (UED) and microscopy (UEM) experiments is limited by the brightness of electron beams produced from photocathodes in photoinjectors. Generation of brighter electron beams from photoinjectors requires the development of photocathodes capable of emitting electrons with the smallest possible mean transverse energy (MTE), or equivalently, smallest possible intrinsic emittance.

With the goal of improving the performance of the above applications, over the last decade, a significant effort has gone into understanding the process of photoemission and reducing the MTE of electrons emitted from cathodes. As a result, several ways of achieving low MTEs of 20-30 meV have been developed and MTE as low as 5 meV has been demonstrated. Despite these large improvements in MTE, photoinjectors still use cathodes with a large (~500 meV) MTE.

This proposal aims to identify and resolve the issues involved in using these low-MTE cathodes in photoinjectors and develop cathodes for low-MTE (sub-25 meV) operation in new photoinjectors, resulting in nearly 25 times brighter electron beams. The ultimate goal of the proposal is to demonstrate low-MTE (and thus high-brightness) operation in the existing and new photoinjectors being developed to power future XFEL and UED/UEM facilities.

The proposed increase in brightness will result in a dramatically increased X-ray pulse energy in existing XFELs maximizing their potential to study atomic and electronic structural dynamics in quantum materials, electronic and nuclear coupling in biological and chemical processes and energy materials in situ. It is also critical for the development of compact XFELs to make them widely accessible. For UED/UEM applications, the proposed increase in beam brightness will imply increase in the spatio-temporal resolution greatly increasing the scientific reach of these ultrafast electron scattering techniques. Thus, this work will transform the capabilities of various existing and upcoming DOE facilities, opening new frontiers in ultrafast studies of quantum materials, energy technologies and critical biological processes.

Recent Progress

The progress on this project has been divided into 4 major tasks/goals:

1. Development of an Advanced Photocathode Characterization Lab: This goal aims to develop a lab that has the capability to perform all relevant photocathode materials, surface, and photoemission characterization in UHV to identify the various factors that affect the MTE and

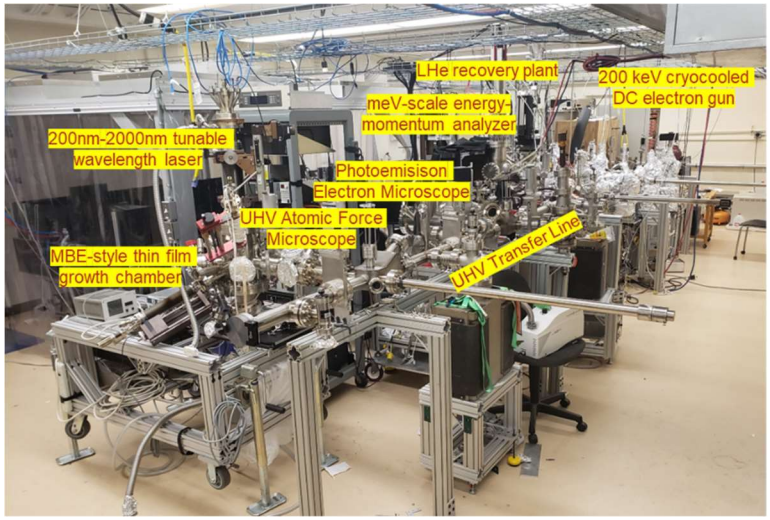

Figure 1: ASU Photoemission and Bright Beams Lab showing the various surface, photoemission diagnostic and electron beam facilities.

develop high brightness cathode materials. This ASU photocathode research facility (Photoemisison and Bright Beams Lab) was completed in 2023. It comprises of a thin-film deposition chamber (capable of growing alkali-antimonide and other materials), atomic scale surface diagnostics and preparation capabilities (like ion-bombardment, annealing, Low Energy Electron Diffraction, Auger Electron Spectroscopy), a PhotoEmisison Electron Microscope capable of measuring the transverse momentum spread and the spatial uniformity of emission to 40 nm resolution, an UHV – Atomic force microscope and Scanning Tunneling Microscope, an meV-energy scale electron energy analyzer [1] and a 200kV DC gun with an electron beam characterization beamline, all connected in UHV [2] (figure 1). It also houses a tunable wavelength, 150 fs, 500 kHz pulsed laser capable of delivering wavelengths from 200 nm to 2000 nm.

2. Characterization under high-fluence and high-field conditions: This goal aims to characterize cathode performance in typical photoinjector conditions of high fluence and high electric fields for cathode which have already demonstrated low (sub-25 meV) MTE otherwise. These include single-crystal metal cathodes (Cu(100) and Ag(111)) and alkali-antimonides. We have performed a detailed characterization of graphene coated Cu(100) and shown that this robust single crystal cathode can deliver an MTE as low as 10 meV at cryogenic temperatures of 90 K at the photoemission threshold with minimal in-vacuum preparation. We also performed measurements of MTE at large laser fluences comparable to those used in photoinjectors for extraction of large charge densities. Our measurements show that MTE from low QE metal cathodes is limited to a few 100 meV due to non-linear photoemission processes [3]. To obtain lower MTE high QE cathodes like alkali-antimonides must be used to mitigate effects of non-

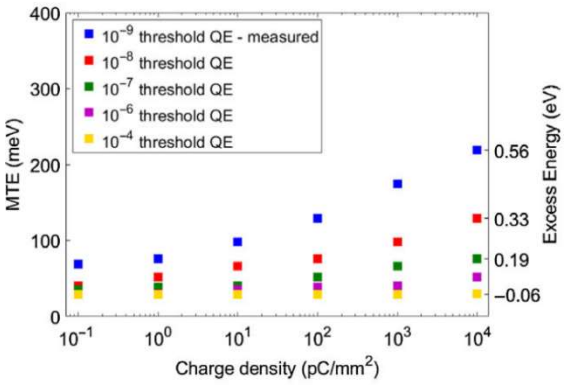

Figure 2: Smallest attainable MTE as a function of charge density for various at-threshold cathode QEs after accounting for non-linear photoemission effects. The right y-axis shows the excess energy at which the smallest MTE will be attained. Threshold QE of 10-4 is essential to obtain near-thermal MTE of 25 meV at large charge density.

linear photoemission. Figure 2 shows the smallest attainable MTE as a function of charge density at the cathode for various QEs at the photoemission threshold.

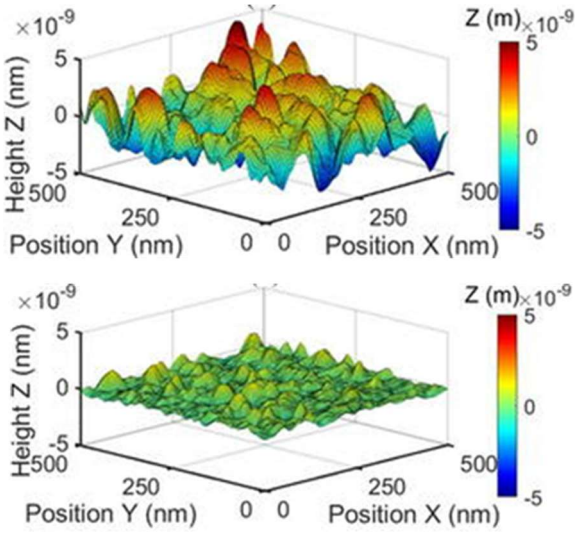

Figure 3: Topography of alkali-antimonide surface grown on disordered Si surface (top) and on lattice matched strontium titanate (bottom). Surface topographies were measured using an UHV AFM in the ASU photoemission and bright beams lab. Calculations show that the growth of Strontium Titanate is smooth enough that the effects of roughness on MTE are negligible even at 100 MV/m electric fields.

Alkali-antimonide cathode thin films have such large at-threshold QEs, but often have large surface roughness making their operation under large electric fields problematic. We have developed techniques to grow atomically smooth polycrystalline Cs3Sb and characterized its QE and MTE performance. According to our calculations, the surface roughness is small enough that it will not impact MTE even in large 100 MV/m electric fields. Our detailed QE, MTE and energy distribution measurements indicate that Cs_3Sb has ~40 meV MTE with 10^{-4} QE at room temperature and 1.8 eV photon energy., sufficient to overcome non-linear photoemission effects. The higher than thermal MTE is due to a low work function of 1.5 eV. Other alkali-antimonides are being explored to obtain sub-25 meV with 10^{-4} QE [4].

3. Discovery of Low MTE Cathode Materials: This goal aims to identify and discover new cathode materials and nanostructures that can deliver low MTE and emittance in photoinjectors. We have investigated the performance of several novel cathode materials including nitrogen incorporated ultra-nano-crystalline-diamond [5], N-polar GaN, and Cd_3As_2 – a Dirac semimetal, to characterize their QE and MTE performance. We have also developed plasmonic nanostructures to focus light down below the diffraction limit on a flat gold surface and emit electrons from a 50 nm rms emission area resulting in an emittance of less than 40 pm. We have also developed photonics integrated cathodes in which light is guided through photonic waveguides nanofabricated onto a substrate to specific areas under a photoemissive film resulting in a new way of spatio-temporally pattering and achieving low MTE, high QE and a quick response time simultaneously.

4. Operation in High Gradient Photoinjectors: This goal aims to test the performance of novel low-MTE photocathode materials in upcoming high rep-rate SRF photoinjectors or high field photoinjectors. Testing will be performed in the ASU DC gun capable of going to 10 MV/m fields at cryogenic temperatures and in the Pegasus RF gun at UCLA. The ASU photocathodes lab allows for easy UHV transfer of cathodes from the growth chamber into the DC gun. For transfer into the

Pegasus RF gun, we have started development of a new alkali-antimonide growth chamber capable of hosting INFN plugs compatible with the Pegasus RF gun at UCLA.

Future Plans

We plan to test the performance of other high QE alkali-antimonide materials in terms of their QE and MTE and test their performance at cryogenic temperatures in the ASU-DC gun. We will commission the new INFN-plug-compatible growth chamber to test the performance of alkali-antimonide cathodes in the UCLA Pegasus RF gun.

We also plan to continue exploration of novel cathode materials and nanostructures to obtain low MTE and emittance with high QE.

References

1. S. Karkare, J. Feng, J. Maxson and H. Padmore, *Development of a 3-D energy-momentum analyzer for meV-scale energy electrons*, Rev. Sci. Instrum. 90, 053902 (2019)

2. G. Gevorkyan, C. Cardenas, A. Kachwala, C. Knill, T. Hanks, P. Bhattacharyya, J. Maxson, I. Bazarov, L. Cultrera, A. Galdi, and S. Karkare *A cryogenically cooled 200 kV DC photoemission electron gun for ultralow emittance photocathodes,* Rev. Sci. Instrum. 94, 091501 (2023)

3. C. Knill, S. Douyon, K. Kawahara, H. Yamaguchi, G. Wang, H. Ago, N. Moody, and S. Karkare *Effects of nonlinear photoemission on mean transverse energy from metal photocathodes,* Phys. Rev. Accel. Beams 26, 093401 (2023)

4. A. Kachwala, P. Saha, P. Bhattacharyya, E. Montgomery, O. Chubenko and S. Karkare, *Demonstration of thermal limit mean transverse energy from cesium antimonide photocathodes,* Appl. Phys. Lett. 123, 044106 (2023)

5. A. Kachwala*, O. Chubenko, D. Kim, E. Simakov, and S. Karkare *Quantum efficiency, photoemission energy spectra, and mean transverse energy of ultrananocrystalline diamond photocathode,* J. Appl. Phys. 132, 224901 (2022)

Publications

1. X. Guo, D. Chaudhuri, N. Bielinski, J. Chen, S. Kim, T.C. Chiang, F. Mahmood, J. Soares, S. Karkare, P. Abbamonte, *Characterization of a LaB6 tip as a thermionically enhanced photoemitter,* Appl. Phys. Lett. 124, 014103 (2024)

2. P. Saha, E. Montgomery, S. Poddar, O. Chubenko, S. Karkare, *Ion-beam-assisted growth of cesium-antimonide photocathodes*, J. Vac. Sci. Technol. B 41, 064004 (2023)

3. C. Knill, S. Douyon, K. Kawahara, H. Yamaguchi, G. Wang, H. Ago, N. Moody, and S. Karkare *Effects of nonlinear photoemission on mean transverse energy from metal photocathodes,* Phys. Rev. Accel. Beams 26, 093401 (2023)

4. G. Gevorkyan, C. Cardenas, A. Kachwala, C. Knill, T. Hanks, P. Bhattacharyya, J. Maxson, I. Bazarov, L. Cultrera, A. Galdi, and S. Karkare, *A cryogenically cooled 200 kV DC photoemission electron gun for ultralow emittance photocathodes*, Rev. Sci. Instrum. 94, 091501 (2023)

5. A. Kachwala, P. Saha, P. Bhattacharyya, E. Montgomery, O. Chubenko and S. Karkare, *Demonstration of thermal limit mean transverse energy from cesium antimonide photocathodes* Appl. Phys. Lett. 123, 044106 (2023)

6. P. Saha, O. Chubenko, J.K. Nangoi, T. Arias, E. Montgomery, S. Poddar, H. Padmore, and S. Karkare *Demonstration of thermal limit mean transverse energy from cesium antimonide photocathodes*, J. Appl. Phys.133, 053102 (2023)

7. C. Knill, H. Yamaguchi, K. Kawahara, G. Wang E. Batista, P. Yang, H. Ago, N. Moody and S. Karkare *Near Threshold Photoemission from Graphene Coated Cu(110)*, Phys. Rev. Applied 19, 014015 (2023)

8. A. Kachwala, O. Chubenko, D. Kim, E. Simakov, and S. Karkare *Quantum efficiency, photoemission energy spectra, and mean transverse energy of ultrananocrystalline diamond photocathode,* J. Appl. Phys. 132, 224901 (2022)

9. L. Cultrera, E. Rocco, F. Shahedipour-Sandvik, L. Bell, J. Bae, I. Bazarov, P. Saha, S. Karkare, A. Arjunan, *Photoemission characterization of N-polar III-nitride photocathodes as candidate bright electron beam sources for accelerator applications*, J. Appl. Phys. 131, 124902 (2022)

10. P. Saha, O. Chubenko, G. Gevorkyan, A. Kachwala, C. Knill, H. Padmore, E. Montgomery, S. Poddar, S. Karkare *Physically and chemically smooth Cs3Sb thin films on lattice matched substrates* Appl. Phys. Lett.. 120, 194102 (2022).

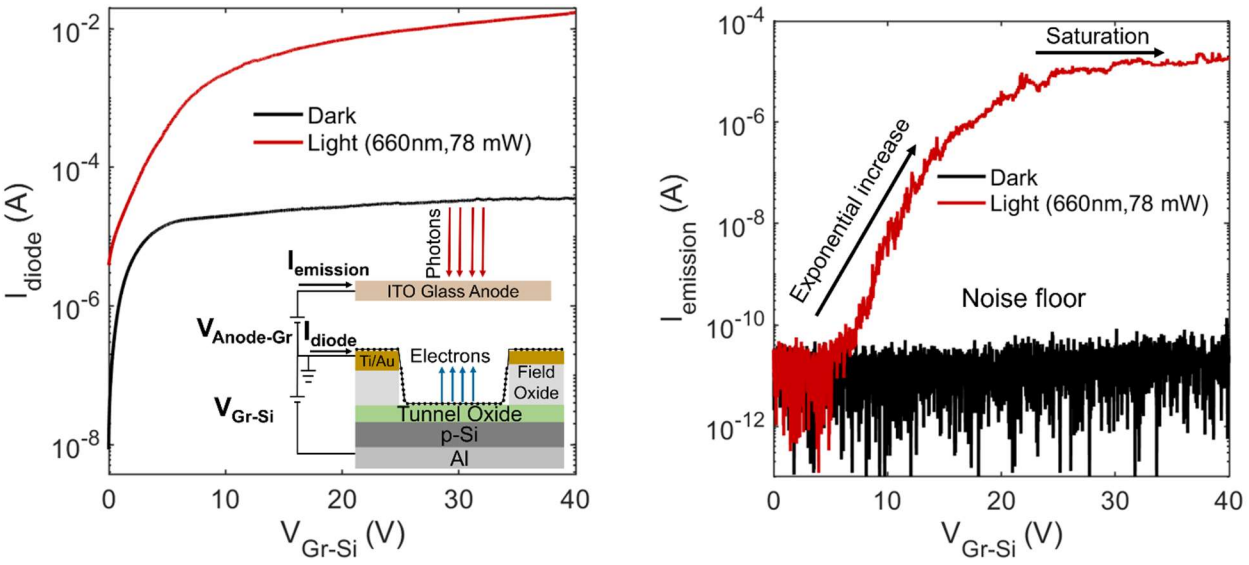

A semiconductor/insulator/graphene heterostructure device under optical illumination emits electron beam into vacuum when an appropriate bias is applied between the semiconductor and graphene. The bias voltage electrostatically generates a tunable negative electron affinity surface at graphene and allows electron emission with high external quantum efficiency. This hot electron laser assisted cathode (HELAC) device shows excellent stability in air and does not suffer from cathode poisoning which is common for typical photocathodes. Courtesy: Rehan Kapadia, University of Southern California (Priyoti, Anika Tabassum, et al. "Electrostatically Generated Air-Stable Negative Electron Affinity Silicon Photocathode." ACS Photonics 10.12 (2023): 4501-4508.)

High Brightness Electronically Tunable Negative Electron Affinity Cathodes for Accelerator Applications

PI: Rehan Kapadia

Keywords: Cathode, Negative Electron Affinity, Semiconductor, Photoemission

Research Project Scope

The goal of this project is to (i) experimentally demonstrate a photocathode that simultaneously exhibits EQE~1%-10%, response times ~1-10 ps, and MTEs<40meV, (ii) establish theoretical limits for the performance of the proposed photocathode technology, and (iii) identify a route towards integrating such a cathode into an electron gun. We aim to achieve this by systematically identifying the challenges, both fundamental and technological, associated with this type of photocathode. We will build on the significant experimental and theoretical studies on NEA and other low-work function cathodes [14-27] and will broadly focus on understanding how the addition of an insulator, field-induced tunneling, and carrier scattering in graphene will affect the resulting device parameters.

Recent Progress

The semiconductor-insulator-graphene heterostructure device is schematically shown in Figure 1a. The device consists of a p-type silicon substrate ($5x10^{15}$ cm^{-3} boron doped), a thin (10 – 50 nm) insulating oxide (SiO_2/Al_2O_3) acting as the tunnel oxide, a thick insulating oxide (> 1 um) acting as the field oxide, a Ti/Au contact (5 nm/50 nm) on the field oxide, and a monolayer of graphene acting as the optically and electronically transparent electrode. A 100 nm thick Al layer acts as the ohmic contact to silicon while the Ti/Au layer acts as the ohmic contact to graphene. The field oxide separates the Ti/Au layer from tunnel oxide and silicon to ensure electron tunneling only through the tunnel oxide. Figure 1b shows a scanning electron micrograph of the device cross-section clearly identifying the tunnel and field oxide. Figure 1c shows the schematic of the measurement setup. A positive voltage is applied between the Ti/Au and Al contacts ($V_{Gr\text{-}Si}$ > 0V) and another positive voltage is applied between the anode and Ti/Au contact ($V_{Anode\text{-}Gr}$ > 0V). An ITO-coated glass slide acts as the optically transparent and electrically conductive anode which is placed at ~100 um distance from the graphene layer. When photons are incident on the device, the photogenerated electrons in silicon can tunnel through the thin tunnel oxide to reach graphene. The graphene-tunnel oxide-silicon junction, therefore, acts as a photoactivated tunneling diode. While tunneling through the oxide, these electrons can gain enough energy from the electric field in the oxide so that they can be emitted into vacuum and extracted by an anode. Figure 1d shows the current through the diode while Figure 1e shows the emission current for a device with 38 nm Al_2O_3 tunnel oxide (active area = 2.5 mm x 2.5 mm) as a function of applied $V_{Gr\text{-}Si}$ both in the dark and under illumination of a laser beam (660 nm, 65 mW). A $V_{Anode\text{-}Gr}$ = 40V was applied to extract the emitted electrons. Under dark conditions, the diode current is small and there is no emission current. However, as we increase $V_{Gr\text{-}Si,}$ we see an increase in both diode and emission

currents under illumination. When the electrons tunneling into graphene do not have enough

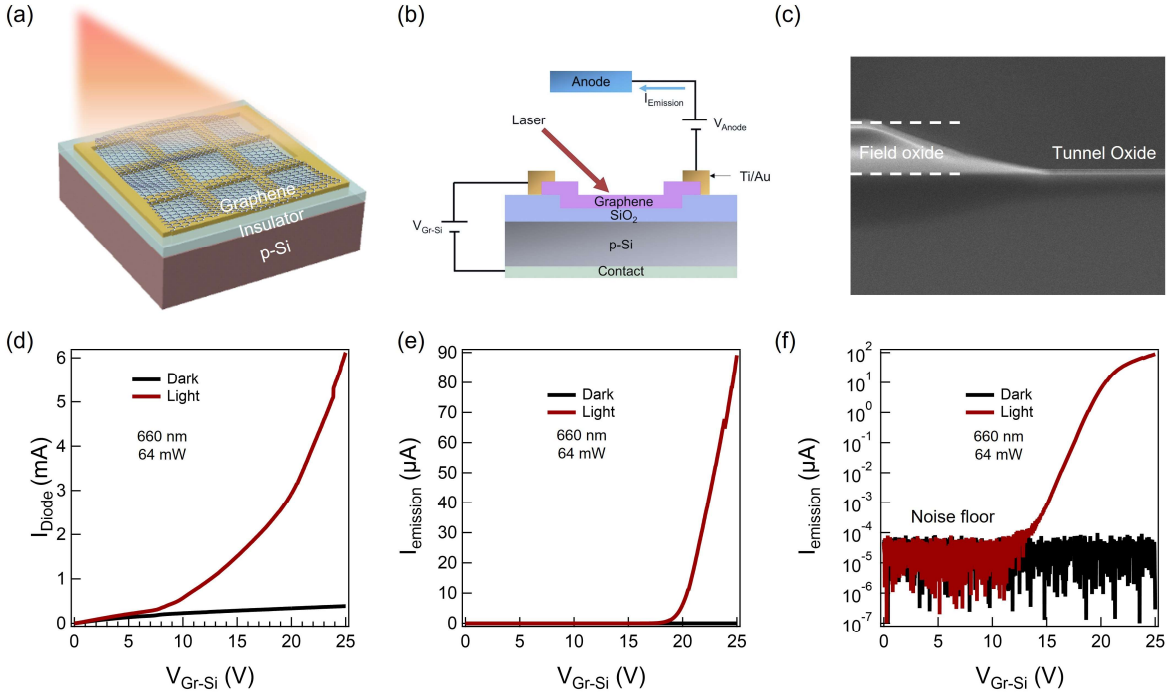

Figure 1: Electron emission from devices. (a) Cartoon schematic of the device (b) Schematic of the measurement setup (c) SEM image showing the thin tunnel oxide and thick field oxide (d) Diode current as a function of V_{Gr-Si} under light and dak conditions (e) Emission current in linear and (f) log scale under light and dark conditions

energy to emit into vacuum, they are collected by graphene constituting the diode current. Figure 1f shows the emission current in log scale where we can clearly observe the onset of electron emission at V_{Gr-Si} = 13V. Above this voltage, there is a fraction of the tunneling electrons which have enough energy to overcome the vacuum energy barrier and therefore constitute the emission current.

Figure 2a shows the emission currents for 38 nm Al_2O_3 tunnel oxide device at different applied V_{Gr-Si} as a function of applied anode voltage. A negative $V_{Anode-Gr}$ suppresses any electron with energy $E < qV_{Anode-Gr} + E_{vac}$ from emitting into vacuum. $\frac{dI_{emission}}{dV_{Anode-Gr}}$ therefore signifies the energy spectrum of the emitted electrons. As shown in Figure 2b, the maximum energy of the emitted electrons linearly increases with V_{Gr-Si}. If there were no scattering in the oxide, we would expect a sharp energy spectrum for the emitted electrons. The broadness of the electron energy spectrum is a direct result of the significant scattering of electrons in the oxide conduction band. At higher V_{Gr-Si} voltages, the electric field across the oxide can be large enough to allow impact ionization so that high energy electrons at oxide conduction band can ionize a valence band electron to conduction band. Such an elastic electron-electron scattering causes averaging of electron energies and significantly broaden the energy distribution of emitted electrons as shown in Figure 2a.

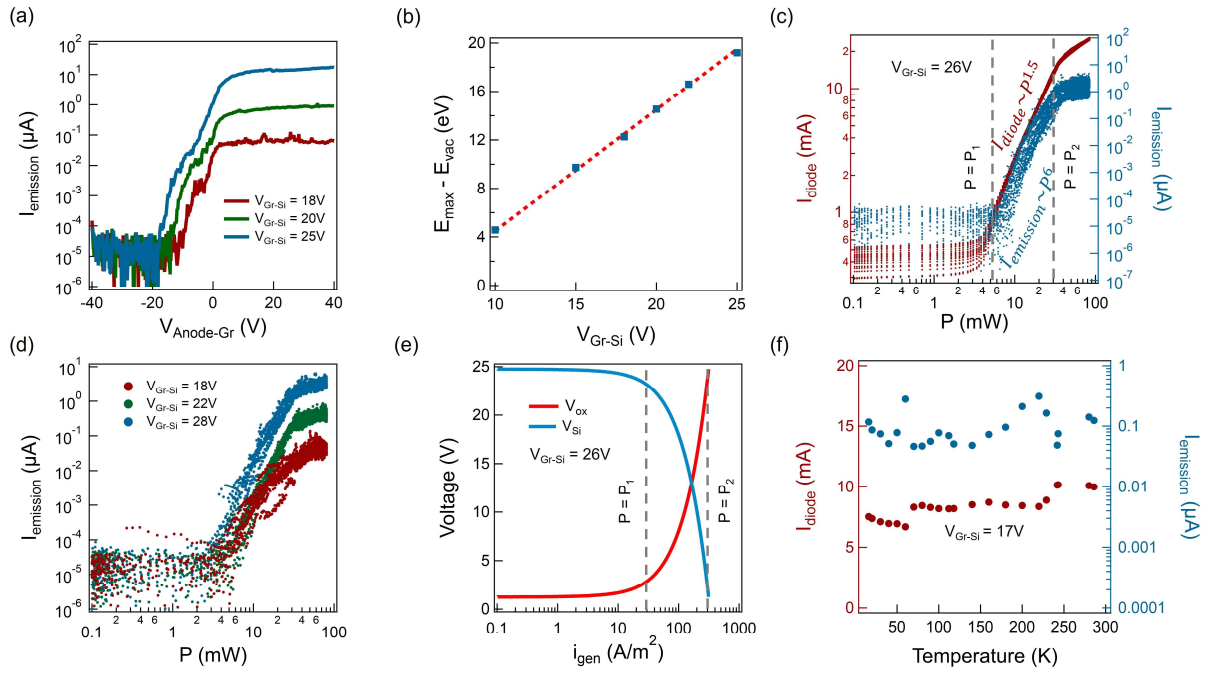

Figure 2: Anode voltage and optical power dependence. (a) Emission current as a function of applied anode voltage showing a broad energy distribution of electrons. (b) Maximum energy of emitted electrons as a function of anode voltage (c) Emission and diode current as a function of optical power showing nonlinear dependence at V_{Gr-Si} (d) Emission current as a function of optical power at different applied V_{Gr-Si} (e) Calculated voltage drops across oxide and silicon as a function of generation current density at V_{Gr-Si} = 26V (f) Temperature dependence of diode and emission current.

Figure 2c shows the diode and emission currents for a 30 nm SiO_2 tunnel oxide device as a function of incident optical power at V_{Gr-Si} = 26V and $V_{Anode-Gr}$ = 40V. Here, we can observe three regimes of operation: (1) small optical powers ($P < P_1 = 5$ mW), (2) intermediate optical powers (5 mW = $P_1 < P < P_2 = 50$ mW) and (3) large optical powers ($P > P_2 = 50$ mW). At smaller optical powers, dark generation rate dominates and the total current ($I_{total} = I_{diode} + I_{emission} \approx I_{diode}$) is nearly constant. When the photogenerated electron density exceeds that of dark electron density, we start seeing an increase in both diode and emission currents. This crossover between dark and optical generation dominated regimes occur at an optical power of ~ 5 mW (~100 mW/cm^2) where dark generation rate equals the optical generation rate (~5×10^{17} $cm^{-2}s^{-1}$). A total tunneling current through the oxide is ~ 1 mA (~16 mA/cm^2) translates to a net tunneling probability of ~0.4 under these conditions. As optical power increases the diode current then increases almost linearly until the optical power reaches ~50 mW. However, the emission current increases superlinearly within this regime where one order of magnitude increase in optical power causes ~6 orders of magnitude increase in emission current. Figure 2d shows similar superlinear increase in emission current at different applied V_{Gr-Si}. This is possible only if the energy gain and loss rates depend on the optical power. Neither electron-phonon nor impact ionization processes are dependent on the electron injection rate. The only other possibility is a change in energy gain rate due to increased optical power. If there is a change in oxide electric field due to a change in optical power, that would

affect the energy gain rate of the electrons in oxide conduction band and therefore result in a superlinear increase in emission current.

Figure 2e shows the calculated voltage drops across silicon and oxide regions as a function of generation current density ($i_{gen} = q(g_{dark} + g_{ph})$). We can clearly see a drastic increase in oxide voltage drop at the cost of silicon voltage for $i_{gen} \approx 30$ A/m^2 which translates to an optical power of ~ 5 mW for the device area (2.5 mm x 2.5 mm). For even larger $i_{gen} > 300$ A/m^2 (~50 mW), we see that V_{Si} would become negative and therefore we expect a saturation in current. These thresholds quantitatively match with the experimentally observed values of P_1 and P_2.

Figure 2f shows the temperature dependent diode and emission current measurements at both light (532 nm, 50 mW) and dark conditions. There is almost no temperature dependence of both the light and dark currents which indicates a predominant FN tunneling behavior of electrons. It is noteworthy that the electrons tunneling into oxide conduction band would still go through phonon scattering at lower temperatures since phonon emission does not require any preoccupation of phonons in the lattice. All these experimental results are in good agreement with our proposed mechanism of electron emission from the devices.

Future Plans

We are continuing to explore devices made from semiconductor substrates and exploring alternative insulators. We have also developed a monte-carlo Boltzmann transport solver for transport in oxides coupled with a Poisson-drift-diffusion solver to enable full simulation of these devices. Through this simulation, we are able to compare predicted and experimentally achieved results and improve our predictive design capabilities.

Publications

Put the list of publications in the recent 2-years SUPPORTED BY BES here. **If more than 10 publications, list only the 10 most relevant.**

1. A. T. Priyoti, R. Ahsan, H.U. Chae, S. Das, J. S. Vazquez, Z. Wu, H.G. Kim, Y. Yu, R. Kapadia, *Electrostatically Generated Air-Stable Negative Electron Affinity Silicon Photocathode*, ACS Photonics, **10**, 4501-4508 (2023).
2. Y. Zhou, R. Ahsan, H.U. Chae, R. Kapadia, P. Zhang, *Theoretical analysis of resonant tunneling enhanced field emission*, Physical Review Applied, **20**, 014043 (2023).

Photocathode material for the LCLSII-HE SRF gun

Lead PI: John Smedley (SLAC)

Participating Researchers: Jared Maxson (Cornell), Siddharth Karkare (ASU), Pietro Musumeci (UCLA), Theodore Vecchione (SLAC), Tianhuan Luo (LBNL)

Keywords: Photocathode, Accelerator, Semiconductor, High QE, Low MTE

Program Scope

The principal goal of this effort is to explore the performance of alkali antimonide and telluride cathodes under high-gradient fields. This information is critical in informing the choice of cathode for the SRF gun being developed for LCLS-II HE, as well as for predicting the ultimate performance of the injector based on this gun. The program has a tertiary goal of involvement in modern cathode development efforts, to ensure technological awareness of the photoinjector community.

This is a collaborative effort among Cornell, ASU, UCLA, LBNL and SLAC. Cornell and ASU lead the materials development effort and the low field testing. SLAC, along with Cornell and ASU, will grow cathodes on plugs compatible with the high field guns at LBNL (HiRES) and UCLA (Pegasus). High field testing is accomplished in these guns, as well as in the proximal probe system at ASU.

Recent progress

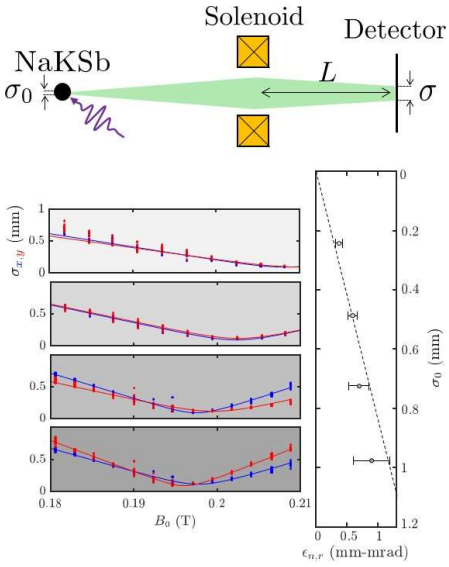

The effort is largely on schedule, with initial high gradient testing already occurring at UCLA with cathodes grown at Cornell and transported by plane. One Na-K-Sb cathode has already been tested in the Pegasus photoinjector at UCLA, with >1% quantum efficiency at visible wavelengths (400 nm) and expected MTE at 266nm. The operational lifetime under continuous operation was 3.5 days – shorter than expected but sufficient for initial testing. A second cathode is awaiting testing at high field for quantum efficiency, lifetime, and emittance.

Figure 8. Measurement of MTE of NaKSb cathode at the UCLA Pegasus laboratory using 266 nm illumination. The retrieved MTE (0.7 eV) is in line with the expectation given the short wavelength illumination.

A new suitcase compatible with INFN plug was fabricated at UCLA, tested on the Pegasus gun and subsequently brought to SLAC. This will enable alkali antimonide cathodes grown at SLAC to be transferred to UCLA in the coming year. A second suitcase compatible with the LBNL gun is being fabricated as well, to enable testing in the program's final year. This suitcase will use plugs that are specially designed to allow the surface field to reach 30 MV/m in the HiRES injector.

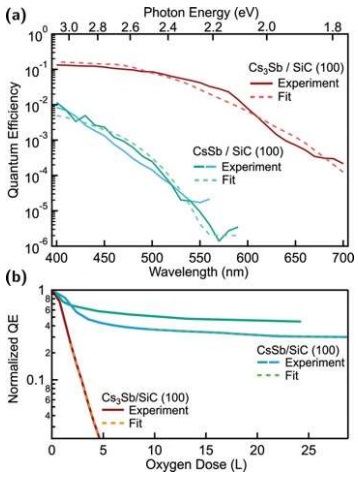

Figure 9: Quantum efficiency (a) and oxygen exposure lifetime (b) of CsSb vs Cs3Sb. The lifetime of the CsSb phase is 15x longer than Cs3Sb.

The Cornell photocathode lab characterized a new phase of alkali antimonide CsSb. This new phase was found to be near atomically flat (atomic rows visible in scanning tunneling microscopy images, and had up to 1% quantum efficiency in the blue region of the spectrum. Perhaps most importantly, this photocathode was an order of magnitude less sensitive to oxygen exposure than its sister phase Cs3Sb, which is a commonly used photocathode. The combination of high efficiency using visible light and vacuum robustness (See Fig. 1) makes it quite unique in the space of photocathode choice—no other cathode material exhibits both. This work was published in APL Materials and was selected as a featured article. [1]

In collaboration with the BNL cathode effort, team members from ASU, Cornell and SLAC demonstrated pulsed laser deposition of alkali antimonides, and partial epitaxy of Cesium Telluride and Alkali antimonides on several substrates. Two papers on this effort are in preparation.

The ASU team demonstrated the thermally limited MTE from Cs3Sb at threshold. Detailed measurements of the QE spectral response, photoemission energy distributions and MTE revealed that the work function at the photoemission threshold is 1.5 eV – 0.4 eV lower than the usually assumed value. We also discovered that Cs3Sb has a very low QE of 10-7 at this threshold photon energy making it unusable for low-MTE-high-charge-density applications. Our results point to the need for investigating the near-threshold performance of other alkali antimonide materials [2].

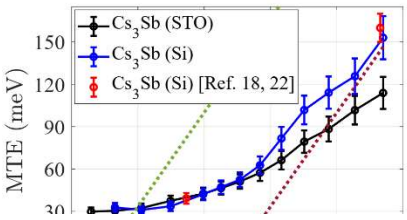

Figure 10:Detailed measurements of MTE as a function of photon energy show near-thermal MTE achieved from Cs3Sb at ~1.5 eV photon energy

ASU has also obtained several components from the old LBNL cathode growth chamber and used them to assemble a new growth chamber at ASU. This growth chamber is compatible with the INFN plugs and will be used to grow cathodes for testing in the Pegasus RF gun at UCLA and HIRES gun at LBNL. Due to the relative proximity of ASU to UCLA and LBNL it is expected that cathode transfer with several percent QE in the green will be possible easily

between ASU and UCLA allowing for a more rigorous high-field near threshold testing of alkali-antimonide cathodes.

The LBNL team is preparing for the high gradient testing at HiRES beamline. The design of a new cathode plug which can achieve Ecathode = 25 MV/m in the HiRES gun has been finished. The tip geometry of this new cathode, as shown in Figure 4, has been optimized so that the Epeak on the gun surface is minimized to mitigate the dark current and prevent the RF breakdown. The plug design has been sent to SLAC for the production and surface preparation. LBNL and SLAC are working together to prepare the suitcase for the cathode growth and the transportation. In parallel, LBNL team is working on restoring the HiRES beamline operation for the upcoming testing, including both the RF gun and the diagnostics for cathode characterization.

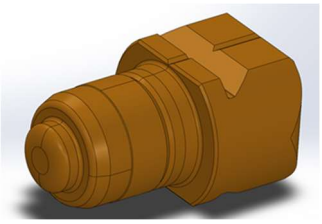

Figure 11: 3D CAD model of the new cathode plug design.

Future Plans

The new INFN plug compatible growth chamber will be commissioned at ASU and alkali-antimonide cathodes will be transferred to UCLA in the next year. Cathodes from SLAC will be transferred to UCLA as well. UCLA will test Cathodes from SLAC, Cornell and ASU, fulfilling the project goal of demonstrating cross-system performance data. The Pegasus laser is being equipped with a tunable spectral extension module in order to complete the cathode characterization at different wavelengths. New cathode plugs for LBNL will be fabricated, and in the final year of the project, LBNL will also test cathodes from SLAC.

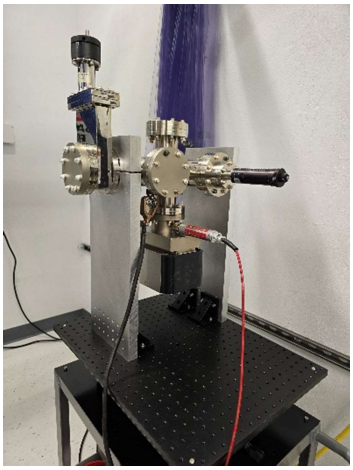

Figure 12: UCLA UHV photocathode suitcase ready for first growth of Cs3Sb photocathodes at SLAC.

Intrinsic emittance as a function of wavelength and temperature will be measured at low field will be measured at both ASU and Cornell for alkali antimonide photocathodes (monoalkali and bialkali). K2CsSb and NA2KSb cathodes will be grown and their near-threshold QE, MTE and energy distributions performance will be characterized.

Figure 13: Scanning Tunneling Microscope probe at ASU to be used as a new method to investigate DC field emisison from alkali-antimonides.

New method to investigate the DC field emission performance of alkali-antimonide cathodes using low voltage near-field probes in a Scanning Tunnelling Microscope will be developed at ASU.

References (also Publications):

1. C.T. Parzyck, C.A. Pennington, W.J.I. DeBenedetti, J. Balajka, E.M. Echeverria, H. Paik, L. Moreschini, B.D. Faeth, C. Hu, J.K. Nangoi, V. Anil, T.A. Arias, M.A. Hines, D.G. Schlom, A. Galdi, K.M. Shen, J.M. Maxson, Atomically smooth films of CsSb: A chemically robust visible light photocathode, APL Materials, 101125 (2023).

2. A. Kachwala, P. Saha, P. Bhattacharyya, E. Montgomery, O. Chubenko and S. Karkare, Demonstration of thermal limit mean transverse energy from cesium antimonide photocathodes, Appl. Phys. Lett. 123, 044106 (2023)

Session Four

Photoinjectors, UED, and Data, AI/ML

Control of Bright Electron Beams at Small Spatiotemporal Scales for Probing Materials Far from Equilibrium

PI: Jared Maxson, Cornell University, Ithaca, NY 14853

Keywords: ultrafast electron diffraction, photoemission, beam dynamics, detector development

Research Project Scope

Ultrafast electron diffraction, microscopy, and spectroscopy are critical enabling technologies for studying quantum matter far from equilibrium. The purpose of this project is to develop broadly applicable techniques to improve performance of ultrafast electron diffraction and spectroscopy systems. Our areas of focus are techniques to improve probe size/coherence, intrinsic time/energy resolution, and spatiotemporal jitter. We explore advances in photoelectron sources via materials with improved emitted 3D momentum spread and emission areas below the optical diffraction limit; beam manipulation techniques to improve electron brightness preservation in the presence of space charge; and novel detector techniques to increase spatiotemporal resolution. We deploy these in proof of principle experiments on a 150 keV ultrafast electron beamline at Cornell, which is instrumented to perform ultrafast electron diffraction (UED).

Recent Progress

The Cornell Ultrafast Electron Source: the high brightness, 150 keV dc photoemission source used in these studies is shown in Figure 1. The source is novel in that it employs high quantum efficiency, low intrinsic emittance alkali antimonide (here Na-K-Sb) photocathodes. These cathodes are grown in-house and are transported to the electron source under ultra-high vacuum. Photoemission is driven by a wavelength tunable femtosecond laser; the wavelength is chosen to match the bandgap of the photocathode; this dramatically reduces the emitted momentum spread, as described below. Emitted pulses are temporally compressed by a radiofrequency bunching cavity, and spatially focused by conventional solenoid lenses on the sample. Optionally, an aperture may be placed just upstream of the sample to reduce the electron beam size down to ~3 micron rms, useful for microdiffraction experiments from small flakes of exfoliated van der Waals materials. The ultimate temporal resolution of the instrument is approximately 200 fs rms, driven primarily by the bunch length of electrons at the sample plane.

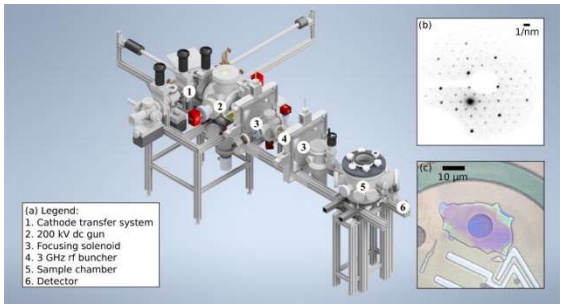

Figure 1: The ultrafast electron source at Cornell. (a): Model of the electron gun and beamline components, 3-4 meters in length depending on configuration. One specialty of the device is the ability to generate diffraction patterns (b) from few-micron sized flakes of quantum materials. (c) shows an optical microscopy image of the flake of Nb_3Br_8 used to generate the diffraction pattern in (b).

Beam Brightness Enhancements with Novel Photocathodes: Beam measurements in comparison with detailed space charge simulation show that the mean transverse energy (MTE) of the emitted electrons from our Na-K-Sb photocathode driven with red (650 nm) light is approximately 70 meV (and thus a FWHM energy of <150 meV), which is approximately 7 times smaller than photoemission from traditionally employed Cu photocathodes in use in many ultrafast facilities. This low energy spread may enable new applications in ultrafast electron energy loss spectroscopy such as the resolution of individual phonon modes, or plasmonic excitations with frequencies in the mid-infrared, such as is found in semiconductors, or to resolve the intricate couplings between plasmons and phonons [1]. The intrinsic energy spread can be reduced further, down to the few 10s of meV, by further red-shifting the laser, but at the penalty of a significant reduction in photocathode quantum efficiency [2]. The emittance performance of the electron source is a strong function of the emitted charge due to space charge effects; 12.5 nm-rad emittance is achieved with 10^5 electrons per bunch, 0.7 nm-rad is achieved with 500 electrons/bunch, down to ~100 pm-rad at the level of single electrons per bunch where space charge is non-existent.

We have developed a technique to measure the 4D transverse phase space with sub-nanometer-radian resolution. This enables the diagnosis of horizontal and vertical phase space coupling, space charge effects, and magnet aberrations. The low emittance performance described above was only achieved after custom quadrupole, skew quadrupole, and sextupole corrector magnets were constructed and installed on the beamline. These aberrations arise from both the solenoid lenses and the input coupler transient kick of the buncher cavity.

Small Source development: Many ultrafast electron scattering applications of the future demand electron beam sizes at the single micron to nanometer scale. To ease demagnification requirements and improve coherence of nanoscale ultrafast electron probes, small area emitters are desired. In ultrafast transmission electron microscopy, emission from electrochemically etched tungsten tips is possible, yielding source sizes in the range of 10 nm and FWHM energy spreads of ~0.5 V. However, in accelerator-based ultrafast electron sources, sharp tips may not be practical due to extreme field enhancement. In accelerator sources, the optical diffraction limit hinders laser shaping at the few micron scale and below. We are developing a new class of microscale (and ultimately, nanoscale) flat photocathode sources amenable for use in accelerator guns. Our technique is work-function masking: using lithography, we generate cathode areas with multiple materials on the surface: low work function islands surrounded by high work function areas that suppress photoemission. Photoemission electron microscopy experiments with Cu-Cs as the low work function material, and Pt as the emission-suppressing layer have been developed and successfully tested at the few micron scale, and ongoing work seeks to bring the ultimate emission size down to <100 nm diameter, with a path to replace Cu-Cs with a high efficiency emitter such as Cs-Sb under active development.

Novel Detectors Enable Noise Reduction, New Experiments: We have installed an Electron Microscope Pixel Array Detector (EMPAD) [3], as the diffraction detector in our instrument. The

EMPAD direct electron detector features a 1 kHz frame rate, single electron sensitivity with SNR~100, and high average dynamic range. The EMPAD was originally designed for use in scanning transmission electron microscopy; our work is its first deployment in the realm of pulsed electron sources. Like findings in pixel array detectors in x-ray free electron lasers, pulsed operation of the EMPAD reveals non-trivial electron-hole plasma dynamics with short pulses, which can modify its saturation dynamics. To highlight the performance of the EMPAD, our first UED studies with it focused on a challenging system not previously characterized with time-resolved electron diffraction: moiré materials. We studied a twisted bilayer heterobilayer of $MoSe_2/WSe_2$. At few-degree twist angles, the van der Walls force generates an atomic reconstruction at the moiré period (~10 nm wavelength). This reconstruction generates a superlattice diffraction very close to the Bragg peak pair; this was visualized for the first time with ultrafast electron diffraction in our system by using a custom post-sample magnetic lens telescope and using sub-nanometer emittance electron probe quality. This data is shown in Figure 2, panels (a)-(c).

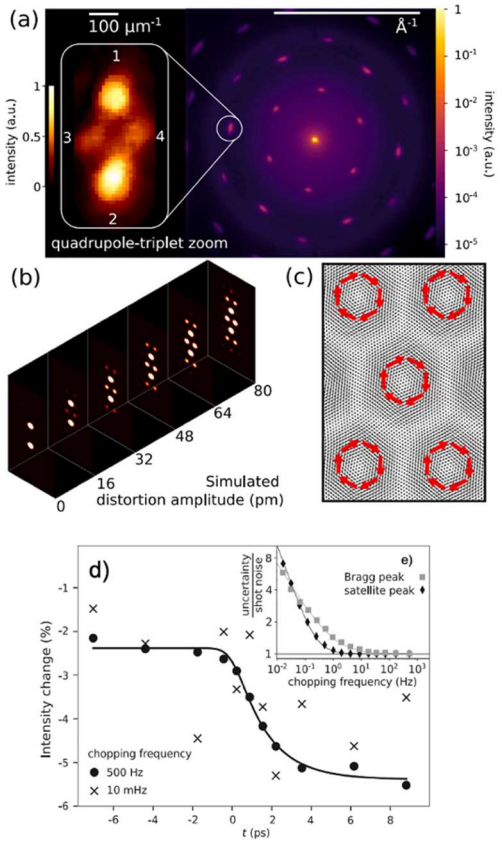

Figure 2: Ultrafast electron diffraction study of moiré materials. a) Left: Short camera length diffraction image of $MoSe_2/WSe_2$ heterobilayer with 2 degree twist. Right: electromagnetic zoom-in on a Bragg peak pair showing satellite peaks caused by the moiré atomic reconstruction. b) simulated diffraction pattern with varying reconstruction displacements. (c) atomic configuration with arrows indicating the atomic displacement field. (d) The effect of rapid chopping de-noises the UED-time series data. (e) With sufficiently fast chopping, our data reaches the shot noise floor.

For pump-probe studies of this material, we discovered that we could utilize the high frame rate of the EMPAD detector to "outrun" machine-related noise in our system. To achieve de-noising, we employ an acousto-optic modulator to "chop" our optical pump at half the frame rate of the EMPAD. We then generate diffraction difference images between pumped and unpumped sample conditions at 500 Hz; machine-related intensity fluctuations (for example, caused by photocathode laser power fluctuations, pointing jitter on the probe-forming aperture, etc) with contributions below 500 Hz are removed from the data. The final data is a sum of many diffraction differences. Both the fast rate detection and the low intrinsic noise of the EMPAD are critical for this technique. We show with sufficiently fast chopping our UED data reaches the shot noise floor, as shown in Figure 2 (d) and (e). The data shown in panel (d) of Figure 2 is the sum over both Bragg and superlattice peaks; rich dynamics are discovered when individual peak responses are resolved; this data is the subject of a publication in preparation.

Future Plans

In the next year, we plan to pivot to the study of ultrafast electron energy loss spectroscopy, utilizing a commercial transmission electron microscope spectrometer with an intrinsic resolution of <100 meV, which should be sensitive enough, for example, to resolve energetic phonons. The spectrometer can also be used as a temporal jitter time-stamping technique when performing simultaneous diffraction and spectroscopy, via the correlation between energy and arrival time [4].

We have recently also installed a cold stage in our sample chamber, permitting operation with samples cooled down to liquid helium temperatures; targets of UED study in future projects include van der Waals magnetic materials and unconventional superconductors.

References

1. Maureen J. Lagos, Isobel C. Bicket, S. Shayan Mousavi M., Gianluigi A. Botton, *Advances in ultrahigh-energy resolution EELS: phonons, infrared plasmons and strongly coupled modes*, Microscopy **71**, i174–i199 (2023).
2. P. Musumeci, J. Giner Navarro, J.B. Rosenzweig , L. Cultrera , I. Bazarov, J. Maxson, S. Karkare, H. Padmore, *Advances in Bright Electron Sources*, Nuclear Instruments and Methods in Physics Research Section A **907,** 209-220 (2018).
3. Mark W Tate, Prafull Purohit, Darol Chamberlain, Kayla X Nguyen, Robert Hovden, Celesta S Chang, Pratiti Deb, Emrah Turgut, John T Heron, Darrell G Schlom, Daniel C Ralph, Gregory D Fuchs, Katherine S Shanks, Hugh T Philipp, David A Muller, Sol M Gruner, *High Dynamic Range Pixel Array Detector for Scanning Transmission Electron Microscopy,* Microscopy and Microanalysis **22,** 237–249 (2016)
4. Lingrong Zhao, Zhe Wang, Chao Lu, Rui Wang, Cheng Hu, Peng Wang, Jia Qi, Tao Jiang, Shengguang Liu, Zhuoran Ma, Fengfeng Qi, Pengfei Zhu, Ya Cheng, Zhiwen Shi, Yanchao Shi, Wei Song, Xiaoxin Zhu, Jiaru Shi, Yingxin Wang, Lixin Yan, Liguo Zhu, Dao Xiang, and Jie Zhang, *Terahertz Streaking of Few-Femtosecond Relativistic Electron Beams,* Physical Review X **8,** 021061 (2018).

Publications

1. C. J.R. Duncan, M. Kaemingk, W.H. Li, M.B. Andorf, A.C. Bartnik, A. Galdi, M. Gordon, C.A. Pennington, I.V. Bazarov, H.J. Zeng, F. Liu, D. Luo, A. Sood, A.M. Lindenberg, M.W. Tate, D.A. Muller, J. Thom-Levy, S.M. Gruner, J.M. Maxson, *Multi-scale time-resolved electron diffraction: A case study in moiré materials,* Ultramicroscopy **253**, 113771 (2023).
2. C.T. Parzyck, C.A. Pennington, W.J.I. DeBenedetti, J. Balajka, E.M. Echeverria, H. Paik, L. Moreschini, B.D. Faeth, C. Hu, J.K. Nangoi, V. Anil, T.A. Arias, M.A. Hines, D.G. Schlom, A. Galdi, K.M. Shen, J.M. Maxson, *Atomically smooth films of CsSb: A chemically robust visible light photocathode,* APL Materials **11**, 101125 (2023).

3. M. Gordon, W.H. Li, M.B. Andorf, A.C. Bartnik, C.J.R. Duncan, M. Kaemingk, C.A. Pennington, I.V. Bazarov, Y.-K. Kim, J.M. Maxson, Phys. Rev. Accel. Beams **25**, 084001 (2022)
4. W.H. Li, C.J.R. Duncan, M.B. Andorf, A.C. Bartnik, E. Bianco, L. Cultrera, A. Galdi, M. Gordon, M. Kaemingk, C.A. Pennington, L.F. Kourkoutis, I.V. Bazarov, J.M. Maxson, *A kiloelectron-volt ultrafast electron micro-diffraction apparatus using low emittance semiconductor photocathodes*, Structural Dynamics **9**, 024302 (2022).
5. A. Bartnik, C. Gulliford, G. H. Hoffstaetter, and J. Maxson, *Ultimate bunch length and emittance performance of an MeV ultrafast electron diffraction apparatus with a dc gun and a multicavity superconducting rf linac*, Phys. Rev. Accel. Beams **25**, 093401 (2022)

Enabling Ultrafast Structural Dynamics at the Nanoscale in MeV-UED Setups

Joel England, SLAC National Accelerator Laboratory

Keywords: ultrafast electron diffraction, mega-electronvolt

Research Project Scope

This joint R&D program between SLAC and LBNL aims to advance the technology and develop techniques to overcome the present limitations in temporal resolution and probe size at the MeV-UED beamline, and fully exploit a key advantage of electrons over x-rays, i.e. the ability to be focused to (sub-)nanometer sizes thanks to their very short wavelength. This work focuses on aspects with a major role in the definition of spatial resolution in diffraction experiments: development of real-time non-disruptive time-stamping techniques to increase the short and long term temporal resolution of the MeV-UED beamline, both at SLAC and at LBNL; generation of high brightness electron beams with picometer-scale emittance; manipulation of beam phase space and conservation of the emittance throughout the beamline; electron beam focusing, measurement and control to nanometer scales; laser pump focusing and alignment to sample, and novel detection methods. The primary tasks under the SLAC FWP, as described in the original proposal, can be classified into two broad categories: (1) development of momentum space (q-range) enhancement methods using electron imaging optics; and (2) testing of gradient limits and brightness enhancements for the SLAC electron gun. Progress under the first of these categories is on track with Year 1 goals of the proposal. Planned experimental R&D time under the second objective however has been delayed due to extended downtime of the SLAC MeV-UED facility with anticipated R&D beam time availability postponed until Q3 of FY24. However, extensive simulational comparative studies have been performed on gun dynamics and brightness enhancements for the existing 1.6 cell ASTA photoinjector, the VHF HiRES gun, and a proposed alternative 1.4 cell gun design. Developments under this program are synergistic with the partner program at LBNL under PI Dan Wang. The developed electron lens optics will be applicable to demonstration of nano-focusing techniques at the LBNL HiRES facility.

Recent Progress

To optimize the electron imaging capabilities of the MeV-UED instrument, we employed simulation models using a combination of GPT, COSY, and RADIA. Our primary objective was to enhance the q-range for improved resolution via a variable camera length optics setup that allows magnification of the electron beam in reciprocal (momentum) space. This approach will enhance the scientific reach of the facility by enabling improved momentum space (q-resolution) for samples with closely spaced diffraction peaks. We evaluated various lens designs and decided on a combination of axially magnetized permanent magnets for the objective and short (few cm) focal length radially magnetized permanent magnet for the imaging lens. See Figure 1(a) for details. We purchased and carried out magnetic field characterization of the axially magnetized lenses and decided upon the design shown in Figure 1(b). For the imaging lens, we designed a

short-focal-length dual lens design using radially magnetized Halbach-style magnet design, see Figure 1(c-d). The magnets were designed in consultation with the vendor and an order placed sufficient to assemble 5 prototypes of the dual-magnet assembly (anticipated delivery in April 2024).

Refer to Figure 1(a) for a visual representation of the lens configuration. Additionally, we purchased and characterized the magnetic fields of the axially magnetized lenses, finalizing the design as depicted in Figure 1(b). Collaborating with Prof. Musumeci's UCLA group, we conducted experiments to demonstrate the q-magnification technique using various lensing options. Simultaneously, we are testing the kHz RF system with the MeV-UED. This testing allows us to measure electron gun emittance and determine brightness scaling.

Furthermore, we have developed and implemented emittance scan software control capabilities using existing electromagnetic focusing magnets on the MeV-UED beam line. Simulation studies for nano-focus options (see Figure 2) indicate the need for an alternate magnet design at the SLAC facility due to HiRES's lower (550 to 750 keV) beam energy and shorter chamber-to-detector distance.

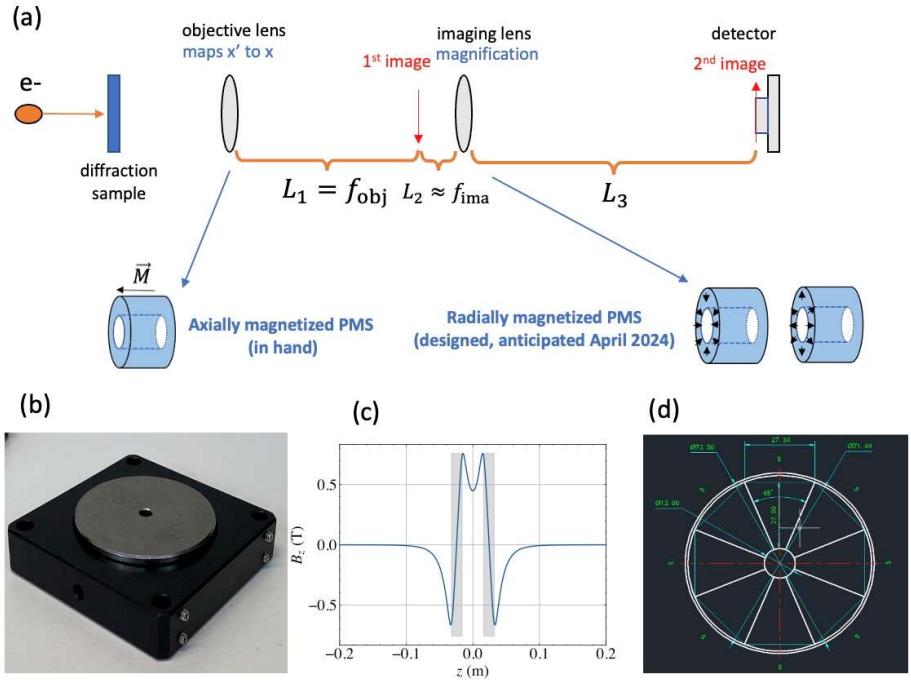

Figure 1. (a) Schematic of the proposed q-range magnification setup SLAC MeV-UED, which employs two permanent magnet solenoidal lenses. The objective lens (b) is axially polarized long focal length objective lens, (c) dual-magnet radially polarized for short-focal length imaging lens on order, and (b) simulated field profile of the imaging lens design.

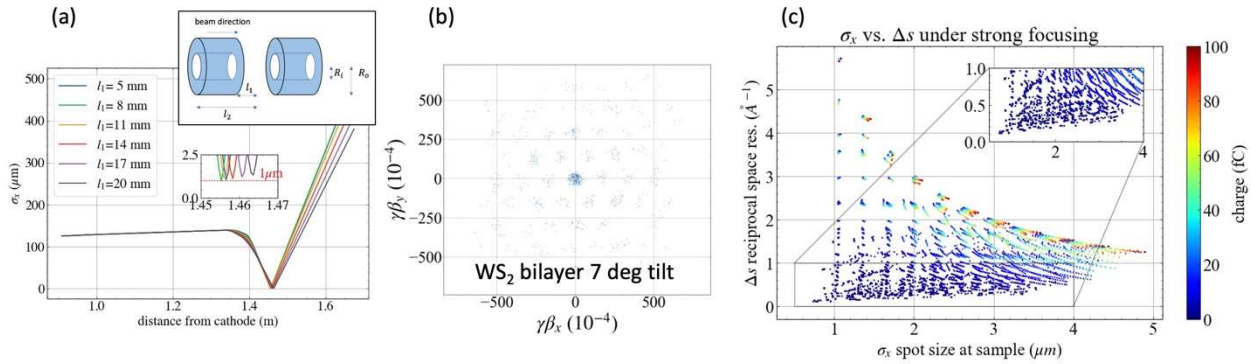

Figure 2. Scenarios for MeV-UED at SLAC using the high-gradient imaging lens in Fig 1(c) for nanofocused beams, showing (a) beam focus as function of intra-magnet spacing, (b) simulated diffraction on WS_2 bilayer of resulting 400nm nanofocused beam followed by 4μm iris to remove divergence, and (c) tradeoff between spot size and q-resolution (*without* iris collimation post-focus).

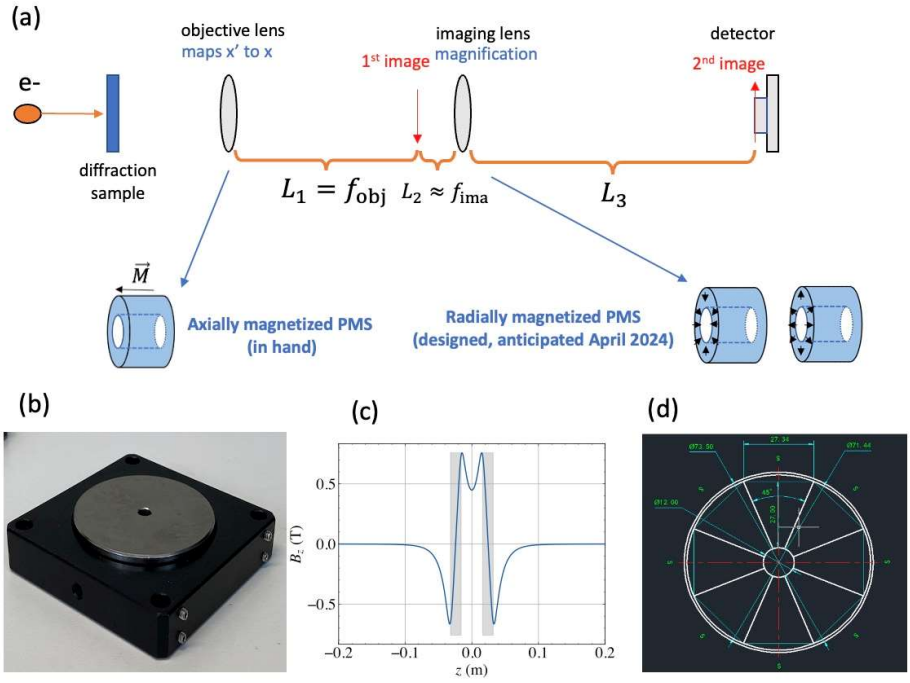

Future Plans

A final magnet design has been ordered and is anticipated delivery in Q3 of FY24 for testing and demonstration in FY25. Various options are being evaluated for initial electron beam characterization of these magnets, including nano-focus testing at HiRES (potentially requiring a magnet design with scaled-down field strength to accommodate the lower beam energy), UCLA Pegasus, and test during R&D beam time at SLAC MeV-UED between user runs. In addition, the originally planned Year 1 testing of gun gradient and brightness characterization will be carried out under planned R&D time scheduled in Q3 FY24 to coincide with commissioning of a

new kHz RF system that was previously purchased and installed under prior funding. Beam studies and emittance measurements to be performed will provide guidance on potential gradient scaling capabilities of our existing gun and resulting brightness enhancement at higher peak power. An alternative klystron model for the kHz system with higher power handling capability has also been ordered under non-R&D (operations) funds as both a spare for the existing klystron and as a potential replacement in FY25.

Publications

P. Denham, Y. Yang, V. Guo, A. Fisher, X. Shen, T. Xu, R. J. England, R. K. Li, and P. Musumeci, "High energy electron diffraction instrument with tunable camera length," Structural Dynamics, 11 (2), 024302 (2024).

F. Ji, A. Edelen, R. Roussel, X. Shen, S. Miskovich, S. Weathersby, D. Luo, M. Mo, P. Kramer, C. Mayes, M. A. K. Othman, E. Nanni, X-J. Wng, A. Reid, M. Minitti, and R. J. England, "Multi-Objective Bayesian Active Learning for MeV-UED," *accepted* for Nat. Comm. (2024).

Enabling ultrafast structural dynamics at the nanoscale in MeV-UED setups

PI: Dan Wang, Lawrence Berkeley National Laboratory

Keywords: nano-UED, APEX Gun, MHz beam, Machine Learning Control

Research Project Scope

UED with femtosecond beams will enable the study of ultrafast phenomena, including phase transitions, chemical reactions, and lattice vibrations. Also, nanoscale beams are essential for probing nanoscale materials like superconductors, thermoelectrics, and electronic devices. The goal of this project is to advance the technology and techniques of MeV-UED towards the final goal of 10 fs and 100 nm temporal and spatial resolutions, which will also provide flexibility in controlling q-space field of view and resolution to enhance the tool's ability to observe long-range correlations. Achieving such high temporal-spatial resolution would enable access to transient structural dynamics in a variety of materials of research significance at nanometer scale. It would also advance the studies in quantum information science by probing quantum state dynamics in quantum materials to validate theoretical models.

Recent Progress

We are applying machine learning (ML) at HiRES for the correction of temporal jitters and drifts in order to achieve a 10fs beam probe for UED. For the first step, ML-based virtual diagnostics were developed for time of arrival prediction, and an adaptive ML method was developed for accurate 6D space prediction of electron beams.

Under a related project (FP00015446) on “Photocathode material for the LCLS II-HE SRF gun,” a new cathode plug was developed, which for this project extends the capability of HiRES RF gun by enabling a higher cathode electric field (> 25MV/m). This advancement yields an approach to generate a low-emittance beam, as shown in Figure 1, which promises to focus electron beams down to nona-scale. Normalized beam emittance revolutions are compared for the new design (Figure 1(b)) with that from the current APEX gun (Figure 1(b)). Preliminary results from GPT simulations indicate the original gun ended with emittance = 3.367 nm, while the new gun ended with emittance = 1.777nm with the same beamline setup, including collimators, which is about a two times reduction in the emittances.

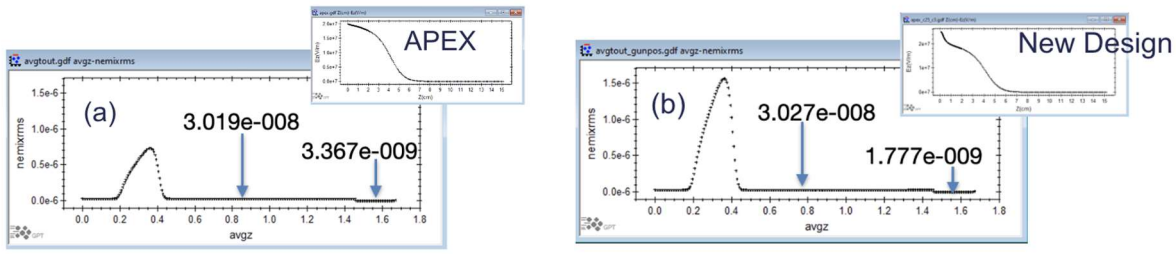

Figure 1: GPT simulations, left: normalized emittance revolution with the original APEX gun (field map shown as the inside figure), right:normalized emittance revolution with the new gun file where the cathode electric field is over 25 MV/m (as shown in the inside figure). Preliminary results show that the original gun ends with 3.367 nm emittance, while the new gun ends with 1.777nm emittance with the same beamline setup including collimators.

Additionally, permanent magnet focus systems are being developed in collaboration with SLAC for nano-probe beams. SLAC group has developed the permanent magnet solenoid (PMS) for objective and imaging lenses for momentum space magnification. To evaluate the effect of this simple lens, we carried out the GPT simulation using a PMS as a final beam probe focusing lens on the HiRES beamline, as shown in Figure 2. The magnetic distribution of the previously designed permanent magnet quadrupoles (PMQ) is also modeled using OPERA 3D, allowing us to implement aberration correction to improve the performance.

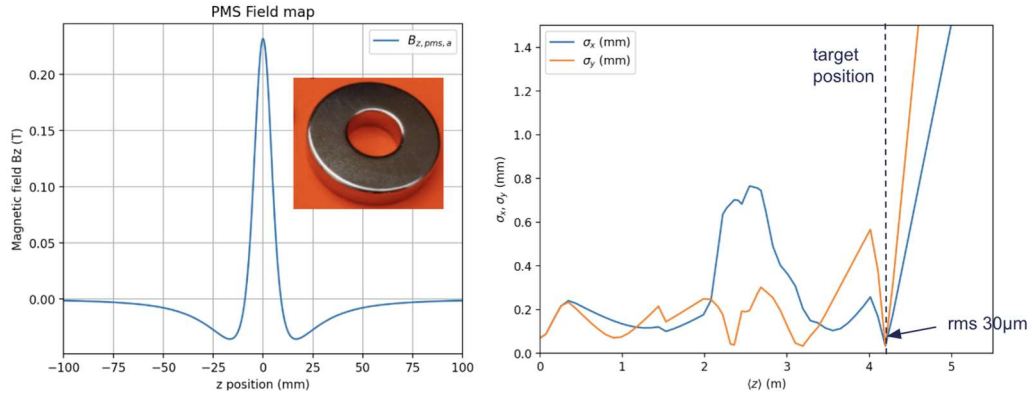

Figure 2: (left) Field map of the permanent magnet solenoid (PMS) from SLAC, and (right) the simulation results of beam size focused by the PMS in HiRES beamline.

Over the last year, a new team has taken over the project and beamline following the departure of the previous PI in 2022. Having trained the new team we are currently on track to generate a photoelectron beam by May this year, marking a significant milestone. This positions the team to focus efforts on more R&D activities going forward.

Future Plans

1. Global optimization of the HiRES beamline is in progress and will be continued, starting from simulations. We will tune all the machine parameters in order to find the optimal working point at different conditions, including with the new cathode design for lower

emittance beam, and with newly designed permanent management solenoid/quadrupoles for nano-focus. The objectives for UED experiments can be either 6D brightness or transverse/longitudinal brightness, which will also be a basis for fast tuning of the UED beamline.

2. We also plan to develop further ML tools to improve HiRES performance to nano-scales. Benefiting from the unique high-repetition (up to MHz) capability of HiRES, we can gather enough data for ML training before the system condition drifts away. ML on LLRF will be developed to control the facility better, as shown in Fig 3. First, we will design and deploy a novel control chassis for phase detection between the UED pump-laser (extracted from a high bandwidth photodiode, one of which is already installed inside the experimental chamber) and an electron beam signal from a passive cavity (beam arrival monitor, BAM) installed in the beamline (red connecting lines). The BAM cavity resonant at about 5 GHz has been installed in the beamline. We will characterize the cavity and test different detection techniques. The second step is to exploit ML-based techniques to overcome the low signal-to-noise issue at low charge. The dataset from the LLRF system will then be used to train a Neural-Network (NN) based surrogate model of the beamline, which can then be used to assign arrival-time tags to the UED measurements with low-charge beams. Ultimately ML-based control algorithms (for example, reinforcement learning as shown in Fig.3) will be implemented directly on an FPGA in the LLRF system, for fast run time and direct feeding of input parameters (edge computing).

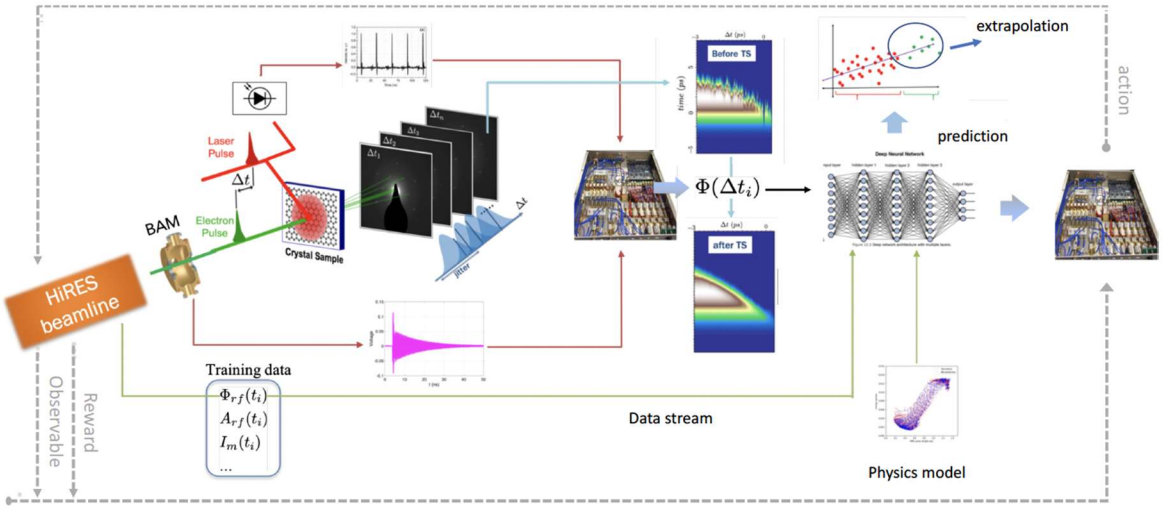

Figure 3. Plans to implement machine learning control algorithms in the LLRF system, to accurately control jitter and drift in the time of arrival (TOA) of the HiRES electron beam, for the purpose of 10fs temporal resolutions on UED.

3. Besides the temporal resolution, we will also collaborate with SLAC to develop and test the short focal length lens, as shown in Fig.4. This electron optical system will serve as both a nano-probe focusing for testing at HiRES and as an objective lens for q-resolution enhancement at SLAC.

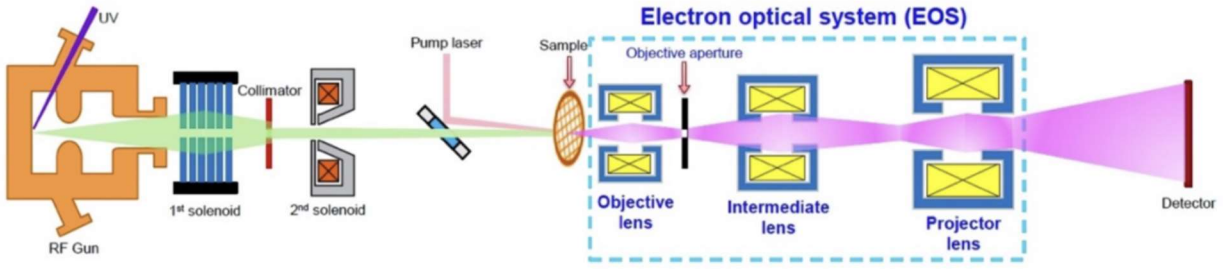

Figure 4. Plans on the short focal length lens development for nano-probe focusing, for the purpose of 100ns spatial resolutions on UED.

4. In collaboration with Alexian Scheinker from LANL on another funded project, we will develop global optimal controlled UED with adaptive ML methods at HiRES. First continue with adaptive diagnostic for robust and accurate prediction with time-varying beam and accelerator components, and then develop adaptive control to reduce time of arrival and spatial jitter, as well as to increase reciprocal space resolution, faster tuning between experiments/materials based on the global optimization simulations in plan 1.

Publications

1. Alexander Scheinker , Frederick Cropp, and Daniele Filippetto, "Adaptive autoencoder latent space tuning for more robust machine learning beyond the training set for six-dimensional phase space diagnostics of a time-varying ultrafast electron-diffraction compact accelerator", Physical Review E 107, 045302 (2023), DOI: 10.1103/PhysRevE.107.045302
2. F. Cropp, L. Moos, A. Scheinker, A. Gilardi, D. Wang, S. Paiagua, C. Serrano, P. Musumeci, and D. Filippetto, "Virtual-diagnostic-based time stamping for ultrafast electron diffraction," Physical Review Accelerators and Beams` 26, 052801 (2023), DOI: 10.1103/PhysRevAccelBeams.26.052801.
3. Daniel B. Durham, Colin Ophus, Khalid M. Siddiqui, Andrew M. Minor, Daniele Filippetto, "Accurate quantification of lattice temperature dynamics from ultrafast electron diffraction of single-crystal films using dynamical scattering simulations, Struct Dyn 9, 064302 (2022)
4. D. Filippetto, P. Musumeci, R. K. Li, B. J. Siwick, M. R. Otto, M. Centurion, and J. P. F. Nunes, "Ultrafast electron diffraction: Visualizing dynamic states of matter", Rev. Mod. Phys. 94, 045004 – Published 6 December 2022
5. Christopher M. Pierce, Daniel B. Durham, Fabrizio Riminucci, Scott Dhuey, Ivan Bazarov, Jared Maxson, Andrew M. Minor, and Daniele Filippetto*, "Experimental Characterization of Photoemission from Plasmonic Nanogroove Arrays", Phys. Rev. Applied 19, 034034 – Published 10 March 2023

Integrated Physics Modeling and Online Machine Learning for Characterization and Tuning of Particle Accelerator Systems

Dr. Auralee Edelen (PI)

Keywords: machine learning, particle accelerators, modeling, control, neural networks

Research Project Scope

This project focuses on bringing comprehensive, accurate, fast-to-execute system models that are kept updated over time (i.e. "digital twins") into accelerator operation. This involves addressing challenges in continual online learning, efficient physics-guided model calibration techniques, novel machine learning (ML) techniques for representing beam distributions and accelerator systems, and reliable uncertainty quantification. The project aims to address key R&D challenges in the technical ML developments needed and to deploy adaptive system models based on physics and machine learning onto the accelerator and leverage these in tuning complicated beam setups, such as two-bunch operating modes. This ECA will contribute key ML capabilities and components to the infrastructure deployed at SLAC and provide a blueprint for using similar techniques at other accelerator facilities. It will also integrate the developed advances in ML-based system modeling into the model-based tuning algorithms.

Recent Progress

Online Physics and ML Modeling Deployment. Substantial progress has been made on online deployment of ML- and physics-based models. This included (1) deploying software infrastructure to couple SLAC's new high performance computing (HPC) system, the S3DF, to the accelerator control system in a secure way, (2) refining software infrastructure components for easy ML model deployment and continual learning, and (3) working with the S3DF team to assess different approaches for on-demand job scheduling. Simulations and ML models can now be launched from SLAC's control system and run on the S3DF, where they read in live process variables (PVs) from the accelerator and display visualizations and write to PVs back into the control system (e.g. for model-based tuning and use with standard control room applications, such as model-based beam matching). A prototype version of this software was used to aid LCLS-II injector commissioning. In that work, an online physics simulation was used to aid physicists' intuition while tuning the LCLS-II injector, which lead to better emittance values. This was then followed by Bayesian optimization to fine-tune the emittance, and resulted in the best emittance values that had been observed at that time for the injector. At present, the injector IMPACT-T simulation and ML models are deployed, and we are extending deployment to the linacs and undulators for LCLS/LCLS-II.

Model Calibration and Continual Learning. Progress was also made in the area of model calibration (i.e. "sim2real"), in which an ML model trained on physics simulations (or alternatively, a parameterized physics simulation) is made to match the real system measurements

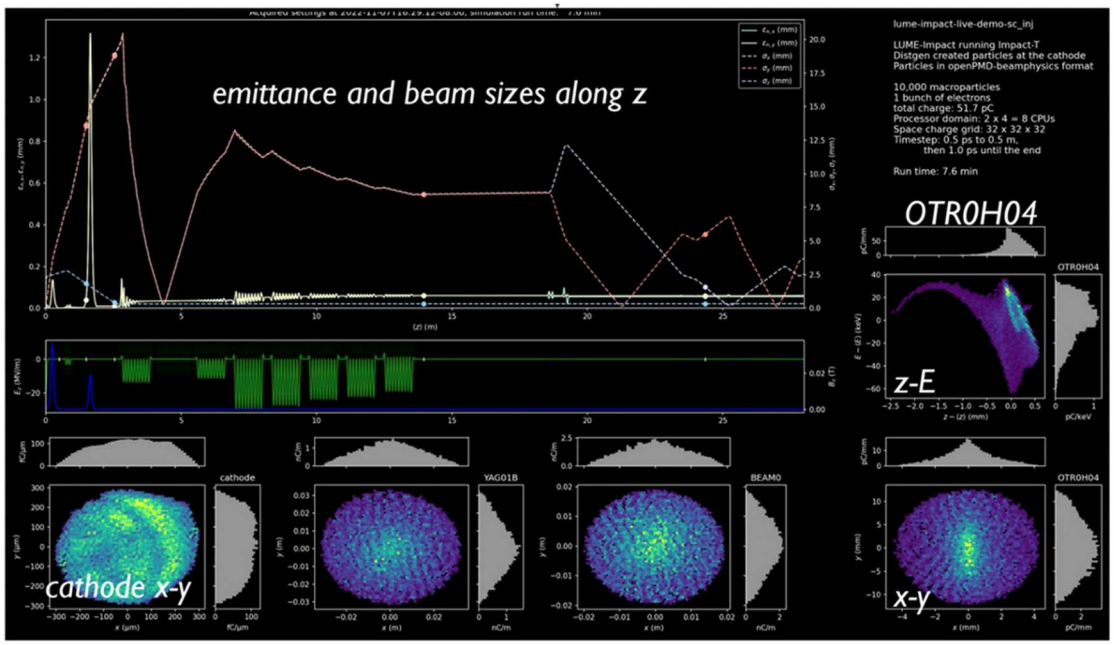

Live online simulation of LCLS-II injector used to aid commissioning.

more closely. In our approach, we learn a main representation from simulations and then alter scaling and offset parameters on the inputs and outputs automatically by re-training on measured data. We refined the details of our approach, using a neural network model of the LCLS injector as a test case. One of the advantages of having an accurate, fast system model is that it can be used to speed up automated tuning algorithms. To this end, we examined the impact of different types of error metrics used during calibration. We found in the context of optimization that getting the function correlations to be accurate (as opposed to minimizing prediction error alone) was essential for good optimization performance. We contributed to a paper (in collaboration with FWP 100637) that demonstrated calibrated neural network system models can be used to speed up Bayesian optimization [1]. We also developed a python package to easily conduct model calibration and use the deployed models in the Xopt optimization software (which is a first step toward deploying this algorithm into regular accelerator operations) interchangeably with our online modeling software. We are now beginning to examine this type of model calibration in the context of continual learning and automatic model adaptation to account for system changes over time.

Combined Physics and ML Modeling. This project has also contributed to examination of differentiable simulations as an alternative approach to model calibration. This approach has advantages in that the physics itself (as opposed to a learned representation of it) can be used to constrain the free calibration parameters, resulting in greater data efficiency in learning. This lends itself well to cases where a high degree of accuracy is needed and many free parameters are involved, but speed of model execution is not essential. We examined using differentiable simulations to find typical lattice errors automatically, such as magnet misalignments and rotations. We found it suitable for quickly discovering these [2]. We also have demonstrated a new technique for advanced phase space reconstruction that can use arbitrary machine measurements

(such as quadrupole and phase scans) to quickly reconstruct the detailed high-dimensional phase space of particle beams. This approach leverages both ML and physics representations by combining generative neural network modeling and differentiable physics simulations. In [3], we showed experimentally that the 4D phase space distribution could be reconstructed with just 10 quadrupole measurements and screen images, in several minutes and with a very high level of detail. This was recently extended to 6D phase space reconstruction, with over 100x faster reconstruction than existing approaches. Extensions to reconstruction of magnetized and flat beams were conducted with collaborators. This new approach, called generative phase space reconstruction (GPSR), has very broad potential in accelerators to be used with a variety of different type of measurements. By enabling fast, detailed phase space reconstruction, this technique will greatly improve the accuracy with which the initial beam distributions can be characterized for accelerator simulations and online models.

Novel ML Model Structures. We have also continued investigation of novel ML modeling approaches that will eventually be combined into online models for SLAC's accelerator systems. At present, we are investigating the use of conditional variational autoencoders and recurrent neural networks for start-to-end simulations, point-cloud representations and normalizing flows to deal with 6D beam distribution information directly, and modular surrogate models for individual expensive calculations such as Coherent Synchrotron Radiation [5]

Future Plans

We are extending the simultaneous deployment of online physics simulations and ML models to the broader accelerator complex at SLAC. At present, we are also constructing software components to support MLOps and continual learning, including designing and deploying databases for models and results. This will aid the continual learning component of the research and also enable users in the control room to easily switch between different requested models for online display or use in tuning. Work is also being conducted on deploying the GPSR technique on the LCLS-II Diag0 line, which will enable continuous, automatic, non-invasive characterization of the 6D phase space for LCLS-II. This information will then aid online model calibration and updating. Extensions are also being planned to provide information about the 6D beam phase space distribution in front of the undulators for hard and soft X-rays, which could provide valuable information for improving modeling and control of LCLS/LCLS-II.

In terms of ML modeling, we are working on several aspects ranging from novel modeling approaches to construction and deployment of models. We are working on a novel model calibration approach that uses multi-fidelity modeling and Bayesian statistics to provide uncertainty estimates on learned calibration parameters. This approach should give physicists an idea of how likely different possible deviations between the idealized simulation and real machine are, and help identify corrective courses of action where appropriate. This approach also will not require a pre-made ML surrogate model, but rather identifies the appropriate fidelity of simulation to run at a given point in time in the process automatically. Within the next year, we plan to finish

our work combining recurrent neural networks and variational auto-encodes to predict the beam phase space at multiple points along a given accelerator, and deploy this for LCLS and LCLS-II. We are also working with Stanford on various approaches to better learn representations of the accelerator from system data using novel neural network architectures (such as graph neural networks and point-cloud consuming networks). We are also working with LCLS photon science staff to link ML models of the accelerator to photon diagnostics and experiment data. This will aid construction of more comprehensive start-to-end models and also help identify correlations that could be used to aid tuning for user experiments.

In terms of complete model construction and deployment, including continual learning, we are currently targeting the normal-conducting FEL (injector to end of undulator), because it is a well-established machine and has signals we can continuously monitor to aid calibration (including the FEL pulse intensity, longitudinal phase space images, monochrometer, and in some cases spectra). We are in the process of gathering data for model calibration, and will examine various continual learning methods based on the archived data. Finally, we will deploy the model and continual learning approaches in the online modeling software. This will later be extended to deploying models for two-bunch operating modes, for which longitudinal phase space images for two-bunch experiments have already been gathered. A second target in this thrust of the effort will be the LCLS-II injector and Diag0 line, since this also will provide continually-updating measurements. Finally, we will extend this to the LCLS-II FEL. The novel ML architectures developed in the other thrust of the work will be applied where appropriate.

Integration of deployed models into novel ML-based tuning schemes will continue alongside model development and deployment, particularly for more efficient multi-modal tuning with multiple target output parameters of interest (e.g. spectral bandwidth, longitudinal phase space including dynamic adjustment of pulse separation, FEL pulse intensity).

References

1. T. Boltz, J.L. Martinez, C. Xu, K.R.L. Baker, R. Roussel, D. Ratner, B. Mustapha, A.L. Edelen, *More Sample-Efficient Tuning of Particle Accelerators with Bayesian Optimization and Prior Mean Models,* under review, (2024).

2. J.P. Gonzalez-Aguilera, Y.K. Kim, R. Roussel, A. Edelen, C. Mayes, *Towards fully differentiable accelerator modeling,* Proc. IPAC'23, WEPA065 (2023).

3. R. Roussel, A. Edelen, C. Mayes, D. Ratner, J.P. Gonzalez-Aguilera, S. Kim, E. Wisniewski, and J. Power, *Phase Space Reconstruction for Accelerator Beam Measurements Using Neural Networks and Differentiable Simulations,* Phys. Rev. Lett. **130,** 145001 (2023).

4. S. Kim, J.P. Gonzalez-Aguilera, P. Piot, G. Chen, S. Doran, Y.K. Kim, W. Liu, C. Whiteford, E. Wisniewski, A. Edelen, R. Roussel, J. Power, *Four-Dimensional Phase-Space Reconstruction*

*of Flat and Magnetized Beams Using Neural Networks and Differentiable Simulation*s, under review, (2024).

5. R. Robles, W. Lou, C. Mayes, R. Roussel, A. Edelen, *Efficient Computation of Two-Dimensional Coherent Synchrotron Radiation with Neural Networks,* Proc. IPAC'23, (2023).

Publications

1. R. Roussel, A. Edelen, C. Mayes, D. Ratner, J.P. Gonzalez-Aguilera, S. Kim, E. Wisniewski, and J. Power, *Phase Space Reconstruction for Accelerator Beam Measurements Using Neural Networks and Differentiable Simulations,* Phys. Rev. Lett. **130,** 145001 (2023).

2. J.P. Gonzalez-Aguilera, Y.K. Kim, R. Roussel, A. Edelen, C. Mayes, *Towards fully differentiable accelerator modeling,* Proc. IPAC'23, WEPA065 (2023).

3. R. Robles, W. Lou, C. Mayes, R. Roussel, A. Edelen, *Efficient Computation of Two-Dimensional Coherent Synchrotron Radiation with Neural Networks,* Proc. IPAC'23, (2023).

4. R. Roussel, D. Kennedy, A. Edelen, S. Kim, E. Wisniewski, J. Power, *Demonstration of Autonomous Emittance Characterization at the Argonne Wakefield Accelerator*, Instruments **7**, 29 (2023).

5. S. Kim, J.P. Gonzalez-Aguilera, P. Piot, G. Chen, S. Doran, Y.K. Kim, W. Liu, C. Whiteford, E. Wisniewski, A. Edelen, R. Roussel, J. Power, *Four-Dimensional Phase-Space Reconstruction of Flat and Magnetized Beams Using Neural Networks and Differentiable Simulation*s, under review, (2024).

6. (secondary project contributor, FWP 100637 primary) T. Boltz, J.L. Martinez, C. Xu, K.R.L. Baker, R. Roussel, D. Ratner, B. Mustapha, A.L. Edelen, *More Sample-Efficient Tuning of Particle Accelerators with Bayesian Optimization and Prior Mean Models,* under review, (2024).

7. (secondary project contributor, FWP 100637 primary) C. Xu, R. Roussel, A. Edelen, *Neural Network Prior Mean for Particle Accelerator Injector Tuning*, Proc. NeurIPS Workshop on Machine Learning and the Physical Sciences, (2022).

Machine Learning for Autonomous Control of Accelerators

PI: Daniel Ratner (SLAC), Co-PIs: Michael Borland (ANL), Guimei Wang (BNL), Auralee Edelen (SLAC), Xiaobiao Huang (SLAC)

Keywords: AI, Machine Learning, XFELs, Light Sources

Research Project Scope

Efficient, robust, automated tuning of accelerators can help to commission new scientific user facilities, accelerate recovery from downtime, switch between operating modes, and deliver the highest quality beam to scientific users. Advanced control and data strategies enable novel modes of operation and incorporate user signals directly into accelerator optimization, improving the quality of the collected data and guiding experiments. Finally, failures can cause many hours of interruption to normal accelerator operation, and anomaly detection can direct preventative steps and assist recovery to reduce downtime. Machine learning (ML) methods show promise addressing these challenges. In this project we develop novel ML tuning methods, benchmark against existing approaches, and test them on simulated platforms as well as live on both synchrotron and FEL accelerators. We also characterize anomalies typical of FELs and storage ring light sources, create benchmark data sets, and develop methods of prediction and root cause analysis to improve accelerator reliability. Finally, we develop mechanisms to improve AI-operator interaction, both to facilitate operator use of algorithms and to improve collection of new datasets. The R&D effort will benefit existing and future accelerator-based scientific user facilities and computer-controlled, large scale, complex systems in general.

Recent Progress

Tuning thrust: The tuning thrust focuses on new methods and applications of Bayesian optimization (BO), along with associated online analysis tasks. For example, Multipoint Bayesian Algorithmic Execution (Multipoint BAX) is a new framework that extends BO to tasks where the objective and modeled space are distinct; we recently showed Multipoint-BAX can minimize LCLS injector emittance 20 times faster than BO in simulations, and resulted in a 25% smaller emittance in the first online test at LCLS. We have studied various methods for incorporating temporal variation in BO, for example showing that BO supported by hysteresis-aware GPs can be both faster and more effective than standard GPs when controlling magnets. Adaptive BO (ABO) was developed for tasks affected by drifts outside the control space. Similarly, RCDS-S (an RCDS variant) adds performance safety awareness when optimizing in the presence of drifts.

We have also investigated related topics in online analysis, both as a means to circumvent difficult control tasks and to support optimization tasks. Projects include developing new methods for reconstructing accelerator and x-ray beam parameters, improving time resolution for LCLS users, and providing beam parameters for accelerator operators. Recent work in collaboration with an

ECA developed a method to reconstruct detailed 4-D beam distribution profiles in high dimensional phase spaces using differentiable beam dynamics simulations.

Failure detection thrust: The failure detection thrust tasks includes identifying subsystems responsible for beam performance issues at LCLS, and finding faults in injector, magnet, and power supply systems at synchrotrons. A new beam-based approach identifies faulty subsystems (e.g. a particular RF station) by leveraging beam data. This method is fully automated and identifies ten times more events than manual methods, and while reporting six times fewer false positives. The automated fault identification system has also been used to create a new benchmark data set for future algorithm development. The RF station task spurred the development of Coincident Anomaly Detection (CoAD), a new unsupervised AI algorithm capable of identifying anomalous subsystems within a larger complex system (e.g., RF stations in a particle accelerator), currently being patented by Stanford.

NSLS-II is focusing on magnet and power supply trips, which are a leading contributor to downtime. An ML model predicts anomalous temperature trends at an early stage, providing time for experts to develop minimally invasive repair plans. The model is now running and has alerted technicians to do repairs 22 times over the last three months. APS has trained LSTM networks to predict power supply temperature anomalies, since power supply faults are one of the two largest sources of beam losses and downtime (the other being the RF systems). In tests where failure of a power supply fan is simulated, the algorithm correctly identifies temperature anomalies with an F1 score of 0.97, indicating simultaneously high precision and recall. APS also began using low-resolution infrared cameras to expand the amount of data available beyond the typical handful of sensors available in a power supply. IR camera data has been used to train LSTM networks, which have shown similar success to those based on traditional discrete sensors. These hold the promise of being able to detect anomalies that would be missed by discrete sensors.

Where possible, all algorithmic and application development have been tested on SUFs or associated test facilities, including physics-informed kernels, MG-GPO for DA and Touschek lifetime optimization, BAX for emittance optimization, RCDS-S for kicker-bunch matching, hysteresis modeling in magnets, electron beam phase-space reconstruction, and RF fault detection. Deployment platforms are being developed in collaboration with this project to support both R&D and deployment to operations, and to disseminate results across the SUFs. For optimization algorithms, *Xopt* is a python package for optimization algorithms, and *Badger* provides a user interface to *Xopt* specifically for real-time optimization at accelerators. Both are now in use at facilities worldwide. APS has its own existing infrastructure; *APSopt* is a newly-implemented Python tuning platform designed for compatibility with the existing APS systems and facility-agnostic functionality in *Xopt*. We are developing interoperability between *APSopt* and *Badger*, and exploring the possibility to merge the two platforms.

Future Plans

The renewal will address three areas critical for uptake of AI tuning methods within the light source accelerator community: robustness, scalability to high dimensions, and AI-operator interfaces. First, algorithms must be robust, i.e., have low probability of failure, require minimal expert supervision, and cover a high percentage of applications. Second, algorithms must be scalable, e.g., tuning methods should handle large numbers of parameters, and fault detection methods should scale to complex phenomena with large numbers of inputs and subsystems. Finally, AI-operator interfaces should maximize algorithmic success and human decision-making.

For fault detection, we have similarly identified three requirements for wider utilization: scaling to large datasets with complex relationships and conditions, scaling to large numbers of systems without expert supervision, and increasing operator engagement through improved data presentation. During the initial project, we developed two promising fully-unsupervised deep-learning methods, both capable of handling complex phenomena and able to be deployed with minimal hand-labeling and expert input. We will continue research into these methods, with an emphasis on developments that will make them applicable to a wider range of problems and more intuitive for operators.

For both tuning and fault detection, the existing project has identified high-value application areas. At LCLS, tuning work will continue to focus on algorithms for emittance minimization and FEL power optimization (both key to achieving saturation at the future LCLS-II high-energy upgrade, LCLS-II-HE), but also with a renewed emphasis on directly incorporating user-side signals into tuning. At rings, we will continue existing research into maximizing the dynamic aperture and beam lifetime, critical for future storage rings, as well as efforts to maximize stability and charge efficiency in injector chains.

The tuning thrust has identified several research areas: first, we will work on incorporating prior information into AI optimization routines. Priors will make BO both faster and more likely to converge, especially in high-dimensional input spaces and when initial performance is far from the optimum. For example, we will build on work using NN surrogates as priors. Related to this, we will continue BAX research on new multi-point optimization tasks using NN surrogates. For example, tuning the longitudinal phase space distribution requires a secondary re-minimization of the betatron beam size. We have recently begun work using multipoint BAX to maximize dynamic/momentum aperture in storage rings, and preliminary work shows more than an order of magnitude speed-up.

Second, `safe' optimization methods lessen the impact to users during tuning, as even successful AI tuning methods may temporarily reduce the machine's performance. Continuously active, operations-safe algorithms with rigorous constraints on stability, minimal performance, and safety would obviate the need for expert intervention, reduce dedicated machine tuning time, improve operator confidence in deployment, and generally increase adoption of AI methods. We will extend

previous research into safe exploration methods for RCDS and BO and develop new methods for improving the use of constraints. We are investigating improvements for trust-region BO (TuRBO) for safe, high-dimensional tuning, and ABO for safe optimization under drift.

As a parallel means to improve tuning efficiency, we will investigate methods for improved sampling efficiency and passive data collection during operations. We are developing methods for passive data acquisition; e.g. ghost imaging (GI) to monitor cathode quantum efficiency (QE) maps without machine interruption. We are also developing novel measurement schemes to speed up optimization; recently, APS began testing a new concept for simultaneous measurement of both DA and lifetime by storing the beam continuously in some buckets for lifetime measurements, while using other buckets for measurement of DA or injection efficiency.

The anomaly thrust is continuing development of multi-modal, unsupervised failure detection methods. We are building on the success of CoAD by looking for new applications, e.g. extending to the synchronous RF phase data for the first time. The richer phase data doubles our sensitivity and may enable explainability, i.e. classifying the fault type as well as the subsystem. We are also exploring new technologies to provide additional data for AI algorithms. In addition to the low-cost, low-resolution IR cameras mentioned above for power supply monitoring, APS will study low-cost vibration sensors for continuous monitoring of water pumps to support predictive maintenance; presently, pumps can only be evaluated at several-month intervals using an instrument that must be moved from one pump to the next. At NSLS-II we are deploying the magnet cooling failure detection algorithms developed in the initial project into production as well as testing more powerful methods. Additionally, problems such as RF cavity arcs, BPM glitches, power supply failures, and controls-network failures often occur abruptly and most likely cannot be predicted or prevented. We are investigating methods (e.g. CoAD) for identifying the root cause buried amongst hundreds of process variables (PVs) in the fault state related to the affected subsystems. Additionally, we will investigate the use of root cause analysis to understand the propagation chain of anomalies over time and pinpoint the faulty PV by incorporating associations between relevant PVs that contribute to anomalies.

We propose several research avenues to improve the AI-operator interaction at accelerators: First, we will design methods to collect operator feedback on AI method performance. Second, we will research interpretability methods, so that the AI methods under development will aid both operator performance *and* understanding. For example, we are extending the visualization interface of Badger so that operators can explore "what-if" scenarios for different solutions after an optimization run. Finally, we will explore using large language models (LLMs) to improve querying of electronic logbooks (elog) and to assist operators writing entries. Later work will apply the same methods to failure detection tasks, e.g. using "what-if" concept to search for causality as an operator recovers from a fault. Likewise, visualization of algorithm outputs will help operators make real-time decisions in narrowing down possible fault sources.

Publications (last 2 years)

1. R. Roussel, A. Edelen, D. Ratner, K. Dubey, J. P. Gonzalez-Aguilera, Y. K. Kim, and N. Kuklev. *Differentiable Preisach modeling for characterization and optimization of particle accelerator systems with hysteresis,* Phys. Rev. Lett., **128,** 204801 (2022)

2.. R. Humble, F. H O'Shea, W. Colocho, M. Gibbs, H. Chaffee, E. Darve, and D. Ratner. *Beam-based rf station fault identification at the slac linac coherent light source*, Phys. Rev. Accel. Beams, **25**, 122804, (2022)

3. Z. Zhang, M. Song, X. Huang, *Optimization method to compensate accelerator performance drifts*, Phys. Rev. Accel. Beams, **25**, 122801 (2022)

4. S. Miskovich, W. Neiswanger, W. Colocho, C. Emma, J. Garrahan, T. Maxwell, C. Mayes, H.D. Nuhn, S. Ermon, A. Edelen, and D. Ratner, *Multipoint-BAX: A New Approach for Efficiently Tuning Particle Accelerator Emittance via Virtual Objectives*, MLST, **5,** 015004, (2024)

5. R. Humble, 7. R. Humble, Z. Zhang, F. O'Shea, E. Darve, D. Ratner, *Coincident Learning for Unsupervised Anomaly Detection*, Under review, MLST

6. T. Boltz et al., *More Sample-Efficient Tuning of Particle Accelerators with Bayesian Optimization and Prior Mean Models*, Under review, Phys. Rev. Accel. Beams

7. R. Roussel et al., *Bayesian Optimization Algorithms for Accelerator Physics*, Under review, Phys. Rev. Accel. Beams

Machine Learning for Improving Accelerator and Target Performance

Willem Blokland (ORNL) and Malachi Schram (JLAB)

Keywords: Machine Learning, prognostics, accelerator, operations, infrastructure

Research Project Scope

We integrate Machine Learning (ML) techniques into the online monitoring and control systems of the Spallation Neutron Source (SNS) Accelerator and Target to prevent equipment failures, reduce radioactivation of beam line areas, and detect target system anomalies to increase the scientific output of the DOE facility.

With the experience gained in the previous phase in the grant [R1-2], we move from off-line analysis to online application of ML as part of Operations. An important aspect in practical application of ML models in operations is data drifts. Accelerators are dynamic machines that produces drifting data due to various reasons. The ML models trained on historical data may fail if the new data it encounters during operation is from outside the training data distribution. This need to be addressed with continual re-training or fine-tuning of ML models [R3-4]. To do so we are extending the SNS accelerator infrastructure with additional computing resources to implement a ML workflow with a continual learning framework [R5].

The grant work is performed by various experts in Machine Learning, Operations, Infrastructure, Accelerator Physics and Diagnostics, and Control Systems from Oak Ridge National Laboratory and Jefferson Laboratory. We apply ML to three use-cases: prediction and prevention of Errant Beam to reduce radioactivation and downtime, automatic and fast Optimization of Beam losses using Beam Orbit, and detection and prediction of Anomalies in the Target Support Loops.

Recent Progress

In the use-case of **Errant-Beam Prediction** and Prevention, we have achieved significant advancements with the Siamese Neural Network (SNN) and Variational Auto-Encoders (VAE) models developed under the previous grant. These models have demonstrated good performance, enabling us to achieve a true positive rate of over 40% in predicting faults while maintaining false positives below 0.1% using beam current data obtained from the Differential Current Monitor (DCM) [P1]. However, we have discovered that when the beam configuration changes, models trained on

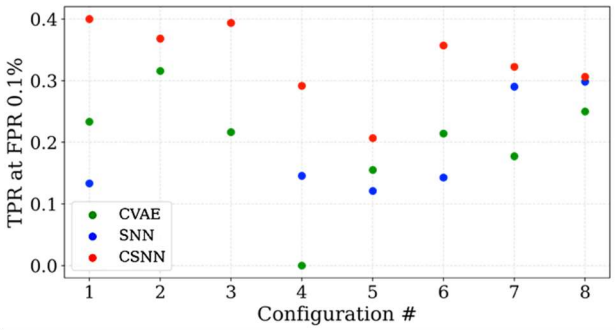

Figure 1. Performance comparison between the SNN, CSNN and CVAE models.

prior configurations become obsolete. In response, we have implemented conditional-SNN (CSNN) and conditional-VAE (CVAE) models. These new models incorporate beam configuration parameters as conditions, allowing them to adapt to varying configurations. The introduction of conditional inputs enables the models to utilize data from diverse beam configurations during training, even facilitating learning from configurations with limited data samples. With rigorous comparison, see [P2], we have determined that CSNN surpasses both SNN and CVAE in performance, as illustrated in Figure 1. We have also started work on using data from Beam Position Monitors, the beam phase data. This data is related to the energy of the beam and thus directly related to the performance of the accelerating cavities. We applied a multi-layered perceptron and found that we can predict about 25% of the errant beam pulses with 0.1 % of false positives [P3].

For the **Target Anomaly Detection**, we chose the mercury loop system as the use-case. Critical parameters for the system were identified and the historical data was extracted from the SNS archiver to serve as a trial set for different anomaly detection algorithms. Historical operational logs were used to provide example anomalies. Several ML techniques have been trialed for the initial unsupervised/semi-supervised phase, including physics-based models and purely mathematical models. Initial results verified that single variable anomaly detection did not provide good results due to the interplay of many different parts of the system, see Figure 2. We are now focusing on multi-variate approaches. Some, such as the long short-term memory (LSTM) model have shown themselves to be good at predicting the expected behavior of the system. Others, such as the isolation forest approach can identify anomalies, but have shown problems in isolating anomalies associated with a particular system in the presence of impacts from other linked systems. To prepare for future steps where we move to continuous learning, we have developed a framework for processing future systems anomaly reports and collecting human feedback using existing SNS reliability tracking tools.

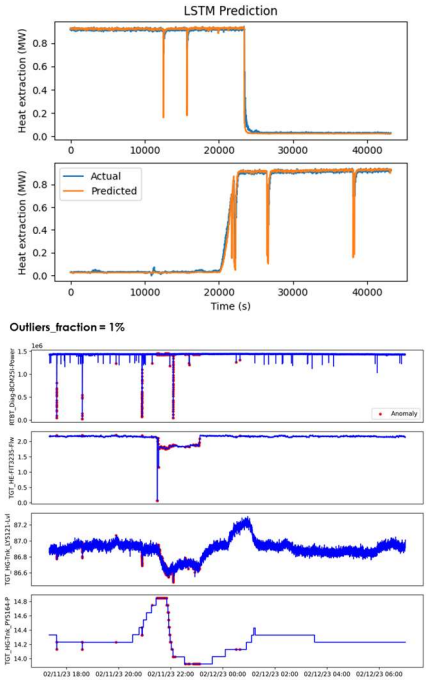

Figure 2. LSTM prediction (top) and isolation forest (bottom).

The **Beam Loss Optimization** use-case uses ML to optimize losses online by slightly tuning accelerator parameters during SNS production. The optimization should not affect machine availability. We identified the software infrastructure needed for reliably running beam loss optimization during SNS production as well as training ML models. The infrastructure includes:

1. *ML agent framework*: It is based on JLab's Data Science Optimization Toolkit. The framework provides set of swappable agents for Reinforcement Learning (RL) and abstracts away specifics of optimization problem.
2. *Virtual Accelerator* (VA)– accelerator simulation software: VA uses PyORBIT3 code to simulate beam dynamics and imitates EPICS (control system used at SNS) which makes it a digital twin of the real SNS accelerator.
3. *Proxy server* between ML agent and the real accelerator: It secures accelerator to avoid machine downtime if optimization process requested a potentially unsafe (in terms of loss or other Machine Protection System parameters).

We have implemented the first version of the Virtual Accelerator and tested model learning and inference on pilot case of orbit flattening with Bam Position Monitors (BPM) and dipole correctors. For this test case we tried Deep Deterministic Policy Gradient (DDPG) and more advanced Twin Delayed DDPG (TD3). This is a fully integrated test case where ML agent interacts with VA over EPICS. We also started the development of the proxy server to leverage the ScanEngine (SNS data collection and scanning tool).

For the **ML Infrastructure**, we now have access to a NVIDIA-based GPU system for the training of the various models and an 1 Petabyte storage system both to be located within the accelerator network. We are leveraging the planned accelerator network upgrades for fast connection between the edge computers, storage and GPU systems. The supporting infrastructure, partially implemented, is shown in Figure 3.

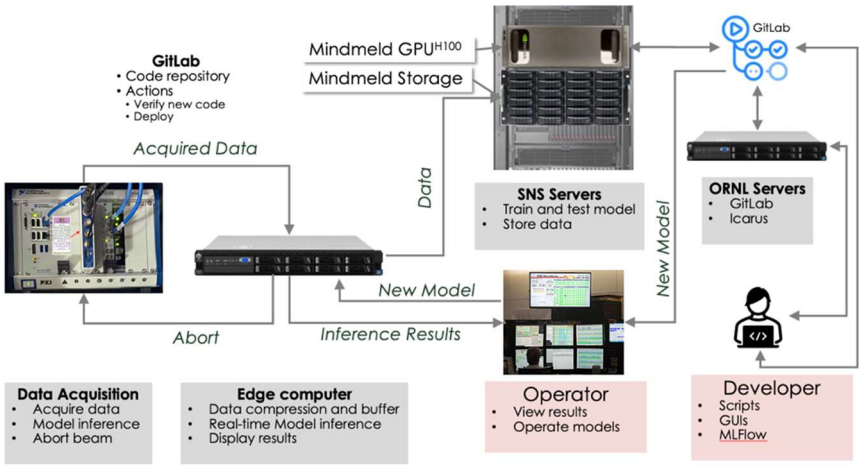

Figure 3. Infrastructure supporting the Machine Learning applications.

After the current post-doc left, we have arranged with a ML group at ORNL for support on the ML infrastructure. We have also opened a search for a new post-doc. We are also in the process of involving students (including from MSI) for the summer.

Future Plans

The next immediate steps in the **Errant-Beam Prediction** case involve evaluating these models using the data collected at a 60Hz rate during the last run and fine-tuning them to enhance their robustness. This process will enable us to conduct online testing of the models once the

accelerator is in operation this summer. In the long term, our goal is to develop a continual learning framework that allows us to continuously train and fine-tune the machine learning models as necessary to address data drifts. Additionally, we plan to explore the integration of data from Beam Position Monitors alongside the data from the Differential Current Monitors (DCM) to improve the performance further. We plan to select the most promising unsupervised approaches and use them to generate lists of potential anomalies. These would be graded by human experts and used to rate the methods and well as to increase the pool of available training data. We expect this to also help develop best practices for tagging and labeling data that can be extended to our future systems. We will also continue surveying methods for the future continuous learning phase.

We plan for the **Target Anomaly Detection** use-case to select the most promising unsupervised approaches and use them to generate lists of potential anomalies. These would be graded by human experts and used to rate the methods and well as to increase the pool of available training data. We expect this to also help develop best practices for tagging and labeling data that can be extended to our future systems. We will also continue surveying methods for the future continuous learning phase. Regarding **the Beam Loss Optimization**, we plan to have a data collection system integrated with ML agents by July – August 2024 and start collecting data from the real SNS accelerator while modifying magnet settings. For the infrastructure, we plan to move the GPU and storage system to their final location in the accelerator server room.

Additional publications from the previous phase of the grant are in [P5-10].

References

R1. M. Rescic, R. Seviour, and W. Blokland, “Predicting particle accelerator failures using binary classifiers,” Nuclear Instruments and Methods in Physics Research, Section A: Accelerators, Spectrometers, Detectors and Associated Equipment, vol. 955, Mar. 2020.

R2. M. Schram, K. Rajput, K. S. P. Li, J. S. John, and H. Sharma, “Uncertainty aware ml-based surrogate models for particle accelerators: A study at the fermilab booster accelerator complex,” 2022. [Online]. Available: https://arxiv.org/abs/2209.07458

R3. A. Scheinker, F. Cropp, S. Paiagua, and D. Filippetto, “An adaptive approach to machine learning for compact particle accelerators,” Scientific Reports, vol. 11, no. 1, Sep. 2021. [Online]. Available: https://doi.org/10.1038/s41598-021-98785-0

R4. G. Pang, C. Shen, L. Cao, and A. V. D. Hengel, “Deep learning for anomaly detection,” ACM Computing Surveys, vol. 54, no. 2, pp. 1–38, Mar. 2021. [Online]. Available: https://doi.org/10.1145/3439950

R5. A. Chen, A. et. al, “Developments in mlflow: A system to accelerate the machine learning lifecycle,” in Proceedings of the Fourth International Workshop on Data Management for End-

to-End Machine Learning, ser. DEEM'20. New York, NY, USA: Association for Computing Machinery, 2020. https://doi.org/10.1145/3399579.3399867

Publications

P1. W. Blokland, K. Rajput, M. Schram, T. Jeske, P. Ramuhalli, C. Peters, Y. Yucesan, A. Zhukov, "Uncertainty aware anomaly detection to predict errant beam pulses in the Oak Ridge Spallation Neutron Source accelerator," Physical Review Accelerators and Beams, vol 25, p.122802, Dec 2022. Available: https://doi.org/10.1103/PhysRevAccelBeams.25. 122802

P2. K. Rajput, M. Schram, W. Blokland, Y. Alanazi, P. Ramuhalli, A. Zhukov, C. Peters, R. Vilalta, "Robust Errant Beam Prognostics with Conditional Modeling for Particle Accelerators" Machine Learning: Science and Technology. https://doi.org/10.1088/2632-2153/ad2e18

P3. Y.A. Yucesan, W. Blokland, P. Ramuhalli, A. Zhukov, C. Peters, D. Brown, C. Long, "A machine learning approach for particle accelerator errant beam prediction using spatial phase deviation," Nuclear Instruments and Methods in Physics Research Section A: Accelerators, Spectrometers, Detectors and Associated Equipment Volume 1063,2024, 169232, ISSN 0168-9002, https://doi.org/10.1016/j.nima.2024.169232.

P4. C. Elliott et al., "From Physics Study to Operations: Progress for Production Deployment of ML-Driven Beam Loss Optimization", 4th ICFA Beam Dynamics Mini-Workshop on Machine Learning Applications for Particle Accelerators, March 5 – 8, Gyeongju, South Korea. https://www.indico.kr/event/47/contributions/582/

P5 N. R. Miniskar, A. Young, F. Liu, W. Blokland, A. Cabrera, J. S. Vetter, "Ultra Low Latency Machine Learning for Scientific Edge Applications," 32nd International Conference on Field-Programmable Logic and Applications (FPL), pp. 01-07, Aug 2022. Available: https://doi.org/10.1109/FPL57034.2022.00068. The FWP provided the support to the design, implementation, testing and deployment of the FPGA-based ML solution at SNS.

P6. B.P. Maldonado, F. Liu, N.Goth, P. Ramuhalli, M. Howell, Ryuji Maekawa, S. Cousineau, Data-Driven Modeling of a High Capacity Cryogenic System for Control Optimization, IFAC-PapersOnLine, Volume 56, Issue 2, 2023, Pages 3986-3993, doi: 10.1016/j.ifacol.2023.10.1365.

P7. K. Rajput, M. Schram, K. Somayaji, "Uncertainty Aware Deep Learning for Particle Accelerators," Machine Learning and the Physical Sciences workshop, NeurIPS, 2022.

P8. M. I. Radaideh, C. Pappas, J. Walden, D. Lu, L. Vidyaratne, T. Britton, K. Rajput, M. Schram, S. Cousineau, "Time series anomaly detection in power electronics signals with re- current and ConvLSTM autoencoders," Digital Signal Processing, vol 130, p. 103704, Oct 2022. Available: https://doi.org/10.1016/j.dsp.2022.103704

P9. Y. Alanazi, et al, "Multi-module-based CVAE to predict HVCM faults in the SNS accelerator," Machine Learning with Applications, Volume 13, 2023, 100484, ISSN 2666-8270, https://doi.org/10.1016/j.mlwa.2023.100484.

P10. M. I. Radaideh, C. Pappas, S. Cousineau, “Real electronic signal data from particle accelerator power systems for machine learning anomaly detection,” Data in Brief, vol 43, p. 108473, Aug 2022. Available: https://doi.org/10.1016/j.dib.2022.108473

Actionable Information from Sensor to Data Center

Jana Thayer (SLAC), Ryan Coffee (SLAC), Ryan Herbst (SLAC), Ian Foster (Argonne), Peter Kenesei (Argonne), Michael Prince (Argonne), Hemant Sharma (Argonne), Antonino Miceli (Argonne), Nicholas Schwarz (Argonne), Rajkumar Kettimuthu (Argonne)

Keywords: Machine Learning, Edge ML, Bragg Peak, High-Energy X-ray Diffraction Microscopy, Serial Crystallography

Research Project Scope

The goal of the Actionable Information from Sensor to Data Center (AISDC) project is the development of adaptable ML algorithms performing inference at the experiment edge to provide real-time feedback to experiments taking the next critical steps needed to render the information generated by ML routines from sensors to data centers fully actionable. Importantly, these advances will meet the challenge of high data volumes by closing the automated feedback loop during active experiments. We are pursuing five specific avenues of research -- two devoted to general infrastructure and three related to specific experiments -- to achieve this goal.

On the infrastructure side, we will expand the SLAC Neural Network Library (SNL)[P1,P2] to accommodate a wider range of FPGAs and hardware typically available at sensors to generalize our AI inference capabilities. The framework will focus on larger networks such as transformers, and to optimize aspects of attention-based architectures by making use of more integer-friendly arithmetic methods such as Hopfield networks to replace conventional attention in transformer-like foundation models. Complementing these efforts at the experiment edge, we will develop an optimized Framework for Rapid ML model Re-training (FRMR) at remote data centers and generalize it so it can be deployed at other facilities and applied to new models and data. As part of this effort, the FairDMS framework [R1] will be expanded to develop capabilities to search for the most suitable embedding and clustering models. In principle, this system will learn on the fly from streaming data, enhancing discovery capability. Underpinning this framework is the ability to stream data between instrument and data center AI/HPC and to accelerate the model training process using stream learning, the incremental training of models on streaming data.

On the experimental side, we will first explore different representations of multi-channel time-series data to optimize its delivery to the sensor as actionable information in a form that can be used for control. Multi-channel time-series detectors in the new Time-resolved atomic, Molecular and Optical Science instrument (TMO) at LCLS-II will support gas phase photochemistry and attosecond electron dynamics. By deploying the previously developed CookieNet [P3] in FPGA at the Edge, we can produce actionable information at the rate of data production, 1 MHz. This information can then be converted into a control directive to direct and optimize experiment conditions. Data from a second diagnostic, the TimeTool, will be characterized and a model developed to provide a direction and magnitude for the laser timing

control system. Second, we will leverage the SNL library to chain calibration, assembly, and inference tasks to overcome the bottleneck to providing near real-time feedback for imaging experiments on tiled detectors with high repetition rates. We previously developed PeakNet and SpeckleNN for Bragg peak finding in Serial Femtosecond Crystallography (SFX) and classification in Single Particle Imaging (SPI), respectively. In this project we will render these ML engines LCLS-II ready by 1) integrating them into the LCLS-II Data Reduction Pipeline (DRP) for real-time inference at the edge and 2) leveraging the fairDMS architecture for rapid model retraining and delivery of updated parameters to the sensor. To achieve this, we will explore and benchmark different solutions to the compute bottlenecks presented by next-generation detectors such as potentially offloading the per-tile detector calibration tasks in the analysis pipeline to FPGA or training PeakNet [P4] and SpeckleNN [R3] on uncalibrated images and deploying in FPGA using SNL. Collectively these advances will enable PeakNet and SpeckleNN to veto undesirable events and identify anomalies in real-time, information that could be used to semi-autonomously steer SFX and SPI experiments at LCLS-II. Finally, we will refine the ML algorithms we deployed at both the experiment edge and remote data centers for High Energy X-ray Diffraction Microscopy (HEDM) experiments, with a focus on reliably extracting the smallest possible data features to optimize performance. We will enhance BraggNN [R2] to predict peak location addressing the specific problem regarding BraggNN's limitation in predicting overlapped peak locations and non-uniform peak sizes. In addition, a new method for rapid anomaly detection applied to in-situ HEDM will be developed, attempting to isolate the grain that caused the anomaly. Finally, we will investigate the use of Electron Backscatter Diffraction (EBSD) maps as ground truth for HEDM to improve the HEDM peak detection accuracy. These advances will be instrumental for handling the massive data throughputs of LCLS-II and APS-U. Efficiently distributing analysis and inference between the experiment edge and remote data centers will rapidly generate a stream of actionable information that can be used to steer experiments in a fully autonomous fashion for the first time. Taken together, these advances will provide an integrated approach to data analytics that fully leverages the resources of the DOE complex to support novel experiments enabled by the upgrades.

Recent Progress

In the Multi-channel Time-series Detectors research thrust, the CookeNetAE model has been deployed and demonstrated at the Edge and is awaiting deployment with the MRCO endstation to the TMO instrument. There has been some early exploration of non-uniform quantization for optimized ingestion of pre-processed data into ML models for FPGA to convert the output of the TimeTool into a metric of control direction and magnitude. A candidate dataset has been identified and a model has been developed and is being evaluated.

Significant progress has been made in the areas of Real-time Machine Learning for Tiled Detectors. The PeakNet architecture has been re-designed to enable better integration with various sized feature extraction backbones from HuggingFace's model hub

(https://huggingface.co/models), enhancing flexibility. More importantly, the new architecture offers a vast design space to trade off computation and accuracy, accelerating the identification of optimal models both for the edge and data center AI. Concurrently, a notable challenge to effectively train our models has been the scarcity of labeled data. To address this, we have developed a scalable data engine infrastructure for PeakNet to automate dataset curation, including the creation of PeakNet-10k, a curated dataset featuring 10,000 labeled, full-resolution images for Bragg peak segmentation. Furthermore, from the perspective of edge AI, SpeckleNN is being ported to FPGA using SNL which is under continuous development to add features and improve structures.

In-situ High Energy Diffraction Microscopy has developed a new workflow for the rapid detection of the onset of plastic deformation in HEDM data using AI/ML methods (see figure). Building on the previously developed fairDMS workflow, we developed a robust, self-supervised, machine learning-based framework that enables rapid identification of, and thus automated response to, the minute changes in diffraction spots measured by FF-HEDM and probable microstructural changes in polycrystalline metals as shown in the Figure below. A polycrystalline sample is subject to mechanical loading while we acquire HEDM data. Bragg diffraction spots from the initial material state are used to train an image representation model (encoder) and a clustering model. These two models combined are sensitive to changes in the diffraction spots. Using these models, the rare event indicators are computed as we continue to apply mechanical loading to the sample and acquire HEDM data. A significant increase in REI is quantitative actionable information that the experimenters can use to steer the course of the experiment.

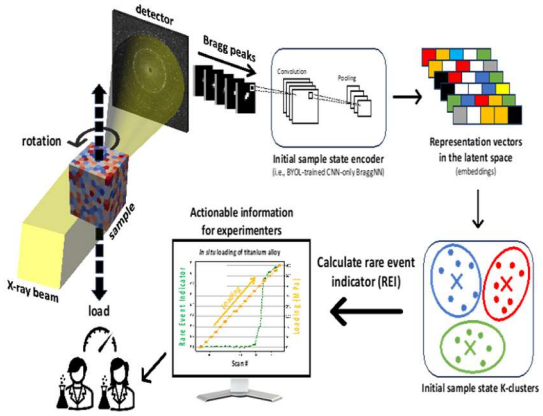

The Framework for Rapid Model Retraining (FRMR) has demonstrated the transfer of training data from the APS to the HPC system, such as Polaris followed by the execution of BraggNN model training and retraining using the transferred data. The model has been successfully transferred to other computing facilities (NERSC's Perlmutter) where inference operations were performed using fresh data and the previously trained model. This demonstration will be used to prepare for the rapid model retraining.

Future Plans

The new MRCO endstation will be deployed at LCLS-II in September 2024 offering an opportunity to demonstrate real-time inference at the edge using CookieNet and the real-time retraining loop under experimental conditions. Although the control point to the experiment has been identified and exercised, the connection between the acquisition loop and the control loop

has not yet been made. The TimeTool research thrust, to characterize and control the laser timing system, is still in the beginning stages with remaining work as follows: ML for spectral analysis, phase tagging for high power laser, and X-ray pulse time-energy reconstruction. ML for Tiled Detectors is investigating neural architectures to find a compact-sized SpeckleNN that is performant on the limited resources of an FPGA. Meanwhile, the PeakNet dataset will be scaled up to contain 1 million labeled images. FRMR will be employed for rapid re-training of a compact PeakNet with new experimental data. We will create an index map for SFX images. Concretely, we will apply the following methods to learn a good data representation via self-supervised learning: 1) BYOL (Bootstrap Your Own Latent) [R4] relies on an online network and a target network that interact and learn from one another. The online network is used to predict the target network representation of the same image under a different augmented view. This approach was previously demonstrated in BraggNN; 2) DINO (self-DIstillation with NO labels) [R5] is a self-supervised learning method that involves a student network and teacher network providing categorical distributions between student and teacher networks from two augmented views of the same input. In-situ High Energy Diffraction Microscopy is planning on enhancing BraggNN to expand to overlapping peaks. To augment the rapid anomaly detection applied in-situ HEDM workflow, visualize which grains in the sample cause the anomaly. Finally, we will use ex situ measurements, electron backscatter diffraction (EBSD), as ground truth for peak detection algorithms to enhance HEDM peak detection accuracy. FRMR will extend the rapid re-training workflow to multiple facilities, including key components such as data store, model store, and the methodology to compare different data and decide whether retraining is needed. FRMR aims to enhance the existing retraining framework by overcoming current limitations, such as scaling to larger systems and improving methods for identifying data similarity/dissimilarity. Additionally, we will introduce advanced functionalities, including parallel hyper-parameter search and automated steering, to bolster the retraining framework's capabilities. This new retraining framework can then be applied to more applications such as PeakNet and SpeckleNet and the anomaly detection methodology can be used to evaluate the differences between the data.

References

1. A. Ali, H. Sharma, R. Kettimuthu, P. Kenesei, D. Trujillo, A. Miceli, I. Foster, R. Coffee, J. Thayer, Z. Liu, “fairDMS: Rapid model training by data and model reuse” in 2022 IEEE International Conference on Cluster Computing (CLUSTER) (IEEE Computer Society, Los Alamitos, CA, USA, 2022; https://doi.ieeecomputersociety.org/10.1109/CLUSTER51413.2022.00050), pp. 394–405 (2022).

2. Z. Liu, H. Sharma, J.-S. Park, P. Kenesei, A. Miceli, J. Almer, R. Kettimuthu, I. Foster, BraggNN: fast X-ray Bragg peak analysis using deep learning. IUCrJ **9** (2022).

3. C. Wang, E. Florin, H.-Y. Chang, J. Thayer, C. H. Yoon, SpeckleNN: a unified embedding for real-time speckle pattern classification in X-ray single-particle imaging with limited labeled examples. IUCrJ **10**, 568–578 (2023).

4. J.-B. Grill, F. Strub, F. Altché, C. Tallec, P. H. Richemond, E. Buchatskaya, C. Doersch, B. A. Pires, Z. D. Guo, M. G. Azar, B. Piot, K. Kavukcuoglu, R. Munos, and M. Valko, *Bootstrap Your Own Latent A New Approach to Self-Supervised Learning*, arXiv:2006.07733 (2020)

5. M. Caron, H. Touvron, I. Misra, H. Jégou, J. Mairal, P. Bojanowski, and A. Joulin, *Emerging Properties in Self-Supervised Vision Transformers*, arXiv:2104.14294, http://arxiv.org/abs/2104.14294 (2021).

Publications

1. R. Herbst, R. Coffee, N. Fronk, K. Kim, K. Kim, L. Ruckman, J. J. Russell, *"Implementation of a framework for deploying AI inference engines in FPGAs"* in Accelerating Science and Engineering Discoveries through Integrated Research Infrastructure for Experiment, Big Data, Modeling and Simulation, K. Doug, G. Al, S. Pophale, H. Liu, S. Parete-Koon, Eds. (Springer Nature Switzerland, Cham, 2022), pp. 120–134.

2. SLAC NeuralNet Library Source. https://github.com/slaclab/snl/releases/tag/v0.2.0. Accessed 2023-03-16.

3. N. Layad, Z. Liu, and R. Coffee. Open source implementation of the CookieNetAE model. https://github.com/AISDC/CookieNetAE. Accessed 2024-04-06.

4. C. Wang, P.-N. Li, J. Thayer, C. H. Yoon, *PeakNet: An Autonomous Bragg Peak Finder with Deep Neural Networks*. arXiv arXiv:2303.15301 (2023). http://arxiv.org/abs/2303.15301.

5. C. Wang, E. Florin, H.-Y. Chang, J. Thayer, C. H. Yoon, *SpeckleNN: a unified embedding for real-time speckle pattern classification in X-ray single-particle imaging with limited labeled examples*. IUCrJ **10**, 568–578 (2023).

6. C. Benmore, T. Bicer, M. K. Y. Chan, Z. Di, D. Gürsoy, I. Hwang, N. Kuklev, D. Lin, Z. Liu, I. Lobach, Z. Qiao, L. Rebuffi, H. Sharma, X. Shi, C. Sun, Y. Yao, T. Zhou, A. Sandy, A. Miceli, Y. Sun, N. Schwarz, M. J. Cherukara, *Advancing AI/ML at the advanced photon source*. Synchrotron Radiation News **35**, 28–35 (2022).

7. H. Sharma, J.-S. Park, P. Kenesei, J. Almer, Z. Liu, A. Miceli, *"Speeding up diffraction analysis using machine learning"* in ACTA CRYSTALLOGRAPHICA A-FOUNDATION AND ADVANCES (INT UNION CRYSTALLOGRAPHY 2 ABBEY SQ, CHESTER, CH1 2HU, ENGLAND, 2022) **vol. 78**, pp. A141–A141.

8. Z. Liu, H. Sharma, J.-S. Park, P. Kenesei, A. Miceli, J. Almer, R. Kettimuthu, I. Foster, *BraggNN: fast X-ray Bragg peak analysis using deep learning*. IUCrJ **9** (2022).

9. A. Ali, H. Sharma, R. Kettimuthu, P. Kenesei, D. Trujillo, A. Miceli, I. Foster, R. Coffee, J. Thayer, Z. Liu, *"fairDMS: Rapid model training by data and model reuse"* in 2022 IEEE International Conference on Cluster Computing (CLUSTER) (IEEE Computer Society, Los Alamitos, CA, USA, 2022; https://doi.ieeecomputersociety.org/10.1109/CLUSTER51413.2022.00050), pp. 394–405.

10. M. Levental, A. Khan, R. Chard, K. Yoshi, K. Chard, I. Foster, *OpenHLS: High-level synthesis for low-latency deep neural networks for experimental science* (2023). https://doi.org/10.48550/ARXIV.2302.06751.

This material is based upon work supported by the U.S. Department of Energy, Office of Science, Office of Basic Energy Sciences under Award Number FWP-100643.

MLExchange: A Collaborative Machine Learning Platform for Scientific Discovery

Alexander Hexemer (ALS, LBNL), Daniel Allan (NSLS-II, BNL), Apurva Mehta (LCLS, SLAC), Nicholas Schwarz (APS, ANL), Subramanian Sankaranarayanan (CNM, ANL), Rama K. Vasudevan (CNMS, ORNL)

Keywords: Machine Learning framework, autonomous, materials discovery, scientific data labeling, Segmentation

Research Project Scope

The Department of Energy's (DOE) Scientific User Facilities (SUFs) stand as pivotal entities in the scientific community, renowned globally for producing detailed, high-quality scientific data through a myriad of experiments, models, and simulations. This data, characterized by its complexity and diversity, requires specialized expertise for accurate interpretation and application. Scientific machine learning (ML) offers a unique chance to harness the scientific community's collective knowledge. Incorporating scientific ML into SUF operations could create a synergistic framework that enhances understanding of the field's strengths and weaknesses. By bridging the gap between ML experts, software developers, SUF researchers, and materials scientists, MLExchange aspires to offer an open-source, web-based holistic solution to the challenges at hand. Developed in collaboration with scientists from six DOE-funded SUFs, MLExchange offers an ecosystem where users can access a variety of analytical and ML-based software solutions, along with community-shared algorithms and user interfaces for data analysis.

Recent Progress

Significant advancements have been made in the MLExchange infrastructure, notably through the integration of *Tiled* for data access and *Prefect* for workflow management. This integration has enabled MLExchange to operate nearly in real-time close to the beamline, which has been successfully tested in recent phases at a scattering beamline and a tomography beamline using web interfaces for seamless data interaction. Current efforts work towards improving the user experience and facilitating autonomous operations, focusing on human-in-loop and autonomous data collection with electron microscopy data. There are plans for these capabilities to soon be extended to synchrotron beamlines. Similarly, current improvements to the CASTING framework aim to finalize the pipeline and initiate the materials discovery process.

Infrastructure Improvements: MLExchange 2.0 represents a significant upgrade aimed at deploying ML tools directly at beamlines that can integrate with experimental workflows seamlessly. A pivotal development in this renewal is *Tiled*, which emerged from *Bluesky*. *Tiled* simplifies data management for ML by offering secure remote data access and abstracting variations in file formats. This revamped MLExchange framework has been successfully deployed and tested at a tomography beamline at Diamond Light Source. As data was acquired, tomographic reconstructions were automatically parsed to MLExchange for use in a segmentation application,

which received positive feedback and is slated for installation and use at the Advanced Light Source (ALS) during tomography beamtime with the ML models trained at Diamond.

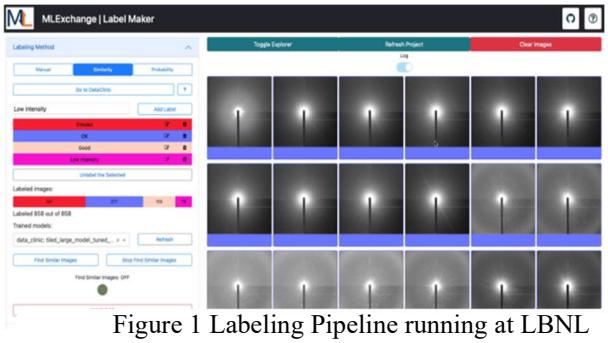

Figure 1 Labeling Pipeline running at LBNL and labeling data from NSLS-II.

MLExchange Web Applications: Within MLExchange, Label Maker allows to accelerate the labeling process of large scientific datasets through manual and AI-guided labeling techniques, as shown in Fig. 1. Label Maker integrates with other apps like Data Clinic, MLCoach, and Latent Space Explorer for pre-labeling ML model training, offering a streamlined approach to data labeling and analysis. Using MLExchange capabilities, it is possible to run the Label Maker webapp at the ALS but labeling and viewing data from the National Synchrotron Light Source (NSLS-II) seamlessly. Other webapp developed recently is a segmentation application for tomography and imaging as shown in Fig. 2. The ML component used in this application is a CAMERA development, DLSIA. Moreover, we have developed and integrated front-end ptychography software, *ptychodus*, which combines both conventional and ML-based approaches for ptychography reconstructions at beamlines. The software not only improves data analysis efficiency but also grants researchers direct access to ML advancements.

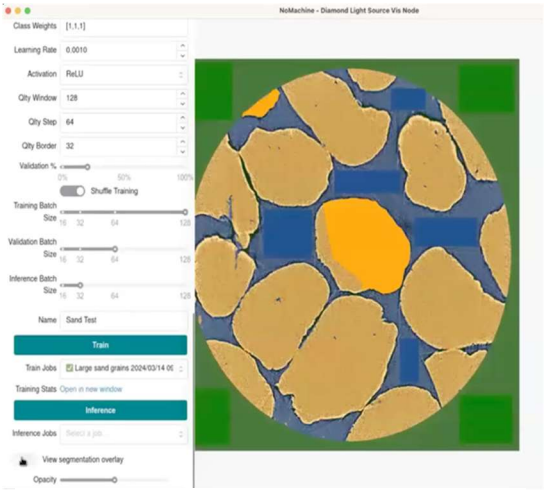

Figure 2 MLExchange Segmentation app for imaging data using CAMERA's DLSIA framework: running at ALS, DIAMOND and to be tested at APS and CNMS.

Additionally, we are enhancing the identification and separation of single-crystal diffraction spots in X-ray Diffraction (XRD) data with ML, significantly cutting processing times while retaining texture and orientation details often missed by traditional methods. By eliminating artifacts during the XRD image integration process, our methods enable a more precise analysis of powder diffraction rings. Remarkably, when trained on small but highly diverse datasets, the gradient boosting method delivers consistent high-accuracy results, with true positive rates between 87.5% and 97.4%, and nearly 100% true negative rates [1]. A commodity GPU maintains prediction times of ~1 second regardless of model complexity or dataset size, making these ML methods ideal for near real-time data processing. In parallel, we have implemented data streaming capabilities from instruments at large-scale facilities to supercomputers, enabling real-time data processing and feedback. This approach allows for applications and workflow models, including ML training and inference, as shown in our successful demonstration with data from the Advanced Photon Source (APS) processed on the Polaris supercomputer. The system's throughput has proven capable of handling data production rates [2], proving the potential for widespread application.

Autonomous and Human-in-the-loop: In any autonomous experiment, goals are usually defined a priori. However, in real experiments with human agents, goals can change dynamically based on data patterns. Human experts bring valuable prior knowledge that proves especially beneficial in initial trials, while AI agents excel at solving optimization problems once the parameter space is narrowed down. Recent progress at Oak Ridge National Laboratory (ORNL) has focused on the alignment of AI with the goals of human agents. To this aim, we have created a Bayesian Optimization Active Recommender System (BOARS) [3], which leverages human expertise to shape targets during automated experiments by means of a voting system, as shown in Fig. 3. Specifically, we used it to show individual spectra captured on a ferroelectric thin film and enable users to upvote or downvote datapoints, followed by Bayesian optimization autonomously identifying spectra that 'closely' match the votes of the user.

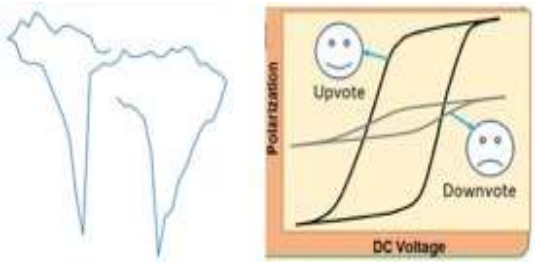

Figure 3 BOARS. A single spectrum is shown to the user, who approves or disapproves (left). Over time, upvoted spectra are weighted and combined to form a target for Bayesian Optimization (right).

Materials Discovery and Design: We hypothesize that mapping metastable phases and their stability under various thermodynamic conditions can fundamentally decode nonequilibrium synthesis pathways. This in-depth understanding is crucial for accurately synthesizing metastable materials and grasping the competitive pathways affecting their distribution in the end product. Hence, we aim to build on the workflow developed in MLExchange 1.0 to combine experimental synthetic pathways and empirically-achieved phases with computer vision, first-principles computations, ML algorithms, and high-performance computing. The approach is data intensive, as shown in Fig. 4 [10], but it could enable reliable predictions of synthesis pathways for metastable materials under various conditions. The validation of these predictions will be supported by experimental work from co-PI Apurva Mehta at SLAC. Our initiative represents a significant shift in materials science towards precision synthesis, leveraging AI and computational methods to identify metastable states and their formation processes. Within MLExchange, ML techniques will be employed to correlate with experimental results, aiming to solve DOE-relevant materials challenges in catalysis and energy storage for binary and ternary alloy systems.

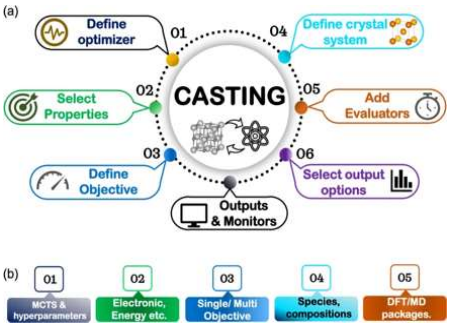

Figure 4 Schematic of the CASTING framework for performing inverse design.

Future Plans

The development roadmap for MLExchange aims to enhance scientific research through ML tools functionality and accessibility at SUFs. A critical milestone in this journey is completing

the integration of technologies, such as DVC (Data Version Control), *Tiled*, and *Prefect* to streamline workflows, making data management and workflow automation efficient, scalable, and reproducible. Furthermore, there is a concerted effort to bring applications closer to the beamlines to further align MLExchange with the needs of experimental scientists. This initiative aims to exploit the near real-time capabilities of our system, enabling researchers to process and analyze data on-the-fly providing fast feedback to users. This capability is crucial for adjusting experiments in real-time based on human insights, thus enhancing the quality of scientific outcomes and operational efficiency. Within these efforts, we aim to deploy a multi-objective extension to the BOARS model, to enable simultaneous optimization of multiple human-defined targets on-the-fly.

We plan to enhance our ptychography reconstruction capabilities by integrating Physics Informed Neural Networks into the *ptychodus* framework and expanding our training data set with varied ptychography data from the ALS, APS, and the Linac Coherent Light Source (LCLS). This initiative aims to facilitate the evaluation of these techniques against traditional analysis methods, boost interoperability, and enhance ptychography techniques across facilities. Concurrently, we aim to deploy U-Net based XRD methods at APS beamlines and expand our training data sets with XRD data from multiple facilities to refine feature engineering within the MLExchange framework. Moreover, we aim to develop innovative exploratory algorithms that merge knowledge from simulations with intrinsic curiosity driven reinforcement-learning. By using Physics-based models to predict state transitions and rewarding deviations, we will create new training datasets to enhance predictive accuracy, boosting materials predictions. The overarching strategy for MLExchange is aimed at technology refinement and ecosystem enrichment, integrating advanced ML tools to boost their accessibility and impact for scientific research at beamline facilities.

The expansion of MLExchange's deployment across SUFs remains a top priority. By broadening our footprint, we aim to democratize access to advanced ML tools for a wider scientific community, fostering collaboration and innovation across research fields. This expansion also involves extending the content registry to encompass a more comprehensive suite of applications, algorithms, and data sets tailored to the diverse needs of researchers. In our initial phase of extended deployment, we aim to implement and assess MLExchange image segmentation tools at APS high-energy beamline. This holistic strategy marks a significant advancement in applying ML to scientific research and highlights a dedication to promoting collaboration across facilities.

References

1. H. Yanxon, J. Weng, H. Parraga, W. Xu, U. Ruett, and N. Schwarz. *Artifact identification in X-ray diffraction data using machine learning methods*. J. Synchrotron Rad. **30**, 137-146. (2023).

2. S. Veseli, J. Hammonds, S. Henke, H. Parraga, and N. Schwarz. *Streaming Data from Experimental Facilities to Supercomputers for Real-Time Data Processing*. In Proceedings of the SC '23 Workshops of The International Conference on High Performance Computing, Network,

Storage, and Analysis (SC-W '23). Association for Computing Machinery, New York, NY, USA, 2110–2117. (2023).

3. A. Biswas, Y. Liu, N. Creange, J. C. Yang, S. Jesse, S. V. Kalinin, M. A. Ziatdinov and R. K. Vasudevan, "*A dynamic Bayesian optimized active recommender system for curiosity-driven partially Human-in-the-loop automated experiments*," npj Computational Materials **10**, 29 (2024).

Publications

1. A. Biswas, Y. Liu, N. Creange, J. C. Yang, S. Jesse, S. V. Kalinin, M. A. Ziatdinov and R. K. Vasudevan, "*A dynamic Bayesian optimized active recommender system for curiosity-driven partially Human-in-the-loop automated experiments*," npj Computational Materials **10**, 29 (2024).
2. O. Hoidn, A. A. Mishra, and A. Mehta, *Physics constrained unsupervised deep learning for rapid, high resolution scanning coherent diffraction reconstruction*, *Sci Rep* **13**, 22789 (2023). https://doi.org/10.1038/s41598-023-48351-7
3. H. Yanxon, J. Weng, H. Parraga, W. Xu, U. Ruett, and N. Schwarz. *Artifact Identification in X-ray Diffraction Data Using the Gradient Boosting Method*. In: Arai, K. (eds) Intelligent Systems and Applications. IntelliSys Lecture Notes in Networks and Systems, vo825. Springer, Cham. (2023). https://doi.org/10.1007/978-3-031-47718-8_34
4. J. Hammonds, S. Henke, P. R. Jemian, S. Kandel, H. Parraga, L. Rebuffi, X. Shi, S. Veseli, M. Wolfman, M. Wyman, T. Zhou, R. Chard, B. Cote, W. Allcock, L. Assoufid, M. J. Cherukara, S. Kelly, A. Sandy, J. Sullivan, and N. Schwarz. *Advanced Computational Technologies for Experiment Control, Data Acquisition, and Data Analysis at the Advanced Photon Source*. *Synchrotron Radiation News*, *36*(6), 4–11. (2024). https://doi.org/10.1080/08940886.2023.2277136
5. T. Chavez, E. J. Roberts, P. H. Zwart, and A. Hexemer. "A comparison of deep-learning-based in- painting techniques for experimental X-ray scattering". In: *Journal of Applied Crystallography* 55.5 (Sept. 2022), pp. 1277–1288. DOI: 10.1107/S1600576722007105.
6. S. Srinivasan, R. Batra, D. Luo, T. Loeffler, S. Manna, H. Chan, L. Yang, W. Yang, J. Wen, P. Darancet, and S. K. R. S. Sankaranarayanan. "Machine learning the metastable phase diagram of co- valently bonded carbon". In: *Nature Communications* 13.1 (June 2022). DOI: 10.1038/s41467- 022-30820-8.
7. H.-T. Zhang, T. J. Park, A. N. M. N. Islam, D. S. J. Tran, S. Manna, Q. Wang, S. Mondal, H. Yu, S. Banik, S. Cheng, H. Zhou, S. Gamage, S. Mahapatra, Y. Zhu, Y. Abate, N. Jiang, S. K. R. S. Sankaranarayanan, A. Sengupta, C. Teuscher, and S. Ramanathan. "Reconfigurable perovskite nick- elate electronics for artificial intelligence". In: *Science* 375.6580 (Feb. 2022), pp. 533–539. DOI: 10.1126/science.abj7943.
8. 14. Z. Zhao, T. Chavez, E. A. Holman, G. Hao, A. Green, H. Krishnan, D. McReynolds, R. J. Pan- dolfi, E. J. Roberts, P. H. Zwart, H. Yanxon, N. Schwarz, S. Sankaranarayanan, S. V. Kalinin, A. Mehta, S. I. Campbell, and A. Hexemer.

"MLExchange: A web-based platform enabling exchange- able machine learning workflows for scientific studies". In: *2022 4th Annual Workshop on Extreme- scale Experiment-in-the-Loop Computing (XLOOP)*. IEEE, Nov. 2022, pp. 10–15. DOI: 10.1109/ xloop56614.2022.00007. arXiv: 2208.09751 [cs.LG].

9. M. Ziatdinov, A. Ghosh, C. Y. Wong, and S. V. Kalinin. "AtomAI framework for deep learning analysis of image and spectroscopy data in electron and scanning probe microscopy". In: *Nature Machine Intelligence* 4.12 (Dec. 2022), pp. 1101–1112. DOI: 10.1038/s42256-022-00555- 8.
10. Suvo Banik, Troy Loeflller, Sukriti Manna, Henry Chan, SrilokSrinivasan, Pierre Darancet, Alexander Hexemer and Subramanian K. R. S. Sankaranarayanan npj Comput Mater 9, 177 (2023). https://doi.org/10.1038/s41524-023-01128-y

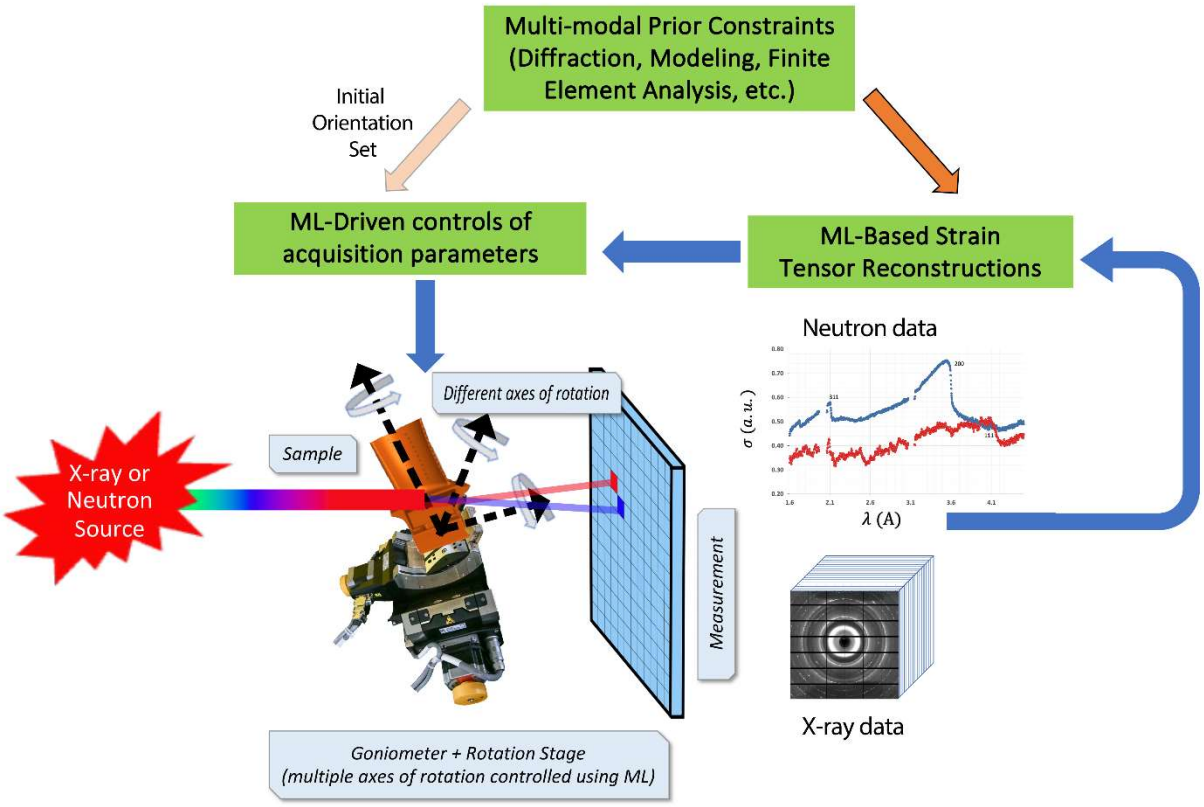

The novel autonomous closed-loop artificial-intelligence driven tensor tomography instrument workflow aims at accurately reconstructing 3-dimensional tensors with the fewest possible measurements. X-ray or neutron measurements are processed using machine learning-based tensor reconstruction algorithms which can be informed by prior constraints such as diffraction, modeling, and finite element analysis. Both preceding reconstruction and constraints determine the orientation and angle of the new projections

Intelligent Acquisition and Reconstruction for Hyperspectral Tomography Systems: Solving Tensor Tomography

Hassina Bilheux, Singanallur (Venkat) Venkatakrishnan, Jean Bilheux, Shimin Tang, Oak Ridge National Laboratory; Stuart Campbell, Xiaogang Yang, Nghia Vo, Dmitri Gavrilov, Brookhaven National Laboratory; Charles Bouman, Gregery Buzzard, Mohammad Samin Nur Chowdhury, Purdue University

Keywords: machine learning, tensor field, hyperspectral tomography, X-ray imaging, neutron imaging

Research Project Scope

Our research project focuses on developing artificial intelligence (AI) driven acquisition and reconstruction methods to solve the complex challenge of reconstructing 3-dimensional (3D) tensor quantities in crystalline materials from neutron or X-ray hyperspectral tomography systems. Our goal is to implement this capability at X-ray and neutron facilities at the Department of Energy

(DOE) Basic Energy Sciences (BES) Scientific User Facilities (SUFs) namely the National Synchrotron Light Source II (NSLS-II) and the Spallation Neutron Source (SNS). Our proposed research builds on the previously funded DOE BES AI project "Intelligent Acquisition and Reconstruction for Hyperspectral Tomography" which developed novel intelligent machine learning (ML) acquisition and reconstruction methods for hyperspectral tomography systems at DOE BES SUFs (see our past two years publications below, Refs. 4-6).

One of the main concerns related to the behavior of crystalline materials is the ability to predict their lifetime performance, failure mechanisms, under or after an applied load (temperature, pressure, etc.). These concerns can be addressed by studying simultaneously both the structure (defects, porosity) and behavior of the crystalline materials (changes in the microstructure, texture, etc.). In continuum mechanics, stress is a tensor field that measures the internal force distribution within a solid object [1]. When an object fails, disastrous consequences may arise such as catastrophic failure of concrete, steel rebar or suspension cables in bridges, aircraft advanced nickel superalloy components, and medical titanium-based metal implants (artificial joints). Hence, experimental measurements of stress are of paramount importance for materials scientists who utilize them to validate predictive models but also to anticipate the behavior of materials made with novel manufacturing techniques such as Additive Manufacturing. Our research project provides a unique opportunity to provide crucial data to the materials science community.

Recent Progress

At the SNS, our primary objective is to design a system that can reconstruct the residual strain tensor from a collection of hyperspectral neutron Bragg edge measurements obtained by re-orienting the sample and doing so in a manner where we acquire the least number of measurements without compromising the quality of the recovered strain fields. Broadly, we intend to use the mathematics of inverse problems combined with AI/ML algorithms to achieve this objective.

Our efforts so far have focused on designing algorithms that can recover 2D planar strain tensors at each point in a sample from simulated neutron Bragg edge measurements. First, we have surveyed the literature and developed a new simulation tool that implements the forward model i.e. predicts what the measurements should be if we had access to the ground truth strain tensors. This forward model is based on the Longitudinal Ray Transform (LRT) [2] and relates the shift of the measured Bragg edges from a strain-free value to the integrated value of the projected strain along a given direction. Fig.1 shows a ground-truth strain tensor pattern along with the simulated "strain sinogram" based on the LRT obtained by rotating the sample along a single axis perpendicular to the neutron beam obtained using our simulator. In an experimental setting, one can extract such a strain sinogram from the measured experimental data and the goal is to infer the underlying strain tensors in the sample.

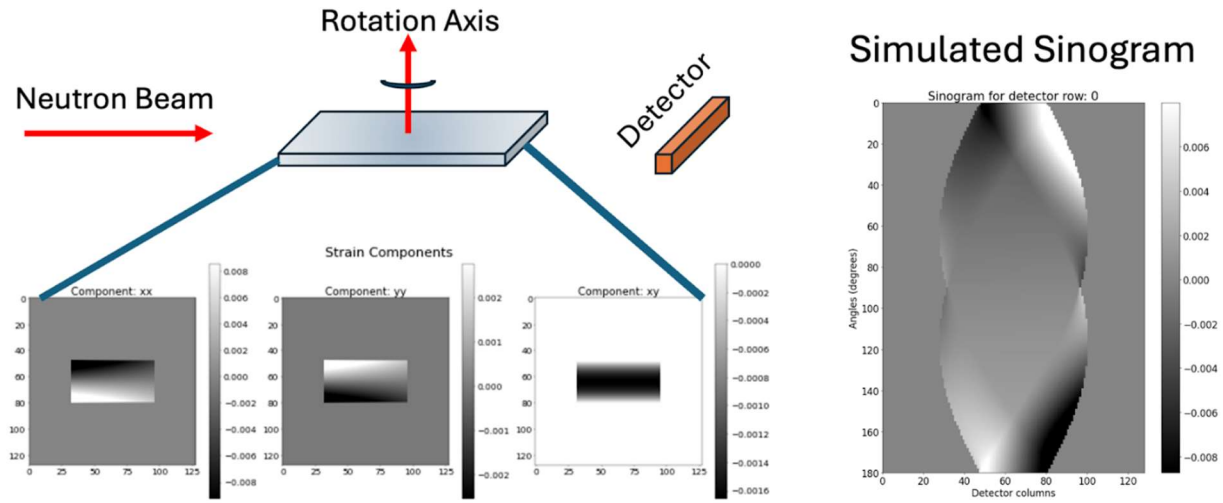

Fig.1 Illustration of the forward model for a Bragg edge strain CT system. The object of interest with residual strain is rotated about a single axis and hyperspectral measurements are made. From these measurements an average value of strain can be extracted and organized into a strain sinogram. The figure shows the 3 components of strain associated with a plate sample and the associated simulated strain sinogram using our software.

Next, having established a forward model, we focus on recovering the strain patterns from such measurements. Even for the 2D planar case, since number of measurements obtained by rotating the sample is far fewer than the number of unknowns, the reconstruction constitutes a highly ill-posed inverse problem. To address this challenge, we are in the process of developing reconstruction algorithms that allows for the integration of various constraints on the object's strain tensor to be recovered. Fig.2 shows a preliminary reconstruction of the 3 components of the strain tensor from our methods constraints. The figure shows that while we can recover an approximate strain tensor, these are not accurate due to the highly ill-posed nature of the problem. We have started to develop more sophisticated techniques that improve upon these results which we will highlight in our talk.

At NSLS-II, we further developed the functionality of the GANrec platform [3], an advanced deep learning network, to analyze X-ray scattering data. This method allows for the detailed reconstruction of the crystalline structure in real space using a single diffraction pattern measurement. As illustrated in Fig.3, the results of the GANrec reconstruction are identical to the Electron Microscopy (EM) measurements. This novel advance in crystallography not only enables us to determine the crystalline structure with precision but also sets the stage for subsequent strain calculations.

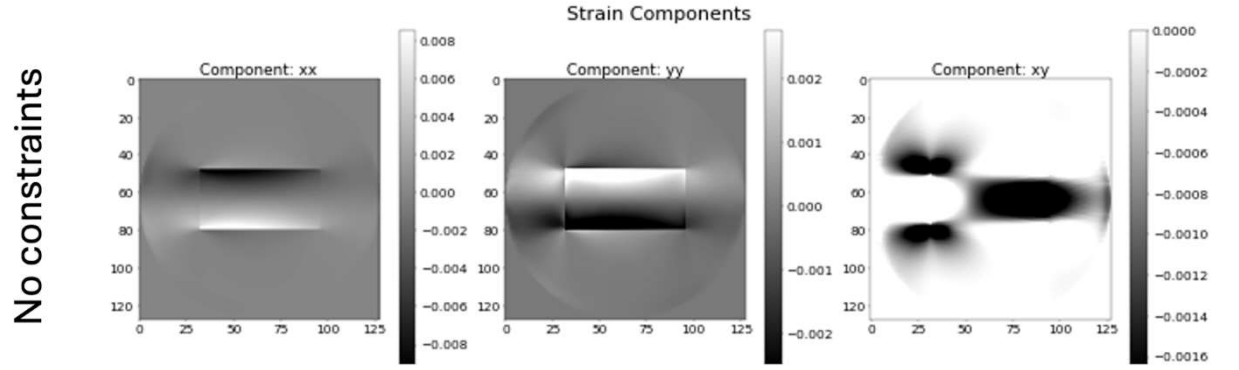

Fig.2 Illustration of the results of reconstructions using an algorithm we developed for 2D strain tensors from a Bragg edge strain sinogram in Fig.1. Notice that when no constraints are applied, we get significant artifacts in reconstruction quality for this severely ill-posed inverse problem where we have to estimate 3 unknowns at each position.

Our pioneering work serves as a foundation for enabling a highly efficient strain measurement technique that leverages X-ray scattering technologies. The current measurement method, such as 3D X-ray diffraction (3DXRD), relies on laborious pixel-to-pixel scanning, which is not practical in tomographic measurements for high-resolution strain imaging. Our approach would enable the concept of field scanning. This breakthrough is instrumental in paving the way to rapid strain tomography using X-ray scattering, revolutionizing the current methodologies.

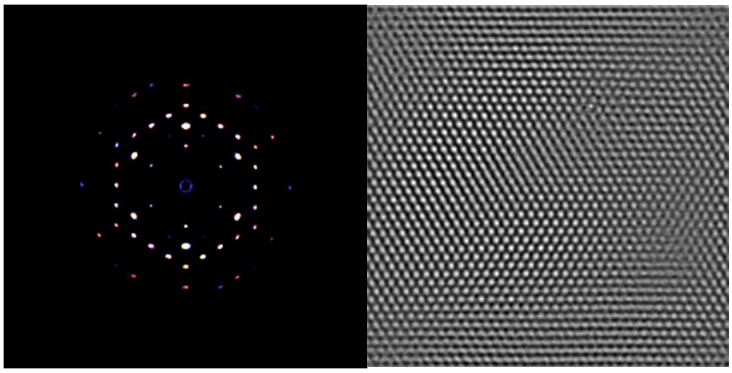

Figure 3. Scattering data reconstruction with GANrec. Left is the X-ray scattering measurement data. Right is the real space data reconstruction from the left by using the GANrec.

Future Plans

We group our future plans at the SNS and NSLS-II into two major thrusts:

1. Algorithms:

   We plan to refine the type of constraints we will use in order to improve the quality of reconstructions. These include better methods to account for boundary conditions as well as other known values of strain that we may be able to measure from techniques such as neutron diffraction. We also plan to use different basis functions in contrast to the standard voxel basis which might be more amenable to the use of constraints for the strain CT problem. Once we establish the

correctness of the method on multiple simulated data including in the presence of noise, we will test our method on experimental data. Next, we will design new methods based on AI in the spirit of reducing the number of measurements (see Yang et al., 2023 in our publication list) to be made so that the overall scan time decreases for this modality for which each measurement may take on the order of hours (for the highest spatial resolution).

We also plan to continue refining and validating our GANrec-based approach for reconstructing crystal structures from X-ray scattering data. Additionally, we aim to enhance and streamline the process of strain reconstruction from X-ray diffraction datasets through the GANrec framework. Our objective is to establish a comprehensive data analysis workflow that will enable the implementation of a field scanning technique for tomographic strain measurements.

Moreover, we are in the process of integrating simulation code for Bragg edge neutron strain tomography into the GANrec platform. The versatility of GANrec as a plug-and-play tool for diverse data reconstruction tasks has already been demonstrated. By applying it to the complex challenge of neutron strain tomography, we anticipate bypassing the traditional decomposition of the problem and directly addressing the forward model. This direct approach is expected to yield more precise outcomes than conventional methods by tackling the original model and its data structure head-on.

2. Experiments:

We have reached out to another subject matter expert in the area (Prof. Chris Wensrich, University of Newcastle, Australia) to access thoroughly measured samples at other neutron facilities. Since these samples are well measured, we plan to use these as our first calibration examples to test and evaluate our algorithms for 2D strain reconstructions. We are also in the process of fabricating our own samples (strain-free and as built steel rods and plates). Once fabricated, we will determine the strain tensors using the slower neutron diffraction technique (to serve as a reference) followed by measuring these at the SNS.

Concurrently, we also intend to carry out X-ray scattering experiments at NSLS-II to assess strain using this field scanning approach. We will also corroborate the effectiveness of our methodology through comparative analysis with neutron source measurements on identical samples.

References

1. Flügge, W., Tensor analysis and continuum mechanics. 1972: Springer.
2. Gregg, A., Hendriks, J., Wensrich, C., Wills, A., Tremsin, A., Luzin, V., Shinohara, T., Kirstein, O., Meylan, M., and Kisi, E, Tomographic reconstruction of two-dimensional residual strain fields from Bragg edge neutron imaging, Physical Review Applied, vol. 10, no. 6, p. 064034, 2018.
3. Yang, X. and C. Schroer. Strategies of deep learning for tomographic reconstruction. in 2021 IEEE International Conference on Image Processing (ICIP). 2021. IEEE.

Publications

4. Yang D, Tang S, Venkatakrishnan SV, Chowdhury MS, Zhang Y, Bilheux HZ, Buzzard GT, Bouman CA. An Edge Alignment-based Orientation Selection Method for Neutron Tomography. In ICASSP 2023-2023 IEEE International Conference on Acoustics, Speech, and Signal Processing (ICASSP) 2023(pp. 1-5).

5. Chowdhury MS, Yang D, Tang S, Venkatakrishnan SV, Bilheux HZ, Buzzard GT, Bouman CA. Autonomous Polycrystalline Material Decomposition for Hyperspectral Neutron Tomography. In2023 IEEE International Conference on Image Processing (ICIP) 2023 (pp. 1280-1284).

6. Bilheux HZ, Bilheux JC, Hanks RA, Byrd A, Jones A, Skorpenske H, Donnelly ME, Mangus R, Conner D, Lessard TL, Venkatakrishnan S. The VENUS imaging beamline at the Spallation Neutron Source: Layout, expected performance and status of the construction project. In Journal of Physics: Conference Series 2023 (Vol. 2605, No. 1, p. 012004).

Notice of Copyrights

Acknowledgments

This research used resources at the Spallation Neutron Source, a DOE Office of Science User Facility operated by the Oak Ridge National Laboratory.

Artificial Intelligence for MultiModal Analysis (AIMM): Integrated Platform for Multimodal Data Capture, Exploration and Discovery Driven by AI Tools

Eli Stavitski, Daniel Allan, Stuart Campbell, Deyu Lu, Xiaohui Qu, Shinjae Yoo (Brookhaven National Laboratory), Maria K. Chan, Steve M. Heald, Nicholas Schwarz, Chengjun Sun (Argonne National Laboratory) Dylan McReynolds, Wanli Yang (Lawrence Berkeley National Laboratory)

Keywords: synchrotron facilities, multimodal methods, X-ray absorption spectroscopy, autoencoder

Research Project Scope

Accelerating scientific discovery by leveraging large complex multimodal datasets generated at BES user facilities, and developing shared infrastructure to store, curate, analyze and disseminate the data are the focus of this project. We will build data analysis tools that reveal correlations in multimodal data and apply Machine Learning (ML) methods and train Artificial Intelligence (AI) models that efficiently extract synergistic information and embed such models in new workflows for rapid scientific discovery. This team will develop tools to address the data scale of multimodal experiments. We will deploy infrastructure needed to manage the datasets, offering transparent access across facilities as well as interoperable data pipelines and analysis tools on top of the Bluesky/Databroker ecosystem thus making both synthetic and experimental data accessible, interoperable, transparent, and reusable, promoting data standardization across SUFs. It also will enable access to multimodal datasets and their unsupervised alignment. ML based data reduction will allow generation of physically meaningful information on the timescale of experiment, to be used as feedback to the instrument or system under investigation. These AI driven knowledge extraction capabilities will dramatically accelerate scientific discovery at SUFs.

Recent Progress

AIMMdb. AIMM project is in charge of making the diverse data sources gathered from across the collaboration mutually accessible, searchable, and usable. This means that it is not sufficient to merely gather the data in one place, such as a shared drive of some kind (Dropbox, Google Drive, SharePoint, etc.). Measurements, simulations, and sample metadata were stored in highly varied forms using disparate formats and conventions. The more challenging requirement is to enable all collaborators to find data of interest and interpret it correctly. To address this, the team has developed AIMMdb service. It is deployed using NERSC's cloud infrastructure ("Spin"). Some open-source data sets are available publicly for anyone to explore; the rest are available securely to authorized users. ORCID is used for log-in so that AIMMdb is not tied to any one facility or institution. AIMMdb includes a web application that can be used from a web browser (navigate to https://aimm.lbl.gov) on a computer or mobile phone where data can be searched and downloaded. Also, the AIMMdb application can be used directly by data science software to read data and metadata efficiently into AI/ML data analysis programs. AIMMdb was built by extending

the Bluesky Tiled [1]. project from NSLS-II, adapting and customizing Tiled to the requirements of the AIMM collaboration. Currently AIMMdb stores the data from multiple facilities and beamlines in a standardized format, allowing for fast search, combination, cross-correlation, and augmentation of the different data streams. The multimodal dataset on ion lithium battery cathode recorder materials at four different instruments at APS/BNL and LBNL in the center of the project Science Case has been ingested and the analysis is underway.

AI-driven analysis of X-ray emission spectra with AXEAP2 program. Which increasing sophistication and speed of modern synchrotron methods, the bottleneck of translating data into meaningful scientific information. Tasks such as conversion of raw detector imaging into a spectrum and extraction of structural descriptors from the spectra are often human supervised, require specialized expertise, and therefore slow. We developed software package addressing these shortcomings: Argonne X-ray Emission Analysis (AXEAP) This code targets X-ray emission spectroscopy, which provides important electronic structure information such as oxidation and spin state. First release of the software was designed to automate the conversion of 2D detector images into XES spectrum in real time using unsupervised machine learning. AXEAP2 enable unsupervised analysis of XES data. Using a library of synthetic spectra calculated using multiplet theory, and the genetic algorithm (GA) for optimization, it can find a set of parameters that result in a high-quality fit of the experimental spectrum with minimal intervention and provide insights into the 3d electron spin state, 3d–3p electron exchange force and Kβ emission core-hole lifetime.

Unraveling trends in multimodal data using data analytics methods. A critical step in taking full advantage of multimodal approach is the ability to correlatively analyze the results from different techniques. Few physical models that take multiple datasets as input exist. We demonstrated that by stitching multiple datasets and using other data to set constraints in the analysis, one can obtain unique, self-consistent solution [2]. We used combinatorial thin films of binary metal oxides (Ti–Zn) with continuously varying Ti:Zn ratio, prepared by high throughput synthesis. The atomic structure and electronic properties are probed by spatially resolved techniques including X-ray absorption at two absorption edges and X-ray fluorescence (XRF), X-ray diffraction, and spectroscopic ellipsometry. We were able to resolve the observed properties as a function of Ti:Zn ratio into a mixture of five distinguishable phases by deploying multivariate curve resolution analysis on the XANES spectral series, under constraints set by results from the other techniques. First-principles computations based on density function theory connect the observed properties of each distinct phase with structural and spectral characteristics of crystalline polymorphs of Ti–Zn oxide.

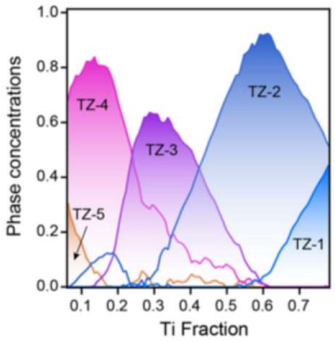

Figure 1. Unique solution of five Ti-Zn-O phases obtained by MCR analysis of multimodal data.

Lightshow: a package for generating computational x-ray absorption spectroscopy input files. One of the keys aims of the AIMM project was to build multimodal data libraries of experimental and computational data. We used X-ray absorption spectroscopy, a vastly popular synchrotron characterization technique, as a test case. First-principles simulations are used to rationalize experimental data by solving quantum mechanical equations numerically. These quantum calculation codes require setting up so-called input files describing the atomic arrangement in the system of interest, which is a non-trivial task even for experts in the electronic structure field. In addition, crafting input files by hand makes it hardly possible to set up high throughput calculations. We developed a Python package called Lightshow [3] which solves this problem by providing a uniform abstraction for writing computational x-ray spectroscopy input files for multiple popular codes, including FEFF, VASP, OCEAN, exciting and XSpectra. Its extendable framework will also allow the community to easily add new functions and to incorporate new simulation codes. We are currently working on incorporating FDMNES code into Lightshow.

Accurate, uncertainty-aware classification of molecular chemical motifs from multimodal X-ray absorption spectroscopy. The ability to characterize a complex system on different time and length scales in the heart of multimodal approach is certainly beneficial over singular modality. We were able to demonstrate it by developing an ML based approach to elucidate chemical structure of a molecule from multimodal data [4]. Specifically, we developed a neural network ensemble classifier for predicting the presence of 41 different chemical motifs on small molecules from simulated C, N, and O K-edge spectra (Figure 3). Molecular structures from a database containing 143,000 molecules were used for spectra calculations which were used for training, validation, and testing. The classifiers not only achieve accuracies of more than 0.95 but also accurately quantify uncertainty. The accuracy of the classifiers was shown to be significantly higher when using multiple signals from different absorbing elements when compared to that when using only single modalities independently, clearly demonstrating "multimodal advantage". While targeting a limited chemical space in this work, the developed workflow is entirely general and can in principle be applied to different levels of theory, more complex data sets, and experiment, if a large number of labeled measurements are available.

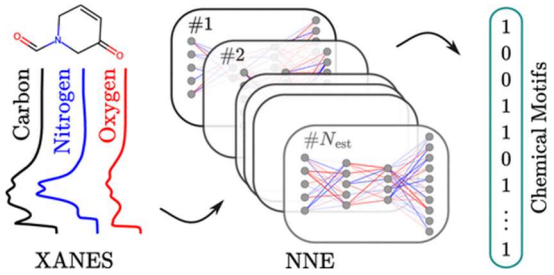

Figure 2. ML pipeline. Multimodal spectra (C, N, and O signals) are fed into individual neural networks, which constitute a neural network ensemble (NNE) of E estimators, to predict a binary vector, each entry of which corresponds to the presence (or lack thereof) of a specific chemical motif.

Robust Machine Learning Inference from X-ray Absorption Near Edge Spectra through Featurization Many important structural and electronic parameters such local coordination and valence state are encoded in the X-ray absorption near edge spectra (XANES) [5]. We have already demonstrated that machine learning is instrumental to extract this information. In the extension of our work, we included spectral transformations and dimensionality reduction

techniques into ML predictions, in addition to raw spectral intensities. We focused on systematically comparing the impact of different featurization methods on the performance of ML models for XAS analysis. We evaluated the classification and regression capabilities of these models on computed data sets and validated their performance on previously unseen experimental data sets. Our analysis revealed that, the cumulative distribution function feature achieves both high prediction accuracy and exceptional transferability. This remarkably robust performance can be attributed to its tolerance to horizontal shifts in the spectra, which is crucial when validating models using experimental data. While this work exclusively focuses on XANES analysis, we anticipate that the methodology presented here will hold promise as a versatile asset to the broader spectroscopy community.

Future Plans

Benchmark XAS simulation against experiment on 3d transition metal K-edge. We plan to benchmark of XAS simulation against experiment on 3d transition metal K-edge based on the workflow we have developed. This is an extension of our previous work on synthetic data and

is crucial for XAS spectral analysis. We will systematically identify the discrepancies between theory and experiment and develop more accurate models to improve the predictive power of the theory.

Understanding the electrochemical process in battery materials using multimodal experiment, simulation and machine learning. We have acquired experimental multimodal datasets of experimental Nickle-Manganese-Cobalt (NMC) constructed at different voltages, which include electrochemical data and x-ray absorption spectroscopy (XAS) data. This data will be analyzed based on atomic structure models sampled from relevant material space and their corresponding simulated XAS spectra. To relate the spectral features to structural changes in NMC under different voltage loads, the simulated XAS will be analyzed using unsupervised learning, such as K-means clustering where clusters can be correlated with experimental spectral fingerprints.

References

1. M. Rakitin, S. Campbell, D. Allan, T. Caswell, D. Gavrilov, M. Hanwell and S. Wilkins, *Next generation experimental data access at NSLS-II*, Journal of Physics: Conference Series **2380**, 012100 (2022).
2. R. Li, X. Jiang, C. Zhou, M. Topsakal, D. Nykypanchuk, K. Attenkofer, D. Stacchiola, M.S. Hybertsen1, E. Stavitski, X. Qu*, Deciphering phase evolution in complex metal oxide thin films via high-throughput materials synthesis and characterization*, Nanotechnology **34**, 125701 (2023).
3. M.R. Carbone, F. Meng, C. Vorwerk, B. Maurer, F. Peschel, X. Qu, E. Stavitski, C. Draxl J. Vinson, D. Lu, *Lightshow: a Python package for generating computational x-ray absorption spectroscopy input files.* Journal of Open Source Software, **8**, 5182 (2023)

4. M.R. Carbone, P.M. Maffettone, X. Qu, S. Yoo, D. Lu, *Accurate, Uncertainty-Aware Classification of Molecular Chemical Motifs from Multimodal X-ray Absorption Spectroscopy*, J. Phys. Chem. A **128**, 1948 (2024)
5. Y. Chen, C. Chen, I. Hwang, M.J. Davis, W. Yang, C. Sun, G.-H. Lee, D. McReynolds, D. Allan, J. Marulanda Arias, S. Ping Ong, M.K.Y. Chan, *Robust Machine Learning Inference from X-ray Absorption Near Edge Spectra through Featurization*, Chem. Mater. **36**, 2304 (2024)

Publications

1. Y. Chen, C. Chen, I. Hwang, M.J. Davis, W. Yang, C. Sun, G.-H. Lee, D. McReynolds, D. Allan, J. Marulanda Arias, S.P. Ong, M.K.Y. Chan, *Robust Machine Learning Inference from X-ray Absorption Near Edge Spectra through Featurization,* Chem. Mater. **36**, 2304 (2024)
2. F. Meng, B. Maurer, F. Peschel, S. Selcuk, M. Hybertsen, X. Qu, C. Vorwerk, C. Draxl, J. Vinson, and D. Lu, *Multicode benchmark on simulated Ti K-edge x-ray absorption spectra of Ti-O compounds*, Phys. Rev. Materials **8**, 013801 (2024)
3. R. Li, X. Jiang, C. Zhou, M. Topsakal, D. Nykypanchuk, K. Attenkofer, D. Stacchiola, M.S. Hybertsen1, E. Stavitski, X. Qu*, Deciphering phase evolution in complex metal oxide thin films via high-throughput materials synthesis and characterization*, Nanotechnology **34**, 125701 (2023).
4. H. Kwon, T. Hsu, W. Sun, W. Jeong, F. Aydin, J. Chapman, X. Chen, M. R. Carbone, D. Lu, F. Zhou & T. A. Pham. Spectroscopy-Guided Discovery of Three-Dimensional Structures of Disordered Materials with Diffusion Models. arXiv:2312.05472 (2023).
5. I.-H. Hwang, S.D. Kelly, M.K.Y. Chan, E. Stavitski, S.M. Heald, S.-W. Han, N. Schwarz and C.-J. Sun, The AXEAP2 program for Kβ X-ray emission spectra analysis using artificial intelligence, J. Synchrotron Rad. 30 923 (2023)
6. M. R. Carbone, P. M. Maffettone, X. Qu, S. Yoo & D. Lu. Accurate, uncertainty-aware classification of molecular chemical motifs from multi-modal X-ray absorption spectroscopy. The Journal of Physical Chemistry A 128, 1948 (2024).
7. M. R. Carbone, F. Meng, C. Vorwerk, B. Maurer, F. Peschel, X. Qu, E. Stavitski, C. Draxl, J. Vinson & D. Lu. Lightshow: a Python package for generating computational x-ray absorption spectroscopy input files. The Journal of Open Source Software 8, 5182 (2023).
8. Z. Liang, M. R. Carbone, W. Chen, F. Meng, E. Stavitski, D. Lu, M. S. Hybertsen & X. Qu. Decoding Structure-Spectrum Relationships with Physically Organized Latent Spaces. Physical Review Materials 7, 053802 (2023).
9. A. Ghose, M. Segal, F. Meng, Z. Liang, M. S. Hybertsen, X. Qu, E. Stavitski, S. Yoo, D. Lu & M. R. Carbone. Uncertainty-aware predictions of molecular X-ray absorption spectra using neural network ensembles. Physical Review Research 5, 013180 (2023).
10. I.-H, Hwang, M.A. Solovyev, S.-W. Han, M.K.Y. Chan, J.P. Hammonds, S. M. Heald, S.D. Kelly, N. Schwarz, X. Zhang, X., C.-J. Sun, C.-J. *AXEAP: a software package for X-*

ray emission data analysis using unsupervised machine learning, J. Synchrotron Rad. **29** 1309 (2022)

A Digital Twin for Spatiotemporally Resolved Experiments

Subramanian Sankaranarayanan [1], Maria K. Chan [1], Pierre Darancet [1], Henry Chan [1], Tom Peterka [1], Mathew Cherukara [1], Bobby Sumpter [2], Stephen Whitelam [3]

1) Argonne National Laboratory; 2) Oak Ridge National Laboratory; 3) Lawrence Berkeley National Laboratory

Keywords: Multi-fidelity Models, Inverse problem, AI Workflow**,** Coherent Diffraction Imaging, X-ray Photon Correlation Spectroscopy

Research Project Scope

The DOE scientific user facilities (SUFs) are home to world-class spatiotemporal-resolved characterization modalities and theory groups engaging in simulations across multiple spatiotemporal scales. Given the large number of users and the intense competition for instrument times, each user can only perform a small number of actual experiments, with experimental time being costly and scarce. *To address this challenge, we proposed to develop a physically accurate, flexible and efficient Digital Twin for in-silico spatiotemporally resolved experiments, bringing the laboratory environment virtually to users before actual experiments are performed.* Digital Twin brings together a multi-disciplinary, experienced, and accomplished team of SUF scientists that included computational materials scientists and physicists, experimental collaborators (X-ray, neutron, spectroscopy and microscopy), as well as computer scientists. We built on many of the complimentary AI/ML tools & shared workflows independently developed by PIs from the various DOE SUFs to successfully realize the Digital Twin platform. Our Digital Twin framework takes advantage of the fact that many experimental capabilities at SUFs characterize either time-dependent atomic positions $\mathcal{R}_i(t)$ and/or time-dependent structure factors $S(\boldsymbol{Q},t) \propto \sum_{i,j} a_i a_j \, e^{-i\boldsymbol{Q}.\left(\mathcal{R}_i(t)-\mathcal{R}_j(t)\right)}$ ($\boldsymbol{Q}$ is the scattering vector, a_i is atom *i*'s form factor, and $\mathcal{R}_i(t)$, its position at time *t*)(*1*). The read-outs can be predicted from dynamical simulations if the underlying models are *physically accurate on time- and length-scales comparable to the ones probed in experiment*. Furthermore, AI/ML assisted multi-fidelity scale bridging allows users to perform dynamical simulations on a "reconstructed" or "inverted" user-defined sample and exhaustively explore experimental controls & expected read-outs in a virtual environment. *Using two representative Digital Twins for coherent diffraction imaging and neutron scattering, we demonstrated that experimental*

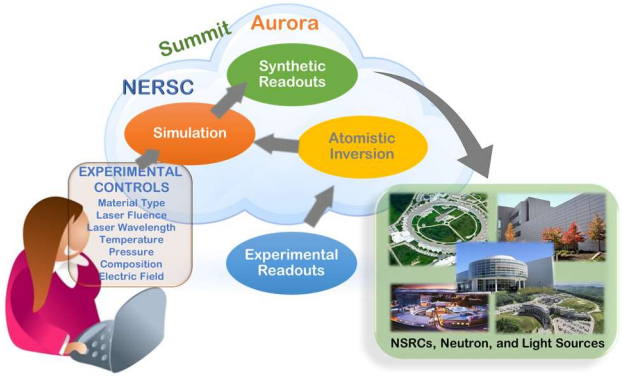

Figure 1: Our vision for Digital Twin – a virtual platform was successfully constructed to enable in-silico spatiotemporally resolved experiments to probe structure and dynamical evolution of material interfaces across disparate spatiotemporal scales. Digital Twin involves use of AI/ML to allow seamless information extraction from experiments that serve as inputs to physically accurate yet efficient dynamical models running on high performance computing (HPC) and exascale machines. A Digital Twin allows users to exhaustively explore experimental controls and obtain read-outs – a small subset that displays the most interesting physics and/or phenomena can be explored in actual experiments. These experiments can iteratively be used as training data for model improvement to close the loop.

spatiotemporally resolved measurements at SUFs can be derived from the accurate prediction of atomic configurations and their dynamical evolution across time- and length-scales.

Recent Progress

Digital Twins has achieved significant success owing to a multidisciplinary, accomplished, experienced and diverse team of SUF scientists who worked cohesively over the last few years to deliver on our proposed milestones. We provide a summary of our progress in the three thrusts below:

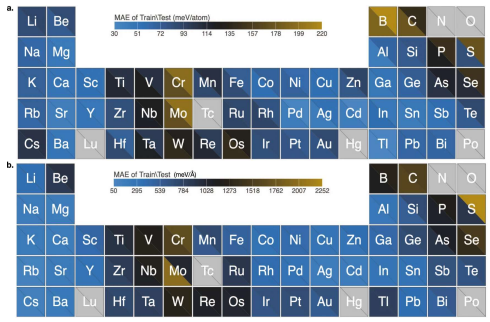

Figure 2. Our exemplary success in developing physics-based ML model across dozens of different elemental systems and alloys using continuous action RL approach based on Monte Carlo Tree Search. A bond-order model formalism for 54 different elements across the periodic table is parameterized using RL based on an extensive training dataset generated from density functional theory (DFT) computations. Mean absolute error (MAE) in **a)** energy and **b)** force predictions are shown using the color bar in meV/atom and meV/Å units, respectively(*2*).

Digital Simulation Environment (AI/ML for multi-fidelity scale bridging in dynamical simulations): In Digital Twins, the development of physically accurate and efficient models is crucial to ensure faithful representation of real spatiotemporal experiments. we have bridged the gap between various simulation models by using active and transfer learning from sparse dataset, multi-objective evolutionary optimization, decision trees such as Monte Carlo Tree Search operating in continuous action space for parameterization, and reinforcement learning to address scale bridging challenges in molecular simulations. In a departure from discrete action and other gradient-based approaches, we have introduced a RL strategy based on decision trees (Monte Carlo Tree Search) that incorporates modified rewards for improved exploration, efficient sampling during playouts and a “window scaling scheme" for enhanced exploitation, to enable efficient and scalable search for continuous action space problems. Using high-dimensional artificial landscapes and control RL problems, we successfully benchmarked our approach against popular global optimization schemes and state of the art policy gradient methods, respectively (2).

AI/ML solutions to inverse problem: We have deployed deep learning approaches to solve the inverse problem, particularly in coherent diffraction imaging (CDI), enabling real-time nanoscale imaging with high accuracy. Cherukara, Chan, Peterka and Sankaranarayanan have successfully trained and deployed a CDI Digital Twin at the APS beamline, using deep learning models that learn to solve the data inversion problem in a single shot(*3*). This was

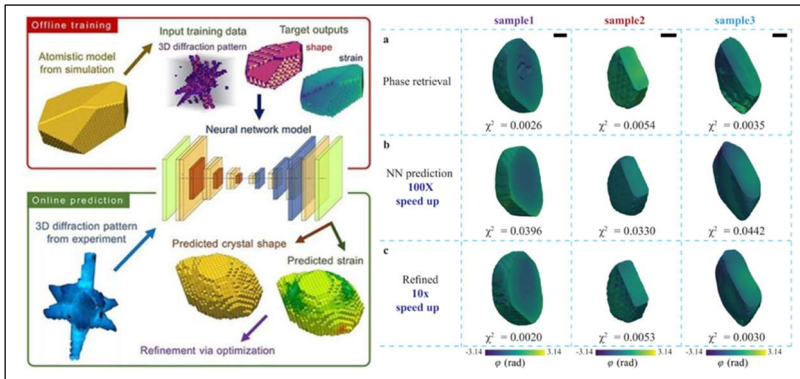

Figure 3*:* Our success in solving inverse problems in X-ray diffraction imaging. **A**: Digital twin workflow that generates high-fidelity training data to train NNs that invert 3D CDI data in a single shot. **B**: Results comparing the NN approach to traditional phase retrieval. AutoPhaseNN is faster, accurate and enables real time information extraction(*3*).

achieved through the development of a digital twin which was used to generate large volumes of high-fidelity training data *in-silico*. Similarly, in neutron scattering, a workflow developed by co-PIs Chan and Kolluru departs from conventional approach and uses an evolutionary approach to optimize input parameters, resulting in well-matched simulated signals to experimental data, facilitating the investigation of complex structural descriptors. In another work, co-PI Sumpter has introduced an ML strategy, based on the framework of Gaussian process, to inversely determine conformation of di-block copolymers from their coherent scattering(*4*).

Shared workflows (Seamless information exchange between models and experiments): We made significant advances in shared workflows and successfully developed a digital twin to identify crystalline defects in samples from the raw coherent diffraction data(*5*). To automate this process, we composed a workflow coupling coherent diffraction data generation with training and inference of deep neural network defect classifiers. We adopted a continual learning approach(*5*), where we generated training and inference data as needed based on the accuracy of the defect classifier instead of generating all training data a priori. Results show that our approach improves accuracy of defect classifiers while requiring fewer data samples. In another high-impact publication(*6*), we helped develop an ML workflow that directly bridges the instrument data stream into Python-based molecular dynamics and density functional theory environments using pre-trained neural networks to convert imaging data to physicaldescriptors(*6*).

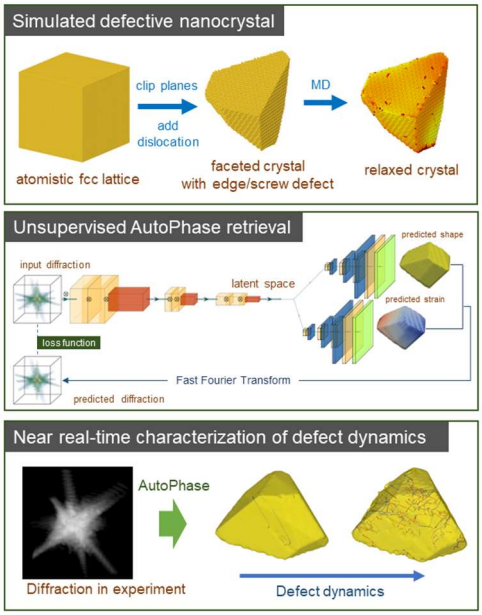

Figure 4: AI model for phase retrieval in BCDI. (top) Training data of defective nanocrystals will be generated using atomistic modeling. (middle) Architecture of AutoPhaseNN, an unsupervised physics-aware deep learning model. (bottom) Inversion of experimental diffraction images for the study of defect dynamics in nanocrystals.

Future Plans

Successful implementation relies on the following three interconnecting thrusts (i) AI/ML Guided multi-fidelity bridging for physically accurate & efficient dynamical simulations. (ii) AI solutions to the inverse problem, i.e., information extraction from time-resolved experiments. (iii) Shared workflows for seamless information exchange between models and experiments.

Digital Simulation Environment (AI/ML for multi-fidelity scale bridging in dynamical simulations): Cherukara and Chan will build on recent work where they have trained AutoPhaseNN(*3*), an unsupervised *physics-aware* deep learning model that inverts 3D diffraction intensities into sample shape and phase in a single pass. For weakly strained samples (e.g., defect free), AutoPhaseNN when combined with a few iterations of traditional phase retrieval is >10X faster while providing image reconstructions that are more accurate than what would be obtained through traditional phase retrieval alone. However, defects play a vital role in material property and response and are ubiquitous in most practical applications especially in structural materials. Using Digital Twin, and leveraging large-scale computing resources at ANL, we will extend AutoPhaseNN to provide real-time, higher fidelity 3D near-atomic resolution x-ray imaging. *Digital Twin* will enable new science by extending the space of samples that can be imaged by the

instrument. We will develop AutoPhaseNN++ by incorporating features of vision transformer (ViT) into our current CNN-based model without the big data requirement of ViT. We are exploring several approaches including gated positional self-attention, Convolutional Cross ViT, and CMT. The model design of AutoPhaseNN++ will enable capturing of local and global level correlations between all pixels in a diffraction image and hence improve the learning of long-range features that are important in reciprocal space data.

AI/ML solutions to inverse problem: Sankaranarayanan, Whitelam and Sumpter propose to go beyond the "pre-defined functional forms" and rather aim to "learn" multiscale physics directly from data across the various disparate spatiotemporal scales (electronic to atomistic to mesoscale) *via* symbolic AI. Briefly, supervised machine learning approaches, such as Gaussian process regression, decision trees, neural networks and symbolic regression, learn a functional mapping between the materials fingerprint and their property using the available materials knowledge/databases (training data). The advantage of the learned *surrogate* mapping is that it can be exploited to quickly make predictions for new cases, without exclusively performing associated experimental measurements or solving time consuming theoretical models. We will focus on SR using genetic programming as well as using equation learner network. Both these approaches perform an unconstrained search on the function space spanned by a collection of given function building blocks, *e.g*. mathematical operators, analytic functions, material property variables, constants, etc. to find the most appropriate solution (with minimum training error). *Using these approaches, we will learn (a) functional forms for MD simulations from first principles to describe molecular interactions (b) learn mesoscale physics from an ensemble of MD trajectories obtained using the learnt functional form in (a)*.

Shared workflows (Seamless information exchange between models and experiments): Shared workflows are essential for enabling seamless data sharing across platforms and between computational and experimental facilities, facilitating the realization of Digital Twins. Recent developments in workflow software address critical needs such as heterogeneous task execution, flexible data model description, and support for dynamic workflow changes. For instance, advancements in workflow composition allow for the automation of shared workflows by integrating tasks like molecular dynamics simulations, experiments, and AI models. Peterka and Yildiz will develop workflows for representation Digital Twin applications, including Coherent Diffraction Imaging (CDI), which aims to rapidly and accurately invert 3D coherent diffraction imaging data for material characterization and prediction. This involves coupling diffraction data training generation with training and inference of unsupervised physics-aware deep learning models, improving performance continuously with data from new coherent imaging experiments. Continual learning strategies will be explored to enhance the accuracy of deep learning models, along with smart data generation strategies to optimize computational efficiency.

References:

1. H. Wen, M. J. Cherukara, M. V. Holt, *Time-Resolved X-Ray Microscopy for Materials Science*. Annual Review of Materials Research **49**, 389-415 (2019).
2. S. Manna *et al.*, *Learning in continuous action space for developing high dimensional potential energy models.* Nature Communications **13**, 368 (2022).
3. Y. Yao *et al.*, *AutoPhaseNN: unsupervised physics-aware deep learning of 3D nanoscale Bragg coherent diffraction imaging*. npj Computational Materials **8**, 124 (2022).
4. M.-C. Chang *et al.*, *A machine learning inversion scheme for determining interaction from scattering*. Communications Physics **5**, 46 (2022).

5. O. Yildiz *et al.*, *Automated Continual Learning of Defect Identification in Coherent Diffraction Imaging.* 2022 IEEE/ACM International Workshop on Artificial Intelligence and Machine Learning for Scientific Applications *(AI4S)*, http://doi.ieeecomputersociety.org/10.1109/AI1104S56813.52022.00006 (2022).
6. A. Ghosh, M. Ziatdinov, O. Dyck, B. G. Sumpter, S. V. Kalinin, *Bridging microscopy with molecular dynamics and quantum simulations: an atomAI based pipeline*. npj Computational Materials **8**, 74 (2022).

Publications

1. B. Varughese, S. Manna, T. D. Loeffler, R. Batra, M. J. Cherukara, and S. K.R. S. Sankaranarayanan, *Active and Transfer Learning of High Dimensional Neural Network Potentials for Transition Metals.* ACS Applied Materials and Interfaces (2024) https://doi.org/10.1021/acsami.3c15399
2. S. Manna, T. D. Loeffler, R. Batra, S. Banik, H. Chan, B. Varughese, K. Sasikumar, M. Sternberg, T. Peterka, M. J. Cherukara, S. K. Gray, B. G. Sumpter, & S.K.R.S. Sankaranarayanan. *Learning in continuous action space for developing high dimensional potential energy models.* Nature Communication **13**, 368 (2022).
3. R. Batra, T. D. Loeffler, H. Chan, S. Srinivasan, H. Cui, I. V. Korendovych, V. Nanda, L. C. Palmer, L. A. Solomon, H. C. Fry, & S. K. R. S. Sankaranarayanan, *Machine learning overcomes human bias in the discovery of self-assembling peptides.* Nature Chemistry **14**, 1427-1435 (2022).
4. W. Judge, H. Chan, S.KRS. Sankaranarayanan, R.J. Harder, J. Cabana, & M. J. Cherukara. *Defect identification in simulated Bragg coherent diffraction imaging by automated AI*. MRS Bulletin **48**, 124-133 (2023).
5. Y. Yao, H. Chan, S. Sankaranarayanan, P. Balaprakash, R. J. Harder, M. J. Cherukara. *AutoPhaseNN: unsupervised physics-aware deep learning of 3D nanoscale Bragg coherent diffraction imaging.* npj Comput Mater **8**, 124 (2022).
6. M. Chang, C. Tung, S. Chang, J. M. Carrillo, Y. Wang, B. G. Sumpter, G. Huang, C. Do & W. Chen. *A machine learning inversion scheme for determining interaction from scattering*. Communication Phys **5**, 46 (2022).
7. O. Yildiz, H. Chan, K. Raghavan, W. Judge, M. J. Cherukara, P. Balaprakash, S. K. R. S. Sankaranarayanan & T. Peterka. *Automated Continual Learning of Defect Identification in Coherent Diffraction Imaging.* IEEE/ACM International Workshop on Artificial Intelligence and Machine Learning for Scientific Applications (**AI4S***)*, 1-6 (2022)
8. A. V. Babu, T. Zhou, S. Kandel, T. Bicer, Z. Liu, W. Judge, D. Ching, Y. Jiang, S. Veseli, S. Henke, R. Chard, Y. Yao, E. Sirazitdinova, G. Gupta, M. V. Holt, I.T. Foster, A. Miceli and M. J. Cherukara, *Deep learning at the edge enables real-time, streaming ptychography*, Nature Communications, **14**, 7059 (2023).
9. S. Kandel, T. Zhou, A. V. Babu, Z. Di, X. Li, X. Ma, M. Holt, A. Miceli, C. Phatak and M. J. Cherukara, *Demonstration of an AI-driven workflow for autonomous high-resolution scanning microscopy*. Nature Communications, **14**, 5501 (2023)
10. C-H Tung, Y-J Hsiao, H-L Chen, G-R Huang, L. Porcar, M-C Chang, J-M Carrillo, Y. Wang, B. G. Sumpter, Y. Shinohara, J. Taylor, C. Do, W-R Chen. *Unveiling mesoscopic structures in distorted lamellar phases through deep learning-based small angle neutron scattering analysis*. Journal of Colloid and Interface Science*,* **659**,739–750 (2024).

Patents and Invention Disclosure:

1. Systems and methods for hierarchical multi-objective optimization
Inventors - Henry Chan, Mathew J Cherukara, Badri Narayanan, Stephen K Gray, Troy David Loeffler, Subramanian Sankaranarayanan, **US Patent App. 16/704,936 (Approved - 2023)**

2. Systems and methods for active learning from sparse training data
Inventors - Subramanian Sankaranarayanan, TD Loeffler, H Chan. **US Patent App. 16/847,098 (Approved - 2023)**

Electron Distillery 2.0: Massive Electron Microscopy Data to Useful Information with AI/ML

PI: Andrew Minor, Lawrence Berkeley National Laboratory

Keywords: Electron Microscopy, AI/ML, Spectroscopy, Electron Detection, 4D-STEM

Research Project Scope

The Electron Distillery 2.0 will develop and deploy methods and tools based on artificial intelligence and machine learning (AI/ML) to analyze electron scattering information from the data streams of fast direct electron detectors, including a new Electron Energy Loss Spectroscopy (EELS) currently under development at LBNL. As a result of the increased proliferation and continuing improvements in high-speed electron detectors, there is a critical need to change the way we design and run electron microscopy scattering experiments and analyze the extremely high rates and large amounts of data. In the initial phase of our project (Distillery 1.0), we emphasized extending our capabilities in electron detection and automation alongside developing tools to distill information from large amounts of data. Here, we propose new workflows that extend, combine, and further automate these modalities, bolstered by improvements in electron detection and computational methods (Figure 1). The Distillery 2.0 project is divided into 4 Thrusts to build end-to-end workflows for automation and correlation of data in real, reciprocal, and energy coordinates. *Thrust 1* will develop ML tools detect and localize electron strikes. *Thrust 2* will extend our ability to perform quantitative EELS interpretation and electronic structure. *Thrust 3* will improve quantitative 4D-STEM analysis methods, and *Thrust 4* will continue to automate HR-

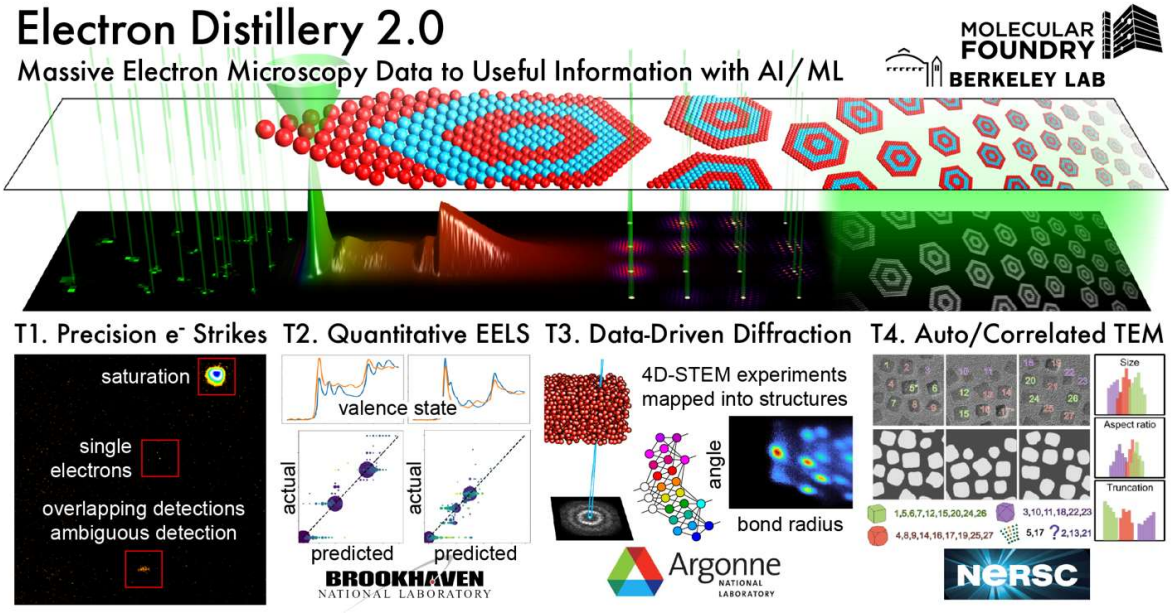

Figure 1: Overview of the Electron Distillery 2.0 with 4 research thrusts

TEM experiments and correlate HR-TEM datastreams with EELS and 4D-STEM data. Together, these four research thrusts will utilize AI/ML to address the diversity and massive amounts of data produced by high frame rate direct electron detectors to produce unique and useful information for scientific studies.

Recent Progress

Work in Thrust 1 has accomplished a highly parallelized electron detection routine on NERSC to reduce the sparse diffraction patterns produced by the 4D Camera to only the necessary information. This has allowed the large data sets produced by the detector to be analyzed nearly live at the microscope to reduce the time required to distill information from data. Traditional methods to detect strike events rely on the centroid of surrounding pixels, but ML can take advantage of the entire distribution of pixel intensities to achieve more accurate predictions and extend the capability to multiple electron strikes.

Thrust 2 focuses on the application of AI/ML tools for the interpretation of Electron Energy Loss Spectroscopy (EELS) data. Accuracy of simulation methods depends on the accuracy of underlying physical description and the ability to capture the complexity of realistic systems. To do so, we have built an ML Random Forest (RF) model capable of predicting the valence of an absorber based on its EELS spectrum. This procedure has been used to calculate all materials predicted to be stable or experimentally observed by the Materials Project containing Cu, Co, Fe, or Ti, resulting in a total database of nearly 10,000 simulated spectra with around two thirds newly calculated by our automated simulation procedure. Using these spectra, we have trained RF models predicting bond valences and applied them to EELS spectra acquired on the TEAM I instrument at the Molecular Foundry [1].

In Thrust 3, we have tackled the problem of multiple scattering in electron diffraction patterns using machine learning [2]. We first selected a large cross section of crystal structures from the Materials Project. We then simulated STEM diffraction patterns for many sample thicknesses and orientations, and various microscope parameters. We augmented this data with experimental errors including pattern shift, ellipticity, shot noise, inelastic background signals, and detector artifacts. Finally, we developed a new ML architecture which is based on U-Net, adapted to use complex numbers in the activation layers, spectral pooling, and to pool information in Fourier space, which we named FCU-Net. The trained FCU-Net developed in the Distillery project has been fully implemented into the py4DSTEM toolkit and trained networks are available in open source repositories.

In Thrust 4, we have systematically identified how data preprocessing, neural network architecture, and training data bias subsequent HR-TEM image analysis, focusing on how to customize machine learning workflows for the unique features in HR-TEM data and robustness across microscope sessions. To enable reusable models across microscope sessions and users, we identified critical data preprocessing protocols like standardization and flat-field correction that

convert raw camera output into a robust form suitable for data-driven model training or inference. In addition, we have collected and curated experimental datasets to cross-validate network performance across various microscope conditions and sample parameters. These results give important insights towards building workflows for ML based analysis of HR-TEM data.

Future Plans

Future work in Thrust 1 will focus on developing and deploying ML methods for improved "counting" with sub-pixel resolution in low-dose imaging and EELS. Techniques for dealing with higher occupancies will play key roles in low-loss EELS as well as *in-situ* imaging will be implemented. In Thrust 2, we intend to extend our techniques to measure the dependance of the

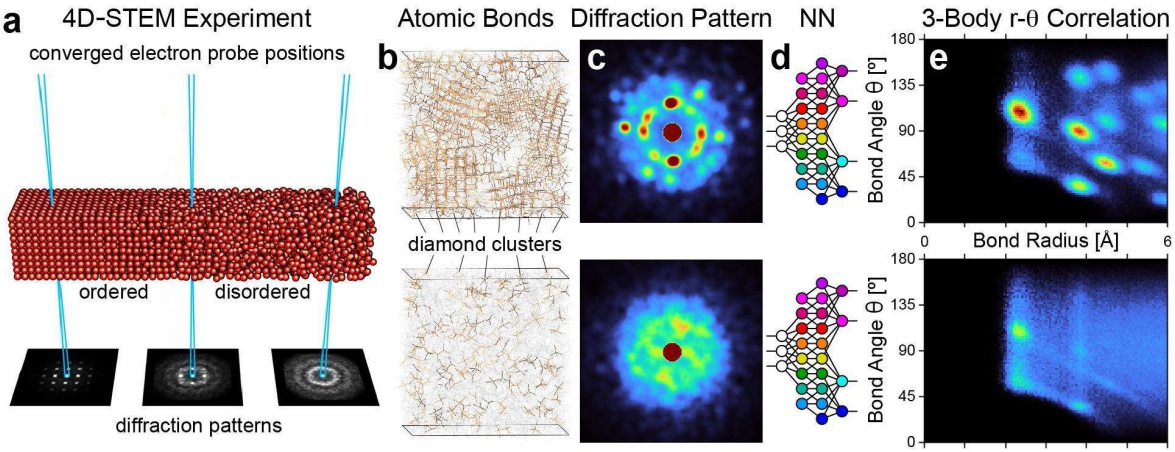

Figure 2: (a) 4D-STEM experiment showing diffraction ordered to disordered structures. (b) atomic structures of nanocrystalline and amorphous silicon, with (c) characteristic diffraction patterns. (d) Neural network trained to predict (e) a three-body radial-angular bond distribution.

electronic structure on scattering angle and/or beam impact parameter will allow us to directly compare EELS derived electronic structure to the dispersion relations obtained through ARPES providing a much sought information on the role of lattice defects and interfaces on the properties of functional heterostructures. In Thrust 3, we will extend our methods of analyzing crystalline materials to the challenge of characterizing disordered materials by combining 4D-STEM experiments with AI/ML is shown in Figure 2. We will use our ML methods to characterize a wide variety of disordered materials, going beyond single-component systems and directly measuring useful structural information such as cluster polyhedra and bonding motifs. Our approach will also allow us to make accurate measurements for thicker samples by including these in the training datasets, and improve robustness by augmenting the data with experimental limitations such as inelastic backgrounds or limited electron dose.

The Distillery 1.0 program enabled the acquisition of large datasets through experimental automation pipelines and rapid data reduction over a dedicated 100 Gbit network connection. Users interact with the detector and high performance computing environment through the Distiller web application and Jupyter notebooks. We will further integrate the 4D Camera and the new EELS detector with the Distiller to allow for automated data synchronization and analysis. Workflows will be developed to reduce and analyze data taking advantage of the previously developed electron counting, 4D-STEM analysis, and EELS spectroscopy analysis capabilities. This will allow for fully automated data acquisition and analysis without the need for human intervention. In conjunction with automated imaging, there is a simultaneous need for tools that help users visualize and understand large scale HR-TEM data during acquisition. In Thrust 4, we will adapt previously implemented algorithms used to classify data, such as supervised or unsupervised classification of images of nanoparticles [3] to periodically analyze data and cease collection when certain statistical population requirements have been met (Fig. 3). Ultimately, this work will enable efficient instrument usage during large scale analysis of automatically collected HR-TEM data, including immediate statistical feedback of nanoparticle populations during data collection.

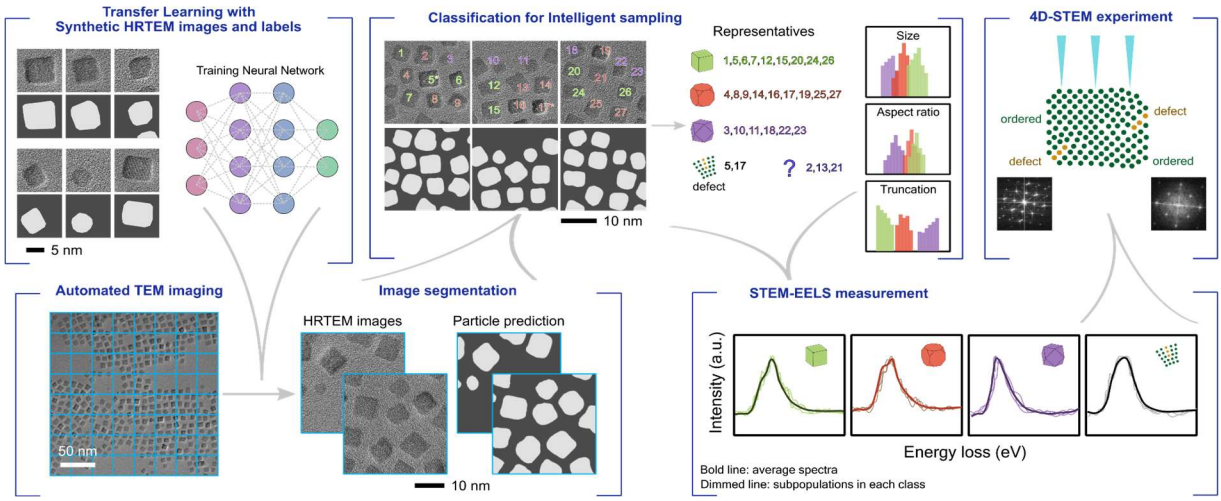

Figure 3. Automated HR-TEM pipeline leveraging transfer learning and class averaging to correlate data streams and enhance signal to noise in measurements.

References

1. S.P. Gleason, D. Lu, J. Ciston, “Prediction of the Cu Oxidation State from EELS and XAS Spectra Using Supervised Machine Learning”, arXiv preprint arXiv:2309.04067

2. Joydeep Munchi, Alexander Rakowski, Benjamin H. Savitsky, Steven E. Zeltmann, Jim Ciston, Matthew Henderson, Shreyas Cholia, Andrew M. Minor, Maria K.Y. Chan, Colin Ophus, “Disentangling multiple scattering with deep learning: application to strain mapping from electron diffraction patterns”. npj Comput Mater 8, 254 (2022).

3. C. K. Groschner, C. Choi, M. C. Scott, “Machine learning pipeline for segmentation and defect identification from high-resolution transmission electron microscopy data”, Microscopy and Microanalysis, 27 (3) 549-556 (2021)

Publications

1. Sytwu, Katherine, Luis Rangel DaCosta, and Mary C. Scott. "Generalization Across Experimental Parameters in Neural Network Analysis of High-Resolution Transmission Electron Microscopy Datasets." Microscopy and Microanalysis, ozae001. (2024):

2. Burns, Kory, et al. "Deep learning-enabled probing of irradiation-induced defects in time-series micrographs." *APL Machine Learning* 2.1 (2024)

3. Joydeep Munchi, Alexander Rakowski, Benjamin H. Savitsky, Steven E. Zeltmann, Jim Ciston, Matthew Henderson, Shreyas Cholia, Andrew M. Minor, Maria K.Y. Chan, Colin Ophus, “Disentangling multiple scattering with deep learning: application to strain mapping from electron diffraction patterns”. npj Comput Mater 8, 254 (2022).

4. Sytwu, Katherine, Catherine Groschner, and Mary C. Scott. "Understanding the Influence of Receptive Field and Network Complexity in Neural Network-Guided TEM Image Analysis." Microscopy and Microanalysis 28.6 (2022): 1896-1904.

5. Colin Ophus, Steven E. Zeltmann, Alexandra Bruefach, Alexander Rakowski, Benjamin H. Savitzky, Andrew M. Minor, Mary C. Scott, “Automated Crystal Orientation Mapping in py4DSTEM using Sparse Correlation Matching,” Microscopy and Microanalysis 28 , 390 (2022)

6. Philipp M Pelz, Ian Johnson, Colin Ophus, Peter Ercius, and Mary C. Scott. "Real-time interactive 4D-STEM phase-contrast imaging from electron event representation data: less computation with the right representation." IEEE Signal Processing Magazine 39, no. 1 (2021): 25-31

7. Sergei V. Kalinin, Colin Ophus, Paul M. Voyles, Rolf Erni, Demie Kepaptsoglou, Vincenzo Grillo, Andrew R. Lupini, Mark P. Oxley, Eric Schwenker, Maria K. Y. Chan, Joanne Etheridge, Xiang Li, Grace G. D. Han, Maxim Ziatdinov, Naoya Shibata, Stephen J. Pennycook, “Machine learning in scanning transmission electron microscopy”, Nature Reviews Methods Primers 2, 11 (2022)

8. Xinxing Peng, Philipp M Pelz, Q. Zhang,P. Chen, Yaqian, Zhang, H.G. Liao, Haimei Zheng, C. Wang, S.G. Sun, and Mary C. Scott., Observation of formation and local structures of metal-organic layers via complementary electron microscopy techniques. Nature communications, 13(1), p.5197. (2022)

9. Dillan J. Chang, Colum M. O'Leary, Su Cong, Daniel A. Jacobs, Salman Kahn, Alex Zettl, Jim Ciston, Peter Ercius, and Jianwei Miao. "Deep-Learning Electron Diffractive Imaging." Physical Review Letters 130 (1): 016101. (2023)

Author
Index

Allan, Daniel 213, 225
Antonsen Jr., Thomas M. 41
Assoufid, Lahsen 54
Barber, Sam 18
Benediktovitch, Andrei 8
Bennett, Douglas 148
Bergmann, Uwe 8
Bilheux, Hassina 219
Bilheux, Jean 219
Blokland, Willem 201
Borland, Michael 196
Bouman, Charles 219
Buzzard, Gregery 219
Campbell, Stuart 219, 225
Carbajo, Sergio 158, 163
Chan, Henry 218, 231, 236
Chan, Maria K. 225, 231
Chen, Si 66
Cherukara, Mathew 231
Chowdhury, Mohammad S. N. 219
Chuang, Yi-De 128, 131
Chubar (Tchoubar), O. 95
Coffee, Ryan 15, 207
Curtis, T.L. 128, 132
Cutler, Grant 54
Dakovski, Georgi 128
Darancet, Pierre 218, 231
de Long, Lance 128
Denes, Peter 133, 136
Doleans, M. 37, 40
Donetski, Dmitri 101
Dragone, Angelo 120
Edelen, Auralee 20, 191, 196
England, Joel 183
Fischer, Peter 128, 131, 132
Fisher, A. S. 32, 35
Foster, Ian 207
Freund, Henry P. 41
Fullerton, Eric 128
Gavrilov, Dmitri 219
Gluskin, Efim 49
Grace, Carl 153
Gulley, Mark 153
Halavanau, Aliaksei (Alex). 8
Hastings, Todd 128, 132
Hayward, Jason P. 145, 147
Heald, Steve M. 225
Hellman, Frances 128, 131, 132
Hemsing, Erik 23, 26
Henstridge, M. 32
Herbst, Ryan 207
Hexemer, Alexander 128, 213, 218
Hine, G. 37
Hoffmann, M. C. 32, 35
Huang, Lei 54, 60
Huang, Xiaobiao 196
Huang, Z. 2, 6, 26, 32, 35, 36
Idir, Mourad 60
Islegen-Wojdyla, Antoine 71
Kanatzidis, Mercouri 140, 143
Kapadia, Rehan 169
Karkare, Siddharth 164, 174
Kenesei, Peter 207
Kettimuthu, Rajkumar 207
Kevan, Steve 128
Kim, Kwang-Je 85, 88, 89
Krejcik, Patrick ..... i, 51
Lanza, G. 2
Lindberg, R. 2, 7
Lu, Deyu 225
Lukosi, Eric 140, 143, 144
Luo, Tianhuan 174
Ma, Yanbao 90
Marinelli, Agostino 12, 15, 16, 17
Maxson, Jared 174, 178, 190
Mazzoli, Claudio 101
McCarter, Margaret 128
McPhate, J.B. 128, 132
McReynolds, Dylan 225
Mehta, Apurva 213, 215
Miceli, Antonino 120, 207
Micelli, Nino 116
Minor, Andrew 237
Montoya, Sergio 128
Morley, Sophie 128
Moss, C. 37
Musumeci, Pietro 174
Naji, A. 32, 36
Nazaretski, E. 76, 79
O'Shea, Patrick G. 41

Othman, M. 32
Padmore, Howard 80
Pellegrini, Claudio 8
Peterka, Tom 231
Podobedov, Boris 101, 105
Prebys, Eric 153
Prince, Michael 207
Qu, Xiaohui 225
Rabedeau, Thomas 54
Raffanti, R. 128, 132
Ratner, Daniel 196
Roy, Sujoy 128, 131, 132
Rumaiz, Abdul K. 116, 125
Saleheen, Ahmad U. 128, 131, 132
Sankaranarayanan, Subramanian ... 213, 231, 236
Scholl, Andreas 128, 132
Schram, Malachi 201
Schumm, Bruce A. 153
Schwarz, Nicholas 207, 213, 225
Segal, Julie 116
Sharma, Hemant 207
Shvyd'ko, Yuri 85, 88, 89
Smedley, John 174
Smedley, Jonathan 153
Stavitski, Eli 225
Sumpter, Bobby 231
Sun, Chengjun 225
Tang, Shimin 219
Tercero, D. 128, 132
Thayer, Jana 120, 207
Thom-Levy, Julia 116
Tremsin, Anton 128
Turner, Josh 128
Turqueti, Marcos 46, 48
Vallerga, J.V. 128, 131, 132
Vasudevan, Rama K. 213
Vecchione, Theodore 174
Venkatakrishnan, Singanallur (Venkat).. 219
Vo, Nghia 219
Voronov, Dmitriy 80
Wang, Dan 183, 187
Wang, Guimei 196
Wang, Jin 88, 106, 111
Wang, Tianyi 60
Wen, Xianfei 145, 147
White, M. 2, 6
Whitelam, Stephen 231
Woods, Justin 128
Wu, Juhao 90
Yang, Wanli 225
Yang, Xiaogang 219
Yoo, Shinjae 225
Zhang, Zhen 15, 16, 17, 27, 29, 30, 31

Participant List

Last Name	First Name	Email Address	Company Name
Assoufid	Lahsen	assoufid@anl.gov	Argonne National Laboratory
Barber	Sam	Sbarber@lbl.gov	LBNL
Benkechkache	Mohamed El Amine	mbenkech@utk.edu	University of Tennessee
Bennett	Douglas	Douglas.Bennett@nist.gov	NIST
Bergmann	Uwe	ubergmann@wisc.edu	University of Wisconsin–Madison
Bilheux	Hassina	bilheuxhn@ornl.gov	Oak Ridge National Laboratory
Blokland	Willem	blokland@ornl.gov	oak ridge national laboratory
Campbell	Stuart	scampbell@bnl.gov	Brookhaven National Laboratory
Cantoni	Claudia	claudia.cantoni@science.doe.gov	U.S. Department of Energy, BES
Carbajo	Sergio	scarbajo@ucla.edu	University of California Los Angeles
Carini	Gabriella	carini@bnl.gov	Brookhaven National Laboratory
Chan	Maria	mchan@anl.gov	Argonne National Laboratory
Chen	Si	sichen@anl.gov	Argonne National Laboratory
Chubar	Oleg	chubar@bnl.gov	Brookhaven National Laboratory
Colby	Eric	Eric.Colby@science.doe.gov	Accelerator Stewardship (HEP, ARDAP)
Cutler	Grant	gdcutler@lbl.gov	Lawrence Berkeley National Lab
Denes	Peter	pdenes@lbl.gov	Lawrence Berkeley National Laboratory
Doering	Dionisio	ddoering@slac.stanford.edu	SLAC National Laboratory
Doleans	Marc	doleansmm@ornl.gov	Oak Ridge National Laboratory
Dorman	James	james.dorman@science.doe.gov	BES
Dragone	Angelo	dragone@slac.stanford.edu	SLAC National Accelerator Laboratory
Dunne	Mike	mdunne@slac.stanford.edu	SLAC National Accelerator Laboratory
Edelen	Auralee	edelen@slac.stanford.edu	SLAC National Accelerator Laboratory
England	Joel	england@slac.stanford.edu	SLAC National Accelerator Laboratory
Feng	Yiping	yiping.feng@science.doe.gov	Basic Energy Sciences
Freund	Henry	hfreund@umd.edu	University of Maryland
Frost	Matthew	frostmj@ornl.gov	ORNL/BES-SUF
Ginsburg	Camille	camille.ginsburg@science.doe.gov	DOE/SC/ARDAP
Gluskin	Efim	gluskin@anl.gov	Argonne National laboratory
Graafsma	Heinz	heinz.graafsma@desy.de	DESY-Hamburg; Germany
Gruner	Sol	smg26@cornell.edu	Cornell University
Haes	Amanda	amanda.haes@science.doe.gov	DOE/BES
Halavanau	Aliaksei (Alex)	aliaksei@slac.stanford.edu	SLAC National Accelerator Laboratory
Hayward	Jason	jhayward@utk.edu	University of Tennessee
Hemsing	Erik	ehemsing@slac.stanford.edu	SLAC

Last Name	First Name	Email Address	Company Name
Hexemer	Alexander	ahexemer@lbl.gov	Lawrence Berkeley Natl Lab
Huang	Zhirong	zrh@slac.stanford.edu	SLAC
Huang	Lei	lhuang@bnl.gov	Brookhaven National Laboratory
Hudson	Paul	paul.hudson@orau.org	ORISE
Idir	Mourad	midir@bnl.gov	Brookhaven National Laboratory (BNL)
Islegen-Wojdyla	Antoine	awojdyla@lbl.gov	Berkeley Lab
Kapadia	Rehan	rkapadia@usc.edu	University of Southern California
Karkare	Siddharth	karkare@asu.edu	Arizona State University
Keavney	Dava	Dava.Keavney@science.doe.gov	DOE Office of Science
Krejcik	Patrick	pkr@slac.stanford.edu	SLAC National Accelerator Laboratory
Lanza	Giulia	glanza@slac.stanford.edu	SLAC National Accelerator laboratory
Lessner	Eliane	Eliane.Lessner@science.doe.gov	DOE/SC/BES
Li	Derun	Derun.Li@science.doe.gov	Office of High Energy Physics
Lindberg	Ryan	lindberg@anl.gov	Argonne National Laboratory
Lukosi	Eric	elukosi@utk.edu	University of Tennessee-Knoxville
Ma	Yanbao	yma5@ucmerced.edu	University of California Merced
Marinelli	Agostino	marinelli@slac.stanford.edu	SLAC
Maxson	Jared	maxson@cornell.edu	Cornell University
Mehta	Apurva	mehta@slac.stanford.edu	SLAC national accelerator Lab
Miceli	Antonino	amiceli@anl.gov	Argonne National Laboratory
Minor	Andrew	aminor@lbl.gov	Lawrence Berkeley National Laboraory
Miranda	Raul	raul.miranda@science.doe.gov	DOE
Nazaretski	Evgeny	enazaretski@bnl.gov	Brookhaven National Laboratory
O'Shea	Patrick	poshea@umd.edu	University of Maryland
Pellegrini	Claudio	claudiop@slac.stanford.edu	SLAC National Accelerator Laboratory
Podobedov	Boris	boris@bnl.gov	Brookhaven National Laboratory
Rabedeau	Thomas	rabedeau@slac.stanford.edu	SLAC
Ratner	Daniel	dratner@slac.stanford.edu	SLAC
Roy	Sujoy	sroy@lbl.gov	Lawrence Berkeley National Lab
Rumaiz	Abdul	rumaiz@bnl.gov	Brookhaven National Laboratory
Sankaranarayanan	Subramanian	skrssank@anl.gov, ssankaranarayanan@anl.gov	Argonne National Laboratory
Scholl	Andreas	a_scholl@lbl.gov	Lawrence Berkeley Lab
Schram	Malachi	schram@jlab.org	Jefferson Lab
Schumm	Bruce	baschumm@ucsc.edu	University of California / Santa Cruz Institute for Particle Physics

Last Name	First Name	Email Address	Company Name
Segal	Julie	jsegal@slac.stanford.edu	SLAC National Accelerator Laboratory
Shiri	Abbass	abbasshiri@ucla.edu	UCLA
Shvydko	Yury	shvydko@anl.gov	Argonne National Laboratory
Smedley	John	smedley@slac.stanford.edu	SLAC
Stavitski	Eli	istavitski@bnl.gov	Brookhaven National Laboratory
Sumpter	Bobby	sumpterbg@ornl.gov	Oak Ridge National Lab
Sun	Chengjun	cjsun@anl.gov	Argonne National Laboratory
Thayer	Jana	jana@slac.stanford.edu	SLAC National Accelerator Laboratory
Thom-Levy	Julia	jt297@cornell.edu	Cornell University
Tremsin	Anton	astr@berkeley.edu	University of California at Berkeley
Turqueti	Marcos	mturqueti@lbl.gov	Lawrence Berkeley National Laboratory
Venkatakrishnan	Singanallur	venkatakrisv@ornl.gov	Oak Ridge National Laboratory
Voronov	Dmitriy	dlvoronov@lbl.gov	Lawrence Berkeley National Lab
Wang	Guimei	gwang@bnl.gov	Brookhaven National Laboratory
Wang	Dan	dwang2@lbl.gov	LBNL
Wang	Jin	Wangj@anl.gov	Argonne National Laboratory
Wen	Xianfei	xwen5@utk.edu	University of Tennessee, Knoxville
White	Marion	mwhite@anl.gov	Argonne National Laboratory
Wu	Juhao	jhwu@slac.stanford.edu	SLAC
Yang	Wanli	WLYang@lbl.gov	Lawrence Berkeley National Lab
Zakharov	Dmitri	dzakharov@bnl.gov	Brookhaven National Laboratory
Zhang	Zhen	zzhang@slac.stanford.edu	SLAC